Aeroelastic Effects on Tall Buildings: Performance-Based Comfort Analysis

Dissertation

submitted to and approved by the

Department of Architecture, Civil Engineering and Environmental Sciences
University of Braunschweig – Institute of Technology

and the

Faculty of Engineering
University of Florence

in candidacy for the degree of a
Doktor-Ingenieur (Dr.-Ing.) /
Dottore di Ricerca in "Riduzione del Rischio da Catastrofi Naturali su Strutture ed Infrastrutture" *)

by
Chiara Pozzuoli
Born 09.07.1983
from Perugia (PG), Italy

Submitted on	14 September 2012
Oral examination on	08 November 2012
Professorial advisors	Prof. G. Bartoli
	Prof. U. Peil

2012

*) Either the German or the Italian form of the title may be used.

To my family
for their love and support
every step of the way

Acknowledgements

First of all I would like to thank my tutors, Prof. Gianni Bartoli and Prof. Udo Peil, for their support and advice. I feel deeply indebted to Prof. Gianni Bartoli for his inspiring and thoughtful direction and guidance throughout my PhD study. I would like to offer my gratitude to Prof. Claudio Borri for his strong efforts for this doctoral course. All my gratefulness to Claudio Mannini for his indispensable help and passion for scientific research. Special thanks go to Massimiliano Gioffrè and Seymour M. J. Spence for the fruitful scientific discussions and exchange of ideas and for cooperation during wind tunnel tests. I sincerely thank all the colleagues of the International Doctoral Course for the help and friendly support I have often received during all these three and a half years. Special thanks to Davide Allori for his help during the most onerous phases of the experimental campaign and to Antonino Maria Marra for his corrections. All my gratitude to all the people of the Institute of Steel Structures of Braunschweig for their warm friendship during the months spent in Germany. I was greeted by all of them with the utmost respect and hospitality. I feel deeply grateful to Mathias Clobes for all the fruitful discussions about the results of my thesis. I would like to thank Lorenzo Procino and Alessandra Borsani for their help during the long test campaign in the CRIACIV wind tunnel and to Serena Cartei who has friendly supported me in all the bureaucratic and organizational issues. It would be difficult to acknowledge everyone who has in some way or another contributed to the research reported in this thesis. I have received help and encouragement from many people in different ways. I am grateful to Marco Guglielmo Ribigini and his father, Vittorio, for their effectual cooperation during the construction of the model tested in the wind tunnel. Thanks also to Gianfranco Stella, for his friendly advice. Moreover, I owe much to my family for always believing in me and encouraging me to achieve my goals. Without their practical support, encouragement and understanding, it would have been impossible for me to complete this work.

Contents

List of Figures

List of Tables

List of Symbols

α	exponent of the power law profile
$\chi^2()$	aerodynamic admittance function
δ	boundary layer thickness
δ	logarithmic decrement
κ	von Kármán's constant
λ_a	acceleration scale
λ_f	frequency scale
λ_l	length scale
λ_t	time scale
λ_U	velocity scale
$[C]$	damping matrix
$[K]$	stiffness matrix
$[M]$	mass matrix
μ	dynamic viscosity
ν	kinematic viscosity
ω	circular frequency
ϕ	mode shape
ρ	density, air density
ρ_b	bulk density
σ	standard deviation
τ_0	shear stress at the ground surface
ξ	damping ratio
ξ_s	structural damping ratio
ξ_a	aerodynamic damping ratio

ξ_{tot}	total damping ratio
a	linear acceleration
a_α	angular acceleration
b	breadth
C_D	drag coefficient
C_F	force coefficient
C_L	lift coefficient
C_M	moment coefficient
C_p	pressure coefficient
D	drag
d	depth
E	Young's modulus
F	force
f	frequency
$F()$	cumulative distribution function
$F()$	wind load
F_a	aeroelastic force
f_n	natural frequency
f_r	reduced frequency
F_s	aerodynamic force
f_s	shedding frequency
G	torsional modulus
$H()$	frequency response function
h, H	height
I	moment of inertia
I_u	turbulence intensity of the along-wind turbulent component
L	integral length scale
L	lift
l	length
M	moment

m	mass
M_D	mass-damping coefficient
$m_{i,e}$	equivalent mass per unit length for mode i
P	probability
p	pressure
$P()$	generalized wind load
$p()$	probability density function
p_0	static pressure
p_{dyn}	dynamic pressure
q	generalized displacement
R	return period
Re	Reynolds number
S	Power Spectral Density (PSD)
Sc	Scruton number
St	Strouhal number
U	mean velocity
u	longitudinal turbulent component
u_*	friction velocity
U_0	velocity of the undisturbed flow
U_∞	free-stream velocity
U_h	wind speed at model height
U_r	reduced velocity
U_{crit}	critical wind speed
$U_{r,crit}$	critical reduced velocity
v	lateral turbulent component
w	vertical turbulent component
z_0	roughness length
z_h	zero-plane displacement
z_{ref}	reference height

Abstract

Recent trends towards increasingly taller and slender buildings have led to a new generation of wind-sensitive structures, that can experience large wind-induced vibrations. Excessive dynamic oscillations can then cause discomfort to occupants, sometimes raising concerns about serviceability design problems. Vibration perception is subjective and depends on the vibration frequency and on physiological and psychological factors.

It is now widely accepted that the perception of wind-induced vibrations is closely related to the acceleration response of structures. It has, therefore, to be checked that the latter is limited under tolerable thresholds.

Wind risk assessment of tall buildings, related to occupant comfort under serviceability conditions, requires, therefore, the proper estimation of the acceleration responses. For tall, slender buildings, their across-wind dynamic responses usually exceed along-wind ones. The across-wind response, compared with that in the along-wind direction, is less related to fluctuations of the incoming wind, since it results mainly from the aerodynamic pressure fluctuations in the separated shear layers and wake flow fields.

Moreover, aeroelastic or motion-induced effects, such as lock-in and galloping, may take place and cause vibrations significantly different from those predicted with the assumption of rigid structures. For these reasons, wind tunnel tests represent the most reliable means for determining across-wind responses of slender structures susceptible of not negligible aeroelastic effects.

A wide experimental activity was carried out in the CRIACIV[1] (Centro di Ricerca Interuniversitario di Aerodinamica delle Costruzioni e Ingegneria del Vento) boundary layer wind tunnel, using a continuous equivalent aeroelastic model of a square-section building, previously investigated through rigid model tests.

The model, which is a "skin-skeleton" type one, is equipped with simultaneously measuring pressure taps and is mounted on a 5-components high-frequency force balance which enables the measurement of the overall forces at the base of the model. The dynamic characteristics (frequency, mode shape and damping) of the model-support system for the first three modes of vibration were identified by means of free vibration tests.

Wind tunnel tests were carried out orienting the model so that the incoming wind direction is perpendicular to the direction of the first identified bending mode. Three displacement laser transducers and three mono-axial accelerometers were used to measure across-wind displacement and along- and across-wind acceleration responses, respectively. Measurements were carried out for a wide range of wind speeds, including the critical velocity for vortex-induced vibrations. The main goal

[1] Interuniversity Research Center of Building Aerodynamics and Wind Engineering

of this experimental activity was the simultaneous measurement of pressures, overall forces, displacements and accelerations on an aeroelastic model, even in lock-in conditions.

From the analysis of the measured pressure field and responses, several results were obtained, including the possible variation of the Strouhal number with height over the tunnel floor, the correlation structure of pressures, the lock-in wind speed range, the RMS acceleration and displacement responses as functions of wind speed. Moderate motion-induced effects involving the pressure field were observed, while aeroelasticity was found to play an important role in the measured components of across-wind responses, in terms of displacements and accelerations.

A Finite Element Method model was also developed in order to compare the measured aeroelastic response with that predicted numerically from pressures measured on a rigid model. The benchmarking of the two responses allowed the identification of aeroelastic effects in terms of aerodynamic damping. The latter, in the case of high structural damping, gives a positive contribution, which means that, for the structure under investigation, aeroelastic effects decrease the across-wind response. Neglecting them is, therefore, a conservative choice. The identified aerodynamic damping as a function of reduced velocity was also compared with results from other literature works. The across-wind response of the model can be estimated from pressures on a rigid model, taking into account aeroelastic effects by means of an additional damping term.

A general procedure for the assessment of wind-induced discomfort risk of tall buildings is proposed. It is in line with the Performance-Based Wind Engineering approach and with the general risk management framework developed within the IGC 802. The procedure consists in two phases, namely the hazard analysis and the structural vulnerability analysis. According to any comfort criteria adopted, wind-induced risk is expressed in terms of the probability of exceeding the comfort threshold and can be translated into the average number of days per year in which the building experiences unacceptable vibrations. In order to illustrate how this risk assessment procedure works, it is applied to a square-section tall building whose response to the wind action is estimated from wind tunnel tests.

Sommario

L'attuale tendenza verso la costruzione di strutture sempre più alte e più snelle ha portato allo sviluppo di una nuova generazione di edifici alti particolarmente sensibili all'azione del vento. Quest'ultima può, infatti, dar luogo a vibrazioni importanti che causano problemi di discomfort degli occupanti, la cui entità varia da soggetto a soggetto e dipende dalla frequenza di oscillazione e da fattori fisiologici e psicologici.

La percezione delle vibrazioni indotte dal vento è strettamente correlata alla risposta in accelerazione, la quale dovrà essere contenuta entro definiti limiti di tollerabilità. La valutazione della performance degli edifici alti nei confronti del comfort richiede, quindi, la determinazione della risposta in accelerazione dovuta all'azione del vento. È nella direzione trasversale al vento (across-wind) che, in genere, si verificano le maggiori accelerazioni. La risposta across-wind è meno correlabile alle fluttuazioni turbolente del vento incidente rispetto alla risposta along-wind (nella direzione del vento), poiché è determinata prevalentemente dalle fluttuazioni della pressione aerodinamica nella zona di separazione e di scia vorticosa.

Fenomeni moto-indotti, detti aeroelastici, quali il lock-in ed il galloping, possono inoltre verificarsi e determinare risposte sensibilmente diverse da quelle ottenute nell'ipotesi di struttura indeformabile. Le prove sperimentali in galleria del vento su modelli aeroelastici costituiscono oggi lo strumento più diffuso per la stima della risposta trasversale al vento di edifici flessibili per i quali i fenomeni moto-indotti non sono trascurabili.

Un'ampia campagna sperimentale in condizioni di flusso turbolento è stata condotta nella galleria del vento del CRIACIV (Centro di Ricerca Interuniversitario di Aerodinamica delle Costruzioni e Ingegneria del Vento) su un modello aeroelastico equivalente continuo di un edificio regolare a base quadrata, oggetto di prove precedenti su modello rigido. Al fine di misurare la distribuzione delle pressioni durante il flusso in galleria, il modello è stato equipaggiato di prese di pressione acquisite simultaneamente. Il modello è stato inoltre montato su una bilancia aerodinamica per la misura delle forzanti alla base. Le caratteristiche dinamiche (frequenza, forma modale e smorzamento) del sistema modello-supporto così ottenuto sono state identificate, per i primi 3 gradi di libertà, mediante test in oscillazioni libere. Le prove sperimentali sono state quindi eseguite adottando una direzione del vento incidente ortogonale alla direzione di vibrazione del primo modo identificato.

Attraverso tre trasduttori laser e tre accelerometri istallati sul modello è stato possibile misurare, rispettivamente, lo spostamento across-wind e la risposta in accelerazione in sommità, sia in direzione along-wind che across-wind. Le misure sono state effettuate per un ampio range di velocità contenente la velocità critica di lock-in. La campagna sperimentale è stata realizzata con lo scopo fondamentale di

ottenere una misura simultanea di pressioni, forze, spostamenti ed accelerazioni su un modello aeroelastico in galleria del vento anche in condizioni di sincronizzazione.

Dall'analisi dei coefficienti di pressione e delle risposte sono stati ricavati la variazione del numero di Strouhal con la quota, la struttura di correlazione delle pressioni, l'intervallo di lock-in, la variazione delle accelerazioni e degli spostamenti con la velocità. Gli effetti aeroelastici osservati coinvolgono in modo lieve il campo di pressione e più significativamente la risposta across-wind in termini di spostamento e di accelerazione.

È stato inoltre sviluppato un modello agli elementi finiti al fine di confrontare la risposta aeroelastica misurata con quella ottenuta numericamente a partire dalle pressioni misurate su modello rigido. Il confronto tra le due risposte ha permesso di identificare gli effetti aeroelastici nella risposta across-wind in termini di smorzamento aerodinamico. Quest'ultimo, in caso di elevato smorzamento strutturale, rappresenta un contributo positivo per cui, nel caso in esame, gli effetti aeroelastici contribuiscono a ridurre la risposta trasversale. Trascurarli sarebbe quindi una scelta conservativa. La variazione dello smorzamento aerodinamico identificato con la velocità ridotta è stata confrontata con quella di altri lavori di letteratura.

Un ulteriore contributo di questo lavoro consiste nella definizione di una procedura di valutazione del rischio di discomfort indotto dall'azione del vento sugli edifici alti. Tale procedura è stata formulata in accordo all'approccio noto come Perfomance-Based Wind Engineering e può essere collocata all'interno del risk framework proposto dall'IGC 802. La tecnica di valutazione del rischio proposta si articola in due fasi corrispondenti all'analisi dell'hazard (pericolosità) ed alla valutazione della vulnerabilità. Il rischio di discomfort indotto dal vento è stimato in termini di probabilità di superamento di una qualsiasi soglia di comfort adottata e può essere tradotto facilmente in numero medio di giorni all'anno in cui l'edificio è soggetto a vibrazioni non accettabili. Al fine di fornire un esempio pratico di utilizzo della procedura di risk assessment proposta, quest'ultima è stata applicata ad un edificio alto di sezione quadrata, la cui risposta è stata valutata a partire dai dati sperimentali misurati in galleria del vento.

Zusammenfassung

Die derzeitige Tendenz zum Bau immer höherer und schlankerer Gebäude hat zur Entwicklung einer neuen Generation von Hochhäusern geführt, die besonders windempfindlich sind. Starke Gebäudeschwingungen können bei Personen, die sich im Hochhaus aufhalten, ein Gefühl des Unbehagens hervorrufen, dessen Stärke von der Intensität der Schwingungen und individuellen physiologischen und psychologischen Faktoren abhängt.

Die Wahrnehmung windbedingter Vibrationen steht in engem Zusammenhang mit dem Beschleunigungsverhalten, das gewisse Toleranzwerte nicht überschreiten darf. Die Bewertung von Hochhäusern in Bezug auf ihren Komfort erfordert daher die Bestimmung des windbedingten Beschleunigungsverhaltens.

Im Falle hoher und schlanker Gebäude entstehen gewöhnlich höhere Beschleunigungen quer zur Windrichtung (across-wind) als in der Windrichtung (along-wind). Im Unterschied zur Beschleunigung in Windrichtung steht diejenige quer zur Windrichtung nicht in einem direkten Zusammenhang zu turbulenten Schwankungen des betreffenden Winds, sondern hängt hauptsächlich von den aerodynamischen Druckschwankungen in den Scherschichten und den Nachlaufströmungsfeldern ab.

Außerdem können bewegungsbedingte und aeroelastische Phänomene wie Lock-in- und Formanregungs-Effekte (Galloping) auftreten und zu Schwingungen führen, die sich von denen starrer Gebäude stark unterscheiden. Experimentelle Versuche mit Hilfe aeroelastischer Modelle im Windkanal stellen heute die am weitesten verbreiteten Mittel zur Bestimmung des Beschleuningungsverhalten schlanker Gebäude quer zur Windrichtung dar, bei denen aeroelastische Effekte nicht vernachlässigt werden dürfen.

Eine umfangreiche Versuchsreihe unter turbulenten Windbedingungen ist im Windkanal des CRIACIV (Centro di Ricerca Interuniversitario di Aerodinamica delle Costruzioni e Ingegneria del Vento) mit Hilfe des aeroelastischen Modells eines regelmäSSigen Bauwerks mit quadratischem Grundriss durchgeführt worden, das Gegenstand vorheriger Versuche eines starren Modells gewesen war.

Zur Messung der Druckverteilung im Windkanal ist das Modell mit gleichzeitig messenden Druckkappen ausgerüstet worden. Ferner ist das Modell auf eine aerodynamische Waage zur Messung der Kräfte am Sockel montiert worden. Die dynamischen Charakteristiken (Frequenz, Schwingform und Dämpfung) des Modells sind mit freien Schwingungstests für die ersten drei Schwingungsformen bestimmt worden. Die Experimente sind so erfolgt, dass die Windrichtung senkrecht zur ersten festgestellten Schwingungsrichtung war.

Mit Hilfe von drei Laser-Abstandssensoren und drei einachsigen Beschleunigungsmessern konnten die Verschiebung quer zur Windrichtung (across-wind) und das Beschleunigungsverhalten an der Gebäudespitze sowohl quer als auch längs zur

Windrichtung (across-/along-wind) gemessen werden. Die Messungen sind für eine beträchtliche Spanne von Windgeschwindigkeiten einschlieSSlich der kritischen Lock-in-Geschwindigkeit durchgeführt worden.

Das wesentliche Ziel der Versuchsreihe war die gleichzeitige Messung von Drücken, Kräften, Verschiebungen und Beschleunigungen anhand eines aeroelastischen Modells im Windkanal, auch unter Lock-in-Bedingungen.

Durch die Auswertung der Druckkoeffizienten und der Beschleunigungswerte konnten die höhenbedingte Veränderung der Strouhal-Zahl, die Korrelationsstruktur der Drücke, der Lock-in-Windgeschwindigkeitsbereich sowie die Veränderung der Beschleunigungen und der Verschiebungen in Abhängigkeit von der Windgeschwindigkeit ermittelt werden. Die beobachteten aeroelastischen Effekte betreffen weniger stark das Druckfeld, spielen aber eine bedeutende Rolle bei den Beschleunigungen und den Verschiebungen.

Außerdem ist ein Modell nach der Finite-Elemente-Methode (FEM) entwickelt worden, um das gemessene aeroelastische Verhalten mit dem zu vergleichen, das von den an einem starren Modell gemessenen Drücken numerisch ermittelt worden ist. Der Vergleich der beiden Verhalten hat ermöglicht, die aeroelastischen Effekte quer zur Windrichtung (across-wind) im Sinne der aerodynamischen Dämpfung zu bestimmen. Im Falle einer hohen strukturellen Dämpfung hat letztere eine positive Auswirkung, weshalb im vorliegenden Fall die aeroelastischen Effekte dazu beitragen, das Beschleunigungsverhalten quer zur Windrichtung zu reduzieren. Es wäre daher eine konservative Wahl, sie zu ignorieren. Die Veränderung der aerodynamischen Dämpfung in Abhängigkeit von der Windgeschwindigkeit ist mit den Angaben in anderen wissenschaftlichen Arbeiten verglichen worden.

Das Verhalten quer zur Windrichtung (across-wind) des aeroelastischen Modells kann vom numerischen Modell auf der Grundlage der an einem starren Modell gemessenen Drücke abgeleitet werden, indem die aeroelastischen Effekte unter Hinzunahme eines zusätzlichen Dämpfungsterms berücksichtigt werden.

Ein weiterer Beitrag dieser Arbeit besteht in der Definition eines Verfahrens zur Bewertung der Gefahr des Empfindens windbedingten Unbehagens in Hochhäusern. Dieses Verfahren wurde in Übereinstimmung mit dem Perfomance-Based Wind Engineering Ansatz bestimmt und kann im Rahmen des Risikomanagements der IGC 802 betrachtet werden. Die Risikobewertung erfolgt in zwei Phasen: der Gefahrenanalyse und der Bewertung struktureller Schwachstellen. Die Gefahr des Empfindens windbedingten Unbehagens wird in Form der Wahrscheinlichkeit des Überschreitens von angenommenen Komfortgrenzwerten bestimmt und mit Hilfe der mittleren Anzahl von Tagen pro Jahr angegeben, an denen das Gebäude nicht akzeptable Schwingungen erfährt. Um ein praktisches Beispiel der Anwendung des vorgeschlagenen Risikomanagement-Verfahrens zu geben, ist das Verfahren auf ein Hochhaus mit quadratischem Grundriss angewandt worden, dessen Verhalten aufgrund der im Windkanal gemessenen Versuchsdaten bewertet wurde.

Chapter 1

Introduction

1.1 Background

Tall buildings, now approaching the frontier of 1000 m height, have enormously spread worldwide in recent years. This modern phenomenon has led to the introduction of new problems that the international engineering community is now facing.

One issue that has started to dominate the serviceability design of tall buildings is wind-induced discomfort. In the case of slender structures with low natural frequencies, the wind action can cause annoying vibrations which can interfere with building occupants' daily activities and general well-being.

Many literature works have been dedicated to the perception of vibrations. However, no single internationally accepted design standard for satisfactory levels of wind-induced vibrations in tall buildings has been set, yet.

If a modern building is prone to experience wind-induced vibrations, it is very important to estimate the risk of exceeding acceptable vibration limits and of causing discomfort. For this reason, management and treatment of wind risk related to motion perception in tall buildings is of major relevance today.

It is widely accepted that the perception of vibration is closely related to the acceleration response of buildings. Moreover, it is usually in the across-wind direction, that means perpendicular to the incoming wind direction, that buildings usually suffer greater vibrations. In order to satisfy comfort criteria, the wind-induced response has to be accurately estimated.

Many experimental and numerical studies have underlined the complexity of the wind flow and of the wind action around prismatic objects modeling possible tall buildings geometries. In the case of vibrating structures, aeroelastic or motion-induced effects can occur and lead to significantly different responses.

Recent improvements in Computation Fluid Dynamics techniques are very promising, however, wind tunnels have served as the most reliable means for estimating wind-induced responses of tall buildings experiencing aeroelastic phenomena.

One of the possible approaches used to identify aeroelastic effects of tall buildings is that of aerodynamic damping. While in the direction of wind aerodynamic damping is usually positive and small, in the across-wind direction it can be negative and relevant.

From this context it is clear that the accurate design of tall buildings in serviceability conditions is a challenging task involving several topics, including bluff body aerodynamics, aeroelasticity, human perception of vibrations, wind tunnel measure-

ments and also risk management and treatment.

1.2 Scope and Objectives

This research work aims to contribute to the understanding of the wind action and of the aeroelastic effects in tall buildings responses. One of this work purposes is to enlarge the database of wind tunnel measurements carried out on aeroelastic models. One important scope of the thesis is also to provide a general approach to evaluate discomfort risk of tall buildings.

1.3 Major challenges of the research

Serviceability design of tall buildings requires an in-depth study into the wind flow around structures, wind effects on buildings, including aeroelastic phenomena, dynamic properties of tall buildings and the risks of wind hazard. In this context, the primary research challenges of the thesis can be listed as follows:

- experimental wind tunnel tests on an equivalent aeroelastic model of a square-section tall building, aimed at the simultaneous measurement of pressures, overall forces and acceleration and displacement responses;
- experimental identification of the vortex resonance condition and analysis of its effects on the wind loads and responses;
- identification of aeroelastic effects in the across-wind response in terms of aerodynamic damping through an experimental-numerical procedure;
- development of a general procedure for wind risk assessment of tall buildings related to comfort thresholds and application of this procedure to a case study building.

1.4 Thesis organization

The content of the thesis is organized into nine chapters, including this introductory chapter (chapter 1). Chapter 2 formulates the problem of the wind-induced discomfort risk of tall buildings. A general probabilistic risk management framework, proposed for dealing with risk of structures, is illustrated. The Performance-Based Design approach for the assessment of risk is discussed. Some literature studies dedicated to motion perception of tall buildings occupants are reviewed and the comfort criteria currently used for the serviceability design of tall buildings are shown.

Chapter 3 is dedicated to the aerodynamics of the square-section bluff body. The knowledge of the flow behind prismatic bodies is judged of fundamental importance for the design of wind-sensitive tall buildings. The vortex-shedding phenomenon from fixed two-dimensional bluff-bodies is introduced. The aerodynamics of 2-D square-section cylinders is reviewed and then the three-dimensional flow behind square-section prisms of finite length is discussed.

Chapter 4 deals with aeroelastic effects in the wind-induced responses of tall buildings and discusses the aerodynamic damping approach for estimating the motion-induced effects. Literature studies focused on the across-wind aeroelastic response

of tall buildings are reviewed and later used for comparison with results obtained from the experimental activity carried out in this research.

In chapter 5 the experimental techniques of common use in wind tunnels are reviewed, with particular reference to aeroelastic simulations which provide the most complete characterization of the structural responses, including the effects of the motion-induced forces. Similarity requirements for the aeroelastic studies of buildings are also discussed.

Chapter 6 illustrates the wind tunnel tests carried out in the CRIACIV boundary layer wind tunnel on an aeroelastic model of a regular square-section tall building. Experimental results for a wide range of wind speeds, including the lock-in velocity condition, are investigated in detail and compared with data from other literature studies. The effects of vortex resonance on wind loads and model responses are discussed. The acceleration response of the model is found to be dominated by that in the across-wind direction, which is affected by the motion-induced lock-in phenomenon.

In chapter 7 the aeroelastic effects involving the across-wind response of the model tested in the wind tunnel are identified in terms of aerodynamic damping. For this identification procedure, a Finite Element Method model which replicates the physical wind tunnel model is developed. Across-wind aerodynamic damping is evaluated from the comparison between the aeroelastic response directly measured from the model in the tunnel and the response numerically predicted from wind loads measured on a rigid model.

In chapter 8 a general procedure for the serviceability wind risk assessment of tall buildings is presented. This procedure is applied to a case study building with the purpose of showing how the procedure can be used to assess the discomfort risk of tall buildings. Real wind data, registered from an anemometric station located in Italy, are used.

The last chapter (chapter 9) summarizes the major contributions and findings of this research study. Possible future developments of the work are suggested.

Chapter 2

Wind risk of tall buildings related to comfort thresholds

2.1 Introduction

Tall buildings emerged in the late nineteenth century in the United States of America. They constituted a so-called *American Building Type*, meaning that most important tall buildings were built in the USA. Today, however, they are a worldwide architectural phenomenon and the total number of tall buildings have grown up enormously. Ali and Moon (2007) refer to a number of 3482 tall buildings in 1982 and 108924 in 2006.

There is not an absolute definition of what constitutes a "tall building". According to the criteria proposed by the Council on Tall Buildings and Urban Habitat (CTBUH, `www.ctbuh.org`), a building can be defined as "tall" when it shows some element of "tallness" in one or more of the following three categories:

- *Height relative to context.* Differently from absolute height, it relates the building height to the context where it exists. Thus the same building, let's say 14-story building, may not be considered a tall building in a high-rise city, such as Chicago or Hong Kong, while it can be taller than the urban norm in a provincial European city or a suburb.

- *Proportion.* There are many buildings which are not particularly high, but are slender enough to have the appearance of tall buildings. Other buildings, on the other hand, are quite tall, but their size to floor ratio is so low that they can not be classed as tall buildings.

- *Technologies.* A building can be categorized as tall when it contains technologies that can be considered as a product of "tallness", such as, for example, vertical transport technologies and structural wind bracing as a product of height.

A multi-story structure between 35 and 100 meters tall, or a building of unknown height from 12 to 39 floors is classified as a high-rise building by the ESN 18727 Emporis Standards (`www.emporis.com`). The CTBUH defines a building as "supertall" when its height exceeds 300 meters.

In recent years tall buildings have encountered a deep change in geographical location, function and material used. Whereas as recently as 1990, 80% of the 100

world's tallest buildings were located in North America, by the end of 2012, the number of the world's 100 tallest buildings in North America is expected to be only 20%, with 42% in Asia and 32% in the Middle East [Fig. 2.1(a)]. There has also been a major moving away from the predominantly office buildings which have dominated the tallest lists for many decades [Fig. 2.1(b)]. Residential and mixed-use functions are currently heavily influencing the list, up to 38% from 12% in just the last decade. The rapid urbanization of developing countries partially explains why, in order to accommodate the growing populace in the city, many of these buildings are now residential in nature rather than commercial. The changes in structural material have also been very significant over the past few decades [Fig. 2.1(c)]. Steel buildings have dropped in favor of concrete or composite structures.

The major feature characterizing the evolution of tall buildings is, however, the trend towards developing increasingly higher and more flexible structures. The world's tallest buildings are now approaching the frontier of 1000 m height (Fig. 2.2). As a consequence, a new generation of tall and slender structures, that are highly sensitive to wind-induced deflections and vibrations, has developed. Therefore, concerns of perceptible building motions and occupant discomfort have become prominent in the design of tall buildings under the wind action.

Management and treatment of risk related to wind-induced discomfort has become today of major importance in the engineering community.

In section 2.2 a risk management framework defining a general procedure for dealing with risk of structures is briefly described. Section 2.3 refers to the Performance-Based Design (PBD) approach, applied to wind engineering (Performance-Based Wind Engineering, PBWE), as a methodology to be used for the quantitative estimation of wind risk. In section 2.4 human comfort levels and perception criteria are illustrated.

2.2 Risk management

The term *risk*, and therefore also *aeolian risk*, may take several meanings. Risk is commonly identified with the presence of a certain danger, being its counterpart, namely *safety*, identified with the absence of danger. This *yes-or-no* definition doesn't apply to engineering facilities (Augusti *et al.*, 2001). The numerous uncertainties involving natural disasters entail the necessity to assess risk in probabilistic terms. A general *probabilistic risk management framework* (Fig. 2.3) was proposed by Pliefke *et al.* (2006), in compliance with AS/NZS-Standard (1999) and consists of three major steps that are performed chronologically, corresponding to:

1. *risk identification*
2. *risk assessment*
3. *risk treatment*

2.2.1 Risk identification

Risk identification is aimed at answering the question "what can happen and where?" and requires first the definition of the system subjected to risk (e.g. a

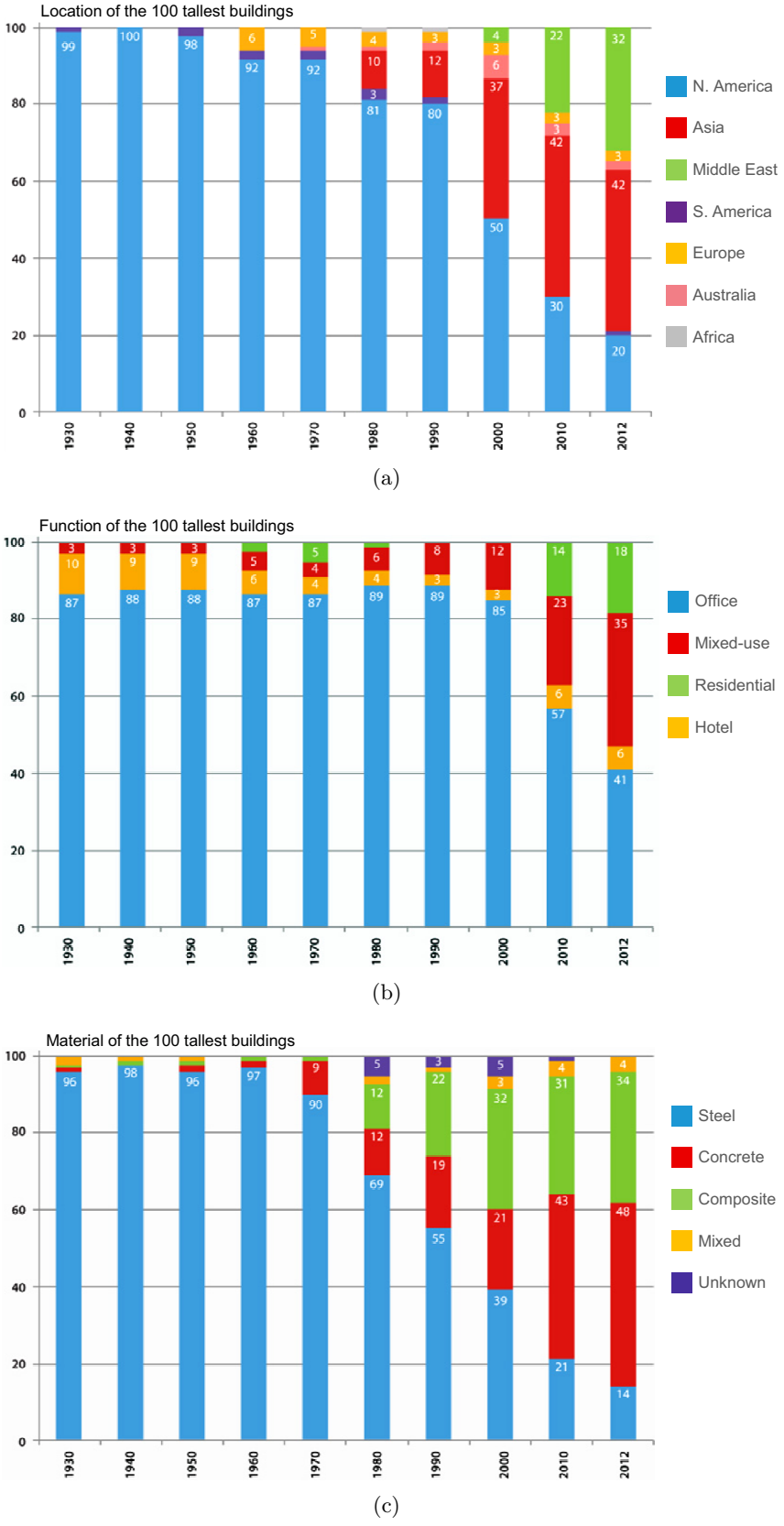

Fig. 2.1 Recent trends of the 100 tallest buildings, from 1930 to 2012 (`www.ctbuh.org`): a) location; b) function; c) material.

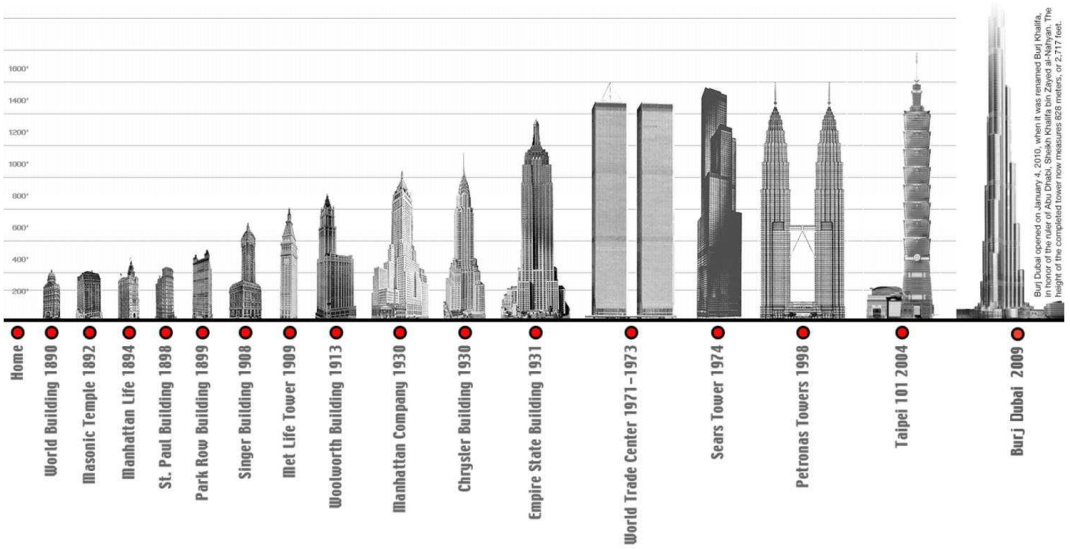

Fig. 2.2 World's tallest towers: timeline of all skyscrapers holding the title of tallest building in the world from 1890 to the present.

structure, a city, ...) and then all the sources of events that can compromise the system functionality (*hazard identification*).

2.2.2 Risk assessment

Risk assessment consists of two sub-procedures: *risk analysis* and *risk evaluation*.

The first phase of risk analysis is *hazard analysis*, aimed at the definition of the probability of occurrence of the previously identified hazards. Knowing the *structural vulnerability*, that is the relation between the hazard intensity and response of the system, damage is quantified (*damage assessment*). Finally, the consequences of damage in terms of losses are determined (*loss assessment*).

Direct losses occur when the disaster takes place, while *indirect losses* arise after a certain time delay. Losses can either be categorized in consequence classes, so that it is distinguished between economic loss, loss of life etc., or accumulated in one single number in order to define a common scale of evaluation for both *tangible* and *intangible* consequences. Tangible or economic consequences are those directly measurable in monetary terms. Intangible ones, are, on the other hand, not quantitatively appraisable losses, e.g. injuries and fatalities, pollution of the environment, loss of cultural, social and historical values, etc.

The final result of risk analysis is the quantification of risk in terms of both *structural risk* and *total risk*. Structural risk is the annual probability of occurrence of the hazard multiplied by the expected damage and can be expressed in [damage measure/year]. Total risk is defined as the product of the annual probability of occurrence or exceedance of the hazard or loss and the expected loss and is expressed in [loss unit/year].

The last stage of the risk assessment procedure is *risk evaluation*, whose purpose is to make the considered risk comparable to other competing risks to the system by the use of adequate risk measures.

2.2.3 Risk treatment

In the final phase pertaining *risk treatment*, a decision is made whether to accept, to transfer, to reject or to reduce a given risk. When *risk mitigation* is performed different risk reduction strategies can be followed, with the common purpose of reducing the vulnerability of the system. Among them, two types of strategies can be used, including pre-disaster interventions (*prevention*, *preparedness*), and post-disasters interventions (*response*, *recovery*).

Prevention includes technical measures that are to be performed with an accurate time horizon before the disaster takes place. Typical examples of prevention measures in the field of tall buildings design are auxiliary damping devices installed for the mitigation of wind-induced responses. A comprehensive description of the entire spectrum of techniques geared specifically toward reducing the effects of wind on structures, particularly those which involve occupant comfort can be found in Kareem *et al.* (1999).

Preparedness regards social activities limiting harm shortly before the disaster occurrence, such as evacuation plans and emergency training.

Response includes the variety of activities that are performed immediately after the occurrence of the disaster, such as the disposing of rescue and shelter for injured and harmed people as well as the coordination of emergency forces.

Finally, recovery embraces all activities that need to be held until the pre-disaster status of the system is restored again.

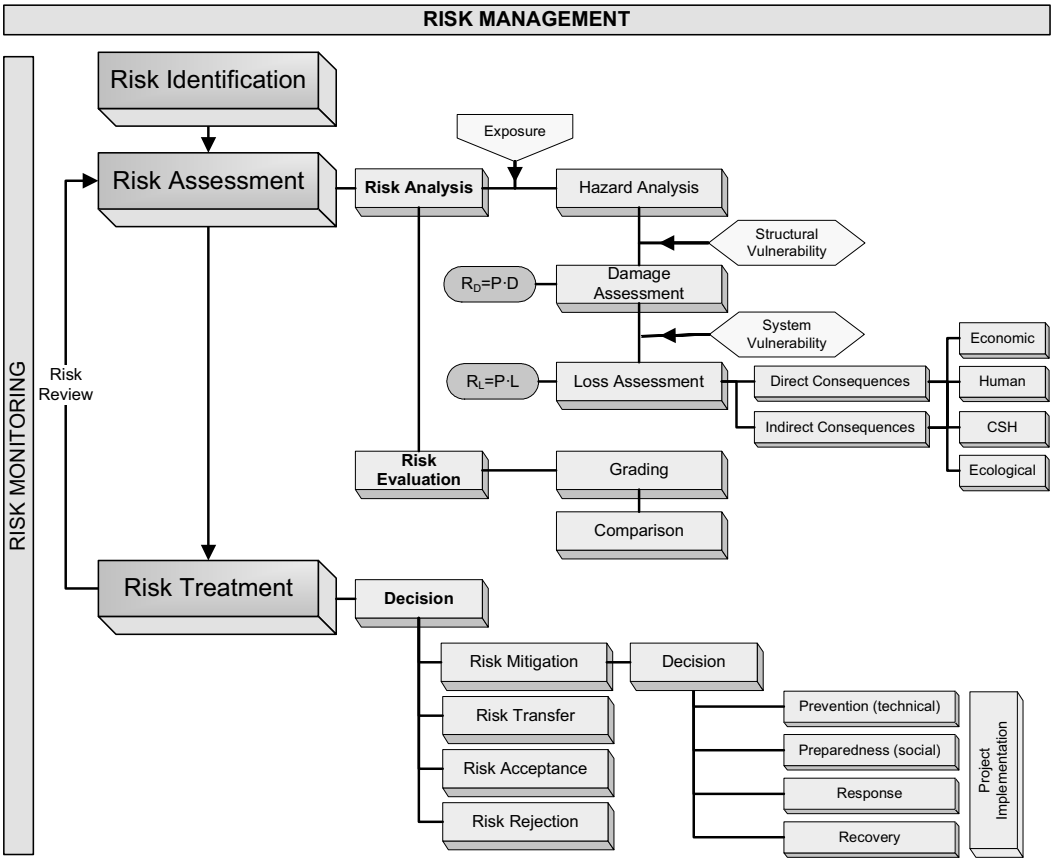

Fig. 2.3 Overview of the whole Risk Management process (Pliefke *et al.*, 2006, 2007).

2.3 PEER's approach for Performance-Based Wind Design

2.3.1 PEER's methodology for Performance-Based Design

It has been recognized that Performance-Based Design (PBD) represents a rational approach to the assessment of risk, also in the wind engineering field. PBD is aimed directly at the achievement of well specified performance objectives with a sufficiently high probability and/or their optimization. PBD has developed mainly in the USA with reference to seismic risk and design. The Pacific Earthquake Engineering Research (PEER) Center, based at the University of California, Berkeley, has focused on the development of a PBD methodology. A central feature of the PEER's approach is that its principal outputs are system-level performance measures: probabilistic estimates of repair costs, casualties, and loss-of-use duration ("dollars, deaths and downtime"). Fig. 2.4 illustrates the PEER methodology (Porter, 2003), that, as shown, involves four stages: hazard analysis, structural analysis, damage analysis and loss analysis. In the scheme, the expression $p\,[X|Y]$ refers to the probability density of X conditioned on knowledge of Y, and $g\,[X|Y]$ is the occurrence frequency of X given Y.

The following equation, based on Porter (2003), can be used to frame the PEER methodology mathematically:

$$g\,[DV] = \iiint p\,[DV|DM]\,p\,[DM|EDP]\,p\,[EDP|IM] \\ g\,[IM]\;dIM\,dEDP\,dDM \tag{2.1}$$

where

- IM is the Intensity Measure and is a measure of the magnitude of the action;
- EDP is the Engineering Demand Parameter and describes the structural response;
- DM is the Damage Measure and expresses a certain level of damage;
- DV is the Decision Variable, the parameter indicating the probabilistic estimation of performance, that governs the design decision.

The term $g\,[IM]$, results from the *hazard analysis*, and evaluates the hazard at the facility, considering its location and structural, architectural and other features. The term $p\,[EDP|IM]$ is obtained from *structural analysis*, aimed at the estimation of the uncertain structural response, measured in terms of EDP, conditioned on the intensity measure. In the following damage analysis, EDP is input to a set of *fragility functions* that model the probability of various levels of damage, DM, conditioned on structural response, $p\,[DM|EDP]$. *Structural vulnerability* refers to the relation between the hazard measure and the resulting damage. The last stage is the probabilistic estimation of performance, parametrized by various decision variables, DV, conditioned on damage, $p\,[DV|DM]$. This is the stage of loss analysis that produces estimates of the frequency with which various levels of decision variables are exceeded. Loss analysis leads to the *decision-making* phase, in which, for example, one can determine whether the facility is safe enough or has satisfactorily low future

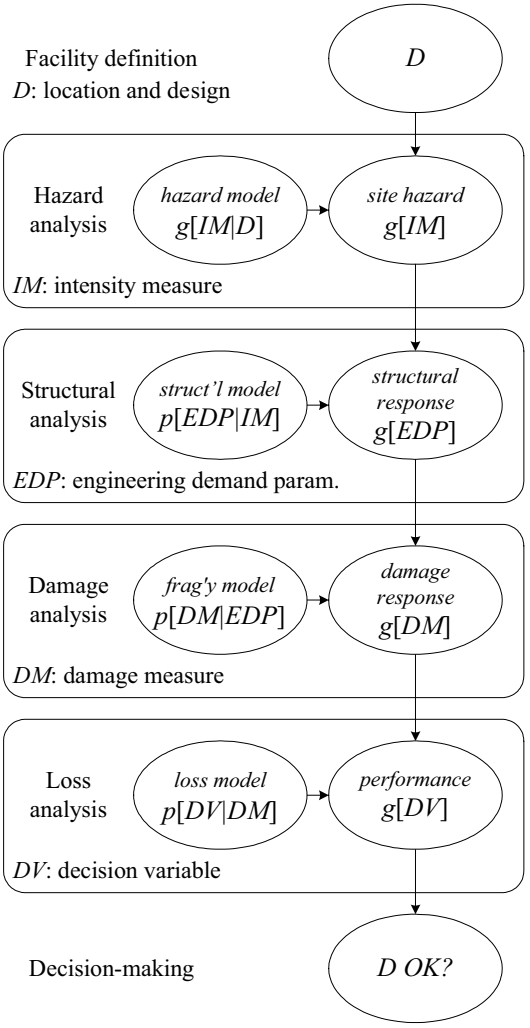

Fig. 2.4 PEER's analysis methodology (conditioning on D in the hazard term, indicates that the hazard at the facility has to be evaluated considering its location and structural, architectural and other features, jointly denoted by design, D) from Porter (2003).

repair costs.

It is easy to see that the logical scheme of the PEER's approach is comparable to that of the risk assessment procedure illustrated in Fig. **??**. As a result, PEER's equation will be used as the mathematical tool for the risk assessment procedure illustrated in this work.

2.3.2 Performance-Based Wind Engineering

As previously mentioned, the first applications of PBD were devoted to seismic engineering and design and often PBD is associated to Performance-Based Earthquake Engineering, PBEE, (Porter, 2003). Recently PBD approach is being applied to different problems, in particular to wind engineering.

The definition Performance-Based Wind Engineering, PBWE, appeared for the first time in 2004 (Paulotto *et al.*, 2004). Augusti and Ciampoli (2008) discussed the general approach of PBD and illustrated two examples of application to aeolian and seismic risk assessment, respectively. Dealing with PBD, as reported in Augusti and Ciampoli (2006) *low* and *high performances* can be considered: the former imply possible consequences on personal and structural safety (e.g. partial or total collapse and permanent damages), the latter are related to serviceability and comfort (displacements, vibrations). In Ciampoli *et al.* (2011) the general framework of the PBWE design approach is illustrated and applied to an example case: the assessment of the collapse and out-of-service risks of a long span suspension bridge. In Ciampoli and Petrini (2012) a probabilistic procedure for the Performance-Based Design of structures subject to the wind action is applied to a 74-story steel building. The performances considered are the occupant comfort, expressed in terms of perception of the wind-induced vibrations, and the structural reliability, evaluated in terms of deformation capacity. Marra (2011) recently used a PEER-type equation based on the PBWE approach in order to develop a procedure for the assessment of vortex-shedding risk of bridge decks.

2.4 Motion perception and human comfort levels in tall buildings

Recent trends towards structures with increasing height, often accompanied by increased flexibility (section 2.1) have led to a new generation of buildings with low natural frequencies of vibration, which position them within an operating range susceptible to wind excitations, particularly for buildings in regions of high wind speeds.

Wind-induced motions of tall buildings include sway motion of the first 2 bending modes, referred to as *along-wind* (in the direction of wind) and *across-wind* (normal to the wind direction) motions, a higher mode torsional motion about the vertical axis, or for buildings with stiffness and mass asymmetries, complex bending and torsion in the lower modes (Melbourne and Palmer, 1992). Prolonged exposure to these wind-induced motions can cause unnerving effects to the structure's occupants, giving rise to serviceability problems related to comfort. Symptoms of discomfort may range from concern, anxiety, fear and vertigo up to more severe effects of dizziness, headaches and nausea. As a result, numerous studies have been devoted to understanding human perception of vibration and determining tolerance thresholds of wind-induced vibrations of tall buildings. These studies generally fall into three

different categories:

- field experiments of building occupants conducted in wind-excited tall buildings;
- motion simulator and shake table experiments testing human test subjects;
- field experiments conducted in artificially excited structures.

In the following section a brief review of these studies is presented. A more detailed one is illustrated by Kilpatrick (1996) and Kwok *et al.* (2009).

2.4.1 Literature studies on comfort and motion perception in tall buildings

First studies concerning human comfort in tall buildings can be traced in very old times. As reported in Davenport (2002), the sky-scraper boom of the 1930s and later in the 1960s resulted in a growing curiosity in, and awareness of, vibrations through both experimental registrations and human perception of motion discomfort.

During the 1930s Rathburn (Rathburn, 1940) made extensive observations on the Empire State Building and stated that in wind it vibrated "*like the tines of a tuning fork*". In Spurr's treatise on wind bracing (Spurr, 1930) he stated: "*the whole question of the vibration in buildings from the effects of variable wind pressures is complicated by the indeterminate nature of the pressures themselves, as well as by the great variation in size, shape, weight, height and location of buildings*". In this work it was already stated that the perception of wind-induced motion is closely related to the acceleration response of buildings as it is nowadays widely accepted (Kwok *et al.*, 2009).

Fig. 2.5 illustrates the results of the study performed by Reiher and Meister (1931), concerning the human perception of steady-state vertical vibrations. The effects of amplitude and frequency of motion are related to different levels of perception.

As early as 1931, the Structural Division of the American Society of Civil Engineers (ASCE), Subcommittee No. 31, recommended that "*structural frames be so designed as to ensure that deflections will be kept within such limits as to render buildings comfortably habitable*"(ASCE, 1931).

One of the first in the literature to suggest limiting wind-induced displacements based on human comfort level was Chang (Chang, 1967). He noted that the strength of a structure is not the only consideration in the design of tall buildings and stated that "*rentals may depend on keeping movement in the upper levels of the building to acceptable human tolerance*". He suggested that, for the evaluation of human comfort levels, the return period of extreme winds is reduced from 50 years, a typical interval for strength consideration, to 10 or perhaps 2 years, depending on the nature of the structure. Considering that acceleration, the rate of change acceleration (commonly referred to as jerk) and frequency of vibration are often looked to as the main causes of discomfort, Chang developed tentative comfort criteria for building occupants. Fig. 2.6 describes the dynamic amplitude of vibration with period, for various acceleration levels. In Fig. 2.6, as a practical example, data points are reported from the earlier study on the Empire State Building by Rathburn (1940). Comfort limits for

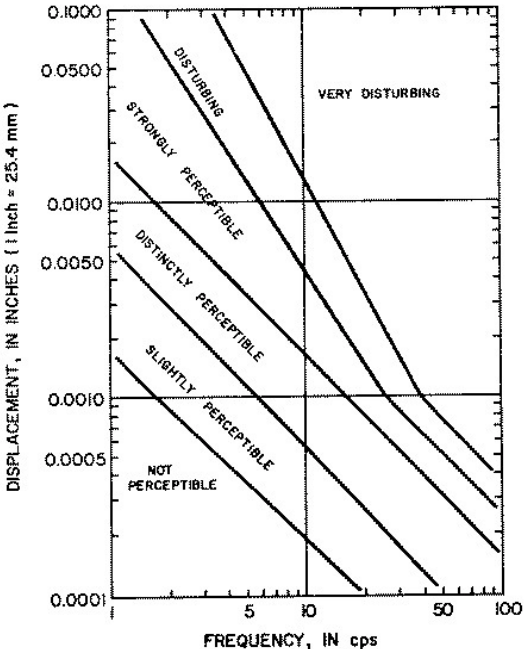

Fig. 2.5 Human perception levels related to steady-state vibration amplitude and frequency (Reiher and Meister, 1931).

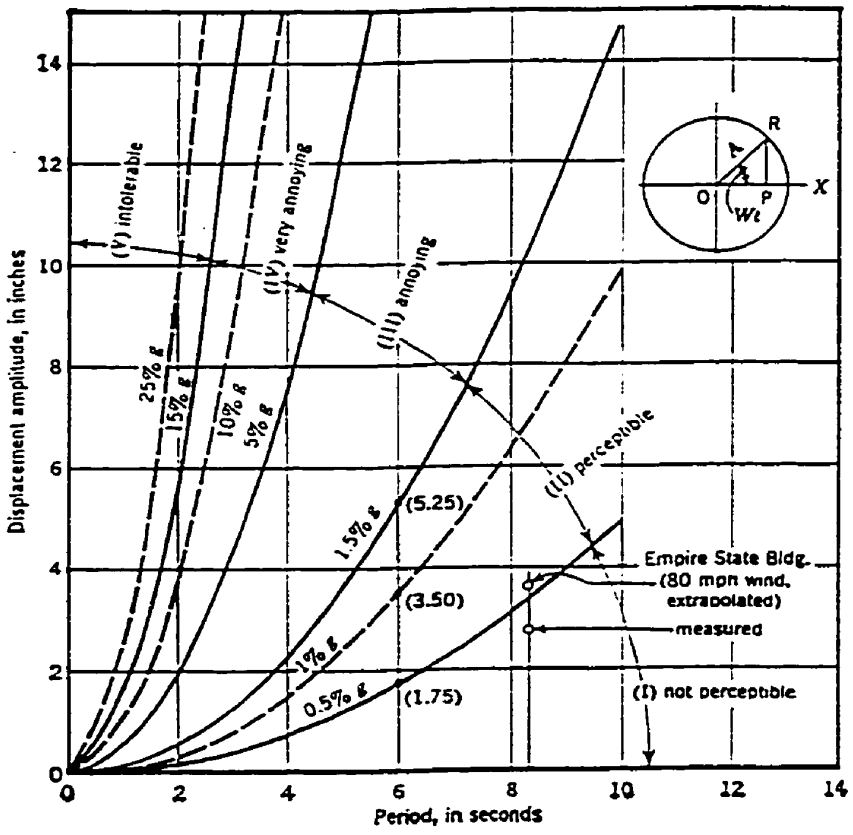

Fig. 2.6 Displacement amplitude versus period with comfort criteria (Chang, 1967).

building occupants with the corresponding acceleration level are listed in Table 2.1.

In a subsequent paper (Chang, 1973) Chang related to his suggested tenta-

Table 2.1 Comfort criteria for building occupants (Chang, 1967).

Acceleration in percent of g	Comfort limits
under 0.5	Not perceptible
0.5 to 1.5	Threshold of perceptibility
1.5 to 5	Annoying
5 to 15	Very annoying
over 15	Unbearable

tive comfort criteria curves (Fig. 2.7) the experimental data from four tall buildings (the Empire State Building, the John Hancock Center, the 1000 Lakeshore Plaza in Chicago and the World Trade Center in New York). The estimated performance and the occupants experience of the four investigated tall buildings supported Chang's comfort criteria.

The first attempt in the literature to examine human perception thresholds of

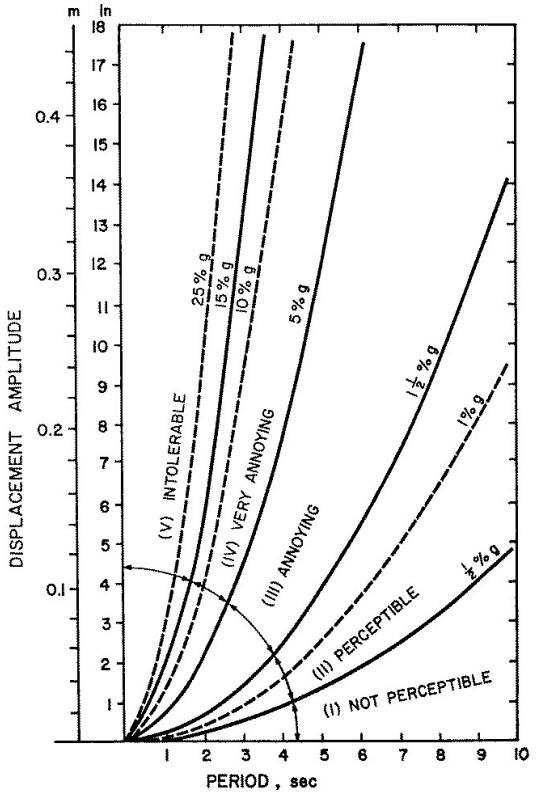

Fig. 2.7 Period dependent comfort criteria curves suggested by Chang (1973).

low frequency vibrations in the horizontal plane is represented by the work of Chen and Robertson (1972). Two separate experiments during the design stage of the World Trade Center in New York were carried out by the authors with the aim of assessing acceptable thresholds of horizontal accelerations. The first one, designated

HATS-I, was addressed to the definition of proper thresholds of horizontal motions. The second one, HATS-II, was used to validate the results of the previous one. The effect of four factors corresponding to (1) period of oscillation, (2) body orientation, (3) body movement, (4) expectancy of building motion, was analyzed using HATS-I. It was assumed that the distribution of the perception threshold of horizontal acceleration was lognormal. Fig. 2.8 illustrates the geometric means of the thresholds under the four factors tested. In Fig. 2.9 an example of the cumulative frequency distribution of the perception threshold for HATS-I is shown.

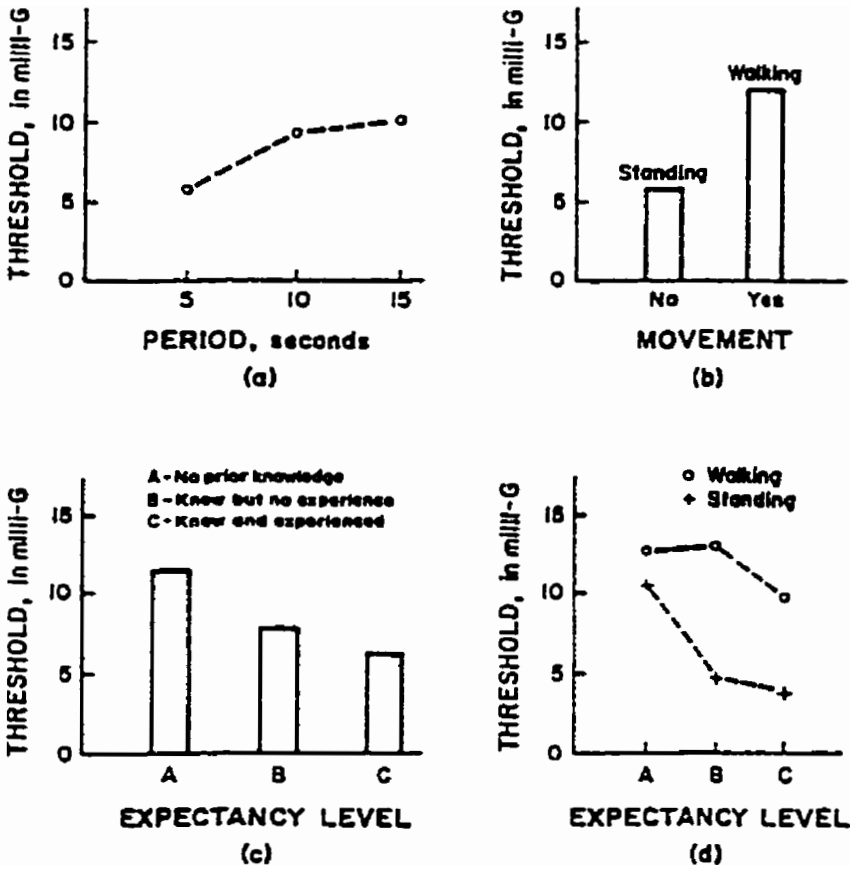

Fig. 2.8 Geometric means of perception thresholds: HATS-I (Chen and Robertson, 1972).

The second experiment, HATS-II, confirmed the results of HATS-I and verified the assumption that the perception threshold was lognormally distributed. In HATS-II only the effect on motion perception of body posture and that of expectancy level were investigated. The work of Chen and Robertson (1972) led to several important findings with implication in the design of tall buildings:

1. period of oscillation, body movement, expectancy of movement and body posture significantly affect the perception thresholds of low frequency horizontal periodic motion;

2. mean perception thresholds increase as the the period of oscillation increases from 5 to 15 seconds (hence, vibration perception is frequency dependent);

3. perception thresholds of standing subjects are significantly lower than those

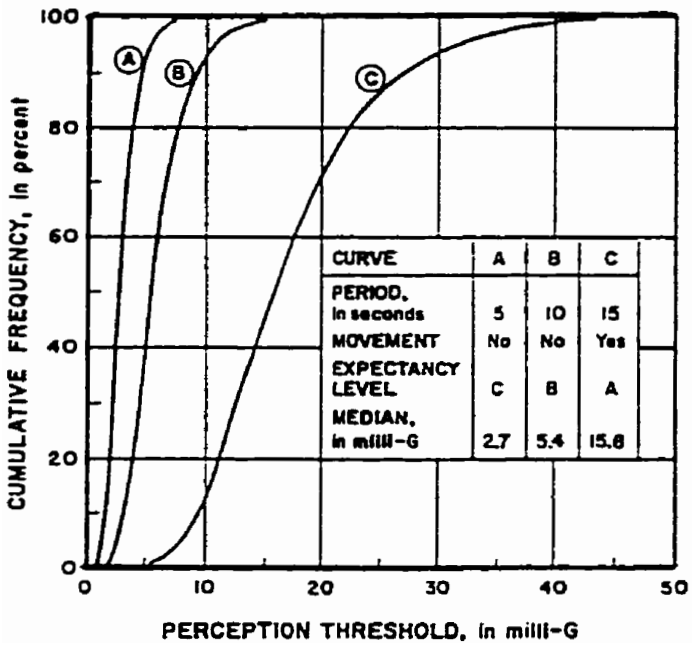

Fig. 2.9 Distribution of perception thresholds: HATS-I (Chen and Robertson, 1972).

of walking subjects (most probably because of the additional movement due to self-motion masking the sensation of vibration caused by the simulated vibration);

4. perception thresholds are smaller when subjects are anticipating motion;

5. perception thresholds are higher in the case of sitting position rather than those in the standing position.

Fig. 2.10 shows probability curves of the acceleration response. It is noteworthy that the research reported by Chen and Robertson (1972) 40 years ago is a landmark study and remains one of the most referenced studies to date.

Hansen *et al.* (1973) performed a study to correlate occupant discomfort with the wind-induced vibrations of two 167 m tall office buildings through occupant surveys after two major wind events that produced building vibrations, which disturbed a significant proportion of occupants of the upper floors. A tentative building vibration criterion was proposed by imposing a limit on RMS (Root Mean Square) acceleration of 5 milli-g occurring no more than once every six years on average, based on an average 2% occupant objection rate (Fig. 2.11).

In Fig. 2.12 the results of the study of Goldman and Von Gierke (Goldman and von Gierke, 1976) on the effects of steady-state vibration on human perception are shown.

Based on the review of the work of Chen and Robertson (1972) and Hansen *et al.* (1973), Irwin (1978) showed frequency dependence of uniaxial sinusoidal motion and recommended frequency dependent acceleration criteria for evaluating low-frequency motion within the range of 0.063 Hz to 1.0 Hz, which later led to the development of the ISO-6897 guidelines (ISO 6897, 1984).

In a more recent study, Von Gierke and Brammer (Von Gierke and Brammer, 1996) defined tolerance criteria for shock and for vibration exposure. Studies on

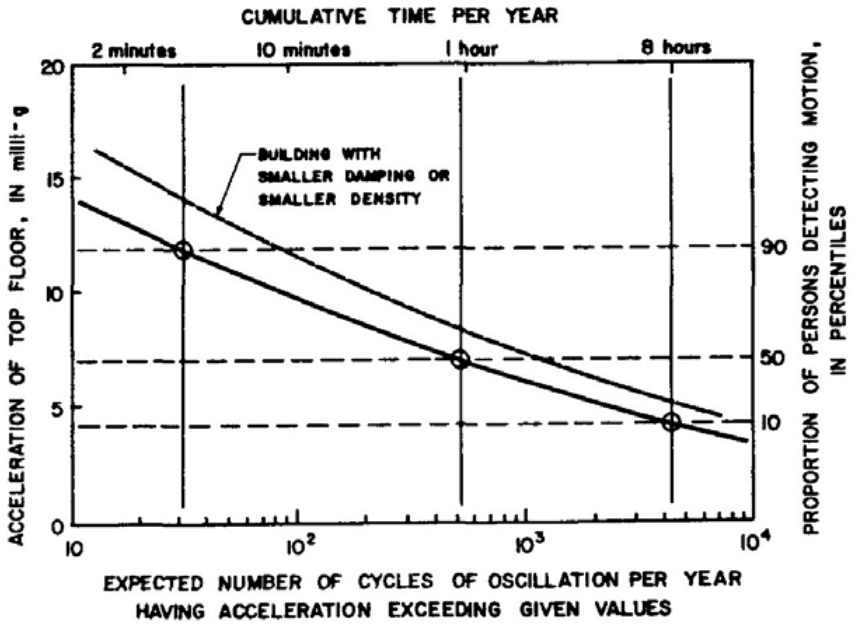

Fig. 2.10 Probability curves of horizontal accelerations (Chen and Robertson, 1972).

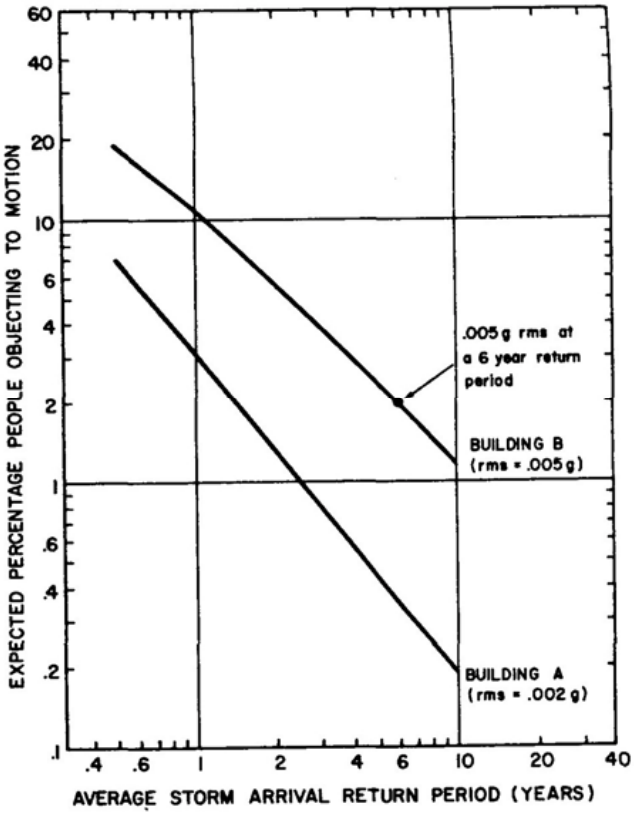

Fig. 2.11 Comfort criteria (Hansen *et al.*, 1973).

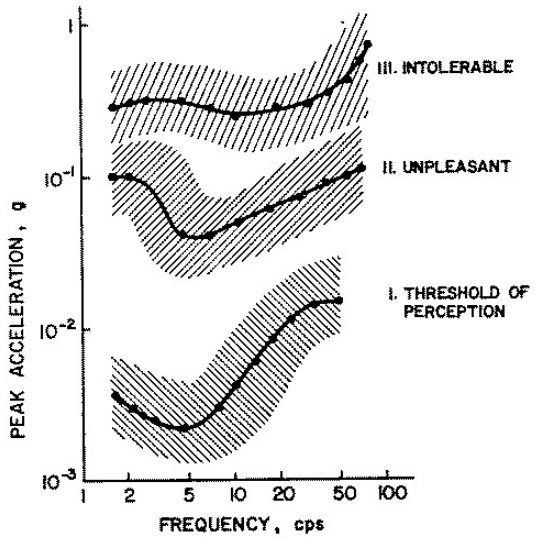

Fig. 2.12 Human perception levels related to steady-state vibration amplitude and frequency (Goldman and von Gierke, 1976).

perception thresholds based on motion simulator tests are illustrated in the work by Goto (1983), while Isyumov (1993) referred to tests on actual structures. Laboratory experiments using uni-axial motions are illustrated in Nakata *et al.* (1993) and in Shioya and Kanda (1993), while other tests were developed for random motions (Kanda *et al.*, 1988, 1990; Shioya *et al.*, 1992) and for bi-lateral elliptic motions (Shioya *et al.*, 1992), although the randomness did not seem to affect the perception threshold (Kanda *et al.*, 1990). Early laboratory tests showed discrepancies with actual building performance. Subjects isolated in the small rooms used in motion simulators were found to lack the visual and audio clues contributing to motion perception in actual buildings (McNamara *et al.*, 2002).

2.4.2 Occupant comfort assessment for wind-excited tall buildings. Considerations on recent developments

As seen in the previous section, great research effort has been devoted to investigate human perception thresholds of wind-induced building motion. Although some recommendations on acceleration limitations have been given in a number of current design codes, there is still no internationally accepted standard for limiting wind-induced motions of tall buildings.

Vibration perception and comfort related motion thresholds are still an active research topic in wind engineering (Kwok *et al.*, 2009). The results of several experiments and studies concerning wind-induced motion perception have been mainly collected by Kareem *et al.* (1999) and Tamura (2003) as shown in Fig. 2.14 and Fig. 2.13.

From literature studies on perception thresholds, comfort criteria are defined as limits which may be exceeded in a certain return period. Typically, in North America, a ten year interval is used; on the other hand, in region with frequent typhoon and hurricane events, a shorter return period may be more proper. Fig. 2.13 illustrates some of the perception criteria which are currently in use. North American practice is to use 10-15 milli-g peak horizontal accelerations at top floor for resi-

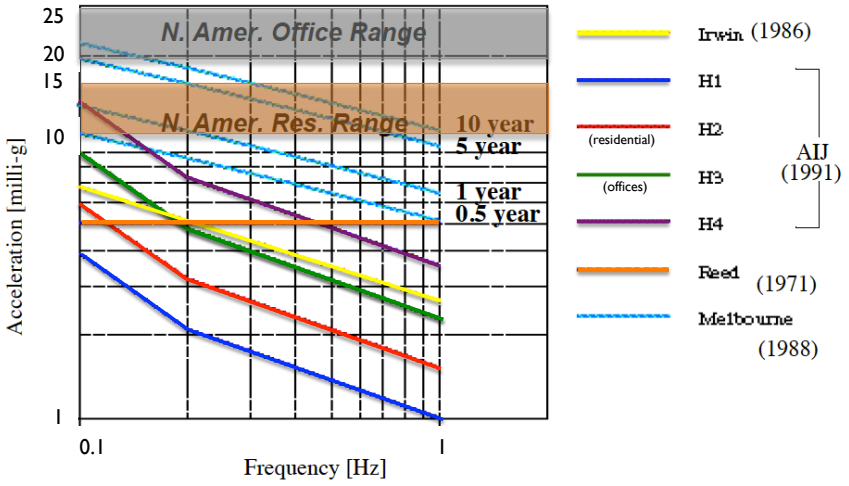

Fig. 2.13 Various perception criteria for occupant comfort (Irwin, 1986; AIJ, 1991; Reed, 1971; Melbourne and Cheung, 1988), from Kareem *et al.* (1999).

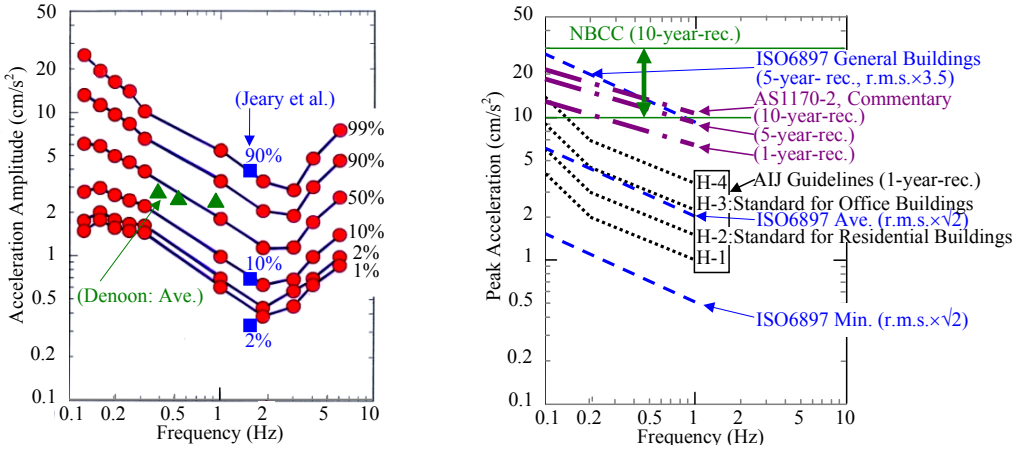

(a) *Probabilistic human perception threshold. (Jeary* et al.*, 1988; Nakata* et al.*, 1993; Denoon, 2000; Shioya* et al.*, 1992)*

(b) *Guidelines / criterion for habitability to horizontal vibrations. (ISO 6897, 1984; Holmes* et al.*, 1990; AIJ, 1991; NBCC, 1990)*

Fig. 2.14 Perception thresholds and guidelines for habitability to horizontal vibrations of buildings (Tamura, 2003).

dential buildings and 20-25 milli-g for office buildings, based upon a 10 year return period (Isyumov, 1993). Kareem (1988) proposed an RMS acceleration threshold of 8 to 10 milli-g for a 10 year recurrence interval. The lines H1-H4, taken from the Japanese AIJ standards (AIJ, 1991) represent various levels of peak acceleration perception, with H2 typically used for residential applications and H3 for office dwellings. It is also shown Reed's (Reed, 1971) constant perception limit of 5 milli-g for a 6-year return period and Irwin's curve (Irwin, 1986) for RMS accelerations, also given in ISO 6897 (1984), illustrating the difference between the use of RMS versus peak accelerations. The peak acceleration criteria of 15 milli-g for residential buildings and 25 milli-g for commercial buildings under 10-year return period are recommended in the National Building Code of Canada (NBCC, 1990), the Chinese code (JGJ 3-2002, 2002), and the Hong Kong Codes of Practice (HKCOP 2004, 2004; HKCOP 2005, 2005). The Japanese guidelines AIJ (2004) offer frequency dependent peak acceleration criteria (Fig. 2.15) and represent the reference basis of the acceleration thresholds given by the current Italian standard for wind action on buildings (CNR-DT 207, 2008). A comparison of perception criteria for 1-year return period

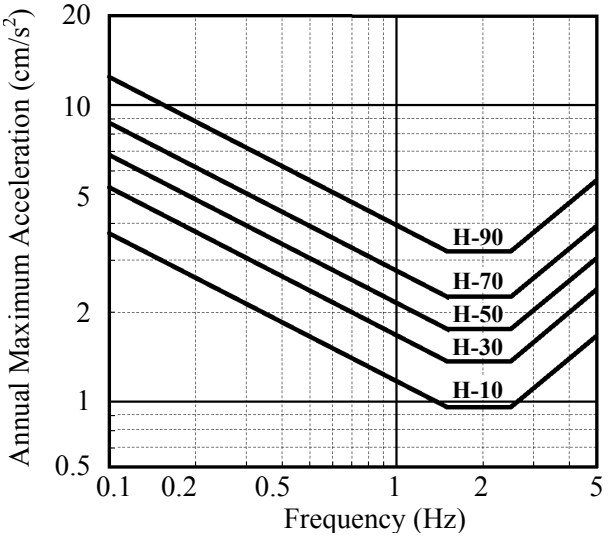

Fig. 2.15 Curves given in the AIJ-Guidelines-2004 (AIJ, 2004).

is reported in Bashor and Kareem (2007) and illustrated in Fig. 2.16.

Both peak and standard deviation acceleration thresholds are currently used. As reported in McNamara *et al.* (2002), the international community has not agreed on a universal descriptor of acceleration for a number of reasons. On one hand, negative reactions to motion may be the consequence of a sustained or ongoing phenomenon, best described by an averaged effect over some time period, leading to the common RMS descriptor. On the other hand, it has been also asserted that people are most dramatically injured by large events, impacting them far more than the typical phenomenon their bodies had become accustomed to. Many studies favor the RMS index due to the ease with which it is measured experimentally or predicted analytically, citing the variability in peak acceleration measurements in wind tunnel tests as one demonstration.

Boggs (1995) investigated the differences between the RMS and peak acceleration methods and the importance of making a rational selection of the appropriate

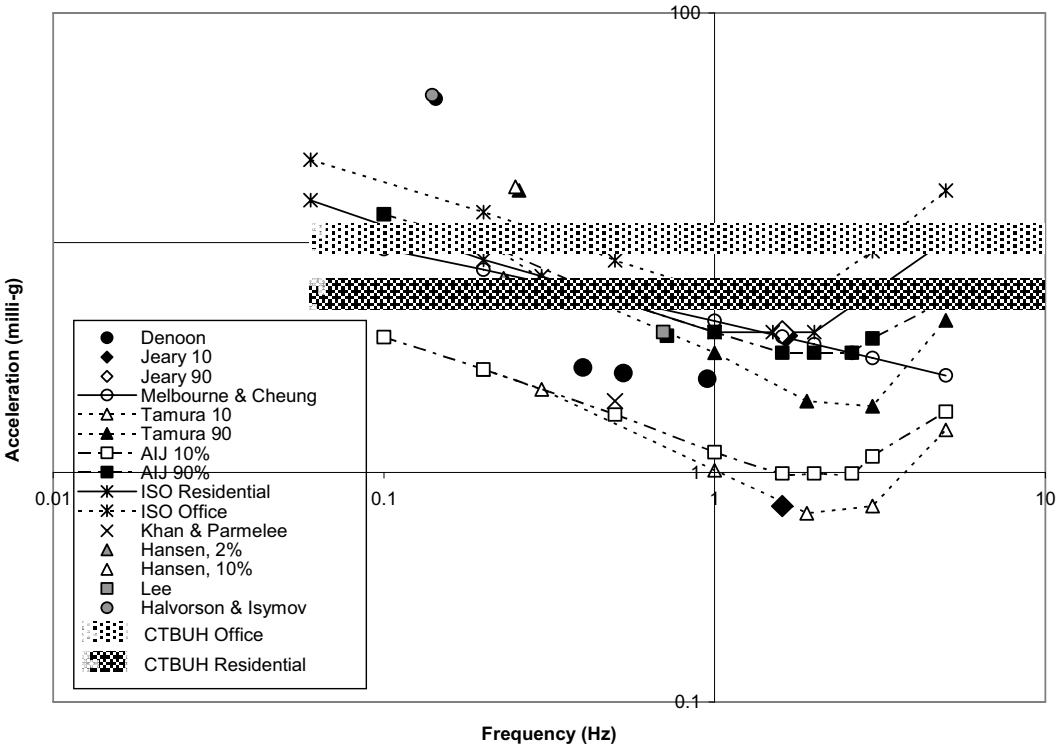

Fig. 2.16 Comparison of occupant comfort perception criteria for 1-year return period (Bashor and Kareem, 2007).

motion index for future standards. It was proposed to adopt the RMS value as the best available index. According to Kareem (1992), criteria based on RMS acceleration thresholds offer a more accurate means of combining response in different directions based on their respective correlations. In the peak acceleration criterion, the first peaks in each direction are determined and subsequently combined by an empirical correlation rule; however, since different response components may have a different probability structure, requiring different peak factors, care must be exercised (Kareem *et al.*, 1999). However, advocates of peak acceleration criteria contend that peak resultant accelerations are difficult to estimate when RMS accelerations are used (Isyumov, 1993). As reported in Huang (2008), since motion perception may be more dominated by the overall averaged effect for long duration events of a stationary vibration, the use of the RMS acceleration may be a reasonable choice to check the occupants comfort of buildings under more frequently occurring wind events, while for short duration infrequently occurring wind events, such as thunderstorms and typhoons, averaging the acceleration over the worst 10 minutes of the non-stationary motion of buildings may be statistically meaningless, and may also underestimate the effects of the largest individual peaks. It seems that peak and RMS acceleration response may characterize different motion effects on human response (Burton *et al.*, 2007). Hence, the choice of a particular acceleration criterion may depend on the type of dominating wind events in the geographical location of the building. Further investigations have shown that the *jerkiness* of the structural response may primarily be responsible for motion perception. While humans are capable of adjusting to acceleration, any change in the acceleration will require additional adjustments for equilibrium. As a result, perception criteria based on a

measure of *jerk* or the *rate of change of acceleration*, may better define perception thresholds under random motion. The adoption of such criteria may override the need of peak acceleration (McNamara *et al.*, 2002).

Finally, the debate about whether human response to wind-induced motion is dependent on the motion frequency is still open. As presented in subsection 2.4.1, Chang (Chang, 1967, 1973) was one of the first to suggest frequency independent occupant comfort criteria. The first code recommending frequency independent peak acceleration criteria was the NBCC (1977). On the other hand, Chen and Robertson (1972), Irwin (1978) and later the ISO 6897 (1984) guidelines suggested the frequency dependency of motion perception.

Burton *et al.* (2006) characterized the biodynamic human body vibration response, occurring during exposures to low-frequency, constant amplitude acceleration sinusoidal motion, and showed a physiological frequency dependence of this motion. The results from a series of motion simulator experiments showed that, as the frequency of oscillation increases from 0.15 to 1.00 Hz, acceleration measured at the head of a human test subject is increasingly magnified. This motion magnification demonstrates that biodynamic human body vibration is frequency dependent in this frequency range. Furthermore, there may also be further implications for visual perception of motion through parallax shift. Evidently, these effects have to be accounted for in developing more refined occupant comfort acceptable criteria for tall buildings motion.

According to the various considerations illustrated before, the comfort criterion which will be used in this research for the discomfort risk assessment and comfort checking under serviceability conditions of a case study tall building (chapter 8), is the ISO 6897's motion perception threshold, expressed in terms of standard deviation acceleration for a 10-minute duration in 5-year-recurrence wind and given as a function of frequency as:

$$\overline{\sigma_a} = exp(-3.65 - 0.41 \ln n) \tag{2.2}$$

where $\overline{\sigma_a}$ denotes the standard deviation modal acceleration response of the building and n is the natural frequency.

2.5 Summary and main remarks

This chapter deals with the problem of discomfort risk of tall buildings, induced by the wind action. A general probabilistic risk management framework is illustrated and the Performance-Based Design approach, based on the PEER's equation, for the assessment of risk is discussed and framed mathematically. The perception of vibration is becoming a more and more significant issue in the serviceability design of modern tall buildings, because the recent trends towards increasing height and slenderness is contributing to the generation of structures which are particularly sensitive to the wind excitation. Numerous studies have been dedicated to the definition of tolerance thresholds of wind-induced vibrations of structures. This chapter presents a brief review of them. It is now widely accepted that the perception of motion is closely related to the acceleration response of structures. However, the international community has not agreed on a universal comfort criterion. The debate about whether human response to wind-induced motion is dependent or not on the

frequency of vibration, together with that about the use of RMS or peak acceleration criteria, is still open. In this research, the comfort criterion proposed by the ISO 6897 standard is chosen and will be applied later for the discomfort risk assessment and comfort checking of a case study structure.

Chapter 3

Square section bluff-body aerodynamics

3.1 Introduction

Recent trends towards increasingly taller and slender structures have developed a new generation of buildings, particularly sensitive to the wind action. The knowledge of the flow field around prismatic objects of square and rectangular cross section is, therefore, receiving considerable attention for its relevance to tall buildings design. The understanding of the flow field around *bluff bodies*[1], such as buildings, and, consequently, the wind loads and effects on them, is a challenging task due to the complexity of the physical phenomena involved, including detachment of large eddies, massive flow separation and re-attachment. Furthermore, air flows around buildings are, usually, strongly three-dimensional (3-D), even for very slender and almost two-dimensional (2-D) geometries. All these aspects pose great difficulty for the accurate prediction of the flow field using computational methods. Current state-of-the-art Computational Fluid Dynamics (CFD) techniques are not able to fully substitute wind tunnel testing for bluff bodies aerodynamics, yet. Nevertheless, recent improvements in both software and hardware make the use of CFD methods ever more valuable to civil engineering applications.

This chapter is dedicated to the aerodynamics of prismatic objects, with particular focus on the square section prism. Section 3.2 is aimed at defining basic concepts and quantities of common use in bluff-body aerodynamics. Section 3.3 reviews the wake and the shedding of vortices from fixed bluff bodies in two-dimensional flows. Section 3.4 is devoted to the aerodynamics of two-dimensional square cylinders. Different flow patterns at various angles of incidence are illustrated. Strouhal number, fluctuating pressure coefficients and aerodynamic lift and drag forces are also discussed. Lastly, in section 3.5 the three-dimensional flow behind a finite-length square cylinder is presented.

[1] *"Bluff bodies"*, in contrast to *"streamlined bodies"*, such as aircraft wings, are characterized by the fact that, when immersed in a flow, the streamlines do not follow the surface of the body but detach from it creating regions of separated flow and a wide trailing wake (Cook, 1986).

3.2 Wind-induced pressures and forces in 2-D and 3-D flows

This section is aimed at the synthetic definition of basic concepts and quantities of bluff bodies aerodynamics that will be used in the following sections.

The flow around a bluff body of generic cross section develops local pressures, p, in accordance to the Bernoulli's equation. The surface pressure on the body could be expressed in the form of a non-dimensional *pressure coefficient*, C_p, defined as:

$$C_p = \frac{p - p_0}{\frac{1}{2}\rho {U_0}^2} \tag{3.1}$$

where p is the pressure, ρ is the air density and p_0 and U_0 are the pressure and velocity in the region outside the influence of the body, respectively. The quantity p_0 is also known as the *static pressure* of the undisturbed flow, while $\frac{1}{2}\rho {U_0}^2$ is called *dynamic pressure* of the undisturbed flow and is referred to as p_{dyn}.

The integration of the pressures over the body surface results in a net force, F, and a moment, M. Aerodynamic forces are conventionally resolved into two orthogonal directions, that may be parallel (along-wind) and perpendicular (across-wind) to the wind direction (or mean wind direction in the case of turbulent flow), in which case the axes are referred to as *wind axes*, or parallel and perpendicular to a direction related to the geometry of the body and referred to as *body axes* (Fig. 3.1). The components of the force in the along-wind and across-wind directions are commonly referred to as *drag* and *lift* respectively. The macroscopic effects of the flow around a bluff body can be, therefore, described in terms of a *drag force*, D, a *lift force*, L, an a *moment*, M.

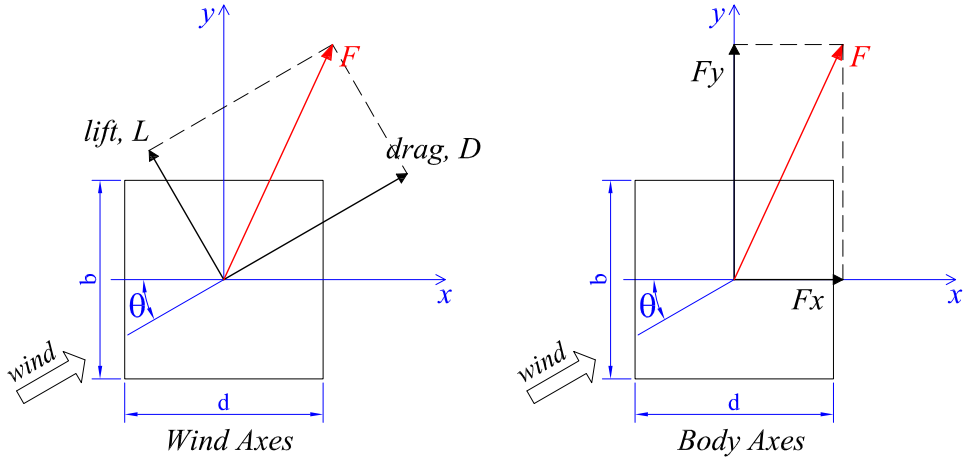

Fig. 3.1 Wind force components along wind axes and body axes.

3.2.1 Aerodynamic forces in 2-D flows

In two-dimensional flows, that means independent of the coordinate normal to the plane of the body cross section, the aerodynamic forces, D, L and M, with reference to the wind axes in Fig. 3.1, represent values per unit of dimension normal to the plane of observation. They can be rendered dimensionless and expressed in

terms of *drag*, *lift* and *moment coefficients*, C_D, C_L, C_M, respectively, as follows:

$$C_D = \frac{D}{\frac{1}{2}\rho {U_0}^2 b} \tag{3.2}$$

$$C_L = \frac{L}{\frac{1}{2}\rho {U_0}^2 b} \tag{3.3}$$

$$C_M = \frac{M}{\frac{1}{2}\rho {U_0}^2 b^2} \text{ or } C_M = \frac{M}{\frac{1}{2}\rho {U_0}^2 bd} \tag{3.4}$$

where b and d are reference dimensions. Usually b is the *width* or *breadth* of the structure normal to the wind and d is the *depth* of the structure in the direction of wind.

3.2.2 Aerodynamic forces in 3-D flows

Fig. 3.2(a) shows the aerodynamic loads acting on a three-dimensional body, representing, for example, a tall building. The approaching wind direction is oriented of an angle θ with respect to the x and y body axes. The corresponding *drag* and *lift coefficients*, C_D and C_L, are defined as:

$$C_D = \frac{D}{\frac{1}{2}\rho {U_0}^2 A} \tag{3.5}$$

$$C_L = \frac{L}{\frac{1}{2}\rho {U_0}^2 A} \tag{3.6}$$

where D and L are the drag and lift forces, in the directions parallel and perpendicular to wind, respectively, and acting on the whole surface, and A is a reference area, often the projected frontal area, e.g. equal to width times height (bh). Analogously, the non-dimensional force components, C_{F_x} and C_{F_y} along x and y body axis, respectively, are defined as:

$$C_{F_x} = \frac{F_x}{\frac{1}{2}\rho {U_0}^2 A} \tag{3.7}$$

$$C_{F_y} = \frac{F_y}{\frac{1}{2}\rho {U_0}^2 A} \tag{3.8}$$

Wind-induced moments, M_x, M_y, M_z, result from the normal pressure and the shear stress actions multiplied by their moment arms and integrated over the building surface [Fig. 3.2(b)]. The corresponding non-dimensional moment coefficients, C_{M_x}, C_{M_y}, C_{M_z} may be defined as:

$$C_{M_x} = \frac{M_x}{\frac{1}{2}\rho {U_0}^2 Al} \tag{3.9}$$

$$C_{M_y} = \frac{M_y}{\frac{1}{2}\rho {U_0}^2 Al} \tag{3.10}$$

$$C_{M_z} = \frac{M_z}{\frac{1}{2}\rho {U_0}^2 Al} \tag{3.11}$$

where l indicates a reference dimension. The product Al is often assumed equal to bh^2.

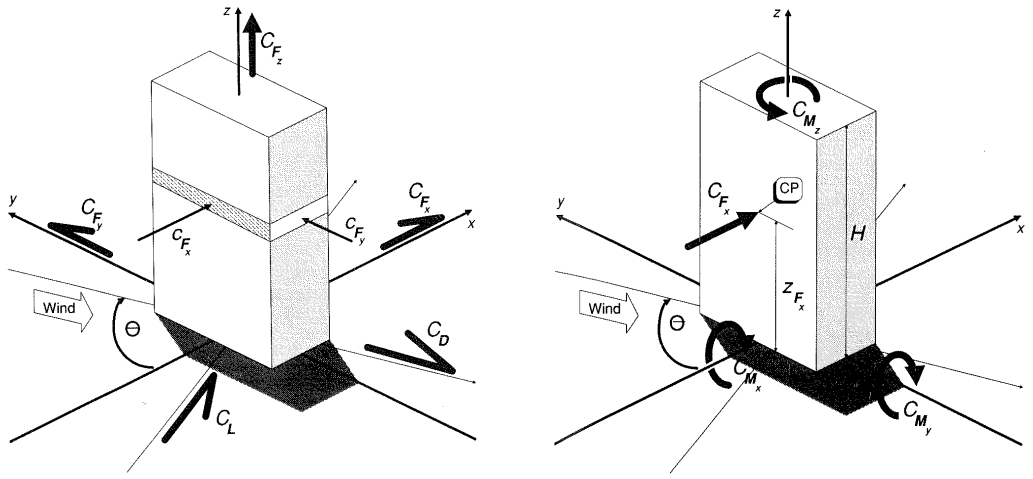

Fig. 3.2 Representation of wind directional loads: a) force coefficients; b) moment coefficients (Cook, 1990).

3.3 Wake and vortex shedding from fixed bluff bodies in two-dimensional flows

Unsteady flow over a 2-D fixed cylinder represents a classical flow paradigm in bluff-body aerodynamics. Even if the flow around buildings is usually three dimensional, in the case of slender structures exposed to cross air flows, the flow field can be studied as predominantly two-dimensional. For this reason, the study of the flow pattern around two-dimensional cylinders having building-type cross sections, such as the simplest case of the square section referred to in this study, is of primary importance in the design of slender structures.

A lot of work has been done so far on the 2-D flow about a circular cylinder rather than a square cylinder. In the renowned case of the circular cylinder, a number of flow patterns can be created by increasing the incoming flow velocity, each situation being identified by a specific range of the Reynolds number Re (Simiu and Scanlan, 1996). The latter expresses the ratio between inertial forces and viscous forces and is defined as:

$$Re = \frac{\rho U l}{\mu} = \frac{U l}{\nu} \tag{3.12}$$

where μ and ν are, respectively, the *dynamic* and *kinematic viscosities* of the fluid, U is the mean velocity of the approaching flow and l indicates here a typical length, that is usually the diameter in the case of a circular cylinder and the side dimension for a square section prism.

The flow regimes past a circular cylinder at varying Reynolds number values were reviewed in detail by Willamson (1996). For a wide range of Re, alternating vortices are shed from the cylinder surface and form the classical *vortex trail* or *vortex street* configuration downstream. This phenomenon was first reported by Bérnard (1908) and Von Kármán (1911) at the beginning of the XX century. Fig. 3.3 depicts the streamlines of the wake flow behind a circular cylinder for various Re values.

The principle of the vortex shedding phenomena is shown in Fig. 3.4, where an infinitely long, rigid circular cylinder is considered. The flow separation on the right side (in the direction of the incoming flow) produces a circulation, $+\Gamma$, in the cylinder wake. After Thomson's vortex law, a counter circulation, $-\Gamma$, occurs around the cylinder surface, producing a circulation current, ΔV, flowing clockwise around the cylinder. This velocity ΔV reduces the flow velocity, V_2, on the right side, while increases it on the left side. As a consequence, on the basis of the Bernoulli equation, the static pressure increases on the right side and decreases on the left side, leading to a cross wind force, indicated with F_y in Fig. 3.4, acting on the cylinder (Ruscheweyh, 2010). Since the vortices are shed alternately from opposite sides of the cylinder, the perpendicular force, F_y, alternates too, and its frequency is the same as the frequency at which the vortex shedding is formed.

Bluff bodies with other cross section shapes give rise to analogous vortex shedding phenomena. For a non-vibrating structure, the distance between vortices rotating in the same direction is proportional to the structure breadth, b, perpendicular to the direction of the wind (that coincides with the diameter in the case of a circular cylinder). The time between vortices is equal to this distance divided by the velocity of vortices, that is proportional to incoming wind speed, U. Therefore, the frequency of the lateral load caused by vortex shedding, f_s, is proportional to U/b. This linear relation, showed at the end of the nineteen century by a study of Strouhal (Strouhal, 1878), allows the definition of a nondimensional quantity, known as *Strouhal number*, St:

$$St = \frac{f_s b}{U} \tag{3.13}$$

Eq. (3.13) defines the Strouhal law, that is valid for stationary, two-dimensional bluff bodies. The frequency normalized by a value of the velocity and a reference dimension, as in the case of Eq. (3.13), is referred to as *reduced frequency*, and indicated hereinafter with f_r. The reciprocal of this parameter is called *reduced velocity* and is indicated with U_r.

Vortex shedding also generates a harmonically varying longitudinal load with a frequency of $2f_s$.

3.4 Aerodynamics of a 2-D square cylinder

The study of flow around prismatic objects of square section has received considerable attention motivated by fundamental aerodynamic interest, and its relevance

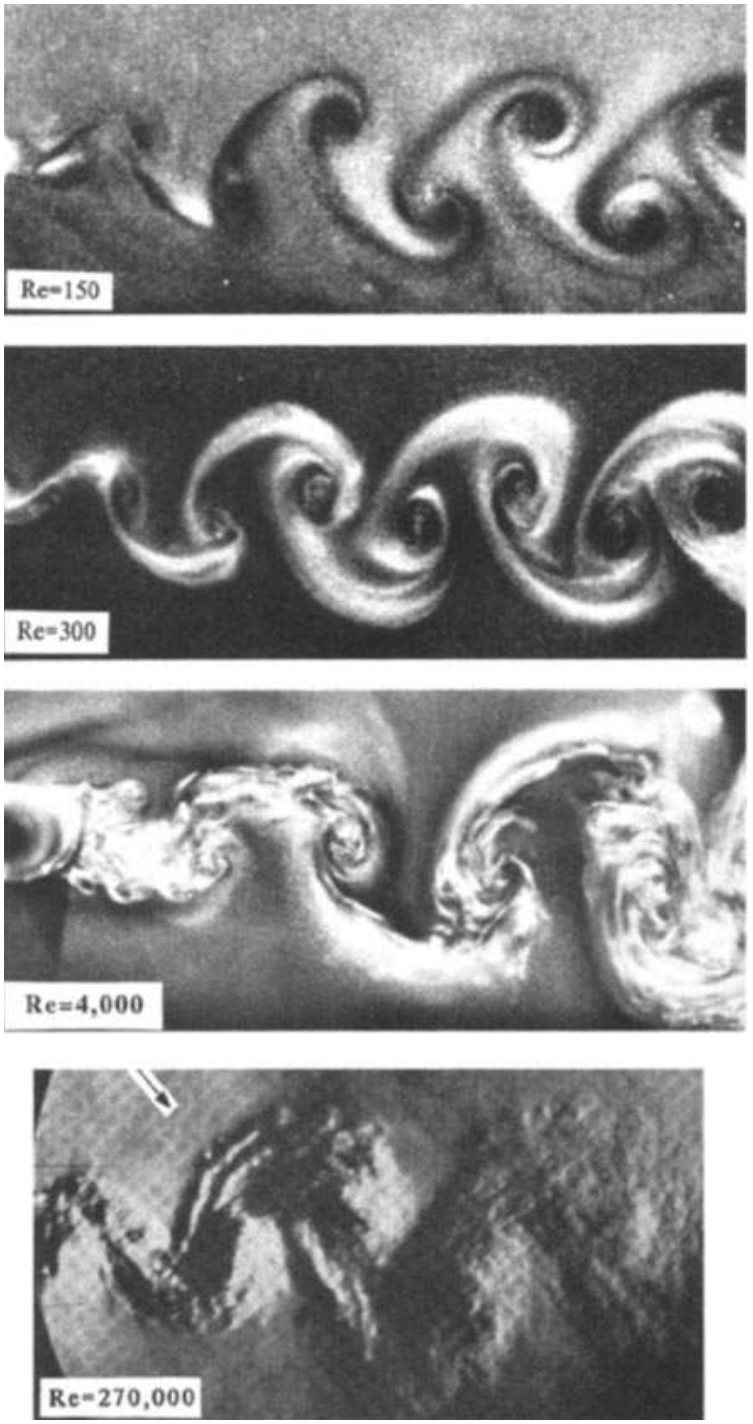

Fig. 3.3 Visualization of the vortex streets behind a circular cylinder over a wide range of Re (Willamson, 1996).

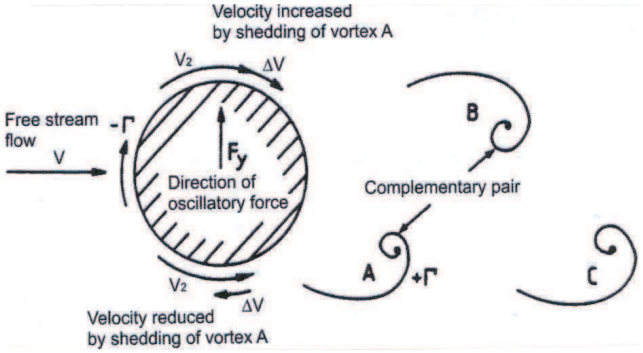

Fig. 3.4 The principle of the vortex shedding phenomena (Ruscheweyh, 2010).

to wind engineering and structural engineering applications, such as flow around buildings. Relevant experimental investigations on flow behind a square cylinder are, for example, those of Saha *et al.* (2000), Dutta *et al.* (2003), Ozgoren (2006), Dutta *et al.* (2008), Van Oudheusden *et al.* (2008). Moreover, many numerical studies (applications of Computational Fluid Dynamics - CFD) have been dedicated to the comprehension of the aerodynamics of square section cylinders [e.g. Bergstrom and Wang (1997); Taylor and Vezza (1999); Oka and Ishihara (2009); Šoda *et al.* (2011)], using different approaches. These include, for example, URANS (Unsteady Reynolds Averaged Navier Stokes), DNS (Direct Numerical Simulation), LES (Large Eddy Simulation) and DVM (Discrete Vortex Method).

3.4.1 Flow patterns

The flow structure behind a cylinder with square cross section resembles that behind a circular cylinder. However, the reasons for flow separation on the cylinder surfaces are totally different. Flow separation on the surfaces of the circular cylinder occurs due to an adverse pressure gradient in the downstream direction and the separation points move back and forth depending on the Reynolds number. On the other hand, in the case of the square section cylinder, as for other geometries with sharp corners, the separation points are fixed either at the leading edges (upstream corners), due to the abrupt geometrical changes at its sharp edges, or at the trailing edge, depending on the Reynolds number. The region of vortex formation is significantly broader and longer for a square section cylinder than for a circular cylinder (Dutta *et al.*, 2008).

Differently from behind circular cylinder, the flow pattern behind a fixed rectangular and, therefore, also square section cylinder is, even intuitively, sensitive to its orientation to the approaching flow, usually refereed to as *angle of incidence*, or *angle of attack*, indicated with θ in Fig. 3.5. While at moderate incidence, the separation points are fixed at the upstream corners, the orientation has a pronounced effect on the shear layer development, wake formation and resulting mean and fluctuating aerodynamic forces.

Dutta *et al.* (2003) examined the sensitivity of the wake properties to the cylinder orientation. Fig. 3.6 shows some images of the flow pattern behind the square cylinder recorded by the same authors in a smoke tunnel facility at a Reynolds number of 3920. At zero angle of incidence the flow separates from the corners of the

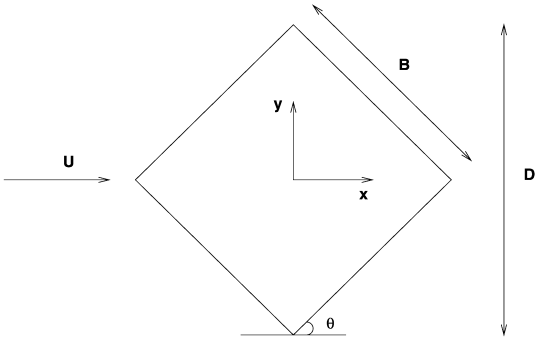

Fig. 3.5 Schematic drawing of a square section cylinder of side B, placed at an angle of incidence, θ to the incoming flow (Dutta *et al.*, 2003).

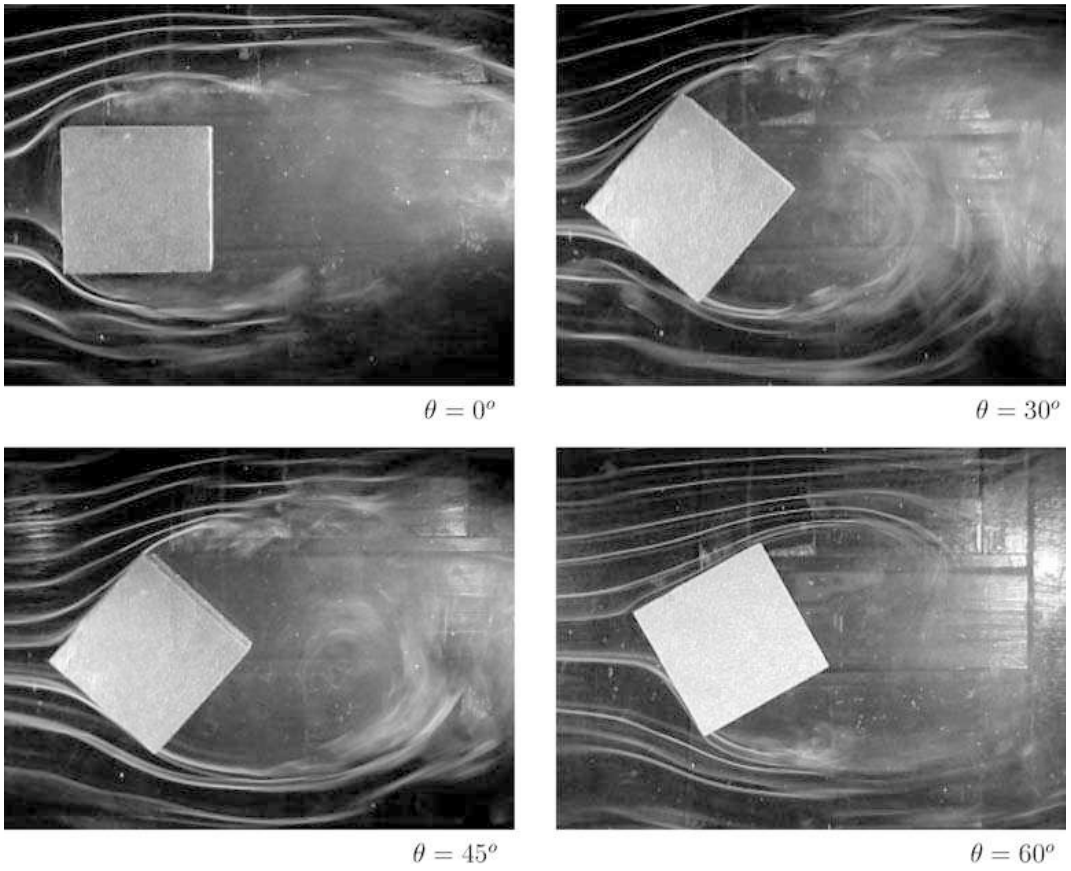

Fig. 3.6 Smoke visualization of flow around a square section cylinder at various angles of incidence with $Re = 3920$ from Dutta *et al.* (2003).

windward face. For inclinations greater than zero, the separation points is delayed up to the cylinder corners on the downstream side and the wake size increases, but the separated shear layer rolls up over a shorter distance. Flow patterns behind a square section cylinder have been classified into the following types depending on the cylinder orientation:

- perfect separation type
- reattachment type

The transition from the first to the second pattern occurs at a low value of the angle of incidence, often identified in the range $10° - 15°$. Van Oudheusden *et al.* (2008) investigated the flow field around a square section cylinder by means of Particle Image Velocimetry (PIV). According to their observations (Fig. 3.7 [2]), at zero incidence, the flow pattern is predominantly symmetric. Flow separation occurs at both upstream corners, small recirculation regions are observed above and below the model and two large recirculation regions appear in the wake behind the cylinder. At higher values of the angle of incidence, the separated region expands. At the leeward side, upper surface in Fig. 3.7, the side and rear recirculation regions gradually merge, while at the windward side, lower surface, the side recirculation is increasingly confined, with reattachment of the shear layer at an incidence between 10° and 15°. It has been noted that the exact angle where reattachment begins to occur depends on the turbulence level and the Reynolds number as well (Vickery, 1966; Lee, 1975). Similar characteristics of the vortex trail behind a square section cylinder were obtained numerically by Taylor and Vezza (1999).

The distance between the end of the time-averaged separated wake, corresponding to the saddle point in the streamlines, and the center of the square is defined as *bubble* or *reattachment length*. The latter is found to be almost insensitive to Reynolds number for 0° and 15°, while a pronounced effect is present for intermediate angles. This phenomenon is possibly due to a Reynolds number effect on the intermittent reattachment of the separated shear layer.

3.4.2 Strouhal number, pressures and aerodynamic forces on a 2-D fixed square cylinder

Fluctuating pressure coefficients and aerodynamic lift and drag forces on a 2-D square section cylinder have been measured by many authors [e.g. Vickery (1966); Chen and Liu (1999); Saha *et al.* (2000); Van Oudheusden *et al.* (2008); Liang *et al.* (2011)]. Fig. 3.8 shows the spectra of the lift force measured at 0° angle of incidence and $Re = 1.0 \times 10^5$ in both smooth and turbulent flow conditions. In both cases the bulk of the energy is in a very narrow band centered on the Strouhal frequency.

Liang *et al.* (2011) investigated Reynolds number effects on wind pressures over a square cylinder. The variation of the Strouhal number with increasing Reynolds number, ranging from 2.7×10^4 and 6.8×10^5, under a 0° angle of attack in smooth, 5% and 15% homogeneous turbulent flow fields was observed by analysing the position of the spectral peak of the across-wind force. As illustrated in Fig. 3.9, St is

[2] Unrealistic streamlines crossing the model surface are motivated by insufficient spacial resolution due to the finite window size of the PIV-image analysis. Higher resolution (zoom in) will resolve the flow details in these areas (Van Oudheusden *et al.*, 2008).

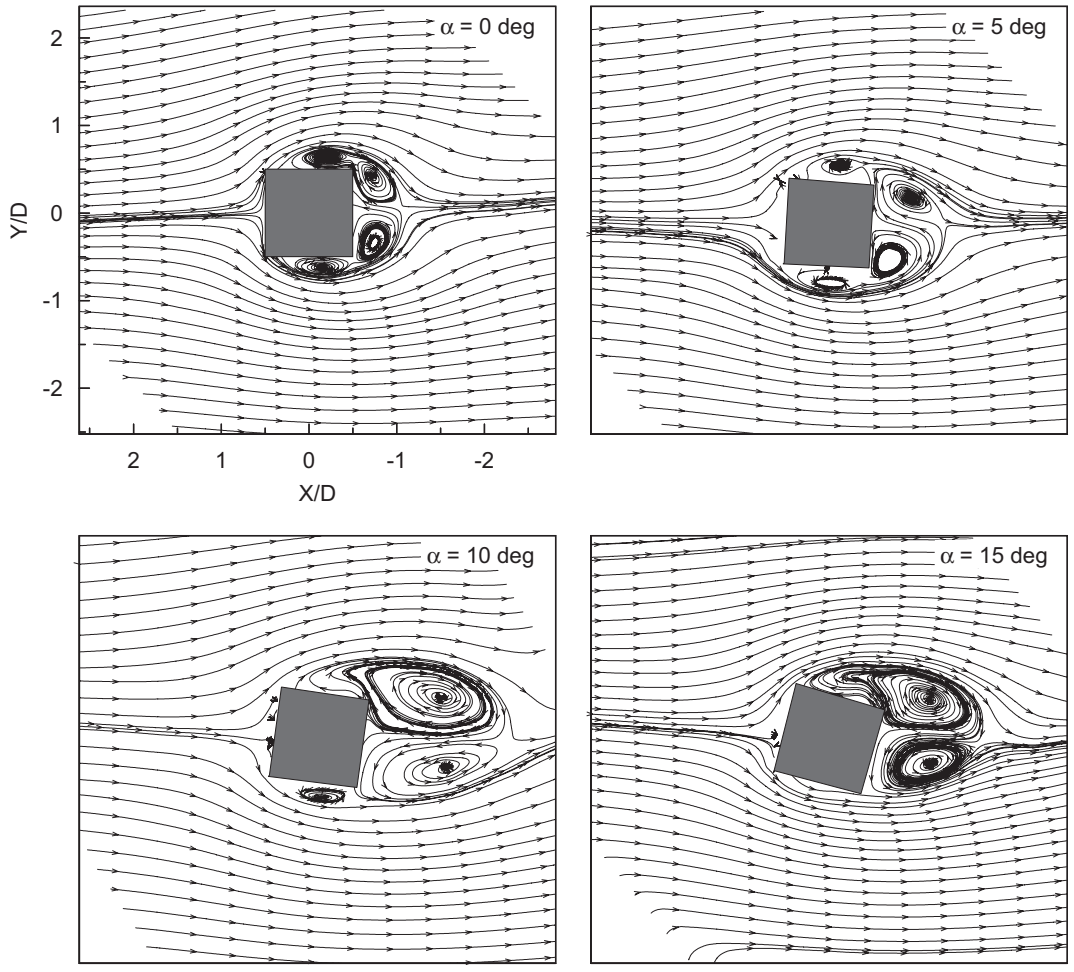

Fig. 3.7 Mean flow streamline pattern around a square section cylinder as a function of angle of incidence, at $Re = 20000$ from Van Oudheusden *et al.* (2008).

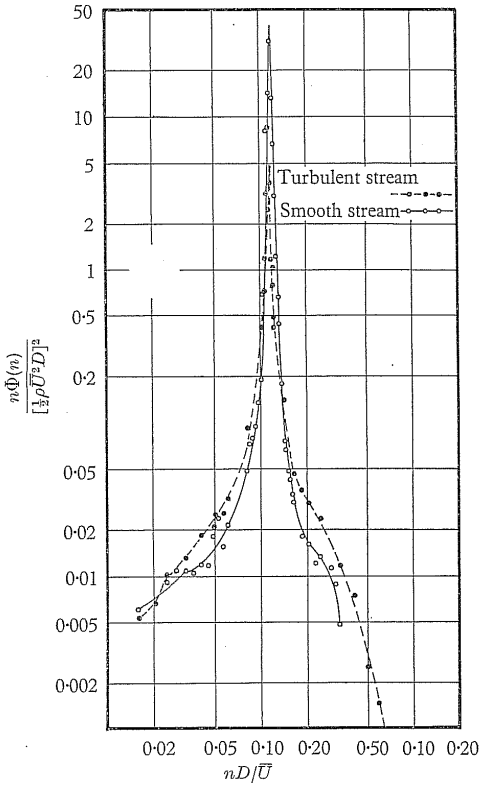

Fig. 3.8 Spectra of lift fluctuations on a square cylinder at 0° angle of incidence and $Re = 1.0 \times 10^5$ in both smooth and turbulent flow conditions (Vickery, 1966).

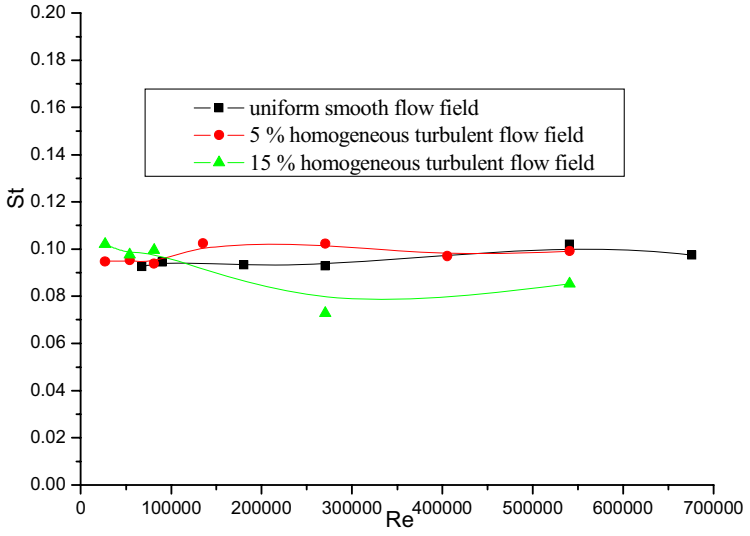

Fig. 3.9 Strouhal number variation with Reynolds number for a square section cylinder at 0° angle of attack (Liang *et al.*, 2011).

approximately equal to 0.1 in uniform and 5% homogeneous turbulent flow conditions, while values lower than 0.09 were observed for the 15% homogeneous turbulent flow field, showing an effect of turbulence on the Strouhal number in the Re range considered.

As seen in subsection 3.4.1, the formation of vortices behind a square cylinder

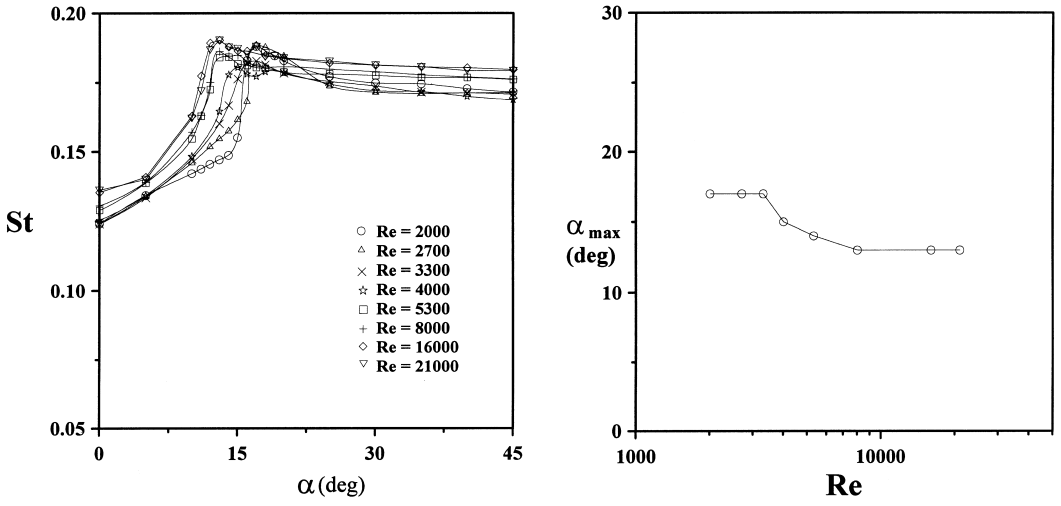

Fig. 3.10 Reynolds number and incidence effects on Strouhal number (Chen and Liu, 1999): a) St as a function of the angle of attack ($Re = 2000 - 21000$); b) angle at which St takes its maximum value as a function of Re.

depends on the orientation to the incoming flow. Fig. 3.10 shows the Strouhal number as a function of the angle of attack for Reynolds number ranging between 2000 and 21000 (Chen and Liu, 1999). At small incidence, St rises rapidly with increasing angle of attack, α, till a maximum at an angle α_{max}, and then it levels off between 0.17 and 0.18 at higher values of incidence [Fig. 3.10(a)]. Fig. 3.10(b) illustrates how α_{max} varies with Re. After a first Re number range where α_{max} takes its highest value, equal to 17°, and after a gradual descent for $Re = 3300 - 8000$, at higher Re values, α_{max} reaches a constant value of 13°.

A number of authors obtained similar relations between St and the angle of incidence, observing a sudden jump of St at comparable incidence, depending of Re [e.g. Vickery (1966); Dutta *et al.* (2008)]. The sudden jump of St at incidence between 13° and 17° is attributed to the onset of flow reattachment to the side face of the cylinder occurring, in fact, at the same incidence values, as seen in subsection 3.4.1, Fig. 3.7. From Fig. 3.10(b), at $Re = 20000$ the angle α_{max} is equal to 13°. This value of the angle of attack is in the range of incidence at which Van Oudheusden *et al.* (2008) observed flow reattachment for the same value of Re.

The achievement of a peak value of the Strouhal number at the onset of flow reattachment may be motivated by the fact that a decrease in the width of the wake can be linked to an increase in St. The angle at which reattachment of the shear layer to the windward side face of a square cylinder manifests corresponds to the narrowest wake and leads to the maximum Strouhal number.

Fig. 3.11(a) depicts the circumferential distribution of the mean pressure coefficients around a square section cylinder at zero incidence for a range of $Re =$

2000 − 16000 (Chen and Liu, 1999). The impingement pressure at the upstream face AB is not discernibly affected by Re. However, the pressure distribution on the side and rear faces, BC, CD and DA, appears to be influenced by Re in the range 2000-5300, while it levels off on the same curve for $Re > 5300$. Fig. 3.11(b) shows the pressure distribution measured at different angles of incidence for $Re = 5300$. The side face (BC) pressure distribution consists of a plateau of low pressure, followed by a recovery to a higher pressure nearing the trailing edge (C). The least pressure plateau as well as the strongest pressure recovery, indicating the onset of reattachment of the shear layer to the side face, occurs at the angle (14°) where the Strouhal number reaches its maximum value, as seen in Fig. 3.10.

Similarly to Chen and Liu (1999), Liang *et al.* (2011) investigated Reynolds

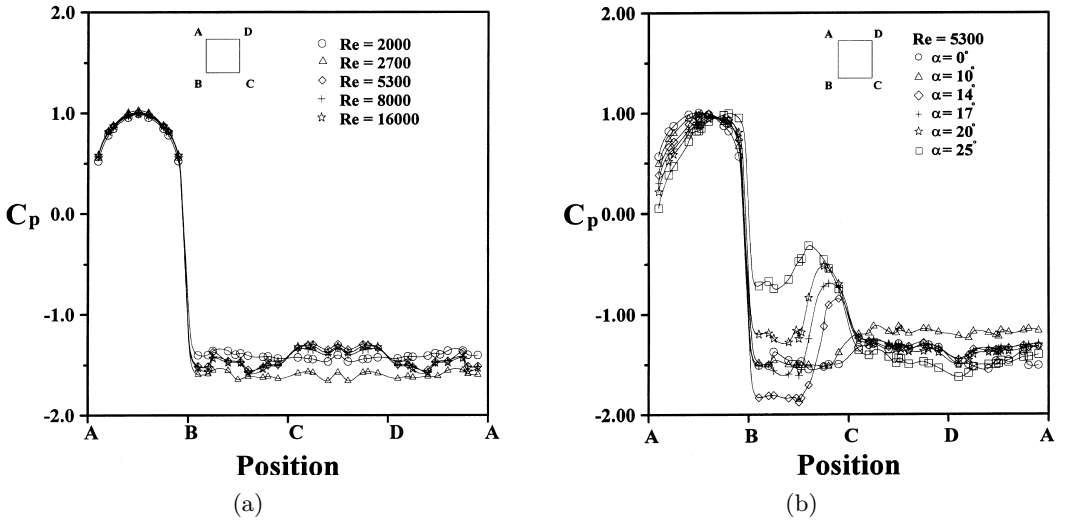

Fig. 3.11 Mean pressure coefficients distribution in uniform air stream at a turbulence level below 0.5%: a) zero incidence for various Reynolds numbers; b) variuos angles of incidence at $Re = 5300$ [Chen and Liu (1999)].

number effects on the pressure distribution around a square section cylinder. Their results concerning zero incidence and 15% homogeneous turbulent flow conditions are reported in Fig. 3.12. Reynolds number effects on the mean pressure coefficient [Fig. 3.12(a)] on the windward side are negligible, while the mean pressure distribution in the negative pressure regions on the sideward and leeward faces shows a sensitivity to Re. Two families of curves can be distinguished, the first for Re ranging from 27040 to 81120, and the second for Re from 270400 to 540800. The maximum difference of mean pressure coefficients in absolute values between the two families is 0.336. A bifurcation between these two Re families is also evident in Fig. 3.12(b). The RMS wind pressure coefficients all around the cylinder surface are much higher (maximum diffence equal to 0.2) for $Re = 27040 - 81120$ than for $Re = 270400 - 540800$.

The mean aerodynamic drag and lift coefficients, $\overline{C_D}$ and $\overline{C_L}$, at angles of incidence ranging from 0° to 45° were reported by several authors. Fig. 3.13 and Fig. 3.14 illustrate a summary of the results of two experimental works (Lee, 1975; Van Oudheusden *et al.*, 2008) and two numerical works (Taylor and Vezza, 1999; Oka and Ishihara, 2009).

At small incidence (perfect separation flow type, subsection 3.4.1), as the angle

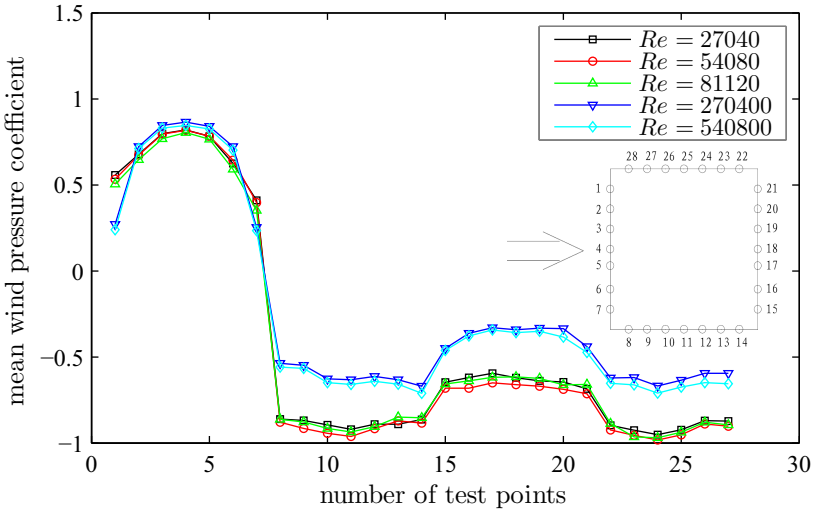

(a)

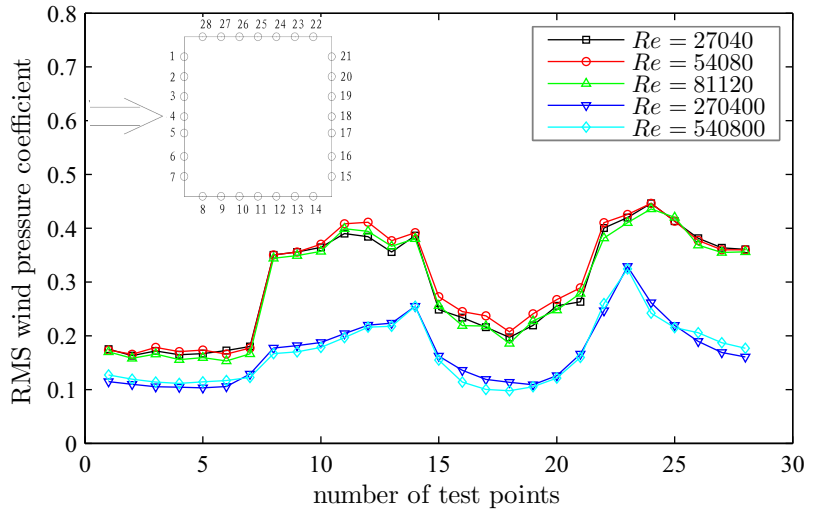

(b)

Fig. 3.12 Wind pressure coefficients in 15% homogeneous turbulent flow field at zero incidence: a) mean values; b) RMS values [Liang *et al.* (2011)].

of attack increases, the mean drag coefficients, $\overline{C_D}$, decreases (Fig. 3.13) primarily because of the shear layer that is shed from the upstream corner (on the lower surface with reference to Fig. 3.7), intermittently contacting the subsequent leeward corner. At the angle where reattachment occurs, between 10° and 15° according to different authors, the shear layer does not separate from the upstream corner on the lower side anymore, giving rise to a narrower wake and a lower value of the mean drag coefficient. Further increases in the angle of incidence simply lead to an enlargement of the wake and a gradual increase in $\overline{C_D}$, from approximately 15° to 45° (reattachment type flow pattern).

Transition from perfect separation to reattachment flow pattern explains also the variation of the mean lift coefficient, $\overline{C_L}$, with angle of incidence, illustrated in Fig. 3.14. Before reattachment, when the angle of incidence increases, side and rear recirculation (Fig. 3.7) gradually merge, giving rise to a separation bubble on the upper side. The separation bubble causes higher local suction pressures than those on the opposite side (lower surface), determining a negative lift coefficient with a maximum absolute value at the angle of full reattachment. As the angle further increases, the separation bubble decreases, so reducing the local suction pressures, which gradually balance with the ones at the opposite side, determining a decrease in the absolute value of $\overline{C_L}$.

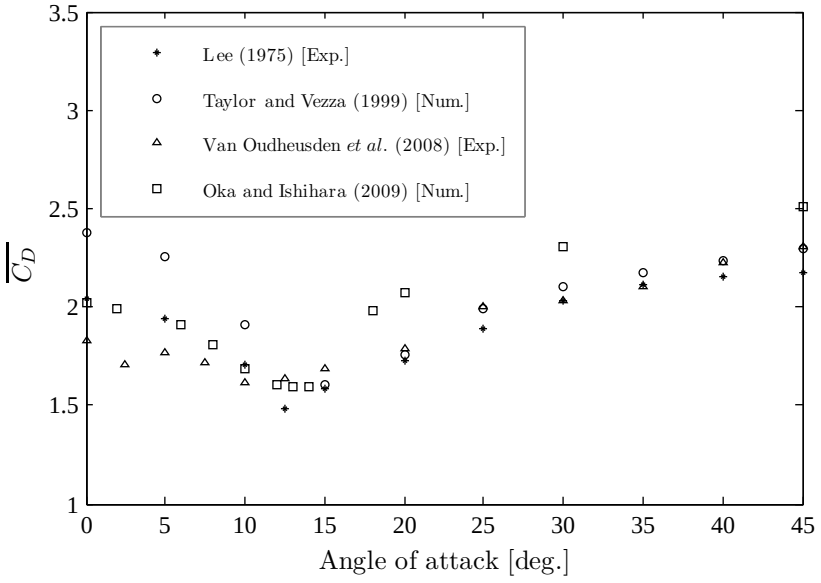

Fig. 3.13 Variation of mean drag coefficient, $\overline{C_D}$, with angle of attack from different authors [Lee (1975); Taylor and Vezza (1999); Van Oudheusden *et al.* (2008); Oka and Ishihara (2009)].

The Root Mean Square (RMS) value of the fluctuating normal force coefficient on a square section is illustrated in Fig. 3.15, as a function of the angle of attack for both smooth and turbulent (turbulence intensity equal to 10%) incoming flow condictions (Vickery, 1966). Turbulence is seen to reduce the RMS value of the normal force below the corresponding laminar flow values at small angles, while increasing them at higher incidences.

The dependence of the drag coefficient, C_D, upon the turbulence intensity is il-

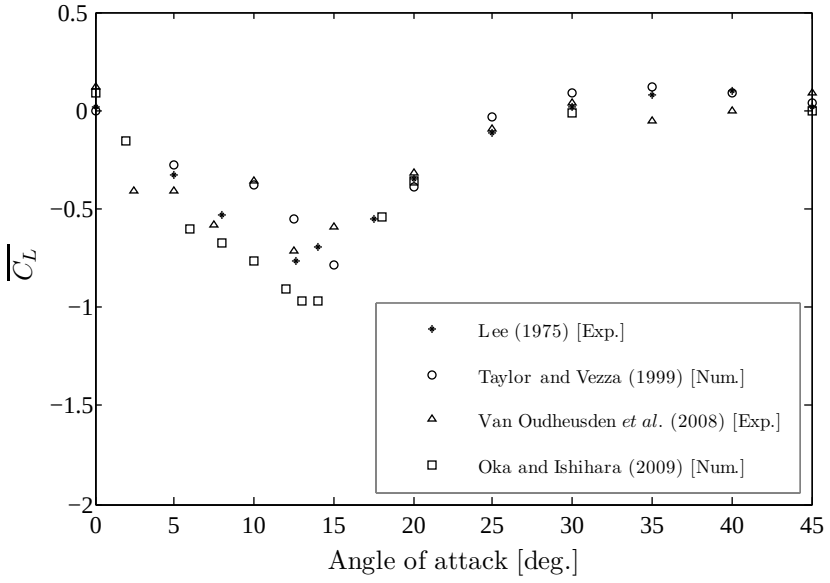

Fig. 3.14 Variation of mean lift coefficient, $\overline{C_L}$, with angle of attack from different authors [Lee (1975); Taylor and Vezza (1999); Van Oudheusden *et al.* (2008); Oka and Ishihara (2009)].

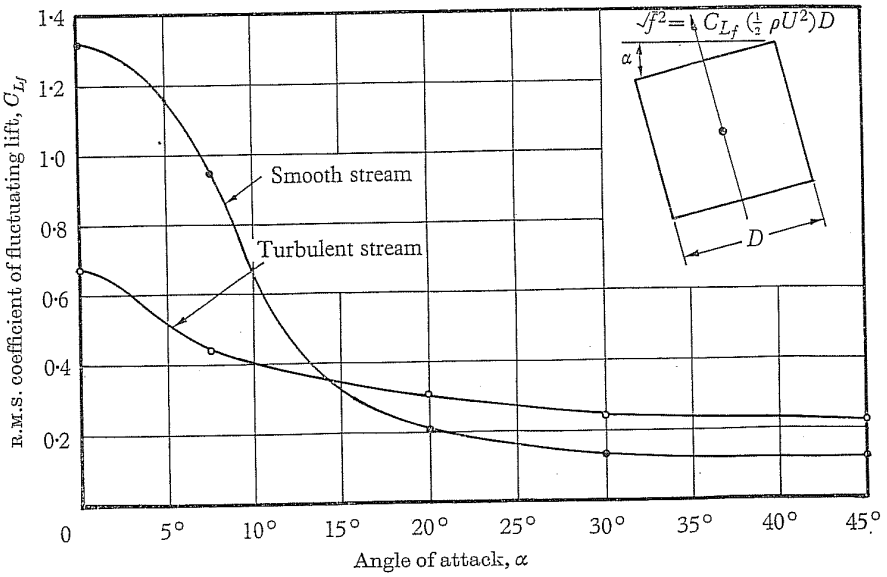

Fig. 3.15 Variation of the RMS normal force coefficient, indicated with C_{L_f} with angle of attack in smooth and turbulent flows (Vickery, 1966).

lustrated in Fig. 3.16, where the curve $b/h = 1$ refers to the square section cylinder. This picture shows that an increase in turbulence leads to a descrease of the drag coefficient.

For bluff bodies with rounded surfaces, the positions of the points of detach-

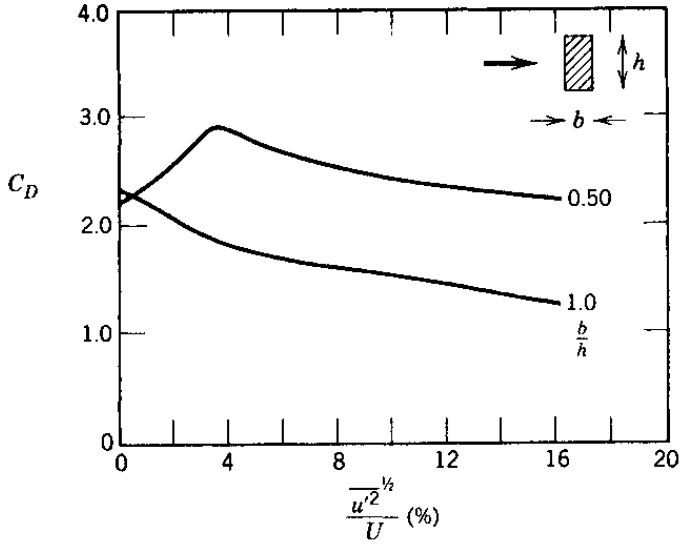

Fig. 3.16 Dependence of drag coefficient on turbulence intensity for rectangular section cylinders (Laneville *et al.*, 1977), from Simiu and Scanlan (1996).

ment of flow from the surfaces are much more dependent on viscous forces that in the case of sharp-edged bodies. This results in a variation of the drag coefficient with Reynolds number, which, as previously mentioned, is the ratio of inertial forces to viscous forces in the flow. Fig. 3.17 shows that a quite moderate rounding of the corners of a long square section prism results in a decrease of the drag coefficient, which also becomes Reynolds dependent. The critical Reynolds number at which the sudden decrease of the drag coefficient occurs is influenced both by surface roughness (see smooth surface and sanded surface lines in Fig. 3.17) and by turbulence in the approaching flow (Scruton, 1981). Both surface roughness and turbulence promote the transition to turbulent boundary layers at lower Reynolds number values. These layers detach from the surface at more rearward positions than do the laminar boundary layers found at sub-critical values. As a consequence, the wake width and the drag coefficient decrease.

In Table 3.1 some results of different numerical and experimental studies on the flow around a square cylinder at 0° angle of incidence are reported.

3.5 Three-dimensional air flows around finite-length square cylinders

In civil engineering applications cylinder-like structures have a finite length (or height), often with one free end and the other end fixed on the ground. These structures, including the case of high-rise buildings, cannot be treated as two-dimensional cylinders. It is now well established that, due to the end effects, the flow structure behind a finite-length cylinder differs drastically from that behind a two-dimensional cylinder, as unveiled in a number of previous studies, mostly focusing on circular

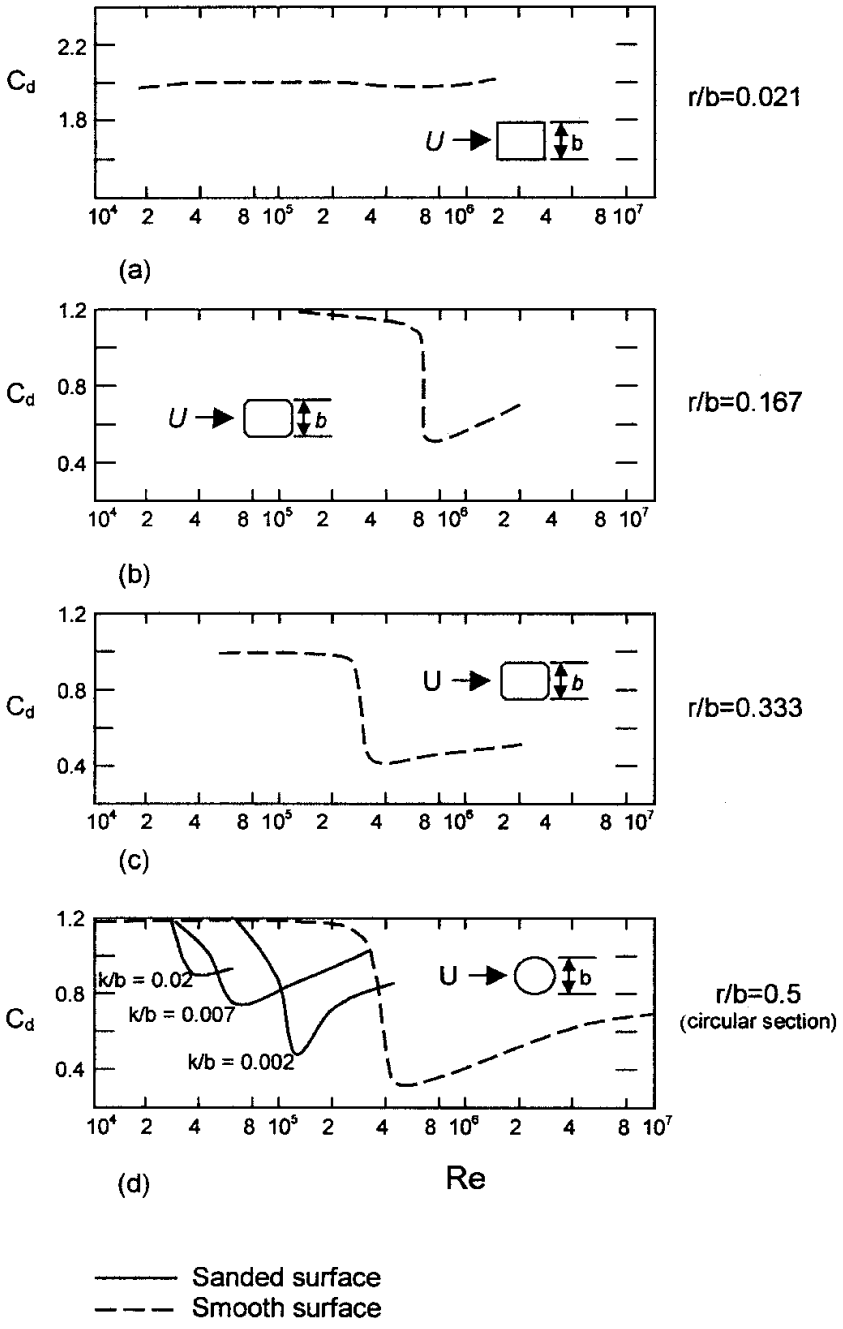

Fig. 3.17 Influence of Reynolds number Re, corner radius r/b and surface roughness k/b (where k is the size of grain) on drag coefficients C_D per unit span for 2-D (aspect ratio considered infinite) prisms of square section and circular cylinders, from Scruton (1981) [see also Holmes (2001)].

Table 3.1 Strouhal number and aerodynamic force coefficients for a square cylinder at 0° angle of incidence, reported from different authors for different Re ($\overline{C_D}$ = mean drag coefficient, $C_D{}'$ = standard deviation of drag coefficient, $\overline{C_L}$ = mean lift coefficient, $C_L{}'$ = standard deviation of lift coefficient)

Author	St	$\overline{C_D}$	$C_D{}'$	$\overline{C_L}$	$C_L{}'$	Re
Experimental works						
Vickery (1966)	0.118	2.05	0.17		1.32	1.6e+5
Lee (1975)	0.1214	2.04	0.23	0.021		1.76e+5
Chen and Liu (1999)	0.124-0.138					0.2-2.1 e+4
Saha *et al.* (2000)	0.144-0.142	2.13-2.2				8700-17625
Liang *et al.* (2011)	0.085-0.1	1.05-1.35	0.035-0.28	0-0.05	0.043-0.6	0.27-6.8 e+5
Numerical works						
Taylor and Vezza (1999)	0.1278	2.38		0.019		2.0e+4
Oka and Ishihara (2009)	0.122-0.125	2.02-2.08	0.14-0.25	0-0.1	1.25-1.32	1e+4
Šoda *et al.* (2011)	0.113-0.126	1.96-2.04	0.11-0.17		1.41-1.46	2.64e+4

cylinders.

The near wake of a wall-mounted finite-length circular cylinder, as reviewed by Wang *et al.* (2004) and Wang and Zhou (2009), was found to be strongly three-dimensional, due to the interaction of tip vortices sprung from the free end and horseshoe vortices shed at the base. Furthermore, the ratio between the cylinder height, h, and the diameter, d, i.e. the aspect ratio, has a great influence on the wake structure. When h/d is below a critical value $(h/d)_{crit}$, vortex shedding changes from the antisymmetrical Kármán type (the *vortex trail* illustrated in section 3.3), to the symmetric arch-type, and the free-end downwash flow dominates the wake. For $h/d > (h/d)_{crit}$, alternate Kármán vortex shedding occurs along the cylinder, except near the free end, where the downwash interacts with the Kármán vortices, and near the base. The critical aspect ratio value, $(h/d)_{crit}$, ranges from 2 to 6, depending on different factors, such as the boundary layer thickness and turbulence intensity of the incoming flow. The wake behind a finite-length cylinder is, therefore, characterized by the presence of the longitudinal tip and base vortices, in addition to possible spanwise Kármán vortex shedding. The interactions between these three types of vortices complicate significantly the flow and make it highly three-dimensional.

Motivated by its primary importance and practical significance in many branches of engineering, such as aerodynamics of cooling towers and tall buildings, the flow around a finite-length square prism has also attracted considerable attention in literature.

On the basis of hotwire and PIV measurements of the turbulent flow structure around a square cylinder of 3 to 7 aspect ratio, Wang *et al.* (2004) proposed the schematic flow structure model illustrated in Fig. 3.18. At $h/b = 3$ [Fig. 3.18(a)], the alternate spanwise Kármán vortex shedding is largely suppressed and the near wake is dominated by tip and base vortices. At higher aspect ratios, $h/b \geq 5$ [Fig. 3.18(b)], periodic spanwise vortex shedding occurs over almost the whole span except very close to the wall. Power spectra of velocities in the flow direction revealed a broad peak occurring at a reduced frequency, f_r, (that is the frequency normalized by velocity and reference dimension, see Eqs. 3.13 and 5.6) equal to 0.09 for $h/b = 3$ and

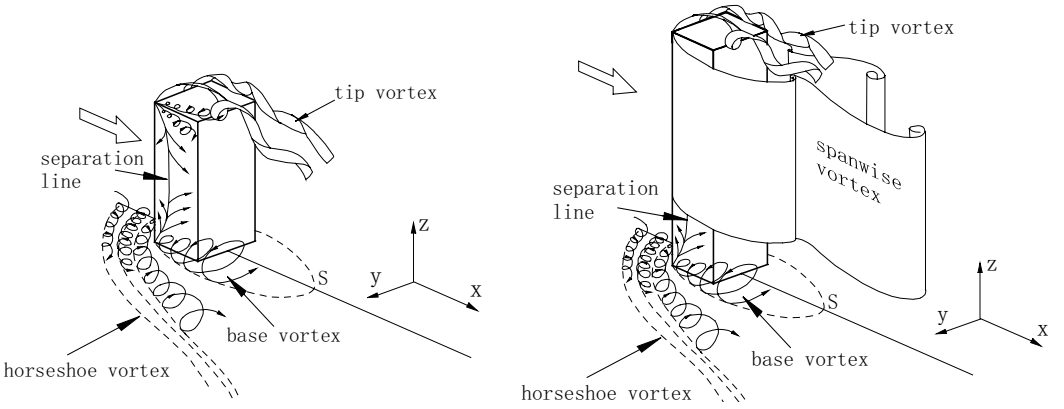

(a) $h/b = 3$ (b) $h/b \geq 5$

Fig. 3.18 Flow structure behind a finite-length square prism (Wang *et al.*, 2004).

a pronounced sharp peak at approximately 0.12 and 0.13 for h/b equal to 5 and 7, respectively. The last mentioned values of the reduced frequency are close to those of dominant Kármán vortices in a two-dimensional square cylinder wake (see Table 3.1). It has to be specified that measurements were carried out by the authors at a free-stream velocity, U_∞, of 7 m/s, corresponding to $Re = 9300$, based on the side dimension of the square cylinder, b. The free-stream turbulence intensity, I_u [Eq. (6.16)], was about 0.7% and the boundary layer effect on the wake was judged negligible, because of the small thickness (2 mm) of the boundary layer at the cylinder position.

Flow around a finite-length wall-mounted square cylinder was systematically investigated by Wang and Zhou (2009). The cylinder was partially immersed in a boundary layer, characterized by a boundary layer thickness, δ, equal to $1.35b$, where $b = d$ indicates the side dimension of the square prism. The aspect ratio, h/b, examined ranged from 3 to 11. Planar PIV measurements were performed in the three orthogonal planes of the three-dimensional cylinder wake, along with flow visualization conducted simultaneously in two orthogonal planes. Laser Doppler Anemometry (LDA) and hotwire measurements were also performed. A huge amount of experimental evidences were discussed and compared by the authors with other literature works. In this section only a brief description of the main results is discussed.

Two distinct types of instantaneous sectional streamlines [Fig. 3.19(a,b)] were observed. One [Fig. 3.19(a)] is characterized by free-end downwash flow meeting with upwash flow from the wall. The saddle point results from interaction between downwash and upwash flows. The other one [Fig. 3.19(b)] is more complicated and characterized by more critical points, including two saddle points, three foci and a node. Time-averaged streamlines [Fig. 3.19(c)] are topologically similar to the instantaneous ones in Fig. 3.19(a) and to those behind a wall-mounted finite-length circular cylinder of the same aspect ratio.

Both symmetrically and antisymmetrically arranged spanwise vortices were distinguished on horizontal planes at different heights, reconfirming the observations of Wang *et al.* (2004). The investigated flow structure is highly three-dimensional, consisting of three types of vortical patterns:

- tip vortices emanating from the free end and constituting a downwash flow;

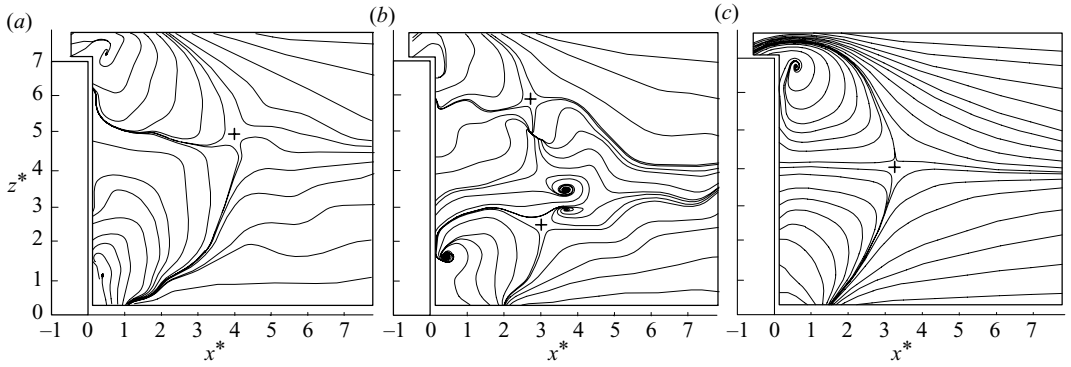

Fig. 3.19 Instantaneous (a,b) and time-averaged (c) sectional streamlines in the vertical plane, viewed on a fixed reference frame. Aspect ratio $h/b = 7$. Saddles denoted by '+' [Wang and Zhou (2009)].

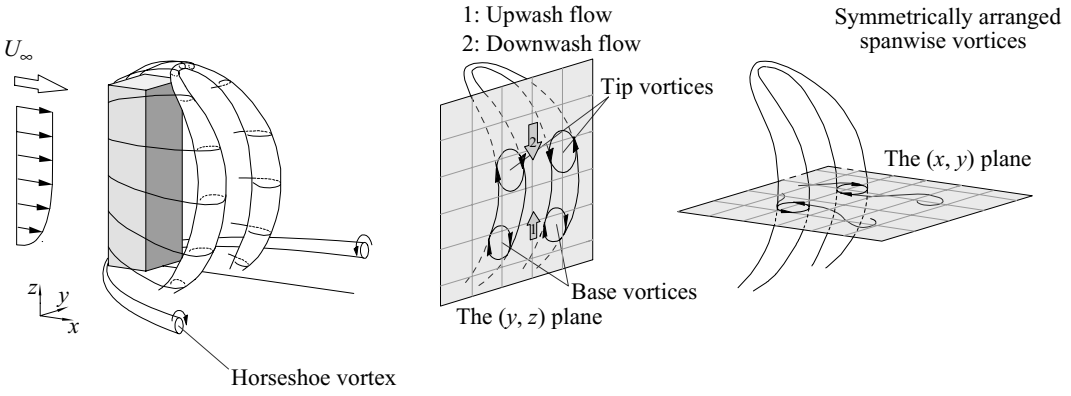

(a) Symmetrically arranged two spanwise vortex roll

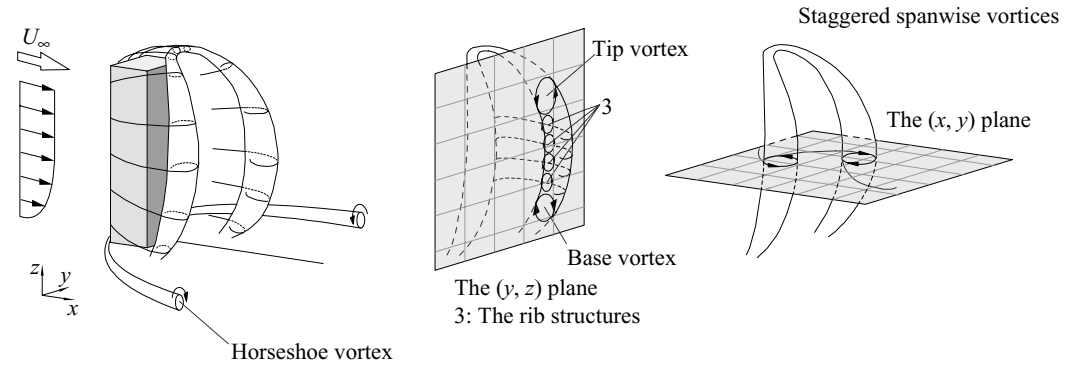

(b) Staggered arranged spanwise vortex roll

Fig. 3.20 Model of the flow structure around a wall-mounted finite-length square cylinder proposed by Wang and Zhou (2009).

- Kármán vortices characterizing a spanwise shear flow;
- base vortices featuring an upwash flow from the wall.

The near wake is characterized by complex interactions between these components.

On the basis of experimental evidences and discussions, Wang and Zhou (2009) proposed the physical model for the flow structure behind a finite-length square cylinder, sketched in Fig. 3.20. In this model, spanwise vortices from both sides of the cylinder are connected with each other near the free end, forming an arch-type vortex. The latter consists of two 'legs' that immerse in the wall boundary layer and merge near the free end. Because of the influence of both the free-end downwash flow and the boundary layer over the wall, the upper and the lower regions of the arch-type structure are inclined upstream. Furthermore, a horseshoe vortex originates at the cylinder base.

Two instantaneous configurations of the arch-type vortex, corresponding to the two types of spanwise vortices observed, are illustrated in Fig. 3.20. Fig. 3.20(a) presents one configuration of the flow structure with spanwise vortices symmetrically arranged. The downwash and upwash flow is predominant. Symmetrically arranged spanwise vortex rolls do not occur frequently. In Fig. 3.20(b) another typical configuration is illustrated. This is characterized by staggered spanwise vortex rolls. The longitudinal rib structures occur on one side of the cylinder, so do the tip and base vortices. The two types of vortices follow rather distinct trajectories, which are, except near the free end, farther from the centerline than those in a two-dimensional wake, suggesting an increased wake width. This observation is ascribed to downwash and upwash flows, which entrain free-stream fluid into the wake and drive the spanwise vortices away from the centerline.

Many spacial configurations of instantaneous spanwise vortices are neither perfectly symmetric, nor perfectly antisymmetric, but, in fact, something in between. The probability of antisymmetrically arranged vortices is largest at midspan and reduces significantly when approaching the cylinder free end or the wall.

The occurrence of symmetrically arranged vortices around the finite-length

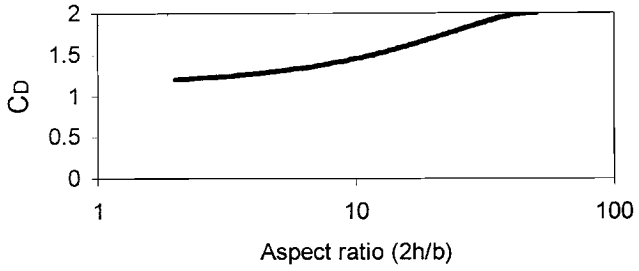

Fig. 3.21 Aspect ratio effect on drag coefficient for finite-length square section bodies (Scruton and Rogers, 1972), taken from Holmes (2001).

cylinder leads to lower drag (C_D) and fluctuating lift ($C_L{}'$) coefficients, compared with those on a two-dimensional cylinder. Moreover, the maximum longitudinal extent of the reverse flow zone (at the saddle point) occurs near the midspan and is larger than in the 2-D case. Because of downwash and upwash flows, the reverse flow zone contracts when approaching the free end and the wall. The high three-dimensionality of the flow leads to a decrease in the Strouhal number compared to the two-dimensional wake.

Fig. 3.21 shows the drag coefficient for a square section prism with finite length with one free end in smooth flow conditions as a function of aspects ratio (Scruton and Rogers, 1972). The latter is defined, in this case, as $2h/b$, where h is the height and b is the breadth (side dimension), since it is assumed that the flow is equivalent to that around a body with a 'mirror image' added to give an overall height of $2h$ with two free ends. At high values of aspect ratio it is clear that the drag coefficient reaches the values corresponding to the 2-D flow conditions (see Table 3.1).

Even if the overall flow structure behind a finite-length square cylinder is independent on the aspect ratio, and increase in the latter is associated to enhanced upwash and downwash flows, such as tip and base vortices, similarly to what was observed in a finite-length circular cylinder.

The evidence that the unsteady spanwise vortices behind a 3-D square prism are connected to form an arch-type structure was also confirmed by Kawai *et al.* (2009, 2011).

3.6 Summary and main remarks

Modern tall and slender buildings are sensitive to the wind action. For this reason, the knowledge of the flow field around building-type prismatic shapes has been receiving increasing importance in the field of wind engineering and aerodynamics.

In this chapter the classical flow paradigm of the unsteady flow behind a fixed 2-D cylinder is presented at first, together with the principle of the vortex shedding phenomenon. The flow pattern behind a square-section cylinder, which this thesis is focused on, is reviewed. The flow behind a cylinder with square cross section is highly sensitive to the angle of attack, and the possible flow patterns can be categorized in two categories depending on the cylinder orientation, namely, perfect separation type and reattachment type. At zero incidence, the Strouhal number is affected by the Reynolds number and turbulence. A number of authors have investigated the influence of the angle of incidence on the Strouhal number. It shows, in general, a sudden jump till its maximum value at incidence between $10° - 15°$, that corresponds to the onset of flow reattachment to the side faces and to a decrease in the width of the wake. The distribution of the mean pressure coefficients around a square-section cylinder is discussed. Reynolds number effects on the windward side are negligible, while a certain sensitivity to Re is shown on the sideward and leeward faces. The strongest pressure recovery on the side face, indicating the onset of reattachment of the shear layer to the side face, occurs at the angle of incidence corresponding to the maximum Strouhal number. This value of the angle of attack corresponds also to a minimum of the mean drag and lift coefficients, reported by different authors. Turbulence is seen to affect the RMS value of the fluctuating normal force coefficient. Some literature results on the dependence of the drag coefficient on turbulence, Reynolds number, corner radius and roughness of the cylinder surfaces are also discussed. Data from different numerical experimental studies on square-section cylinders at zero incidence are collected in order to frame the variability range of some principle quantities, such as Strouhal number, mean and fluctuating drag and lift coefficients.

The last section of this chapter is devoted to the three-dimensional flow behind square section prisms of finite length. Due to the end effects, the wake behind a finite-length cylinder is drastically different from that behind a 2-D cylinder. It is

characterized by the presence of tip and base vortices, in addition to possible spanwise Kármán vortex shedding. The near wake is characterized by complex interactions between these components and both symmetrically and antisymmetrically arranged spanwise vortices may be distinguished on horizontal planes at different heights. The wake structure is influenced by the aspect ratio. The occurrence of symmetrically arranged vortices leads to lower drag and fluctuating lift coefficients than those on a 2-D cylinder.

Chapter 4

Aeroelastic effects in wind-induced responses of tall buildings

4.1 Introduction

This chapter addresses aeroelastic or motion-induced effects involving the wind-induced response of tall buildings. In section 4.2 the different components of the response of buildings to the wind action are discussed and aeroelasticity is introduced in the path from wind loads to wind-induced responses. Section 4.3 is devoted to the lock-in phenomenon which can play a significant role in the across-wind response, dominating the serviceability design of tall buildings.

Section 4.4, constituting the core of this chapter, illustrates, at first, the approach commonly used for estimating the response of tall buildings to aerodynamic loads which neglect motion-induced effects. Some experimental studies dealing with the across-wind aeroelastic response of tall buildings are reviewed in order to draw an overview for comparison for the results of the experimental campaign carried out in this research (chapter 6).

A brief description of the literature approaches for modeling the aeroelastic response is also given. Lastly, the approach of aerodynamic damping for dealing with the aeroelastic effects on tall buildings is illustrated and results from literature works on aerodynamic damping of tall buildings are reviewed. A particular attention is paid on those works which investigate the response of tall buildings with geometric and dynamic features similar to the model tested in the wind tunnel and under similar wind flow conditions.

4.2 Components of the wind-induced response and introduction to aeroelastic phenomena

Because of the fluctuating nature of wind velocity and, therefore, of wind loads, wind-induced response of structures is characterized by a *mean response*, due to the mean component of the wind load, and a *fluctuating response*, which can be further split into the *background* or *quasi-static response*, caused by the fluctuating components of the wind load, whose frequencies differ significantly from the natural

frequencies of the structures, and the *resonant response*, due to the fluctuating wind force components whose frequencies are equal or close to the structural natural frequencies. The natural frequencies of the structure determine whether the fluctuating dynamic response to the wind action is mainly driven by the background response or by the resonant response. Fig. 4.1[1] shows the response spectral density of a structure under wind loading. Subscripts B and R indicate background and resonant components, respectively. The area under the entire curve represents the total *mean-square* fluctuating response, whose square root is known as *Root Mean Square* and indicated with *RMS*. The background response, made up mainly of low-frequency contributions below the natural frequency of vibration, is the largest contributor in Fig. 4.1 and is usually dominant in the along-wind direction (Holmes, 2001). Due to their size and slenderness, tall buildings have, in general, several natural frequencies of vibration of less then 1 Hz, which, together with low damping values, make them susceptible to significant resonance when excited by extreme wind events.

If the structure moves or deforms appreciably under the wind-induced forces,

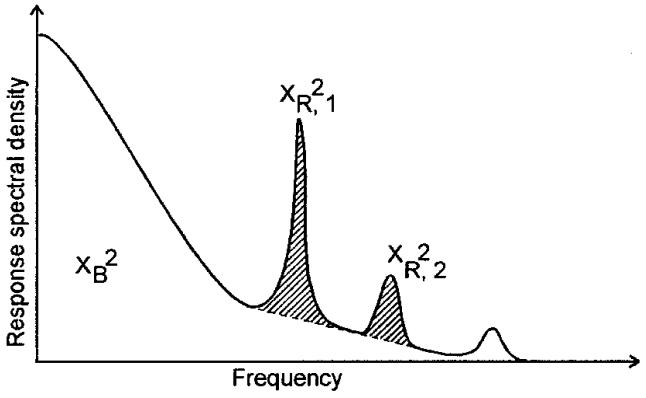

Fig. 4.1 Response spectral density for a structure with significant resonance contributions (Holmes, 2001).

these deflections may affect the fluid forces, which, in turn, will influence the deflections. *Aeroelasticity* describes phenomena involving the interaction between aerodynamic forces and structural deformations. These phenomena are known as *aeroelastic* or *motion-induced* effects. In case of lightweight, low damped, slender structures, these effects are not negligible and a proper assessment of the structural responses R, due to the wind action, can be performed considering that the structure is subject to overall forces $F = F_s + F_a$, where F_s are the *aerodynamic forces*, acting on the "fixed" structure (negligible displacements), and F_a are the motion-induced *aeroelastic forces* (Fig. 4.2).

The flutter of the Brighton Chain Pier Bridge in 1836 and, later, that of the Tacoma Narrows Bridge are notorious examples of aeroelastic behavior. Tall chimneys and high-rise buildings can also respond aeroelastically. The John Hancock building in Boston, which has a relatively flat shape in plan (Fig. 4.3), has experienced across-wind and torsional motions of sufficient severity to warrant the installation of a large tuned-mass damper system at its top. These motions may

[1]The mean response is not included in this plot

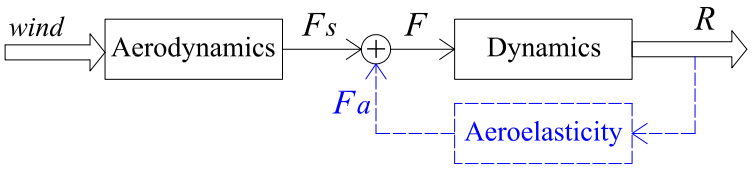

Fig. 4.2 Conceptual scheme illustrating the path from wind loads to structural responses including aeroelastic effects.

have been due to aeroelastic effects[2].

Different types of aeroelastic effects are known, such as torsional divergence,

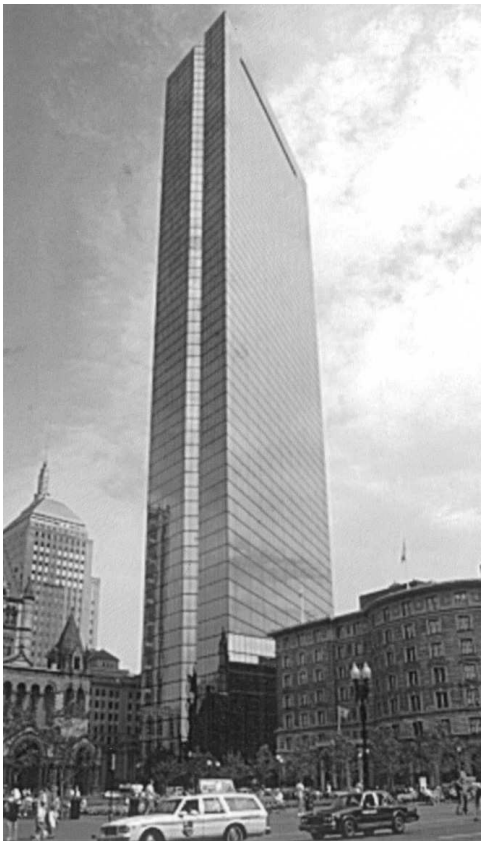

Fig. 4.3 John Hancock Building, Boston (taken from Clark *et al.* (2004)).

flutter, lock-in and galloping. The most relevant phenomena for the across-wind response, which usually dominates the serviceability design of high-rise buildings are lock-in and galloping. However, the present research focuses only on lock-in, since galloping usually occurs at reduced velocities significantly different from those of synchronization for structures and wind conditions similar to that tested in the wind tunnel in this study [see, for example, Cheng *et al.* (2002)]. The main phenomenological aspects of the lock-in phenomenon are illustrated in the following section.

[2]For legal or other reasons, detailed technical reports on the wind-induced behavior of the John Hancock building are not available in the public domain (Clark *et al.*, 2004).

4.3 Lock-in phenomenon and Vortex-Induced Vibrations

It was seen in section 3.3 that alternating vortices are shed from a fixed (or stationary) bluff body, according to the Strouhal relation [Eq. (3.13)]. If the body is let free to vibrate, under the vortex shedding action, it will deflect, wholly or locally, and influence the local flow.

When the dominating shedding frequency f_s is equal or close to the natural frequency f_n of the structure, vibrating in a mode in the across-wind direction, a coupling between this motion and the wake dynamics exists. This results in a complex evolution of the shedding frequency, which deviates from the Strouhal law as the natural frequency of the solid is approached. The shedding frequency remains constant and locks on to the frequency of vibration for a certain range of flow speeds (Fig. 4.4). This aeroelastic or motion-induced phenomenon is referred to as *lock-in*.

Vortex-Induced Vibrations, referred to as VIV, corresponding to this locking-in of the wake to the body's oscillation frequency, occur over a larger velocity range than would be predicted using the Strouhal law. This speed range increases as the structural damping decreases.

The most commonly accepted interpretation of the mechanism underlying frequency lock-in is that of resonance: as the frequency of the unstable system (the wake) approaches that of the oscillator (the bluff body), the oscillating lift force causes an increasing amplitude of motion, by a standard resonance effect. Then, provided this amplitude is large enough, the wake is somehow affected and forced to move at the natural resonating frequency of the solid. This feedback mechanism is implicitly assumed to be nonlinear, as the existence of lock-in and its extent depend on the amplitude of motion.

The condition of "vortex resonance" occurs at a particular value of the wind speed, called "critical wind speed" U_{crit} and defined as:

$$U_{crit} = \frac{bf_n}{St} \tag{4.1}$$

For many structures, the critical wind speed for the first mode is of the order of 10 m/s, i.e. frequently recurring wind speeds that give rise to risk of fatigue.

In addition, the oscillation frequency, in this condition, does not always coincide with the natural frequency of the structure, because of the effect of the airflow added mass, and the drag is different from its steady-state value, e.g. Pastò (2008).

Dividing both terms in Eq. (4.1) by the quantity bf_n, one may conclude that the vortex resonance condition is achieved at a critical non-dimensional reduced velocity $U_{r,crit}$ equal to the reciprocal of the Strouhal number, as follows:

$$U_{r,crit} = \frac{U_{crit}}{bf_n} = \frac{1}{St} \tag{4.2}$$

The magnitude of vortex-induced vibrations is governed both by the structure's inherent damping characteristics and by the mass ratio between the structure and the fluid it displaces. These two effects are often combined in the Scruton number Sc, defined as (UNI-EN 1991-1-4, 2005):

$$Sc = \frac{2\delta_s m_{i,e}}{\rho b^2} \tag{4.3}$$

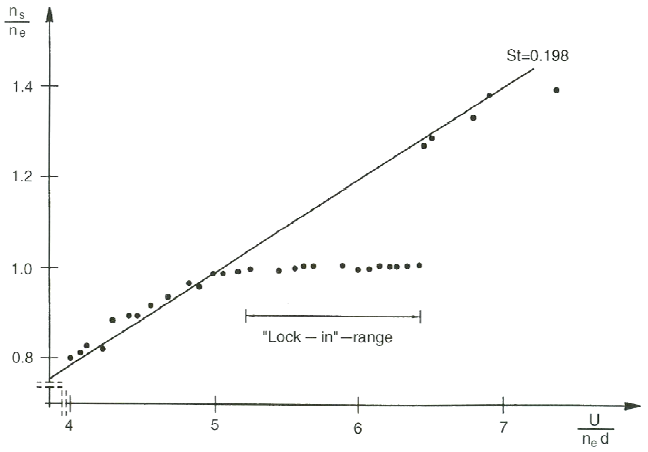

Fig. 4.4 Experimental investigation of lock-in after Feng (1968), from Dyrbye and Hansen (1997).

where ρ is the air density, b is a reference dimension, δ_s is the logarithmic decrement that quantifies the structural damping and can be taken approximately equal to $2\pi\xi_s$, where ξ_s is the structural damping ratio. The equivalent mass per unit length for mode i, $m_{i,e}$, is equal to:

$$m_{i,e} = \frac{\int_0^h m(z)\phi_i^2(z)\,dz}{\int_0^h \phi_i^2(z)\,dz} \tag{4.4}$$

where $m(z)$ is the vibrating mass per unit length, h is height or length of the structure, ϕ_i is the mode shape for mode i.

An extensive review of vortex-induced vibrations of bluff bodies can be found in Willamson and Govardhan (2004, 2008).

As previously explained, the motion of the body leads to synchronization of vortex shedding. This phenomenon occurs along the longitudinal length of the body itself, providing an increase in the correlation of pressures when vortex-induced vibrations occur. Fig. 4.5 shows the spanwise correlation of fluctuating pressures along the center line of a side face of a square cylinder, forced to vibrate at an amplitude A of 1/10 times its cross dimension D ($A/D = 0.10$) for different values of the reduced velocity. Results are compared also with the case of a stationary cylinder ($\bigtriangledown$, $A/D = 0$). In the figure, $R(\rho, z)$ indicates correlation coefficient, plotted as a function of spanwise separation z/D. Results from the oscillating cylinder show much higher correlation than those from the rigid cylinder, particularly around the resonant velocity, U/fD within [7.3;8.5], where a correlation coefficient of 0.9 was recorded at the maximum spanwise separation of $z/D = 13.25$ (Bearman and Obasaju, 1982).

4.4 Aeroelastic effects in tall buildings response estimation

Comprehension of wind-induced loads and effects on tall buildings is a challenging task, motivated by both complexity of 3-D flow patterns (chapter 3) and occurrence

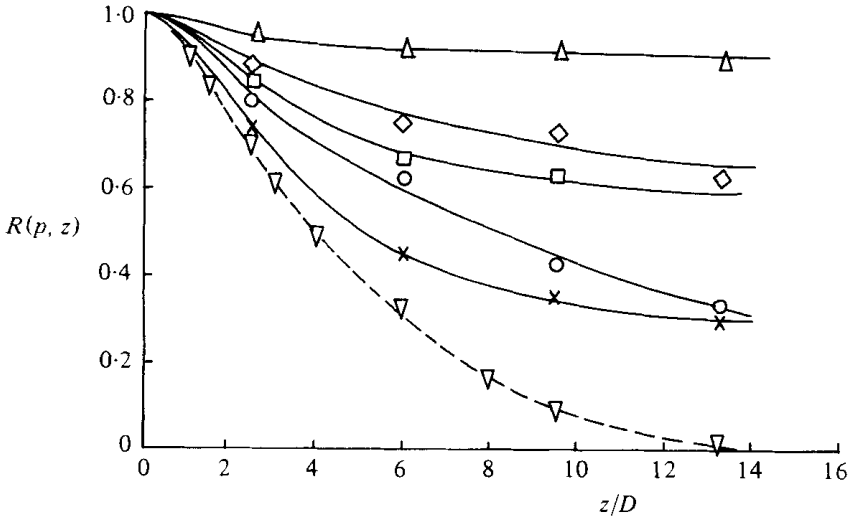

Fig. 4.5 Correlation of surface pressures on an oscillating square section cylinder vs. spanwise separation. ▽, stationary body ($A/D = 0$). Body oscillating with $A/D = 0.10$: ×, $U/fD = 6.2$; ◯, 7.0; □, 12.0; ◇, 8.8; △, U/fD within the lock-in range 7.3-8.5 (Bearman and Obasaju, 1982).

of the motion-induced effects, as previously illustrated. In broad terms, the wind forces resulting in dynamic excitation can be divided into three groups:

1. forces induced by the turbulent fluctuations in the incident flow;
2. forces induced by the unsteady nature of the wake and particularly by vortex shedding (section 3.3);
3. forces induced by motion of the structure (aeroelastic effects).

Furthermore, the three-dimensional simultaneous loading of a structure subject to the wind action results in the three structural components, sketched in Fig. 4.6. With reference to the wind axes, the along-wind component primarily results from pressure fluctuations in the approaching flow and leads to a swaying of the structure in the direction of wind. The across-wind component, due to side-face pressure fluctuations, primarily induced by the fluctuations in the separated shear layers, vortex shedding and wake flow fields, leads to a swaying motion perpendicular to the wind direction. Lastly, the torsional component results from imbalances in the instantaneous pressure distribution on the surfaces of the structure.

4.4.1 Response to aerodynamic loads

The along-wind component of the wind loading primarily results from turbulent velocity fluctuations in the approaching flow. It has been, therefore, successfully estimated using *strip* and *quasi-steady* theories, which imply that the wind pressure on a structure is determined by only the velocity at the height where the pressure acts and that the instantaneous pressure is proportional to the square of the instantaneous velocity pressure of the oncoming flow, respectively (Kawai, 1983). Velocity fluctuations in the oncoming flow may arise from the general nature of the earth's

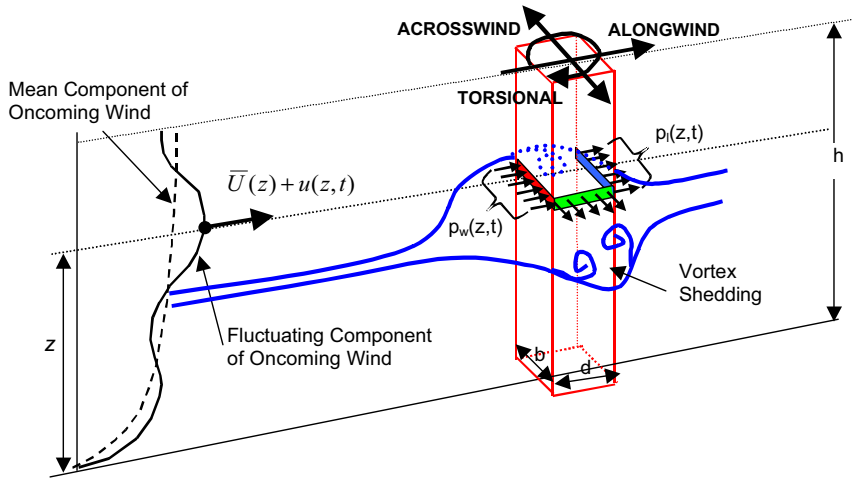

Fig. 4.6 Schematic description of oncoming wind field and resulting wind-induced response components [taken from Kijewski *et al.* (2000)].

turbulent boundary layer or from the unsteady wakes of one or more nearby structures. In the latter case the excitation is referred to as *buffeting*.

Although the along-wind response may include buffeting effects, it is the gust response due to the incoming wind that is of primary importance. Thus, the aerodynamic along-wind load may be expressed in terms of velocity fluctuations as:

$$F_D(t) = \frac{1}{2}\rho b^2 C_D[\overline{U} + u(t)]^2 \tag{4.5}$$

where b indicates the breadth of the structure. The quantity b^2 is often replaced with bh where h indicates the height. Eq. (4.5) implicitly assumes that velocity fluctuations are fully correlated over the entire structure. This assumption may hold for very small structures, but fails for structures with larger dimensions, such as the case of tall buildings, and leads to overestimation of loads. In this case imperfect correlation of wind fluctuations is introduced through an aerodynamic admittance function, $\chi^2(f)$. Describing the loading scenario in frequency domain, Eq. (4.5) is transformed accordingly as (Kijewski *et al.*, 2000):

$$S_{F_D}(f) = (\rho C_D)^2 \chi^2(f) S_u(f) b^4 \tag{4.6}$$

where $S_{F_D}(f)$ and $S_u(f)$ are the power spectral density (PSD) of along-wind load and wind fluctuations, respectively.

It has been recognized that the across-wind and torsional response for many high-rise buildings may exceed the along-wind response in terms of both serviceability and survivability designs [e.g. Kareem (1985); Liang *et al.* (2002)]. Nevertheless, most existing codes and standards provide only procedures for the along-wind response and little guidance for the critical across-wind and torsional responses. This is partially due to the fact that, differently from the along-wind loads, the across-wind and torsional loads and responses result mainly from the aerodynamic pressure fluctuations in the separated shear layers and wake flow fields. This fact has prevented to date any acceptable direct analytical relation between across-wind and torsional responses to the oncoming wind velocity fluctuations. Furthermore, higher order rela-

tionships may exist (Gurley *et al.*, 2001). As a result, experimentally derived loading functions have been introduced. Across-wind and torsional load spectra obtained by synthesizing the surface pressure field on scale models of typical tall building shapes are available in literature. Liang *et al.* (2002) proposed a complete analytical model of across-wind dynamic loads on rectangular tall buildings. This model was found to be in good agreement with some experimental results obtained by wind tunnel tests. Zhou *et al.* (2003) introduced an interactive database of aerodynamic loads obtained from High Frequency Base Balance (HFBB or High Frequency Force Balance - HFFB) measurements on a host of isolated tall building models, accessible to the worldwide Internet community at the URL address `http://aerodata.ce.nd.edu/`. The influence of key parameters, such as side ratio, aspect ratio and turbulence characteristics for rectangular sections was also discussed.

In order to derive the structural response from aerodynamic loads, basic random vibration theory is utilized, as briefly illustrated in subsection 4.4.2.

4.4.2 Random excitation model for aerodynamic response estimation

The equations of motion of a high-rise building represented by a discretized lumped-mass system are given by:

$$[M]\{\ddot{x}(t)\} + [C]\{\dot{x}(t)\} + [K]\{x(t)\} = \{F(t)\} \tag{4.7}$$

where $[M]$, $[C]$ and $[K]$ are the real symmetric mass, damping and stiffness matrices of the discretized system, respectively. $\{x\}$ is the displacement and $\{\dot{x}(t)\}$ and $\{\ddot{x}(t)\}$ are its first two time derivatives, representing velocity and acceleration, respectively. $\{F(t)\}$ indicates the stochastic wind loads applied. In general, Eq. (4.7) provides two translations and one rotation per story level, assumed rigid. For the sake of illustration, it is assumed here that the structure is uncoupled in each direction. By employing the standard transformation of coordinates, the wind response of a tall building vibrating in a natural translational mode, j, is described by:

$$\ddot{q_j} + 2\xi_j\omega_{n,j}\dot{q}_j + \omega_{n,j}^2 q_j = P_j(t) \tag{4.8}$$

where $P_j(t) = \{\phi_j\}^T\{F(t)\}$ are the generalized wind forces, ϕ_j, ξ_j and $\omega_{n,j}$ are the j^{th} mode shape, modal critical damping ratio and circular frequency, respectively. The quantity q and its time derivatives represent generalized modal response quantities, related to x and its derivatives by:

$$\{x(t)\} = [\phi_j]\{q_j(t)\} \tag{4.9}$$

In the time domain, the generalized response, $q_j(t)$, can be calculated through integration of Eq. (4.8) and then any response parameter of interest can be obtained from the generalized displacements.

Using the frequency domain approach, the power spectral density (PSD) of the generalized displacement for mode j, is determined as:

$$S_{q_j}(\omega) = H_j(\omega)S_{P_j}(\omega)H_j^*(\omega) = |H_j(\omega)|^2 S_{P_j}(\omega) \tag{4.10}$$

where $H_j(\omega)$ is the j^{th}-mode *frequency response function* (FRF). $H_j^*(\omega)$ indicates the complex conjugate of $H_j(\omega)$. The circular frequency ω is equal to $2\pi f$.

The square modulus of the FRF, $|H_j(\omega)|^2$, is called *mechanical admittance function* and is equal to:

$$|H_j(\omega)|^2 = \frac{1}{m_j^2 \omega_{n,j}^4} \frac{1}{\left[1 - \left(\frac{\omega}{\omega_{n,j}}\right)^2\right]^2 + 4\xi_j^2 \left(\frac{\omega}{\omega_{n,j}}\right)^2} \tag{4.11}$$

where m_j is the j^{th} modal mass, equal to $\{\phi_j\}^T [M]$.

The mean square value of the modal response for the j^{th} mode can be determined by integrating its PSD as follows:

$$\sigma_{q_j}^2 = \int_0^\infty S_{q_j}(\omega)\, d\omega \tag{4.12}$$

The mean square value of response in physical coordinates, $\sigma_{x^{(r)}}^2$, can be approximated by the weighted superposition of all N modal contributions:

$$\sigma_{x^{(r)}}^2 \approx \sum_{j=1}^{N} \frac{\phi_j^2 \pi f_{n,j} S_{P_j}(f_{n,j})(2\pi f_{n,j})^{2r}}{4(2\pi f_{n,j})^4 \xi_j m_j^2} + \sum_{j=1}^{N} \frac{\phi_j^2 \int_0^{f_{n,j}} S_{P_j}(f)\, df (2\pi f_{n,j})^{2r}}{(2\pi f_{n,j})^4 m_j^2} \tag{4.13}$$

where r indicates the derivative of response, i.e. $r = 0, 1, 2, 3$ denotes displacement, velocity, acceleration and jerk, respectively. The first term on the right side of Eq. (4.13) represents the resonant component and the second term the background component. Eq. (4.13) is an approximation of the area under the PSD of the response which is very close to exact for most lightly damped structures (Kijewski *et al.*, 2000).

Determination of wind-induced response based on random vibration theory, also known as spectral approach, is graphically illustrated in Fig. 4.7, which shows that the total mean square fluctuating response is computed from the spectral density of response. The latter is calculated from the spectrum of aerodynamic forces, which are in turn, calculated from the gust spectrum or wind turbulence. The frequency-dependent *aerodynamic admittance* and *mechanical admittance* functions constitute links between these spectra. For slender structures with low frequencies and damping, the dynamic amplification at the resonant frequency results in higher mean square (and, therefore RMS) and peak responses than structures with high frequencies, not excited by the wind action.

If response contributions from mode shapes higher than the fundamental mode of vibration of frequency f_1 can be neglected, the variance of the across-wind displacement ($r = 0$) response at the top of the building, σ_y^2, at which $\phi_1(h) = 1$, is calculated from Eq. (4.13) as:

$$\sigma_y^2 \approx \frac{\pi f_1 S_{P_1}(f_1)}{4(2\pi f_1)^4 \xi_1 m_1^2} + \frac{\int_0^{f_1} S_{P_1}(f)\, df}{(2\pi f_1)^4 m_1^2} \tag{4.14}$$

Although the wind force spectrum is usually broad band, modern tall buildings, being usually flexible and lightly damped (less than 10%), behave like narrow band filters, thus leading to the results of narrow band response output. Therefore, the

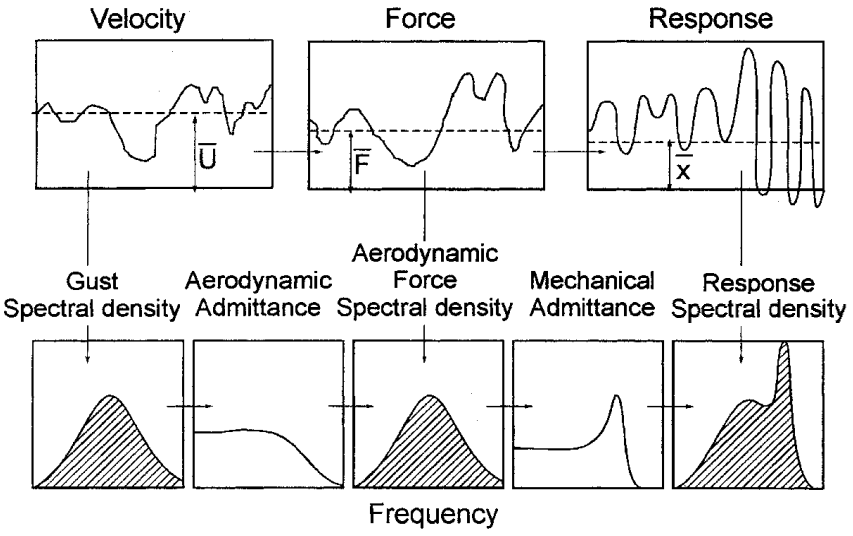

Fig. 4.7 The random vibration or spectral (frequency domain) approach for assessment of dynamic response, after Davenport (1963).

background component of the response can often be neglected (Kwok, 1982). Hence:

$$\sigma_y^2 \approx \frac{\pi f_1 S_{P_1}(f_1)}{4(2\pi f_1)^4 \xi_1 m_1^2} \tag{4.15}$$

so that the standard deviation cross wind response is proportional to $\xi^{-1/2}$. Analogously, the across-wind acceleration ($r = 2$) response may be written as:

$$\sigma_{\ddot{y}}^2 \approx \frac{\pi f_1 S_{P_1}(f_1)}{4\xi_1 m_1^2} \tag{4.16}$$

4.4.3 Experimental studies on aeroelastic response of tall buildings

Aeroelasticity of tall buildings is mainly related to their across-wind response and to vortex-induced vibration and galloping phenomena. Vortex-induced vibrations and galloping of tall buildings have been investigated through several wind tunnel experiments.

In order to investigate across-wind response of tall buildings in lock-in conditions, wind tunnel model tests were carried out by Kwok and Melbourne (1981) on a circular and a square tower with an aspect ratio of 9 and on a square tower with an aspect ratio of 18. Base-pivoted, elastically mounted, rigid models were used, thus maintaining a straight-line deflection mode. Two boundary layer conditions were tested, corresponding to flow over a suburban area and a city center. The power law exponents of the mean longitudinal wind velocity profile were 0.23 and 0.44, and the longitudinal turbulence intensities at the building top were 0.07 and 0.14 for suburban and the city center conditions, respectively. When tested in city center wind conditions, the h:d:b=9:1:1 square tower did not exhibit any significant lock-in response for values of damping higher than 0.25% of critical. This result was thought to be due to the velocity profile and the high turbulence associated with the city center flow condition. Results for the 18:1:1 square tower in suburban wind model were found to be very similar to those for the 9:1:1 square tower. Fig. 4.8(a)

illustrates the normalized standard deviation across-wind displacement response as a function of reduced velocity, indicated with $\overline{U}(h)/(n_0 b)$, where $\overline{U}(h)$ is the mean wind speed at the top and n_0 is the natural frequency, and of structural damping ξ_s. As the structural damping is reduced, large increases of the lateral response are evident particularly at reduced velocity close to 10. This critical reduced velocity represents the wind condition at which the shedding frequency is close to the transverse natural frequency of vibration (vortex resonance condition).

Normalized across-wind tip response displacement versus structural damping ratio was also investigated [Fig. 4.8(b)]. At reduced velocities far from the critical value and at high values of the structural damping, the response is proportional to functions which lie between $\xi_s^{-1/3}$ and $\xi_s^{-1/2}$. Such dependence agrees with the fact that outside the lock-in conditions, the response is dominated by wake excitation of random nature, and, therefore, it can be adequately described by random vibration theory and is proportional to $\xi_s^{-1/2}$ (see subsection 4.4.2). However, the response increases much more rapidly with decrease in damping when the model operates close to the critical velocity, especially at low damping values. Such departure from the random excitation theory suggests that the enhance in across-wind response associated with a decrease in damping might have caused interdependence between excitation and response which resulted in well correlated forces along the structure. From these results, the authors concluded that it is possible to approximately determine a critical value of the normalized across-wind displacement amplitude above which the lateral response cannot be adequately estimated by using the random excitation theory.

The large across-wind response in Fig. 4.8(b) at a reduced velocity of 24 is believed to be caused by galloping excitation. At a reduced velocity of 15 wake excitation effects and displacement-dependent lock-in were increased by aerodynamic damping (see section 4.4.5) associated with galloping excitation which resulted in a significant response enhance, in particular at low structural damping values.

Kawai (1992) carried out wind tunnel tests on aeroelastic models of rectangular prisms with aspect ratio equal to 10, under smooth flow and turbulent (open terrain and urban) flow conditions and at zero incidence of the oncoming flow. Various side ratios (depth/breadth) were considered: 3/1, 2/1, 1/1, 1/2. In the case of the square prism in smooth flow conditions, it was found that, as the structural damping increases, the onset velocity of the VIV increases slightly, the peak of the vibration amplitude decreases and the velocity range of VIV is narrowed. No evidence of VIV was found for critical damping ratio equal to 0.113. The effect of turbulence on the response was also investigated and systematically discussed. Rather surprisingly, it was observed that for the 1/2 side ratio prism, as turbulence increases, the vortex-induced vibrations strengthen. This result was motivated by the fact that turbulence promotes the entrainment of flow through the separated shear layer to produce the stronger vortex shedding when the shear layer does not reattach on the side face. For deeper sections, on the other hand, as the turbulent level increases, the response reduces. It was, therefore, concluded that the response in turbulent flow corresponds to that for a deeper body in smooth flow.

Experiments from Kawai (1992) were limited to the case where the flow is normal to the windward face. In order to investigate the effect of the angle of attack on the occurrence of VIV and galloping, another series of wind tunnel tests was later carried out on the same building models and flow conditions (Kawai, 1995). Selected

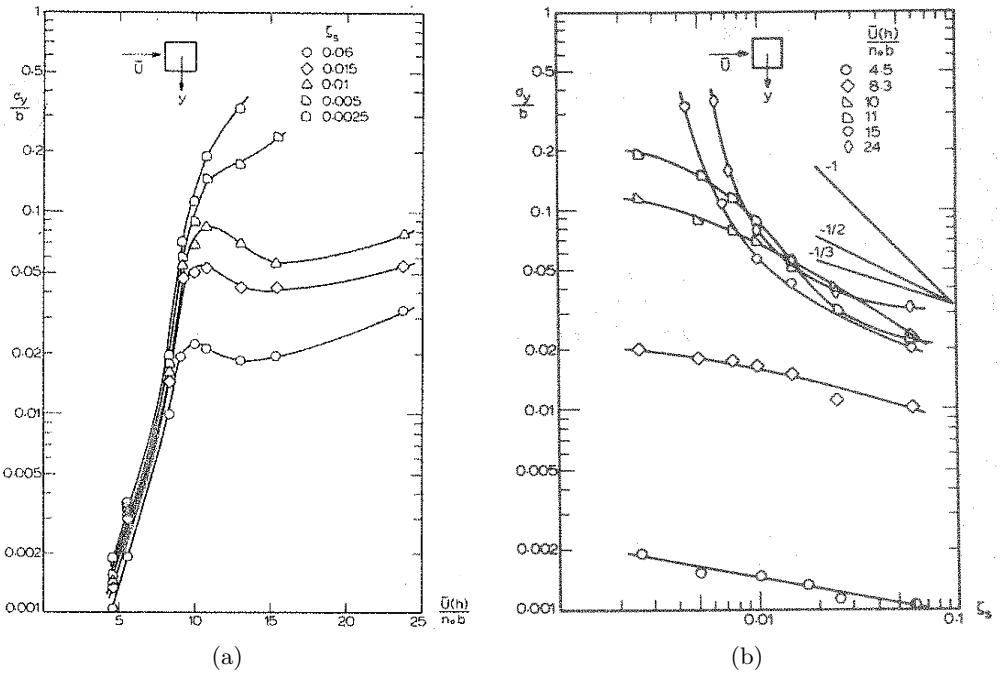

Fig. 4.8 Across-wind displacement response of a 9:1:1 square tower model in suburban wind condition from Kwok and Melbourne (1981): a) normalized response as a function of reduced velocity for various structural damping ratios; b) response dependence on structural damping for different reduced velocities.

results, referred to the square section prism, of primary interest in this research, are shown in Fig. 4.9. It is clear that VIV and galloping vibration are most violent at zero incidence in both smooth and turbulent flow conditions. As the angle of attack increases, the vibration amplitude rapidly decreases and the VIV ceases at the ordinary damping level. It has to be clarified that the y direction in Fig. 4.9 means across-wind direction when the wind is normal to the windward face.

Boggs (1992) performed wind tunnel tests on an 8:1:1 building model. The wind profile corresponded to suburban environment and was characterized by a power law exponent of 0.22 and turbulence intensity at model height of approximately 0.09. One rigid model and two pivoting-type aeroelastic models were used in order to make comparisons between aerodynamic and aeroelastic results. Several values of the mass ratio, corresponding to ratio of the generalized mass to the moment of inertia of displaced air, were considered. The mass ratio can be written as:

$$\text{mass ratio} = \frac{3J}{\rho D^2 H L^2} \tag{4.17}$$

where J is the generalized mass (equal to the moment of inertia about the center of rotation), ρ is the air density, D is the side dimension, H is the model height, L is the length from tip to center of rotation, according to the notation used in Boggs (1992). Comparisons between aerodynamic and aeroelastic results for two values of the damping ratio and four mass ratios are displayed in Fig. 4.10. They are given in terms of RMS moment coefficient $\tilde{C}_M$, normalized tip deflection $\frac{\tilde{\delta}}{D}$ and aeroelastic magnification factor AMF. The predicted RMS moment coefficient

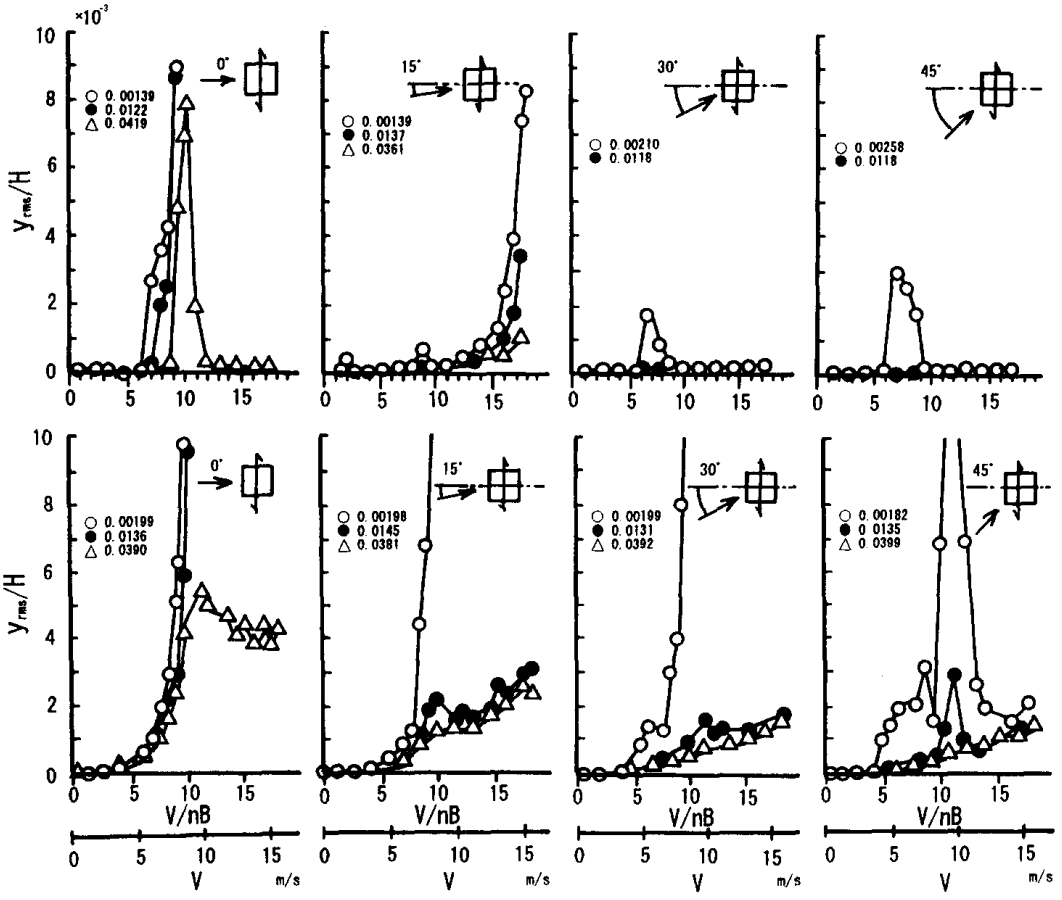

Fig. 4.9 RMS response in y direction of a 10:1:1 prism for various angles of incidence: (top) smooth flow; (bottom) turbulent flow (urban, power law exponent, $\alpha = 0.3$). Numerical values beside the symbols show the critical damping ratio Kawai (1995).

was computed from hypothetical natural frequencies and damping ratios using the random vibration approach (subsection 4.4.2), according to the following equation:

$$\tilde{M}^2 = \int_0^\infty |H_M(f)|^2 \, S_M(f) \, df \tag{4.18}$$

while, in the aeroelastic models the RMS moment coefficient was directly measured by the balance. Displacements were not measured directly, but were computed from the RMS moment coefficient for both the aerodynamic and aeroelastic models. Finally the aeroelastic magnification factor was defined as the ratio between the aeroelastic RMS normalized displacement and the aerodynamic one, allowing immediate comparison between the two results. It can be readily observed that the distance between the observed response and the predicted one may become quite large as the reduced velocity U/f_0D exceeds the critical value for vortex shedding, in particular for the lower mass ratios and damping. Furthermore, the AMF was plotted for two reduced velocity values (8 and 12) as a function of both aerodynamic and aeroelastic RMS normalized displacement and the product of density and damping (Fig. 4.11). This last parameter, similar to the Scruton number was selected as that describing best the observed-predicted response distance, producing the least scatter and defining a functional relationship with the AMF.

Marukawa *et al.* (1996) conducted wind tunnel tests of tall buildings, using a 1/500 scale aeroelastic stick model. The side ratio was varied in the range 0.33-3 and the aspect ratio was varied from 4 to 6. The simulated wind conditions corresponded to a mean velocity profile with a power index of 1/6 and the turbulence intensity at model height was 10.7%. The oncoming wind velocity range was 1-40 m/s.

The relation between the normalized standard deviation of the response displacement (measured by means of two laser displacement transducers) and the reduced velocity was investigated in both along and across-wind directions. According to the authors' observations, the standard deviation of the response increases in proportion to the power of 2.5 of wind velocity in the along-wind direction within the entire range of the wind velocities tested. On the other hand, in the across-wind direction, the standard deviation of the response displacement increases in proportion to the power of 2.5 to 3 of wind velocities, only for values of the reduced velocities not exceeding 8. Moreover, for the square section cylider (side ratio equal to 1), an increase in the structural damping ratio was seen to lead to a decrease in the gradient of the displacements to wind velocities in both along and across-wind directions.

Aspect ratio was found to affect the response gradient, too. In particular, a higher aspect ratio of the model resulted in greater power index increase in the across-wind direction, while in the along-wind direction, there was scarcely any change. Motivated by their strict correspondence with tests conducted in this research, in Fig. 4.12 some selected results from Marukawa *et al.* (1996) are reported. They illustrate the above mentioned normalized response displacement for different values of the structural damping ratio and refer to a 6:1:1 square model at zero incidence.

Cheng *et al.* (2002) conducted aeroelastic tests in a boundary layer wind tunnel, aimed at studying the across-wind response and aerodynamic damping (see subsection 4.4.5) of isolated square-section high-rise buildings. Two boundary layer flows, BL1 and BL2, were generated in order to represent open terrain and urban terrain conditions, respectively. The exponent of the power law of the mean velocity profile

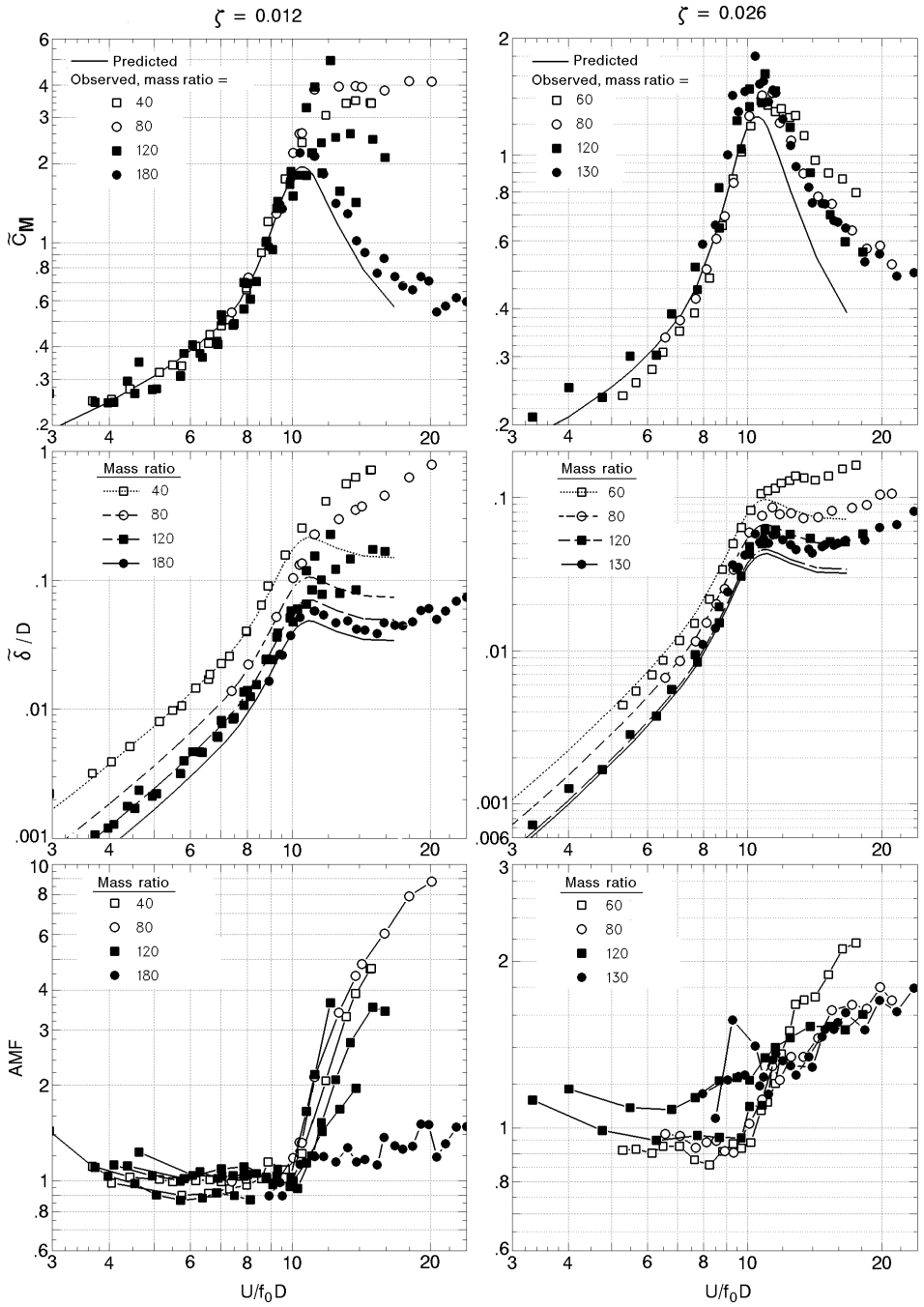

Fig. 4.10 Predicted (aerodynamic) and observed (aeroelastic) response of a 8:1:1 building as a function of reduced velocity for two damping values and four mass ratios (Boggs, 1992).

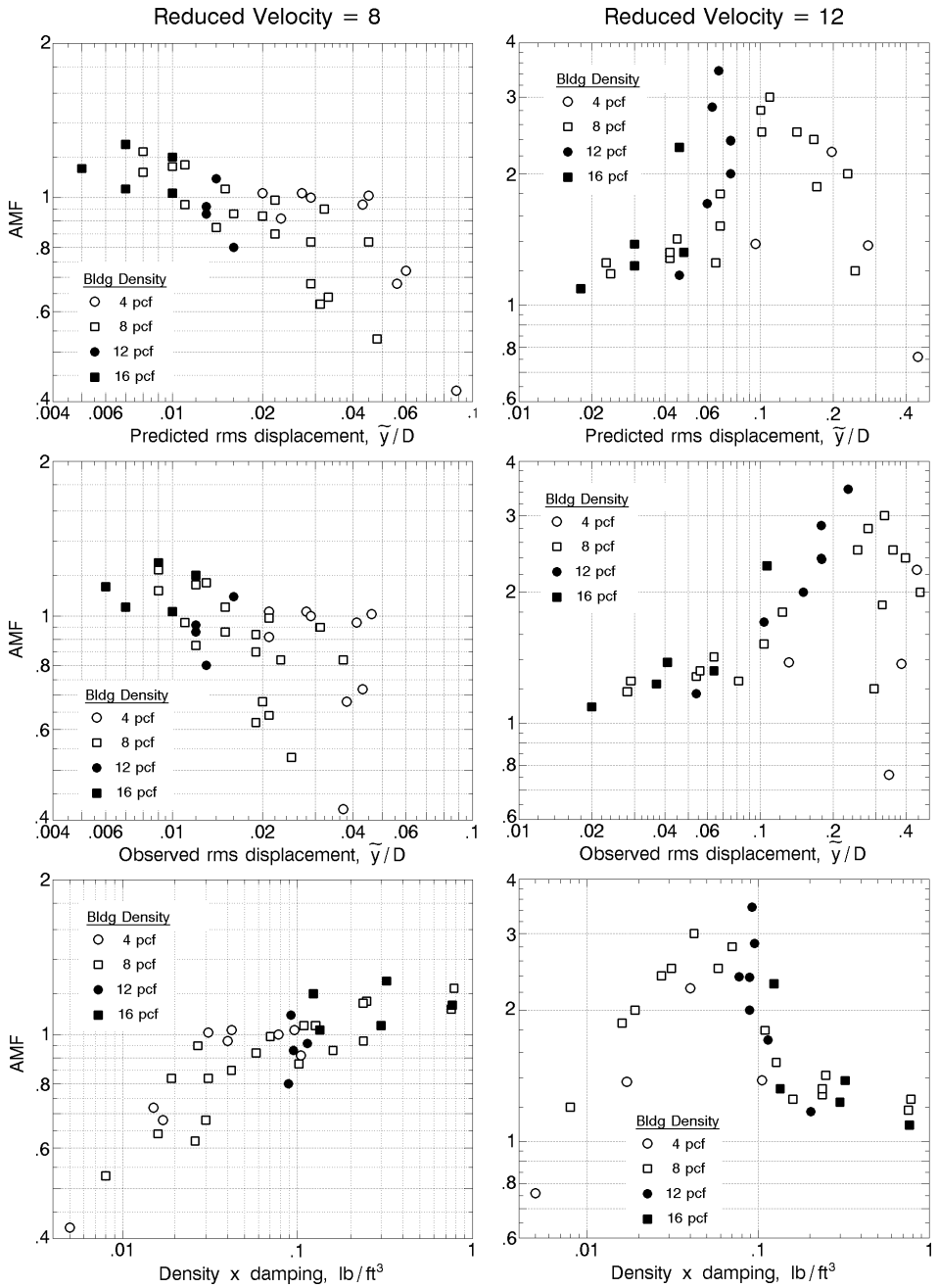

Fig. 4.11 Aeroelastic magnification factor as a function of various parameters for a 8:1:1 building at reduced velocities 8 and 12 (Boggs, 1992).

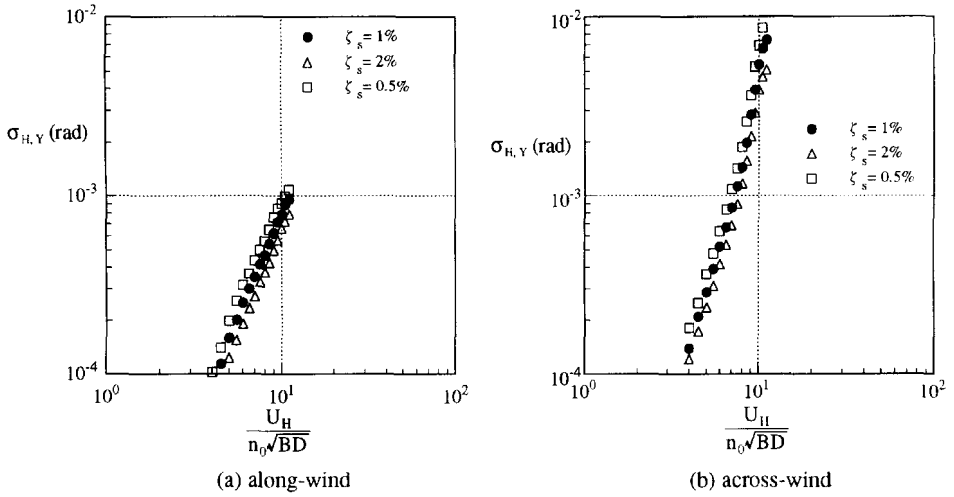

Fig. 4.12 Normalized standard deviation response displacement of a square section cylinder (H/B=6, B/D=1) with reduced velocity for different damping ratios in along and across-wind directions (Marukawa *et al.*, 1996).

α was equal to 0.15 for BL1 and 0.32 for BL2. The turbulence intensity varied from 20% near the ground to 3% at gradient height in BL1 and from 35% to 6% in BL2. A 7:1:1 rigid body base-pivoted aeroelastic model was considered, having two sway modes of vibration. Three structure densities equal to 151, 198 and 231 kg/m^3 were used and the structural damping ratio ξ_s varying from 0.4% to 6% was provided by an oil damper device at the model base. The following mass-damping coefficient M_D was chosen as the experimental controlling parameter:

$$M_D = \frac{\int_0^h m(z)\phi_i^2(z)\,dz}{\int_0^h \phi_i^2(z)\,dz}\,\frac{\xi_s}{\rho D^2} \tag{4.19}$$

By using the definition of the Scruton number given in Eq. (4.3) and from the definition of the equivalent mass per unit length in Eq. (4.4), it can be easily observed that M_D is equal to $Sc/(4\pi)$ (D in Eq. (4.19) indicates the side dimension). Figs. 4.13 and 4.14 illustrate the RMS normalized across-wind responses in BL1 and BL2, respectively. The measured aeroelastic responses (circles) are compared with the aerodynamic ones (dashed lines), calculated from force spectra, and with the ones predicted from force spectra but having added the aerodynamic damping contribution (solid lines) [see subsection 4.4.5].

In BL1 three regions were defined for the across-wind response based on the M_D values. For $M_D \geq 6.28$, called *aerodynamic stable* region [Fig. 4.13(a)], the RMS tip across-wind response displays maximum value at a critical velocity approximately equal to 11. This maximum slightly increases when the mass-damping parameter decreases. The predicted response based on force spectra is in good agreement with the measured aeroelastic one for velocity values lower than the critical wind speed, while, for higher values of wind velocities the predicted response exceeds the measured one, showing that aeroelasticity plays a reducing effect on the across-wind response (positive aerodynamic damping). For $2.76 \leq M_D \leq 5.82$, *aerodynamic unstable* region [Fig. 4.13(b)], the predicted response merges with the measured one up to a reduced velocity of 8, while for higher values, the measured response exceeds the predicted

one. This aeroelastic magnification effects (negative aerodynamic damping) becomes stronger as M_D decreases. For even higher velocity values, above the critical wind speed, aeroelastic effects gradually weaken and the measured response meets the predicted one. Lastly, for $M_D \leq 2.18$, region of *aerodynamic divergence* [Fig. 4.13(c)] the across-wind response becomes even an order of magnitude greater than in the previous two regions. For reduced velocity less than 10, measurements form aeroelastic tests are approximately equal to predictions based on the across-wind force spectrum, while for reduced velocity greater than 10, a significant aeroelastic phenomenon occurs. For models with $M_D = 2.18$ and 1.54 the across-wind response increases monotonically with wind speed well beyond the critical vortex shedding value. At even higher reduced velocities the measured response is seen to decrease rapidly towards the predicted values. For low values of the mass-damping coefficient the across-wind galloping occurs and response diverges. As a matter of fact, the high values of aeroelastic responses observed well after lock-in conditions, where the shedding frequency identifiable from spectral analysis was well greater than the natural frequency of vibration, were attributed to galloping excitation. Examining different values of the mass-damping parameter, the authors identified the model's lock-in velocity U_{crit} and the critical velocity for galloping U_g and concluded that for a square-section building galloping does not trigger spontaneously at the critical galloping velocity. Instead, it is initiated by vortex resonance, i.e. when $U_{crit} \geq U_g$, galloping is delayed until vortex shedding resonance happens. On the other hand, if $U_{crit} < U_g$, vortex shedding resonance will trigger and accelerate the galloping excitation.

The across-wind responses measured in BL2 (Fig. 4.14) indicate that there is no peak value or resonance-then-galloping phenomenon, regardless of the mass-damping parameter value. The presence of high turbulence damps the aeroelastic effect and the predicted response is never lower than the aeroelastic one (positive aerodynamic damping).

4.4.4 Literature approaches for modeling aeroelastic across-wind response of structures

This section is intended to provide a brief description of some different approaches used in literature to deal with the aeroelastic response of structures. In the case of high-rise buildings this response, especially in the across-wind direction, can significantly differ from that estimated solely from lift force data from rigid model tests.

Even if the across-wind excitation mechanisms, namely the wake, incident turbulence and motion-induced forces, are separately identifiable, they often superimpose in causing the response. This is, probably, the main reason why a generalized analytical method for predicting across-wind vibrations of structures is still not available.

Holmes (1998) critically reviewed the commonly used methods for estimating across-wind responses of structures due to vortex shedding. They can be divided into two main classes:

- sinusoidal or harmonic excitation models,
- random excitation models.

Sinusoidal excitation models are based on the assumption that the vortex-shedding phenomenon generates near-sinusoidal cross wind forces. With reference to circular

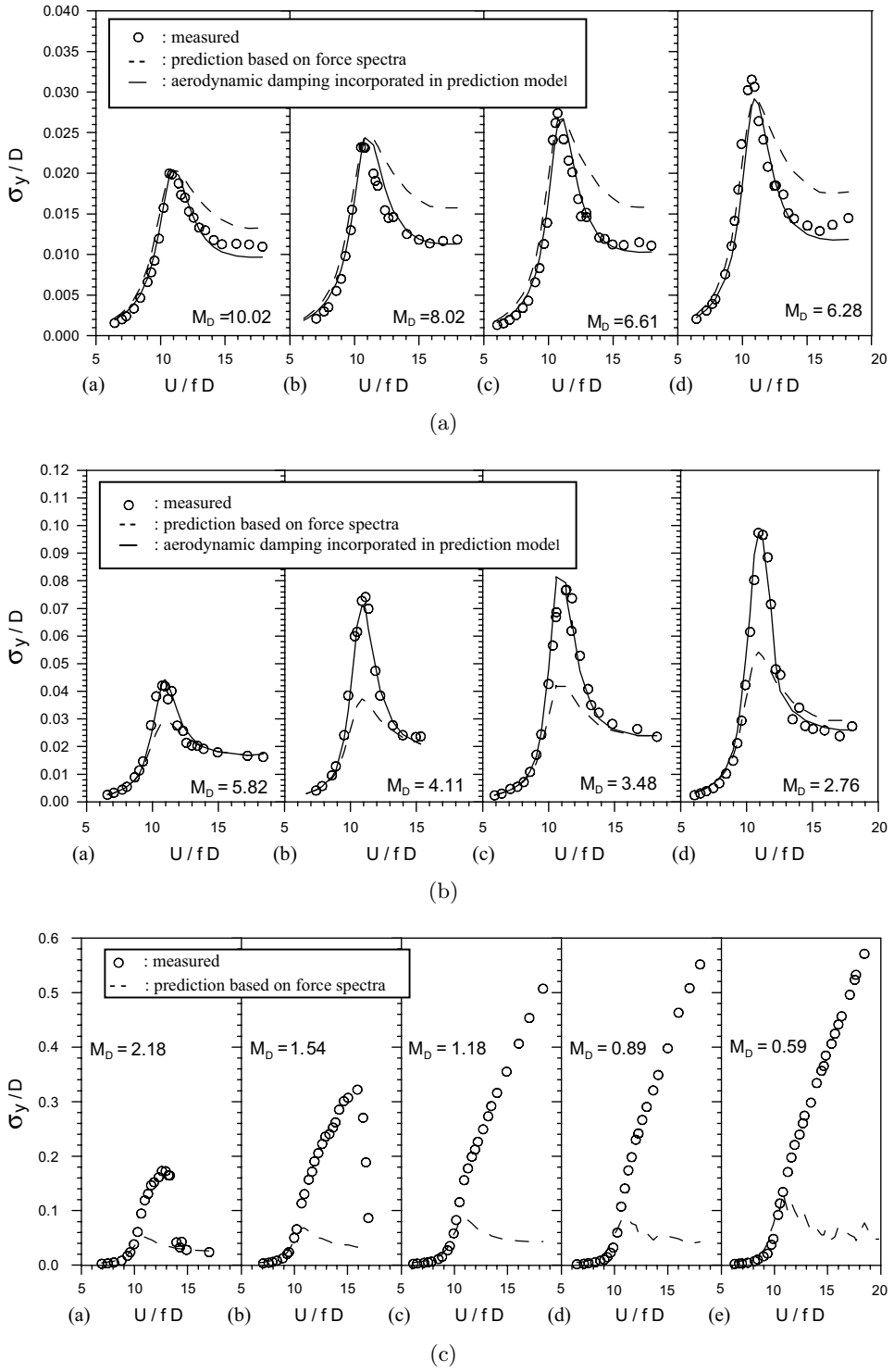

Fig. 4.13 Measured and predicted across-wind response of versus reduced velocity in BL1 from Cheng *et al.* (2002): a) $M_D \geq 6.28$; b) $2.76 \leq M_D \leq 5.82$; c) $M_D \leq 2.18$.

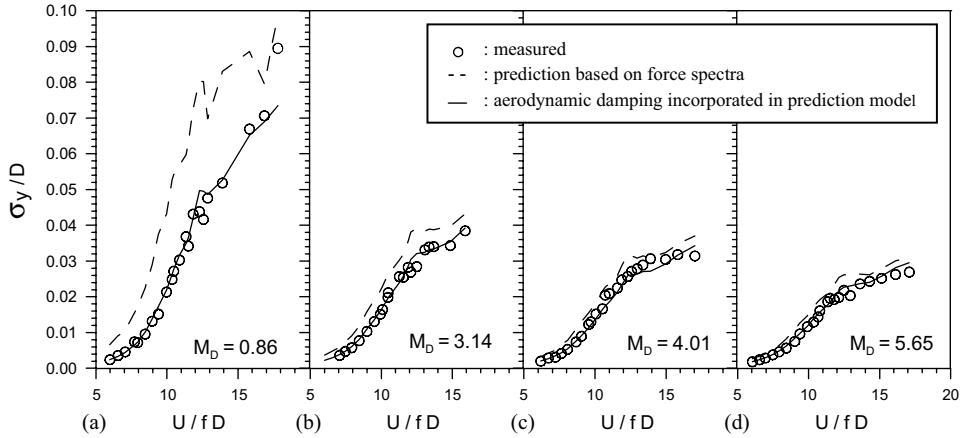

Fig. 4.14 Measured and predicted across-wind response of versus reduced velocity in BL2 from Cheng *et al.* (2002).

cylinders, this assumption is mostly related to the work of Scruton and co-workers in the 1950s and 1960s (Scruton, 1981). Sinusoidal models provide good estimates when large vibrations occur and the shedding has effectively locked-on to the across-wind motion of the structure. Ruscheweyh modified the basic sinusoidal model by the use of a correlation length, which takes into account that the vortex shedding mechanism is not uniformly distributed along the cylinder axis (Ruscheweyh, 2010). Because of lock-in, the exciting force has its maximum at the point of antinode of the mode shape. For a cantilever, for example, it is near the top[3] and for a simple supported beam it is in the mid span. The correlation length, which increases with vibration amplitude, serves the fact that vortex shedding forces are applied over a height range less than the total height of the structure.

Random excitation or spectral model was originally suggested by Vickery and Clark (Vickery and Clark, 1972) and further refined by Vickery and Basu (Vickery and Basu, 1983). In the case of random vibration, as seen in subsection 4.4.2, the response is inversely proportional to the square root of the damping, whereas in the case of sinusoidal excitation model, the peak response is inversely proportional to damping.

Eurocode 1 (UNI-EN 1991-1-4, 2005) proposes two approaches for predicting vortex-induced vibrations of structures. The first one is based on the vortex-resonance or sinusoidal model and the second one on the spectral model. The spectral model is also used in the Canadian and the Danish wind code and in the CICIND model code for chimneys.

Davenport and Novak (1976) proposed a two-stage vibration model for vortex-induced vibration, namely, random excitation and harmonic excitation stages. When the building tip vibration amplitude, in random excitation, exceeds 2% of the building width, harmonic excitation takes over.

On the basis of their experimental results, previously discussed, Kwok and Melbourne (1981) proposed a prediction procedure which consists of a random excitation model and a sinusoidal lock-in excitation model. When lock-in becomes significant, in fact, the response can be considered proportional to ξ_s^{-1}, rather than $\xi_s^{-1/2}$, as in

[3]At the free end of a cantilever, three dimensional flow around the top, tip effect, contrasts the vortex shedding and moves below the top the maximum of the exciting force.

the case of wake excitation. The selection of the excitation model to be used in the prediction process is determined by a critical across-wind displacement amplitude above which lock-in dominates the response. In suburban turbulent boundary layer flow, this was found to be approximately 0.025 of the side for a 9:1:1 square tower. Across-wind response predicted by these models was found to agree well with the measured response.

A number of researchers (Reinhold and Sparks, 1979; Kwok and Melbourne, 1981; Tschanz, 1982b; Kareem, 1982) have demonstrated conditions for both valid and invalid aerodynamic results for specific cases by comparing the results of aeroelastic and aerodynamic models of the same building. These researchers have not provided quantitative or general limits on conditions for validity and even the parameters of most significance have not been agreed upon. It may be stated, for example, that sufficient, but not necessary conditions, for the validity of the aerodynamic method for the response estimation, are that the reduced velocity be less than a critical value for vortex shedding, while others may demonstrate valid results provided the rms tip displacement (affected by varying the damping) is below a certain critical value. The effect of other parameters, including building density, building shape and boundary layer characteristics, have not been studied systematically, jet. Boggs (1992), as illustrated in subsection 4.4.3, compared aerodynamic (predicted) and aeroelastic (observed) response of an 8:1:1 square cylinder in a simulated suburban environment and showed that the reduced velocity, in conjunction with a mass-damping parameter, provides a good characterization of the *aeroelastic magnification factor (AMF)*, computing the distance between aeroelastic and aerodynamic responses.

4.4.5 Aerodynamic damping

The study of the aeroelastic behavior of structures can be addressed following different approaches, like that of flutter derivatives. In this study, however, the model of aerodynamic damping is used to deal with aeroelastic effects in tall buildings response. The generalized load, $P_j(t)$ in Eq. (4.8), may be dependent on the structure's response, so it should be written as:

$$P_j\left(t, q, \dot{q}, \ddot{q}\right) \tag{4.20}$$

The presence of q and its derivatives on the right side of Eq. (4.8) represents *aeroelastic feedback*, rendering the equation nonlinear. Depending on the phase of the force with respect to the motion, aeroelastic or motion-induced forces can be associated with the displacement, the velocity or the acceleration of the structure. Because of these associations, aeroelastic forces can be regarded as "aerodynamic contributions" to stiffness, damping and mass, respectively. They are therefore referred to as aerodynamic stiffness (in phase with displacement), aerodynamic damping (in phase with velocity), aerodynamic mass (in phase with acceleration).

In addition to inducing phase-related forces, the motion of a structure may influence the nature of those forces which already exist on the stationary body. The increase in correlation of the across-wind load with increasing amplitudes of vibration, discussed in section 4.3, is an example of this. Furthermore, aeroelastic effects can couple modes that are not coupled structurally.

Aeroelastic contributions to the overall aerodynamic loading are distinguished

from other unsteady loads by recognizing that aeroelastic loads vanish in absence of structural motion.

Aerodynamic mass and stiffness are not, normally, of great significance, except for very large light structures, such as large span roof systems and, to a lesser extent, bridges (Vickery, 1990).

Several methods have been used in order to estimate aerodynamic damping, using wind tunnel tests on aeroelastic models. They include, for example, the auto correlation function technique, the half power band width technique, the random decrement (RD) technique (Marukawa *et al.*, 1996). Other authors, e.g. Cheng *et al.* (2002), have estimated aerodynamic damping through an inverse approach by adjusting the damping value so that the aerodynamic response calculated from rigid model tests would have equaled the one measured from aeroelastic tests.

It is well known that along-wind aerodynamic damping is often small and positive and almost linearly increasing with the reduced velocity. Neglecting its effect in the response estimation is, therefore, conservative. Across-wind aerodynamic damping, however, may be negative and large for high wind speeds or large building displacements. This gives rise to a certain aeroelastic magnification, invalidating the response calculated using the aerodynamic method (Boggs, 1992).

Various studies have been dedicated to the identification of the aerodynamic damping of prisms. Here some results concerning aerodynamic damping of 3-D prisms are illustrated, with particular reference to the across-wind response of square-section prisms.

Marukawa *et al.* (1996) employed the RD technique to evaluate the aerodynamic damping ratio from the time series of the response displacement, using the stick aeroelastic models previously cited. The effect of side ratio, D/B, aspect ratio, H/B, and structural damping on aerodynamic damping, varying with reduced velocity, was investigated for both along-wind and across-wind directions.

The aerodynamic damping ratio observed in the along-wind direction was almost always positive. For side ratios lower than 1, the smaller the side ratio, the higher the aerodynamic damping ratio, while, for higher side ratios, no clear effect was found of the latter on aerodynamic damping. It increased, in most cases, monotonically with reduced wind velocities. For the square section model the observed values are smaller than those estimated by quasi-steady theory. No clear effect of aspect ratio on aerodynamic damping was found in along-wind direction. Fig. 4.15 illustrates the effect of structural damping on aerodynamic damping for the square section 6:1:1 model. For reduced wind velocities lower than 10, the smallest aerodynamic damping ratio was identified for 1% structural damping ratio. For reduced velocities beyond 10 and a structural damping of 0.5%, the aerodynamic damping ratio increased rapidly with reduced velocity.

Concerning the across-wind direction, models with side ratio lower than 1 showed positive aerodynamic damping at low wind velocities and negative values for higher speeds. The least reduced velocity value at which the negative aerodynamic damping ratio was observed was about 10 for the square section, 7 for side ratios of 0.5 and 0.33. The wind velocities from which positive aerodynamic damping changed to negative was much lower than the onset wind speed for galloping excitation. For side ratios greater than 1, positive aerodynamic damping ratios were observed for the entire range of tested wind speeds.

In across-wind direction, the wind velocity at which the aerodynamic damping

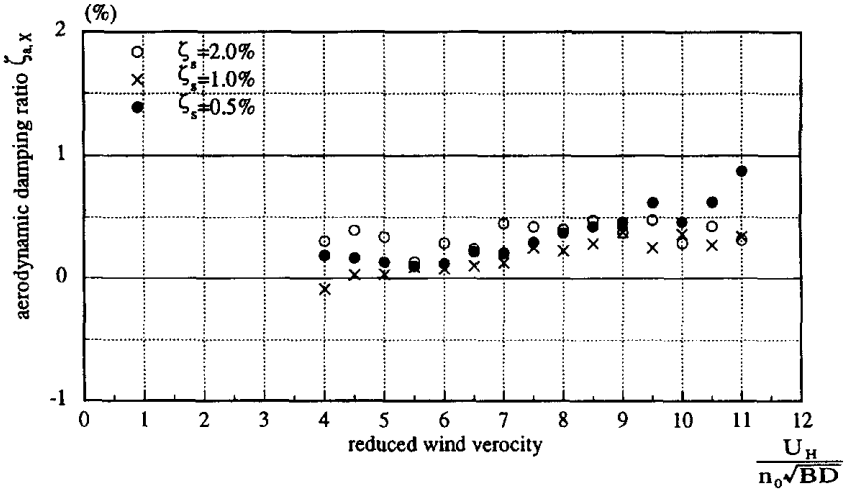

Fig. 4.15 Effect of structural damping ratio on aerodynamic damping ratio in along-wind direction for a 6:1:1 (D/B=1, H/B=6) square cylinder (Marukawa *et al.*, 1996).

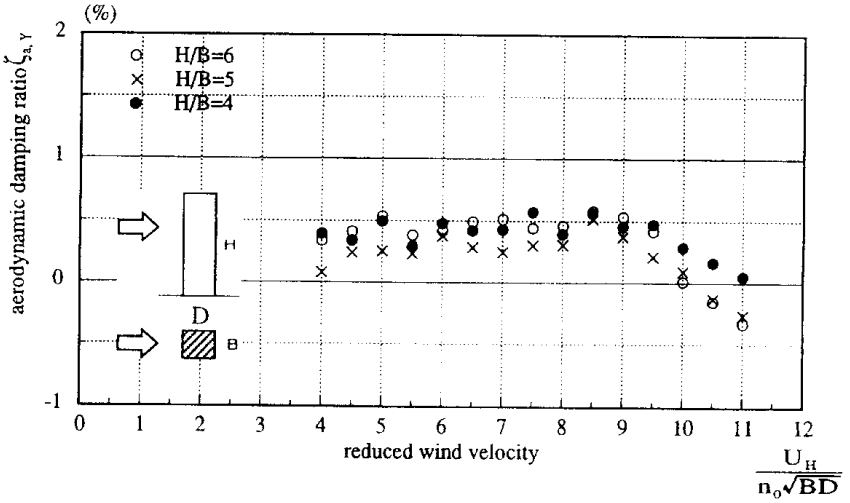

Fig. 4.16 Effect of aspect ratio on aerodynamic damping ratio in across-wind direction for a square cylinder with 1% structural damping (Marukawa *et al.*, 1996).

ratio changes from positive to negative is influenced by aspect ratio (Fig. 4.16). The wind speed where aerodynamic damping becomes negative increases as the aspect ratio decreases. This trend is believed to be related to the weaker Strouhal component of the power spectral density observed for smaller aspect ratios.

In the across-wind direction, moreover, as depicted in Fig. 4.17, referred to the

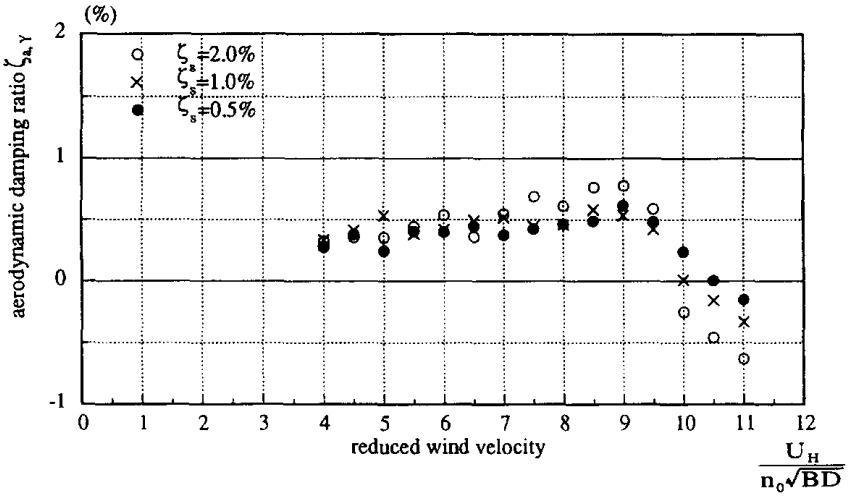

Fig. 4.17 Effect of structural damping ratio on aerodynamic damping ratio in across-wind direction for a 6:1:1 (D/B=1, H/B=6) square cylinder (Marukawa *et al.*, 1996).

6:1:1 square section model, for reduced velocities lower than 9, positive aerodynamic damping ratio increases with structural damping ratio, while for higher reduced velocities, decreases more rapidly. The wind velocity at which aerodynamic damping becomes negative decreases with increasing structural damping.

With reference to the experimental results illustrated in subsection 4.4.3, Cheng *et al.* (2002) identified across-wind aerodynamic damping of a 7:1:1 building in open terrain (BL1) and urban terrain (BL2) conditions. Considering that the total damping of an aeroelastic system ξ_{tot} consists in the sum of the structural damping ξ_s and the aerodynamic damping ξ_a, the latter was identified through an 'inverse response approach'. First, the structural damping ratio of the aeroelastic model was determined, then the total damping was estimated adjusting it numerically so that the calculated response, based on the across-wind force spectra, was equal to the measurements. The aerodynamic damping was then calculated as the difference between total damping and structural damping. The inverse response approach based on the stochastic across-wind load was considered no longer valid in the aerodynamic divergence region, when the occurrence of galloping led from narrow bandwidth random to sinusoidal oscillations.

Fig. 4.18 shows the identified aerodynamic damping values as a function of the reduced velocity and the fitted curves proposed by the authors in order to derive an empirical aerodynamic damping model. In BL1 for $M_D \geq 6.28$ [Fig. 4.18(a)] aerodynamic damping is almost zero at the critical velocity and positive elsewhere. It is slightly influenced by the mass-damping parameter. The empirical model proposed by the authors is a function of the reduced velocity only. In the aerodynamic unstable region [Fig. 4.18(b)] aerodynamic damping becomes negative when the reduced velocity is greater than 8. Afterwards it reaches a minimum value around the critical velocity causing a maximum across-wind response. Aerodynamic damping in this

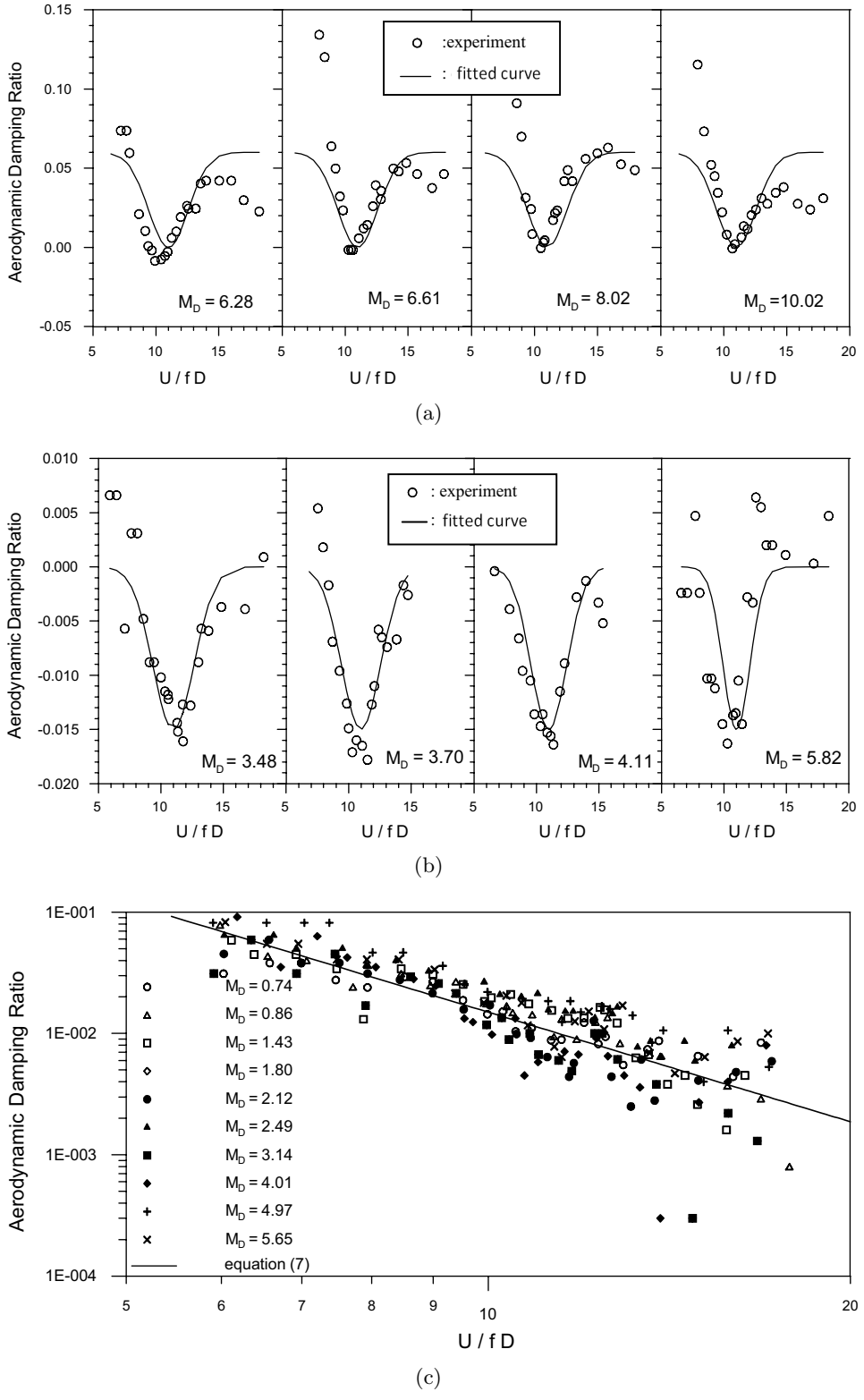

Fig. 4.18 Across-wind aerodynamic damping identified by Cheng *et al.* (2002): a) open terrain (BL1), $M_D \geq 6.28$; b) BL1, $2.76 \leq M_D \leq 5.82$; c) urban terrain (BL2).

region is influenced by both reduced velocity and mass-damping parameter. The empirical model proposed accounts for both these quantities. In BL2 [Fig. 4.18(c)] aerodynamic damping is always positive and proportional to -3 power of reduced velocity. The effect of the mass-damping parameter is negligible. The across-wind response of a high-rise building in this region can be conservatively estimated from the lift force spectrum. The authors, finally, showed that incorporating the identified aerodynamic damping values the response calculated from across-wind force spectra was in good agreement with the measured values.

Gu and Quan (2004) performed wind tunnel tests on a 6:1:1 base-pivoted aeroelastic model. Four kinds of wind conditions, corresponding to categories A, B, C, D, were simulated in the wind tunnel at a length scale of 1/500, according to the Chinese code (GB50009-2001, 2001). The exponents of the mean speed profiles for these categories orderly were 0.12, 0.16, 0.22, 0.30. The longitudinal turbulence intensities at the model top (0.60 m) were about 6.8%, 7.3%, 10% and 14% for the four categories of terrain, respectively. Four different values of the structural damping ratio, $\xi_s = 0.6\%$, 1.2%, 1.88%, 2.17%, were achieved in the wind tunnel, by selecting damping plates with different sizes [see also Quan *et al.* (2005)]. Fig. 4.19 shows the aerodynamic damping ratio ξ_a, identified with the time-averaging random decrement technique, as a function of the reduced velocity $U/(f_1 B)$ in the across-wind direction. Fig. 4.19(a) shows the variation of the aerodynamic damping with the terrain category. Under the conditions of terrain categories A, B and C, for reduced velocity lower than 9, ξ_a is positive and increases with reduced velocity. With a further increase in reduced velocity the aerodynamic damping suddenly decreases and changes from positive to negative values at a reduced velocity between 10 and 11. For terrain category D, however, ξ_a is always positive and its maximum value is much smaller than those under the first three terrain conditions. Fig. 4.19(b) depicts the variation of the aerodynamic damping ratio ξ_a with the structural damping ratio ξ_s under the terrain C conditions. The absolute values of ξ_a, in general, decrease with increasing structural damping. It may be observed that results from Gu and Quan (2004) are in evident agreement with those from Marukawa *et al.* (1996), illustrated before.

4.5 Summary and main remarks

In this chapter the wind-induced response of tall buildings is discussed, illustrating how aeroelastic effects can play an important role especially in the across-wind response of buildings. Aeroelastic phenomena, arising from the interaction between aerodynamic loads and structural deformations, are not negligible for lightweight, low damped, slender structures. In this case, motion-induced effects have to be carefully taken into account for a proper assessment of the responses induced by the wind action, in order to perform, for example, the serviceability design of the structures or to evaluate the comfort level of their occupants.

A vibrating structure, under the vortex shedding action, experiences the aeroelastic phenomenon known as lock-in when the dominating shedding frequency synchronizes with the natural frequency in the transverse direction. This phenomenon gives rise to the so-called Vortex-Induced Vibrations (VIV).

The movement of a structure immersed in an air flow can also affect the correlation structure of pressures.

The common used method for estimating the response of structures to aerody-

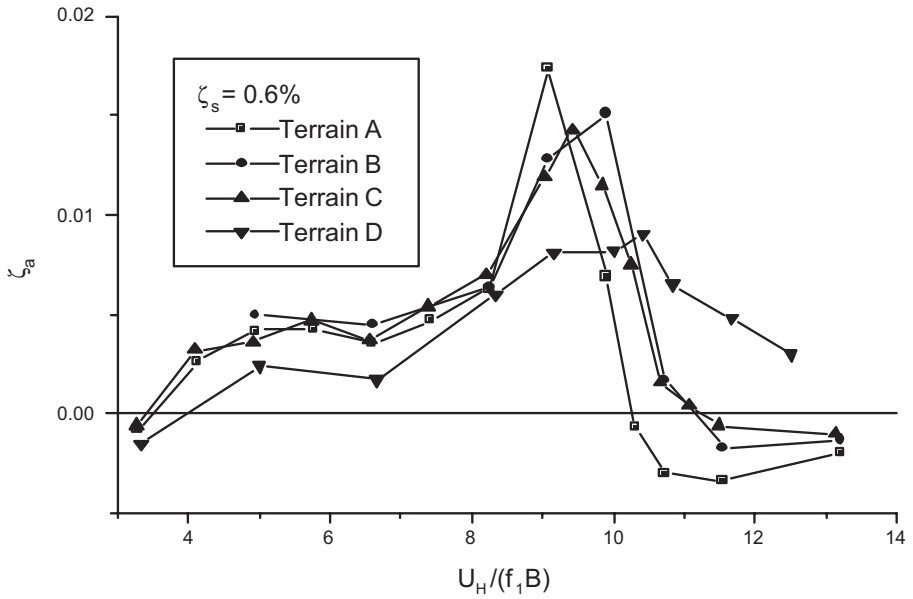

(a)

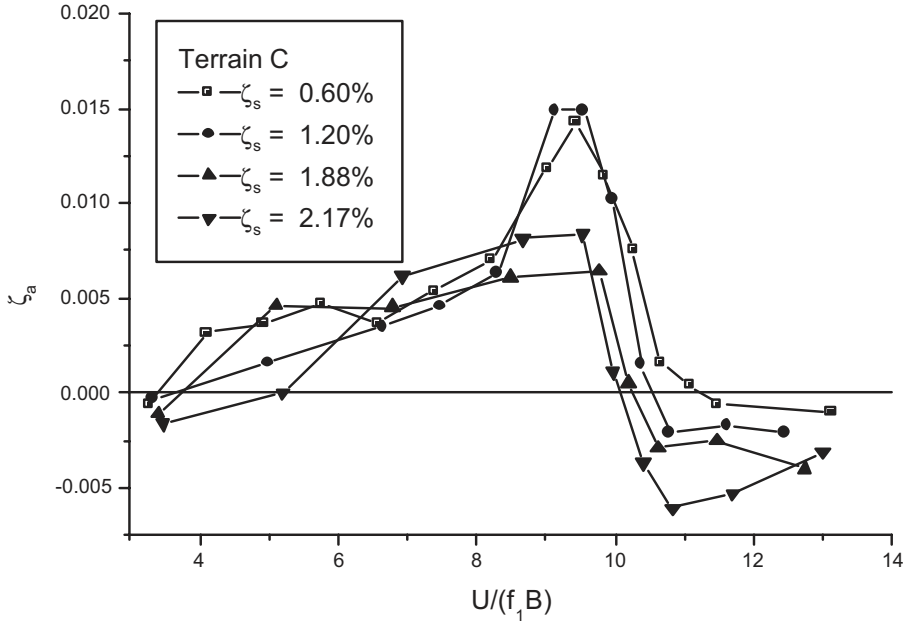

(b)

Fig. 4.19 Across-wind aerodynamic damping versus reduced velocity: a) variation of aerodynamic damping ratio with different terrain categories; b) variation of aerodynamic damping ratio with different structural damping ratios.

namic loads, neglecting aeroelastic effects is discussed. It leads to an approximate estimation of the standard deviation response which is proportional to $\xi^{-1/2}$, where ξ is the damping ratio.

Many literature studies have been devoted to the experimental evaluation of the across-wind response of buildings by means of aeroelastic models, often stick-type models. The across-wind response is usually evaluated in terms of the normalized standard deviation of the tip displacement, which shows a rapid increase at the critical reduced velocity. The latter, being the inverse of the Strouhal number, is approximately equal to 10 for a square section prism. The literature studies illustrated mostly refer to buildings with geometric and dynamic features similar to those of the structure tested in this work. Only in a few literature works the lateral response of square-section prisms, in turbulent flow conditions, was experimentally measured for various angles of incidence and a wide range of wind speeds including the synchronization range. Results from Kawai (1995) are reported in this chapter and will be used in chapter 8 as an illustrative example for the vulnerability analysis of tall buildings.

Different approaches exist in literature for modeling the aeroelastic across-wind response of structures.

The approach based on the aerodynamic damping is used in this work for the identification of aeroelastic effects on the across-wind response of tall buildings. Across-wind aerodynamic damping values identified in some literature works are discussed in this chapter. Differently from the along-wind aerodynamic damping which is often small, positive and linearly increasing with reduced velocity, across-wind aerodynamic damping may be negative and large for high wind speeds or large displacements.

Some experimental evidences are that across-wind aerodynamic damping is affected by the aspect ratio and structural damping of vibrating square-section prisms; at reduced velocities close to the critical value, aerodynamic damping is often observed to pass from positive to negative values; mass-damping characteristics (Scruton number) can define different aerodynamic damping conditions; turbulence of the approaching flow affects identified aerodynamic damping values; positive aerodynamic damping has been observed in high turbulence conditions at all tested reduced velocities, including the critical value.

Chapter 5

The role of wind tunnels in the prediction of tall buildings response

5.1 Introduction

The complete theoretical prediction of the wind-induced structural response is not feasible. The analytical modeling of wind-structure interactions is mathematically impracticable. Although recent advances in computational fluid dynamics are very promising, these are not at a stage of being a designer's tool, yet. Therefore, wind tunnels have served as the most reliable means of investigating the wind action effects on structures. Experimental techniques in common use can be categorized in the two following broad classes:

- rigid models;
- aeroelastic models.

In the case of rigid models (section 5.2), which are only geometrically scaled, the motion of the prototype is predicted by theoretical methods with the motion-induced forces either being ignored or estimated from existing data. Aeroelastic models (section 5.3) are geometrically and dynamically scaled and responses may be directly measured and transposed to prototype scale.

An exhaustive description of the practicable wind tunnel simulations can be found in ASCE (1999) and in Alan G. Davenport Wind Engineering Group (2007). In the following sections only a brief portraiture of them is given with particular reference to aeroelastic simulations of tall buildings. Scaling requirements for aeroelastic models of tall buildings are also illustrated.

5.2 Rigid model techniques

On structures or elements where aeroelastic effects, such as aerodynamic damping, are judged to be not significant, the overall external wind loads can be studied using rigid models, also referred to as *static* or, sometimes, even as *stationary* models, with geometrically scaled external features. The mean and dynamic wind-induced aerodynamic loads may be obtained by using different methods, basically including

High-Frequency-Force-Balance (HFFB) technique (subsection 5.2.1) and integration of surface pressures (subsection 5.2.2). Structural responses, e.g. deflections and accelerations, my be evaluated in *time domain*, using stored time-histories of the aerodynamic loads or, more commonly, in *frequency domain*, using power spectral densities of the applied modal wind loads and assuming steady-state conditions (ASCE, 1999).

5.2.1 High-Frequency Force Balance Tests

The High-Frequency Force Balance (HFFB) technique, first reported by Tschanz (1982a), is founded on an earlier approach proposed by Whitbread (1975). The technique, also known as High-Frequency Base Balance (HFBB), is based on the use of a very stiff high-frequency balance-model system that models only the exterior geometry of the structure. For this reason the HFFB technique can be employed at a stage in the design when only the exterior geometry of the structure has been decided. While with aeroelastic simulations (section 5.3) the measured quantity is the final response, the base balance technique allows direct measurements of good approximations to the steady and unsteady modal forces acting in the fundamental sway and torsional modes of vibration of the building.

The dynamic responses, including resonant amplification at the natural frequencies of the building, are derived analytically for each mode using random vibration analysis methods (subsection 4.4.2) and are subsequently used to estimate the full scale responses. Changes in the structural properties can be easily accommodated by iteration of the analytical procedures. Parametric studies, in which the responses are predicted as functions of the structural parameters, are often feasible. Furthermore, it is unnecessary to retest a new wind tunnel model unless significant changes in the exterior geometry are made. These reasons make the HFFB tests a widely accepted technique for wind tunnel model studies and a relatively economical and expeditious alternative to the aeroelastic model simulations.

The idea of measuring the modal force spectrum and then calculating the responses had been considered prior to the current base balance technique. Saunders and Melbourne (1975) attempted to record the modal spectrum by measuring it as seen through the mechanical admittance of an aeroelastic model. By knowing the model properties, reverse calculation yielded the modal spectrum which could then be combined with the desired structural properties. Major difficulties with this procedure are the errors introduced through aeroelastic model properties, in particular the damping estimation.

The fundamental assumption of the base balance technique is that the generalized or modal forces from the wind can be estimated from the measured base forces and moments experienced by a stationary model. The generalized or modal force is defined as the integral of the applied force weighted by the mode shape at the point of application. The three base moments, measured, for example, by a three component HFFB, including two overturning moments and the base torque, represent direct and exact measurements of the modal forces only when all the following conditions are met (ASCE, 1999):

1. The first three natural modes of the structure are decoupled and geometrically orthogonal in two sway directions and one twist direction.

2. The fundamental bending mode shapes are linear functions of height and piv-

oted at a point where the moments are measured.

3. The fundamental torsional mode shape is a constant (independent on height) over the height of the structure.

4. There are not significant motion-induced forces involved, so that the nature of the forces remains the same on a vibrating structure as it is on a rigid structure.

5. The balance-model system is substantially rigid, with a high natural frequency, so that the measured moments are not significantly amplified by the mechanical admittance of the system in the frequency range of interest.

6. The contribution to the response of the structure from higher modes is negligible.

In practice these requirements are never fully met and adjustments of the technique are needed for its proper application.

If the balance-model system responds dynamically to the wind-loading, then the measured base moments will include the *inertial loading effects* of the system itself. If the motions are large, then the aerodynamic interaction of the model with the wind could also contaminate the measurements. Therefore an attempt is made to take the balance-model system as rigid as possible, while being sensitive enough. In this way, it is ensured that the frequency range of interest falls at the low end of the mechanical admittance function where the dynamic amplifications are small. In cases where the natural frequency cannot be raised sufficiently high and the balance measurements are amplified, adjusting the spectral density is possible, in principle, providing the mechanical admittance of the system is well identified and may be treated as linear and uncoupled.

It must be checked in fact that the balance-model frequency is high enough to neglect the model motion (ASCE, 1999). In practice, however, it is difficult to avoid oscillatory movements of the model, which, together with intrinsic data acquisition system noise, might have a negative impact in the validity and/or accuracy of the measurements. A rough estimation of the magnitude of the inertia loads may be done calculating the acceleration from the amplitude of vibration and the oscillatory frequency and then multiplying it with the mass of the model (González *et al.*, 2011).

For buildings with uncoupled linear mode shapes, the generalized wind forces are equal to the measured base overturning moments and building dynamic responses can be exactly estimated directly solving a set of generalized equations of motion (see subsection 4.4.2). The evolution of tall buildings design and modern architectural forms towards irregular and elongated building shapes, illustrated in section 2.1, results in buildings having significantly nonlinear and/or three-dimensional coupled mode shapes and prone to significant wind-induced torsional loads. Many research works have been dedicated to address the effects of non-ideal mode shapes in the HFFB analysis technique and the use of mode shape corrections, such as Boggs and Peterka (1989); Zhou *et al.* (1999, 2002); Holmes *et al.* (2003). More recently, Tse *et al.* (2009) have proposed a HFBB analysis method, referred to as linear-mode-shapes (LMS) method, which allows the values of the sway components of the generalized wind force to be determined by establishing a new set of centers at which the translational mode shapes are linearized by axis transformation.

In a study by Tschanz and Davenport (1983) the use and advantages of the five component base balance are discussed. In particular, the additional measurement of the base shear forces in two orthogonal directions is shown to permit the magnitude and line of action of the mean forces to be defined and represented by a trapezoidal or parabolic distribution. Furthermore a correction procedure for developing a generalized torsional force from the measured torque component is described. The correction is quite appropriately determined by the ratio of the moments and shears in the translational modes.

5.2.2 Overall loads from local pressure measurements

The development of solid state pressure scanners has allowed the simultaneous measurement of pressures at several points distributed on the wind tunnel model of the building or structure in general. This experimental approach is known as *Synchronous Multi-Pressure Sensing System* (SMPSS) technique. Area loads may be assessed by measuring local pressures acting on tributary areas and used to determine overall loads through bending and torque arms. Key factor to be considered using pressure measurements for the determination of wind loads are the frequency response of the pressure measuring system and the distribution of the measuring points. The technique allows the direct computation of the steady and unsteady modal forces acting in any number of modes of vibration of the structure (Vickery, 1990; Alan G. Davenport Wind Engineering Group, 2007). Similarly to the HFFB approach, the resonant amplification due to the building structural dynamics is derived analytically for each mode using random vibration theory and results are used to estimate the response of the structure at full scale. Major vantages of the pressure measurements technique are that:

- a single model in a single testing session can produce both overall structural loads and cladding loads;
- the generalized forces can be properly determined also for three-dimensional non-linear mode shapes.

On the other hand, a disadvantage of this technique is that it typically includes more instrumentation and takes longer model construction time than the HFFB method. Furthermore, as in the case of the base balance, the method does not include any effects of the motion-induced forces.

5.3 Aeroelastic simulations

Aeroelastic modeling is the principle experimental technique in studies of structures which are sensitive to wind-induced dynamic effects. Aeroelastic wind tunnel models are designed to replicate the deformation and motion of prototype buildings and structures in a simulated flow field. If properly carried out, aeroelastic tests provide the most complete characterization of the wind-induced structural responses, inherently including additional effects of the motion-induced forces. Body motion-excited or aeroelastic forces, which can be significant for some lightweight, flexible and lightly damped structures, cannot be measured with stationary models, such as are used in pressure and force balance model studies.

Two approaches are common in aeroelastic wind tunnel studies. First, such tests

are carried out to provide particular empirical data for analytical formulations of wind-induced effects. Second, aeroelastic studies are carried out to simulate the "entire" process, including the salient characteristics of the structure and its specific setting. The latter approach provides "direct" estimates of the full scale wind-induced response and does not rely on analytical methods. To be representative, such studies must model the properties of the natural wind and the aerodynamically significant features of the exterior geometry, but have also to correctly simulate the stiffness, mass and damping properties of the prototype structure.

In general, aeroelastic simulations are performed at several speeds, selected to simulate a representative range of full-scale wind speeds and for a full range of wind directions, unless there are symmetries of shape, structural properties and surroundings, or unless the important directions of wind can be ascertained at the outset, as in the case of most bridges, or be determined from other studies.

Aeroelastic studies of tall buildings, described in detail by Isyumov (1982), generally fall into the category of direct modeling techniques. The action of wind on buildings is confined primarily to the lower modes of vibration and, as a result, the dominant aspects of wind actions can be studied with relatively simple dynamic models, which provide information that can be scaled up to full scale, without major corrections. The emergence of "direct" modeling approaches in aeroelastic studies of tall buildings is due to different reasons (Isyumov, 1982). Some of them are listed as follows.

1. The aerodynamics of buildings which, excluding super-tall structures, generally have aspect ratio (height/breadth) less than 6 and seldom above 10, tend to be more 3 than 2-dimensional (as explained in chapter 3) and many of the simplifying assumptions, possible in the formulation of wind loads on line-like structures, are not valid. This reduces also the feasibility of analytical methods.

2. Some analytical methods, such as the gust factor approach, are valid to describe the drag response of buildings due to the buffeting action of turbulence. In contrast, lift and torsional excitation are less analytically predictable (see chapter 4).

3. It is common that the influence of the surroundings plays an important role in modifying or determining the action of wind of building. Hence the validity of modeling the presence of surrounding structures directly in the tunnel.

4. The dynamic response of tall buildings can be complex with coupled degrees of freedom or three dimensional mode shapes. This compounds the difficulty of the analytical estimates and favors physical direct modeling.

5. Most tall buildings are sharp-edged and the information obtained in small scale wind tunnel studies is representative of full scale data. As a result, *direct translations* of the model findings to full scale are possible without major corrections.

Finally, a main reason for performing aeroelastic studies of tall buildings is that the detailed direct description of the responses they provide can be used as a basis for estimating the structural performances and developing safe and cost effective optimal designs.

5.3.1 Types of aeroelastic tests

Aeroelastic model techniques include *replica*, *equivalent* and *section models*. A detailed description of the different models can be found in ASCE (1999).

Replica models

Replica models reproduce the prototype in virtually all aspects. These are aeroelastic models in which the geometric scaling of all dimensions results in a scaled reproduction of elastic properties. The use of replica models is practical for structures in which the elastic properties are concentrated on the exterior geometry, such as slender chimneys, cooling towers, tubular structures and so on. Replica models result in *full dynamic similitude* and provide direct measures of the wind-induced response. Despite their advantages, there are also some drawbacks. These models tend to be expensive and are not suited for parametric studies in which structural parameters, such as stiffness, mass and/or damping, are varied. An example of a major concrete structure modeled as an approximate replica aeroelastic model is the 553 m CN Communications Tower in Toronto (Isyumov *et al.*, 1984), shown in Fig. 5.1. The concrete tower is modeled using a metalized epoxy, sold under the trade name Devcon. Devcon and concrete have essentially the same density but the lower modulus of Devcon results in a reduced velocity scale i.e.:

$$\frac{U_m}{U_p} = \frac{\sqrt{(E/\rho)_m}}{\sqrt{(E/\rho)_p}} \tag{5.1}$$

where ρ is the density and E is the elastic modulus.

Replica models are only used for comparatively simple structural systems and only if the model construction materials are available to produce a velocity scale that can be attained in the tunnel.

Equivalent aeroelastic models

Equivalent models are *mechanical analogues* designed to simulate only some aspects of the dynamic characteristics of the prototype structure. Both *continuous* and *discrete* equivalent aeroelastic models are used. The earliest type of equivalent aeroelastic model used in the wind tunnel is the *two-degree-of-freedom* or *"stick"* aeroelastic model, also referred to as *"aeroelastic balance"* (Zhou and Kareem, 2003). It is a rigid model, pivoted near the base, with the elasticity provided by appropriately selected springs, simulating, usually, two orthogonal fundamental sway modes of vibration. Implicit in this technique is the assumption that the sway modes do not include any coupling and can be approximated as linear, and that torsion is considered of secondary importance.

A typical set up of the "stick" type aeroelastic model is schematically shown in Fig. 5.2(a). The model in Fig. 5.2(b) also includes a provision for modeling the torsional degree of freedom, but it only represents a uniform mode shape.

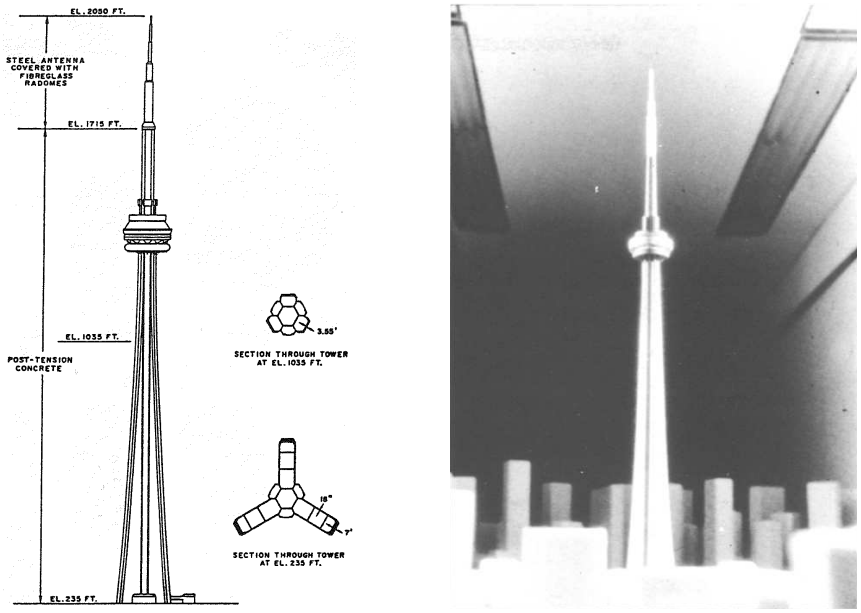

(a) (b)

Fig. 5.1 CN Communications Tower, Toronto: a) elevation of the tower and typical sections (ASCE, 1999); b) picture of the replica model of the tower in the wind tunnel, from Vickery (1990).

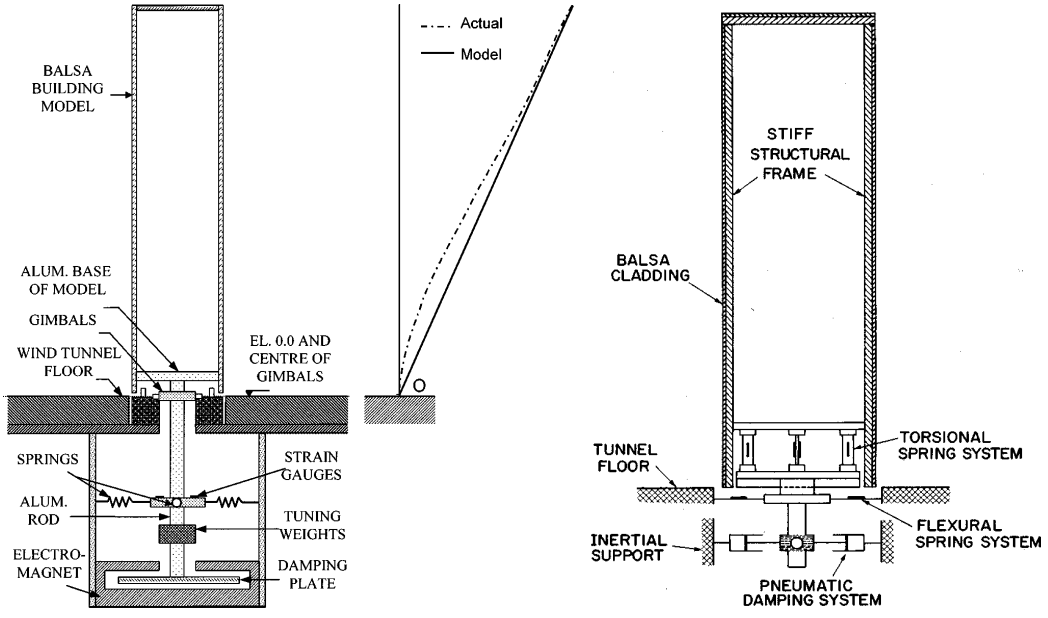

(a) (b)

Fig. 5.2 "Stick" aeroelastic model from Zhou and Kareem (2003): a) schematic representation of a "stick" aeroelastic model, with mode shape modeling; b) "stick" aeroelastic model with a torsional spring system.

The paper by Zhou and Kareem (2003) focuses on the relevant features concerning the role of a "stick" type aeroelastic model in structural design. The direct

similarity between the model and the prototype structure, which is a prerequisite for accurate "direct" assessment of wind effects through the "stick" model, cannot be easily achieved in practice. The first issue concerns the mode shape modeling, because the "stick" model works best for structures with linear sway modes [Fig. 5.2(a)]. The second issue concerns the mass modeling, since tall buildings usually have a complex mass distribution that poses a difficulty in replicating it in a small scale aeroelastic model.

The inconsistency resulting from the mismatch in mode shape modeling has been generally treated in two ways. One approach makes use of a straight-line mode shape to fit a large portion of the actual mode shape, adjusting the pivot point at an "appropriate" height above the building base (Isyumov, 1982). Alternatively, analytical procedures, which follow the techniques routinely used in the HFFB method, may be invoked to adjust observations to nonlinear mode shapes, e.g. Kijewski and Kareem (1998), Zhou *et al.* (1999), Zhou *et al.* (2002).

The effect of imperfect modeling of mass distribution has received relatively less attention. In some of the literature (Cermak, 1977; Isyumov, 1982; ASCE, 1999), the similarities in the total and the first mode generalized masses and the mass moment of inertia are required, while in others the exact modeling of mass has been relaxed.

The category of discrete equivalent aeroelastic models includes also *multi-degree-of-freedom* models, which are discrete mechanical analogues of buildings comprising several interconnected lumped masses each having two translational and one rotational (rotation about a vertical axis) degrees of freedom. This type of model is suited for aeroelastic studies of more complex buildings, where torsional effects are judged to be important and/or in situations where the modes of vibration are highly three-dimensional because of inertial and/or elastic coupling. A schematic representation of a typical multi-degree-of-freedom aeroelastic model is presented in Fig. 5.3. In this case the building is divided into four zones, each represented by a lamped mass. Masses are concentrated at the floor diaphragms, that are connected by flexible columns and the entire mechanical system is enclosed in a non-structural skin which reproduces the exterior geometry. A full discussion on this technique is contained in Isyumov (1982) and Alan G. Davenport Wind Engineering Group (2007).

A common approach for the aeroelastic modeling of tall buildings have historically been the use of the "skin-skeleton" type continuous equivalent aeroelastic model. This model is made of an internal equivalent structural system, referred to as "skeleton" or "spine", which is used to model the mass and stiffness properties, and a non-structural skin to maintain the overall geometry. An example of such a model is shown in Fig. 5.4. Real tall buildings generally comprise of walls and frames. Under lateral load, the walls deflect in a flexural mode, while the frames in a shear mode. Since frames and walls are tied together by rigid floors, the building deflects in a shear-flexural mode. A "skin-skeleton" model with distributed mass and stiffness can simulate this shear-flexural mode of the prototype, as illustrated in Cheong *et al.* (1992).

Section models

Section models provide a rigid representation of a portion of the structure mounted dynamically and are valuable tools to study the action of wind on slender, high aspect ratio structures, which can be referred to as line-like structures, such as long-span

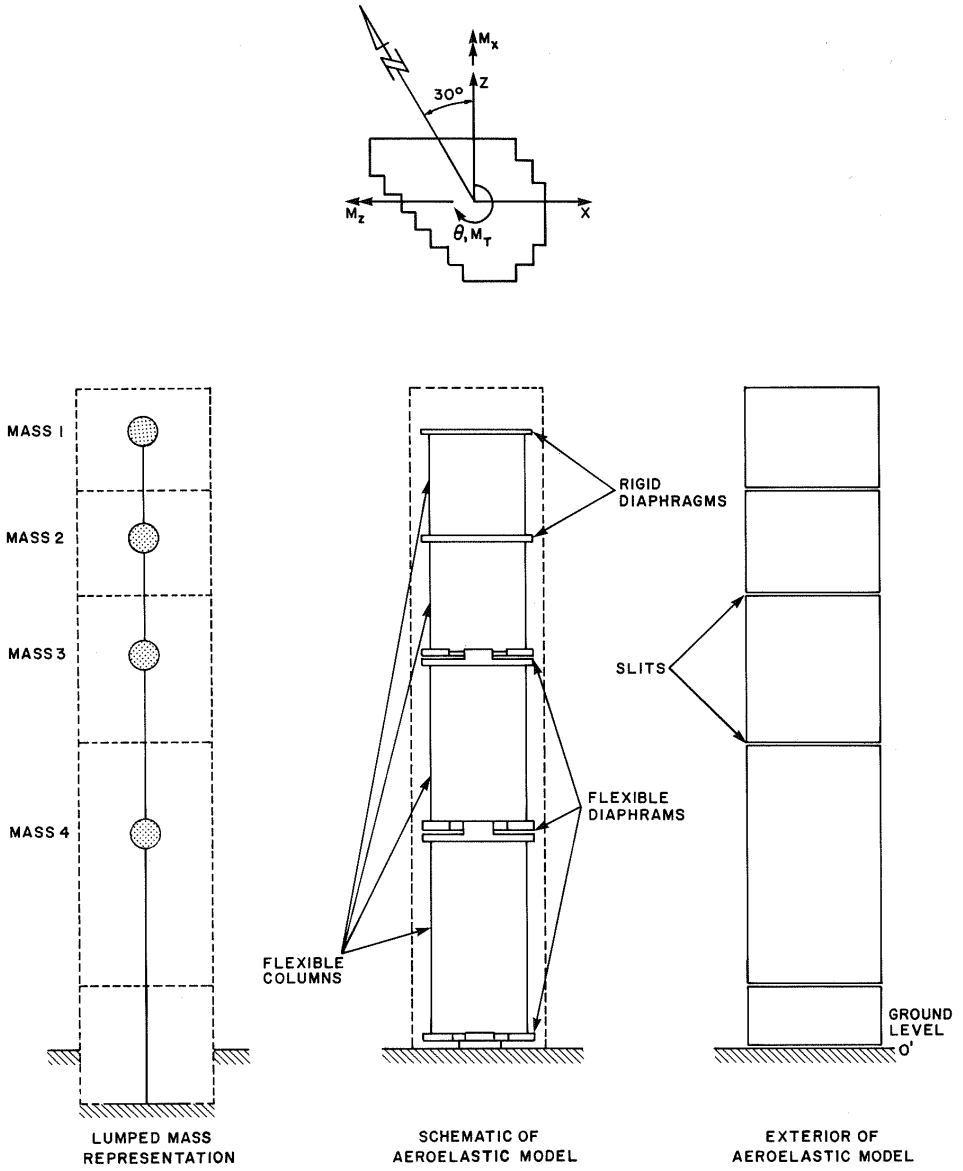

Fig. 5.3 Multi-degree-of-freedom aeroelastic model of a tall building (Isyumov, 1982).

bridges, cables and slender chimneys and towers and other structures in which the flow can be treated as two-dimensional. Typical geometric scales range from 1:10 to 1:100. A particularly important application of these models is the study of the aerodynamic stability of bridge sections. Section models are used to evaluate various aerodynamic derivatives, used in conjunction with theoretical models of the process. These models can be "driven" with controlled amplitudes and frequencies to study the effects of body motion on the aerodynamic forces. Section models are traditionally tested in smooth flow conditions. However, tests in turbulent flows generated with coarse girds or active turbulence generators can be carried out, too. A description of this technique is available in ASCE (1999).

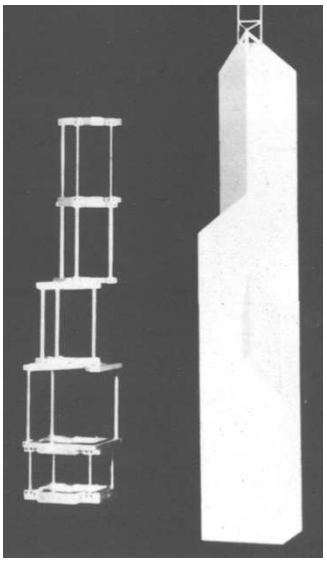

Fig. 5.4 "Skeleton" and completed aeroelastic model of Bank of China, Hong Kong (Steckley *et al.*, 1985), from Vickery (1990).

5.3.2 Scaling requirements for aeroelastic simulations of tall buildings

Unlike rigid model techniques, aeroelastic simulations provide a direct estimation of the wind-induced responses. Therefore, a direct similarity between the model and the prototype structure is a prerequisite for accurate assessment of wind effects.

Similarity requirements for aeroelastic studies are extensively treated in literature, e.g. Isyumov (1982), and based on established similarity theory (Cook, 1986). The principal requirements are:

1. similarity of the mean and turbulent characteristics of the flow;
2. geometric similarity to a scale consistent with the length scaling of the natural wind, including the depth of the boundary layer and the integral scale of turbulence;
3. similarity of aerodynamic forces (achieved by allowing for Reynolds number related differences for rounded shapes);
4. similarity of inertia forces;
5. similarity of stiffness characteristics;
6. similarity of damping.

Generally, the geometric or *length scale* of the model to the prototype, λ_l, defined as[1]:

$$\lambda_l = \frac{l_m}{l_p} \tag{5.2}$$

[1] m subscript refers to the model, p subscript to the prototype

is limited by the wind tunnel facilities and should be chosen with due regard to wind tunnel blockage. Corrections are generally required if the blockage exceeds 5%. Geometric scales of the order of 1:300 to 1:500, commonly used in aeroelastic tests, provide a representative simulation of the aerodynamic forces for sharp-edged structures.

Having selected the length scale, consistent with the length scale of the modeled wind, the similarity of the aeroelastic behavior of a sharp-edged building is achieved by maintaining equality of the following non-dimensional quantities in model and full scale:

$$\text{density ratio} = \frac{\rho_b}{\rho} \tag{5.3}$$

$$\text{elastic forces} = \frac{E}{\rho U^2}, \frac{G}{\rho U^2} \tag{5.4}$$

$$\text{damping ratio} = \xi_s \tag{5.5}$$

where ρ_b, ρ, E, G, U and ξ_s are, respectively, the bulk density, the air density, Young's modulus, the torsional modulus, the wind speed and the structural damping, expressed as a proportion of the critical damping.

Froude number scaling is of negligible consideration for tall buildings and free standing structures, in general, where the stiffness depends predominantly on elastic forces (Isyumov, 1982).

The similarity requirement for elastic forces in Eq. (5.4) can be replaced by the *reduced frequency*, f_r, defined as:

$$f_r = \frac{fb}{U} \tag{5.6}$$

where f is the modal frequency and b indicates a dimension, that has to be the same in model and full scale for the particular modes of vibration included in the simulation.

From Eq. (5.6), the *velocity scale*, λ_U, becomes:

$$\lambda_U = \frac{U_m}{U_p} = \lambda_L \lambda_f = \lambda_L / \lambda_t \tag{5.7}$$

where λ_f and λ_t are respectively the *frequency scale* and the *time scale*, defined as:

$$\lambda_f = \frac{f_m}{f_p} \tag{5.8}$$

and

$$\lambda_t = \frac{1}{\lambda_f}, \tag{5.9}$$

respectively. Consistent with the previous definitions, the *acceleration scale* becomes:

$$\lambda_a = \lambda_L \lambda_f^2. \tag{5.10}$$

For exact scaling it would also be necessary to maintain equality of the *Reynolds number*, *Re*, defined in Eq. (3.12). Reynolds similarity is not practical to be met as full scale Reynolds numbers are typically two or three orders of magnitude greater than those achieved in low speed wind tunnels. Although Reynolds number similarity is of primal importance for rounded shapes, where the location of flow separation from the curved surface is dependent on Reynolds number, it is less significant for sharp edged bodies, where flow separation tends to occur at the building corners (see chapter 3). Therefore, the influence of Reynolds number on the overall flow around buildings is, in general, considered not significant, especially in turbulent boundary layer flows.

Eqs. (5.3)-(5.5) define, in the most general form, the scaling requirements for the proper modeling of the oscillatory behavior of a structure. However, difficulties in the realization of aeroelastic models arise from the following causes (Scruton, 1981):

- the model does not replicate the correct structural damping and the structural damping characteristics on full-scale structures are generally unpredictable;
- it is usually not possible to build replica models using materials with the physical properties required by the similarity requirements.

Therefore, scaling rules are never exactly met. When dealing with aeroelastic simulations, elastic forces can be scaled according to the similarity requirement on reduced frequencies previously mentioned, while similarities on mass and damping characteristics can be expressed by means of the *Scruton number*, *Sc*, also known as "mass-damping parameter" (Holmes, 2001), defined as [see also Eq. (4.3)]:

$$Sc = \frac{2\delta_s m_{i,e}}{\rho b^2} \tag{5.11}$$

Reduced frequency and Scruton number have to be equal in model and full scale for those modes of vibration included in the simulation.

5.4 Summary and main remarks

This chapter reviews the main aspects of the wind tunnel experimental techniques in common use. With rigid model techniques, the responses are derived theoretically from aerodynamic loads, neglecting motion-induced forces. The use of aeroelastic models allows, on the other hand, the direct measurement of responses, inherently including additional effects of the motion-induced forces, which can be significant for some lightweight and lightly damped structures.

Aerodynamic loads may be obtained from rigid models by using different methods, basically corresponding to High Frequency Force Balance (HFFB) technique and integration of pressures, known as Synchronous Multi-Pressure Sensing System (SMPSS) technique. The main advantages and drawbacks of these two methods are discussed. The three base moments measured by a HFFB coincide with the first three generalized forces in the particular case of a system exhibiting uncoupled and linear mode shapes. Using the pressure measurements technique, a single model can be used for both overall structural loads and cladding loads, and the generalized forces can be properly evaluated also for three-dimensional non-linear mode shapes. However, the SMPSS technique typically includes more instrumentation and longer

model construction times.

Aeroelastic models, falling in the category of direct modeling techniques, replicate the deformation and motion of prototype structures in a simulated flow field. Listed in decreasing order of design and construction complexity, aeroelastic simulations include replica, equivalent and section model techniques. Equivalent models range form the "stick" type model, to the more complex multi-degree-of-freedom and continuous "skin-skeleton" type models. Several similarity requirements for aeroelastic studies have to be satisfied for the accurate assessment of wind effects. Such studies must model the properties of the natural wind flow and the aerodynamic features of the exterior geometry, but have also to simulate the stiffness, mass and damping properties of the prototype structure.

Chapter 6

Wind tunnel tests

6.1 Introduction

As explained in the previous chapter, if properly carried out, aeroelastic simulations provide the most complete characterization of the structural responses due to the wind action. An accurate knowledge of these responses, including the effects of possible motion-induced forces, is of primary importance for the serviceability design of tall buildings.

In this research a continuous equivalent aeroelastic model of a regular square-section tall building is built and tested in the wind tunnel in turbulent flow conditions.

A quite complex wind tunnel setup is adopted in order to carry out the simultaneous measurement of pressures, overall forces, across-wind displacements and along-wind and across-wind accelerations for a wide range of wind speeds including the lock-in critical wind speed condition.

The first two sections (6.2 and 6.3) of this chapter are dedicated to the description of the boundary later wind tunnel where the experimental activity is carried out and of the instrumentation used.

Section 6.4 describes the aeroelastic model tested in this research and includes a discussion about how the model geometry is designed on the basis of the experimental purposes. The principal stages of the assembly of the model are illustrated and the identification of its dynamic properties through free vibration tests is described.

Section 6.5 is devoted to the analysis of the simulated flow conditions. The experimental setup adopted and the instrumentation equipment of the model are shown in section 6.6.

The main results of this experimental activity include: the identification of the Strouhal number (section 6.7), the spectral analysis of the response (section 6.8), from which the identification of the lock-in range (section 6.9) and the analysis of modal frequencies (section 6.10) are carried out, the correlation analysis of the pressure-coefficients on the side-faces (section 6.11) and the analysis of the displacement (section 6.12) and acceleration (section 6.13) responses.

The overall forces from HFFB and SMPSS measurements are also analyzed and compared (section 6.14).

6.2 Wind tunnel description

The experimental activity is entirely carried out in the CRIACIV[1]-DICEA[2] Boundary Layer Wind Tunnel (BLWT), located in Prato, Italy (Fig. 6.1). Its technical characteristics are shown in Fig. 6.2.

It is an open-circuit suction-type wind tunnel with a convergent nozzle for the flow acceleration and a T-shaped symmetric diffuser. The total length is about 22 m. The cross-section slightly diverges from a width of 2.20 m and a height of 1.60 m at the inlet to a width of 2.42 m and a height of 1.60 m at the test section, allowing constant pressure along the axis.

The wind flow is generated by an axial fan, placed downstream of the test section, ensuring that the turbulence generated by the fan does not contaminate the flow.

The total length of the developing fetch is 8 m, while the length of the test section is 2.4 m. At the inlet the flow is regularized by a 5 cm thick honeycomb panel, followed by a squared mesh screen.

The growth of the boundary layer in the wind tunnel can be artificially developed through the use of *spires* and *Counihan devices*, which produce an immediate velocity gradient downstream, and which develop into a mean velocity profile representative of that in the atmosphere within a short downstream distance, and *roughness elements* on the floor of the wind tunnel aimed to increase the turbulence intensities on the basis of the full-scale values.

The wind speed, ranging from 0 to approximately 30 m/s, is regulated by both adjusting the pitch of the 10 blades of the fan and regulating the number of engine turns through an inverter. The fan has a power of 158 kW and is equipped with a servomotor for controlling the continuity of the flow. An elastic joint is placed between the test section and the axial fan, to isolate the former from the vibration produced by the propeller system. The exit of the flow is regularized by a T-shaped symmetric diffuser which minimizes the loss of pressure.

The tunnel is equipped with a turning table at the test section, which enables the incident wind direction to be changed with respect to the orientation of the model mounted on it.

6.3 Measurement instrumentation

6.3.1 Pitot tubes

The Pitot tube, consisting in a tube pointing directly into the fluid flow, allows the measurement of both the *stagnation pressure*, also known as the *total pressure* or (particularly in aviation) the *pitot pressure* and the *static pressure*. From the mean dynamic pressure, which is measured form the difference between the stagnation pressure and the static pressure, the mean wind speed can be derived.

During the experimental activity in the CRIACIV Wind Tunnel, 2 Pitot tubes are used. For the signals acquisition, the instruments are connected to a pressure

[1]Centro di Ricerca Interuniversitario di Aerodinamica delle Costruzioni e Ingegneria del Vento (Interuniversity Research Center of Building Aerodynamics and Wind Engineering). Web site: `www.criaciv.unifi.it`

[2]Dipartimento di Ingegneria Civile e Ambientale (Department of Civil and Environmental Engineering)

Fig. 6.1 View of the CRIACIV-DICEA Boundary Layer Wind Tunnel in Prato.

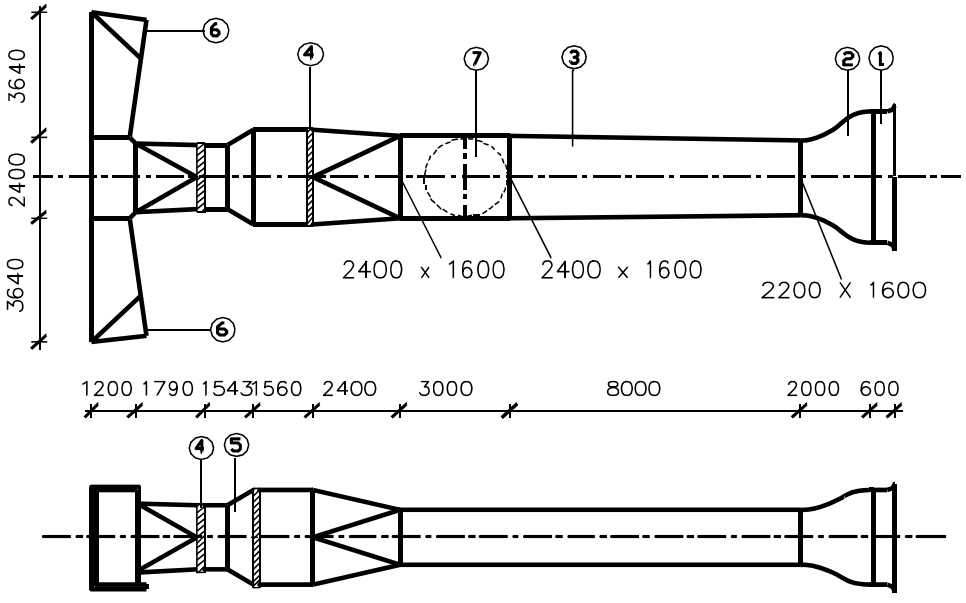

Fig. 6.2 Sketch of the CRIACIV-DICEA Boundary Layer Wind Tunnel: 1. Inlet with honeycomb grid; 2. Contraction; 3. Boundary Layer development zone; 4. Elastic joint; 5. Propelling System (160 kW); 6. Diffuser; 7. Test section with turning table.

Fig. 6.3 Pressure acquisition system PSI 8400.

transducer (Setra System, model 239), then the signal is converted by 32-bit NI card and finally is acquired by a PC.

6.3.2 Two-components hot-wire anemometer

A two components hot-wire anemometer is used to measure the characteristics of the incoming flow in the wind tunnel.

The hot-wire anemometer allows the measurement of the component of the instantaneous wind speed in the plane perpendicular to the wire. It is a thermic transducer with a platinum plated tungsten wire sensor. Electricity warms the sensor up by Joule effect, whereas air flowing past the wire has a cooling effect on the wire by convection. Since the electrical resistance is dependent upon the temperature of the metal, a relationship can be obtained between the resistance of the wire and the flow speed.

6.3.3 Pressure Transducers

Pressure measurements (SMPSS technique, see subsection 5.2.2) are performed by means of a PSI 8400 system by Pressure System (Fig. 6.3). The CRIACIV BLWT is equipped with four acquisition units having 16 piezoelectric transducers each (Fig. 6.4) and two acquisition units having 32 transducers each, so that a total amount of 128 pressures can be recorded simultaneously.

Dynamic pressures can be measured with a sampling frequency up to 1 kHz. The number of acquisition channels used is inversely proportional to the sampling frequency. For example, for the maximum number of pressure signals that can be contemporary measured (128 channels), the sampling frequency decreases to 250 Hz per channel.

Owing to their small dimensions ($13 \times 21.5 \times 69$ mm^3 for the 16-channel type and $26 \times 21.5 \times 69$ mm^3 for the 32-channel type), the PSI scanners can also be located inside the models.

Prior to the pressure data acquisition, the transducers calibration has to be performed, since piezoelectric transducers display drift effects and could be significantly affected by temperature variations. Once defined the expected pressure range,

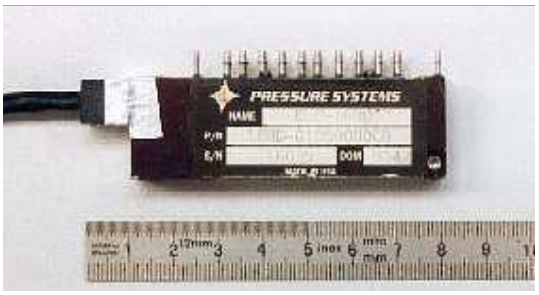

Fig. 6.4 Pressure transducer.

the calibration is performed through a dedicated PCU, which sends five reference pressures, within the estimated range, to each transducer, then acquires the corresponding voltage values and, finally, interpolates these values with a fourth degree polynomial. This system allows pressure measurements in the range of [-254;+254] mm H_2O. The accuracy of the calibration procedure is 0.05 % of the maximum allowed pressure. The maximum error affecting the measured dynamic pressure values 0.2% of the the maximum allowed pressure (full scale) and is equal to:

$$err_{max} = 0.2\% \cdot 254 \approx 0.5 \text{ mm } H_2O \tag{6.1}$$

When, owing to the small dimensions of the model tested, it is not possible to accommodate the sensors within the model, the pressures acting on the model surface must be transmitted to the sensor without distortions. The transmission is carried out through small highly flexible plastic tubes, manufactured in silicone or teflon. To allow the pressures to be transmitted without distortions, each transmission tube is equipped with a damper, which is obtained by a contraction of the tube diameter (Fig. 6.5). The system constituted by tube and damper is properly calibrated so that its frequency response does not influence the pressure measurements. The resulting calibrated tube-damper system, used for this research, is that illustrated in Fig. 6.5, where the total length, L1 + L2 + L3, is 500 mm, L3 is equal to 115 mm and the damper is 20 mm long. The inner diameter of the pneumatic tube is 0.8 mm while that of the damper is 0.3 mm.

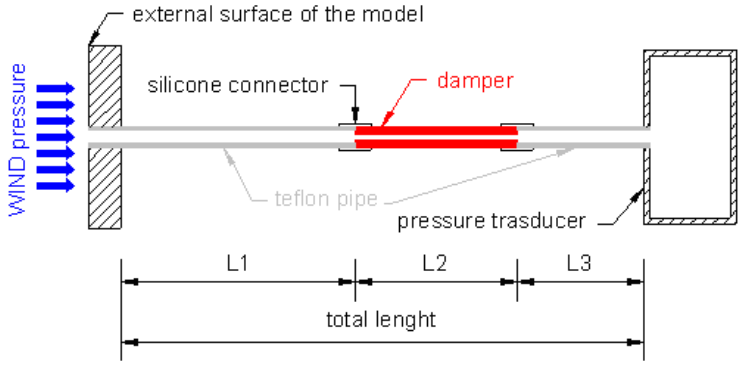

Fig. 6.5 Sketch of the tube-damper system for the transmission of pressures from the model surface to the pressure transducer.

6.3.4 High Frequency Force Balance

A 5-component strain gauged balance (HFFB - High Frequency Force Balance), model FDC 010, manufactured by Metior S.r.l., Como, Italy (`www.metior.it`), is used (Fig. 6.6). It allows the measurement of 2 shear forces, F_x, F_y, 2 bending moments, M_x, M_y, along two orthogonal directions, and of the torque component, M_z (see Fig. 6.7). The capacity and accuracy of the balance corresponding to the different components are reported in Table 6.1.

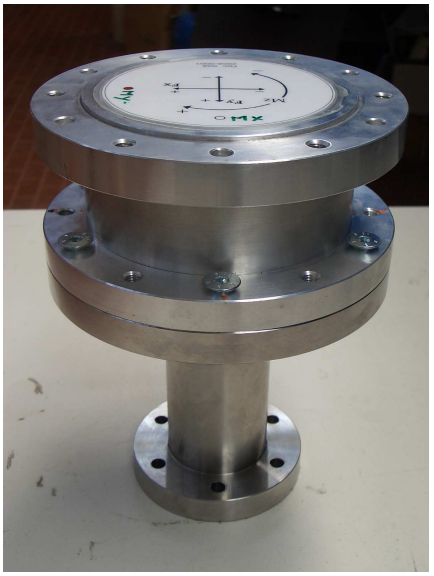

Fig. 6.6 High Frequency Force Balance.

Table 6.1 HFFB capacity and sensitivity.

	Capacity	Sensitivity
F_x	10 kg	0.185 mV/V
F_y	10 kg	0.185 mV/V
M_x	5 kgm	0.270 mV/V
M_y	5 kgm	0.270 mV/V
M_z	5 kgm	0.270 mV/V

6.3.5 Displacement Transducers

Three non-contact optical laser transducers (Micro-epsilon Model OptoNCDT 1605) are available to determine the displacements of the model [Fig. 6.8(a)]. These lasers use a semiconductor with 675 nm wavelength and a maximum output power of 1 mW and their functioning principle is based on triangulation. The output voltage range is ±10 V which corresponds to a displacement of roughly ±100 mm. The lasers are connected to a PC acquisition card. The characteristics of the lasers are reported in Table 6.2. The actual linearity of these transducers and their conversion factor

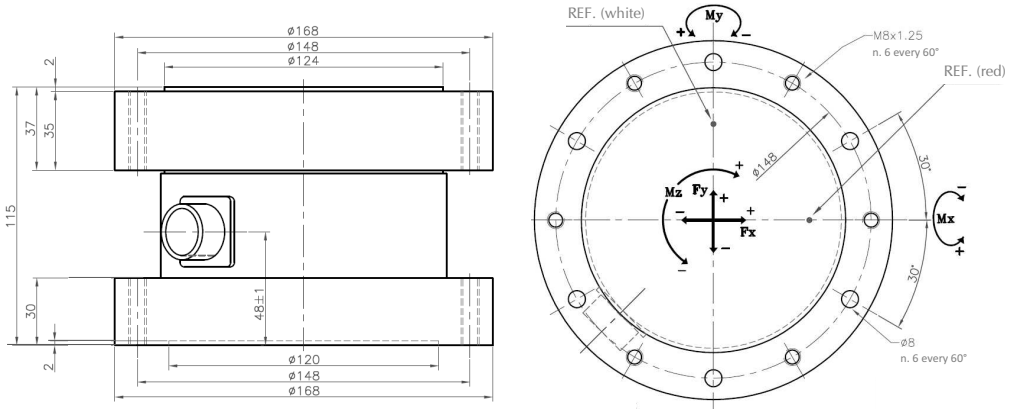

(a) (b)

Fig. 6.7 High Frequency Force Balance technical drawing: a) side view; b) plan view.

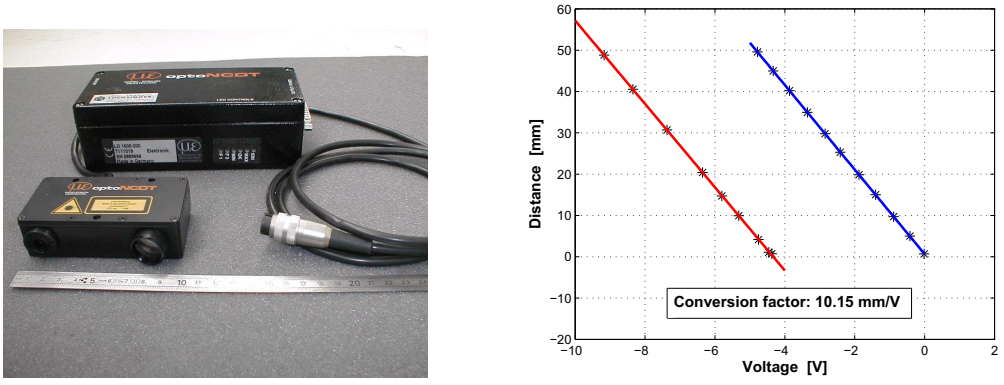

(a) (b)

Fig. 6.8 Micro-epsilon Model OptoNCDT 1605 laser tranducer: a) View of a laser triangulator device for displacement measurement; b) Relationship between laser output voltage and actual object distance (laser 1).

is checked for each laser by means of a high precision mechanical distantiometry [Fig. 6.8(b)].

Table 6.2 Micro-epsilon Model OptoNCDT 1605 laser characteristics.

Sensor type	Laser-Sensor
Model	LD 1605
Type	200
Measuring range	±100 mm
Stand-off midrange	340 mm
Non-linearity $\leq \pm 0.3\%$ d.M.	600 μm
Resolution (noise) static	60 μm
Measuring spot dia. midrange	2 mm
Light source	Laser 1 mW, wavelength:red 675 nm
Sampling frequency	40 kHz
Laser class	2
Analogical output	
Displacement	±10 V
Output impedance	appr. 0 Ohm (10 mA max.)
Angle dependence	appr. 0.5% when turning ±30 about long.axis
Rise time	0.1/0.2/2 or 20 msec selectable
Frequency response	10 kHz, 3 kHz, 250 Hz or 25 Hz
Temperature stability	0.03%/K
Intensity of reflecting light	1 V bis 10 V/max; 0 V bis +13 V
Permissible ambient light	20000 Lux
Life time	50000 h for laser-diode
Insulation	200 VDC, 0 V against housing
Max. vibration	10 g to 1 kHz
Operation temperature	0 to 50 ℃

6.3.6 Accelerometers

A set of 4 mono-axial ICP® accelerometers (Fig. 6.9) produced by PCB Piezotronics, model 352C42, is used. Their technical characteristics are illustrated in Table 6.3.

6.4 The model

6.4.1 Design of the model

The equivalent continuous aeroelastic model (Fig. 6.10) used in this research is designed and built in order to simulate the dynamic response of a regular square-section tall building (the *side ratio*, defined as depth, d, over breadth, b, is equal to 1), which was previously tested in the wind tunnel using a rigid model (Spence, 2009). Its *aspect ratio*, defined as height, h, over breadth, b, is equal to 6. The choice of this dimensional proportion is also motivated by the richness in literature works on models with the same aspect ratio value [see, for example, Marukawa *et al.*

Table 6.3 Model 352C42 Accelerometer characteristics.

Performance	
Sensitivity (±10%)	10.2 mV/(m/s^2)
Measuring range	±491 m/s^2
Frequency range (±5%)	1.0 to 9000 Hz
Frequency range (±10%)	0.5 to 10000 Hz
Frequency range (±3 dB)	0.3 to 15000 Hz
Resonant frequency	≥ 30 kHz
Broadband resolution (1 to 10000 Hz)	0.005 m/s^2 rms[a]
Non-linearity	≤ 1%[b]
Transverse sensitivity	≤ 5%[c]
Environmental	
Overload limit	±49050 m/s^2 pk
Temperature range	-54 to +121 °C
Temperature response	see Fig. 6.9(b)[a]
Electrical	
Excitation voltage	22 to 30 VDC
Constant current excitation	2 to 20 mA
Output impedance	≤ 200 Ohm
Output bias voltage	8 to 15 VDC
Discharge time constant	0.5 to 2.0 sec
Settling time (within 10% of bias)	≤ 10 sec
Spectral noise (1 Hz)	1177 (μm/sec^2)/$\sqrt{Hz}$[a]
Spectral noise (10 Hz)	294 (μm/sec^2)/$\sqrt{Hz}$[a]
Spectral noise (100 Hz)	196 (μm/sec^2)/$\sqrt{Hz}$[a]
Spectral noise (1 kHz)	59 (μm/sec^2)/$\sqrt{Hz}$[a]
Physical	
Sensing element	Ceramic
Sensing geometry	Shear
Housing material	Titanium
Sealing	Welded hermetic
Size (Hex x Height)	9.7 mm x 9.7 mm
Weight	2.8 gm[a]
Electrical connector	10-32 Coaxial jack
Electrical connection position	Top
Mounting	Adhesive

[a] Typical
[b] Zero-based, least-squares, straight line method
[c] Transverse sensitivity is typically ≤ 3%

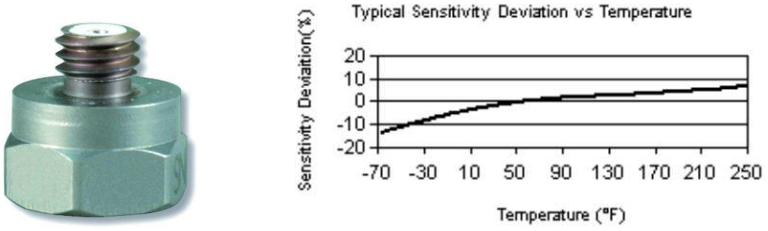

(a) (b)

Fig. 6.9 PCB Piezotronics Mod. 352C42 accelerometer: a) photo; b) temperature response.

(1996); Kijewski and Kareem (1998)]. The overall dimensions of the model, which replicate those of the rigid one, are 10.5 cm × 10.5 cm × 60.8 cm.

The model is a continuous "skin-skeleton" type aeroelastic model (see subsection 5.3.1). The external non-structural "skin", used to maintain the overall geometry and the aerodynamic forces is made of plexiglas. The internal structure, the "skeleton", is made of 4 continuous aluminum bars [Fig. 6.11(a)]. For the aluminum bars to move freely without any constraint from the outer shell, the latter is divided into three separate boxes [Fig. 6.11(b)]. Each box is made of 4 sides and one horizontal floor on the top, glued together. The internal structure and the external boxes are connected together at the three rigid horizontal floors, placed at 1/3 h, 2/3 h and at the top [Fig. 6.11(c)], thus replicating the typical outrigger-braced system used in many buildings (McNabb and Muvdi, 1975; Stafford Smith and Coull, 1991).

The geometry of the different components of the model and the position of aluminum bars within the outer shell is decided on the basis of the testing purposes as explained in the following paragraphs.

The design and building of the model have resulted in a quite complicated stage

(a) (b)

Fig. 6.10 The aeroelastic model: a) global view; b) plan view.

of the work. The reason for this lies in the quality and number of measurements that have been intended to be performed simultaneously. As a matter of fact, the major effort of the experimental activity has set to be the simultaneous measuring of:

1. pressures on the model surface,

2. overall forces and moments,

3. across-wind displacement response,

4. along-wind and across-wind acceleration responses,

in order to have an experimental characterization of the loads and responses of the model as complete as possible, even in lock-in conditions.

The measurement of pressures, using the maximum number of simultaneously measuring pressure taps allowed by the instrumentation capabilities, equal to 128 (see subsection 6.3.3), has led to the need to have a proper distribution of holes on the building surface, a proper path of the pneumatic tubes from the building sides to the pressure transducers and an adequate internal space to allow the casing of the pressure transducers. The last requirement is motivated by the need to avoid the employment of long tubes to limit as much as possible errors in the measurement of fluctuating pressures. As described in subsection 6.3.3, 50 cm long tubes are used in this work.

For the measurement of overall forces and moments a High Frequency Force Balance (subsection 5.2.1) is used. Hence the need to install the model over a supporting system which allows the connection with the balance.

One major purpose of the experimental activity is to measure the model response in lock-in conditions. The achievement of the critical wind speed in the wind tunnel is possible only designing the frequency of the model so that the critical velocity (see section 4.3):

$$U_{crit} = \frac{b f_n}{St} \tag{6.2}$$

where b is the side dimension of the model, f_n is the natural frequency and St is the Strouhal number, falls within the wind tunnel wind speed range, defined by the wind tunnel capabilities illustrated in section 6.2.

On the basis of these considerations, the geometry of the external and internal components of the model is set, even with the help of a simplified finite element model which enables a first control of the frequencies of the model. However, because of the complexity of the model and of the connections between the different components and with the real supporting system, the actual frequencies can be determined only through dynamic identification of the real model mounted in the wind tunnel (see subsection 6.4.3).

Fig. 6.12 illustrates the dimensional drawing of the model with the geometrical characteristics of the internal structure and of the outer shell.

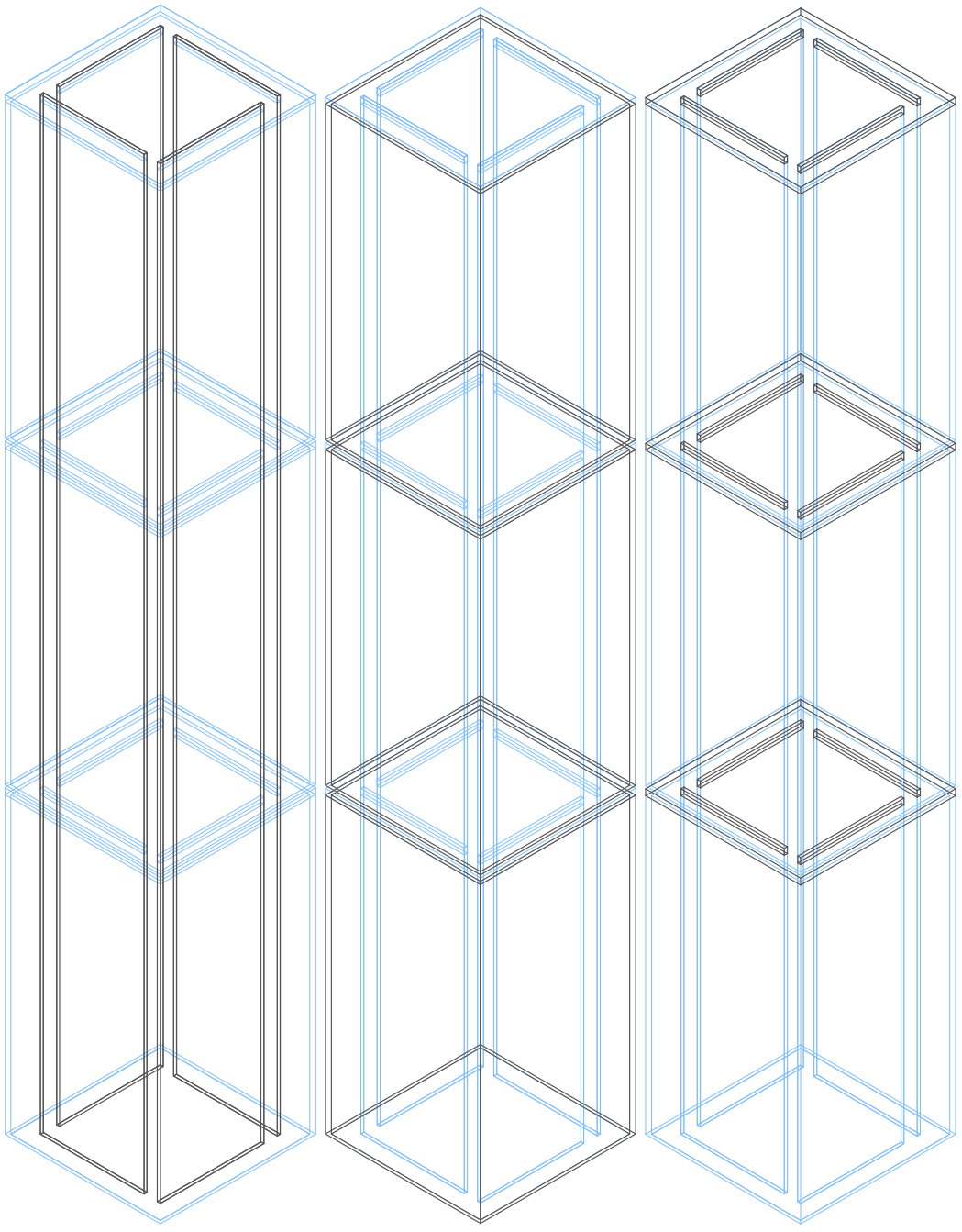

(a) (b) (c)

Fig. 6.11 3D sketch of the model: a) the “skeleton”; b) the “skin”; c) rigid floors.

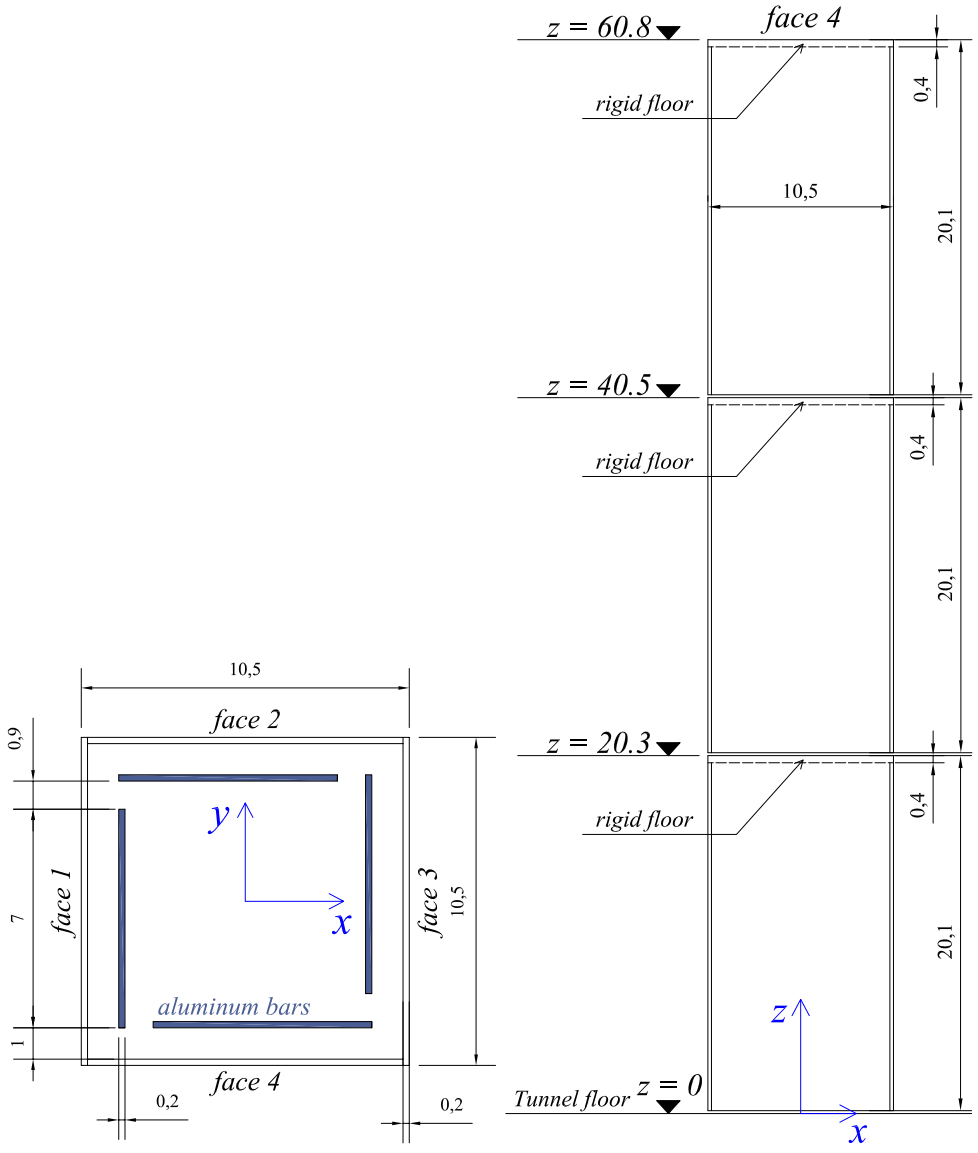

Fig. 6.12 Dimensional drawing of the model: a) plan view; b) side view (face 4).

6.4.2 The assembly of the model

Each side of the three external boxes, of 2 mm thickness, is equipped with the pneumatic tubes [Fig. 6.14(a)], according to the pressure tap distribution reported in Fig. 6.13. As explained later (see subsection 6.7.1), the total number of pneumatic tubes connected to the model outer surfaces is 126. Pressure taps are distributed on 8, approximately equally spaced, different levels whose height over the tunnel floor is reported in Fig. 6.13. As described in subsection 6.3.3, the pneumatic tubes

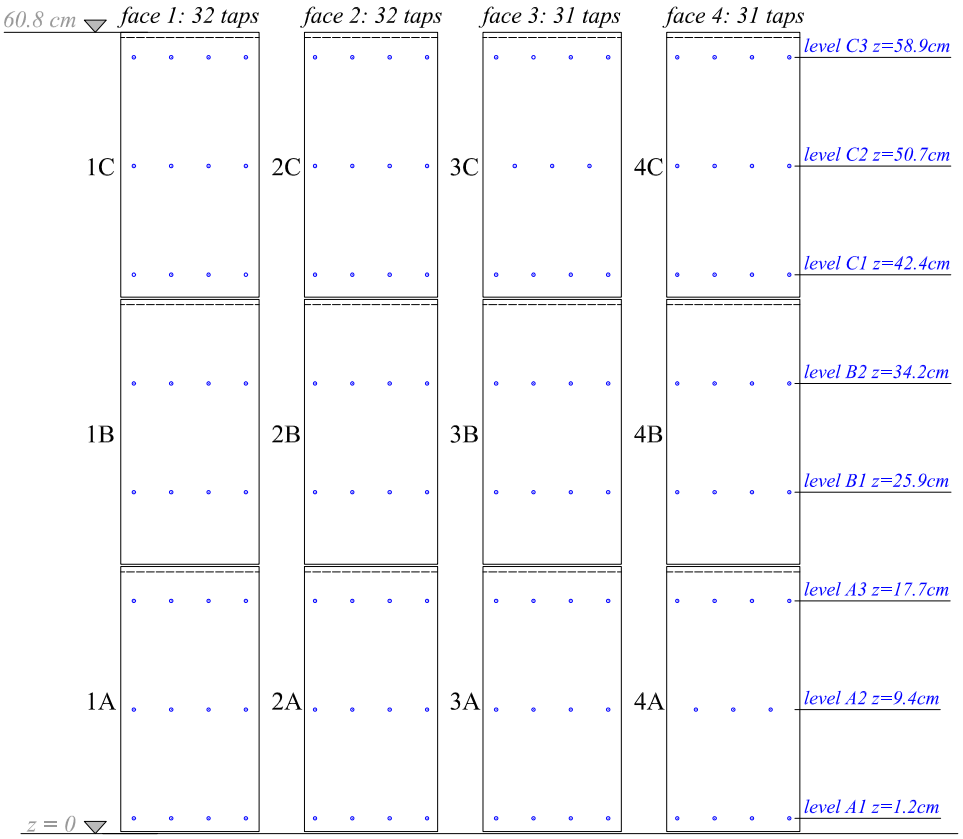

Fig. 6.13 Pressure taps distribution on the model surface.

have a total length of 50 cm, but their are divided in two parts, connected by a 2 cm long damper. As a consequence, the first part of each tube is glued to the model, the other part is installed to the PSI unit. The plexiglas, 4 mm thick, square plates constituting the horizontal floors are shaped with laser cuts in order to have 4 rectangular holes through which the continuous aluminum plates can be threaded. The four sides of each box are glued together and with one floor at the top. At this stage, the principal elements constituting the model, corresponding to the 4 plates and the three boxes are weighted [Fig. 6.14(b), Fig. 6.14(c), Fig. 6.14(d), Fig. 6.14(e)].

As shown in Fig. 6.13, the three boxes are referred to with the letters A, B and C, from the bottom to the top and each side with a number from 1 to 4, indicating the face of the model.

A preliminary mounting of the model outside the wind tunnel is performed. For the connection between the internal structure and the outer shell, a system of aluminum L-shape elements and screws is designed and realized (Fig. 6.15).

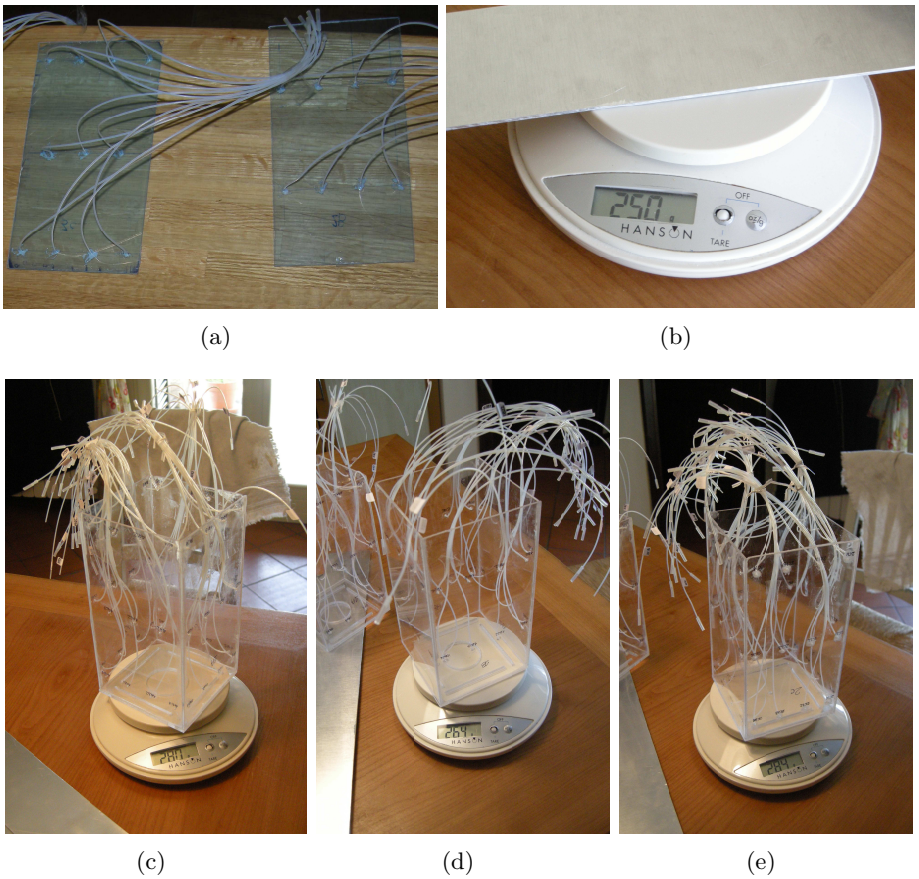

(a) (b)

(c) (d) (e)

Fig. 6.14 Assembly of the model. First stage. a) pneumatic tubes glued on plexiglas surfaces; b) one aluminum plate weight; c), d), e) assembled plexiglas boxes and their total weight.

A wooden supporting system, visible in Figs. 6.15(e), 6.15(f), 6.16(b) and 6.16(c), is built in order to accommodate the aluminum bars in it and to provide a proper connection with the base balance. The wooden support is made of a prismatic core with a central circular hole with vertical axis and two horizontal lateral holes allowing the exit of the pneumatic tubes from the internal gap to below the tunnel floor. The presence of the two horizontal holes under two parallel faces (2 and 4) is responsible for a geometric asymmetry which translates into different stiffnesses in the two orthogonal directions.

The central prismatic core is connected to a circular disk at the bottom, which will be directly fixed to the balance and a second circular disk at the top, whose function will be only to close the hole on the tunnel floor between the lateral surfaces of the model and the circular plug of the floor which will be mounted in the test section (see Fig. 6.32). The overall thickness of the wooden support is approximately equal to 5 cm.

Since the outer shell is made of separate boxes, there are small slits between them. In order to prevent air from entering the model during wind tunnel tests, self adhesive felt strips [Fig. 6.15(e)] are glued at the top of box A and box B and on the support surface [Fig. 6.15(f)].

In order to perform wind tunnel tests, the model is mounted in the test section of the wind tunnel (Fig. 6.16). Fig. 6.16(a) shows the pneumatic tubes connections from the boxes sides to the pressure transducers. The 4 aluminum plates are first installed on the wooden support. The first box (box A) is positioned sliding from the top of the plates. The plates are inserted through the floor of the first box paying attention to the passage of the pressure tubes from the external faces, where they are fixed, to the interior area through the free spaces between the plates at the corners. The 47 pneumatic tubes of the first box are pulled outside from the model support and connected to three 16-channel type pressure transducers below it. The position of the first box with respect to the internal structure is fixed trough L-shaped aluminum elements and screws. The second box (box B) is then placed in its position [Fig. 6.16(b)], repeating the procedure illustrated for the first one. However, in this case, the 32 tubes on the box B surfaces are connected with one 32-channel type PSI unit, which is left inside the model. Finally, box C is inserted from the top [Fig. 6.16(c)]. Its 47 tubes are connected with one 32-channel type and one 16-channel type PSI units, both placed inside the model.

Finally, the model with its wooden support is installed on the balance which is mounted over the tunnel steel tripod, whose height is properly regulated in order to align the model basis to the tunnel floor.

Each pressure tap is identified with a 4-character code, “FBLN”, where:

1. F=1,2,3,4 indicates the *Face* number;
2. B=A,B,C denotes the *Box*, from the bottom to the top;
3. L=1,2,3 is the *Level* (each box has up to three levels of taps);
4. N=1,2,3,4 is the *Number* which indicates the horizontal position of the tap from the left to the right side (each level has up to 4 taps per each side).

Tap 4A31 is, for example, the first tap to the left side of the third level of box A on face 4.

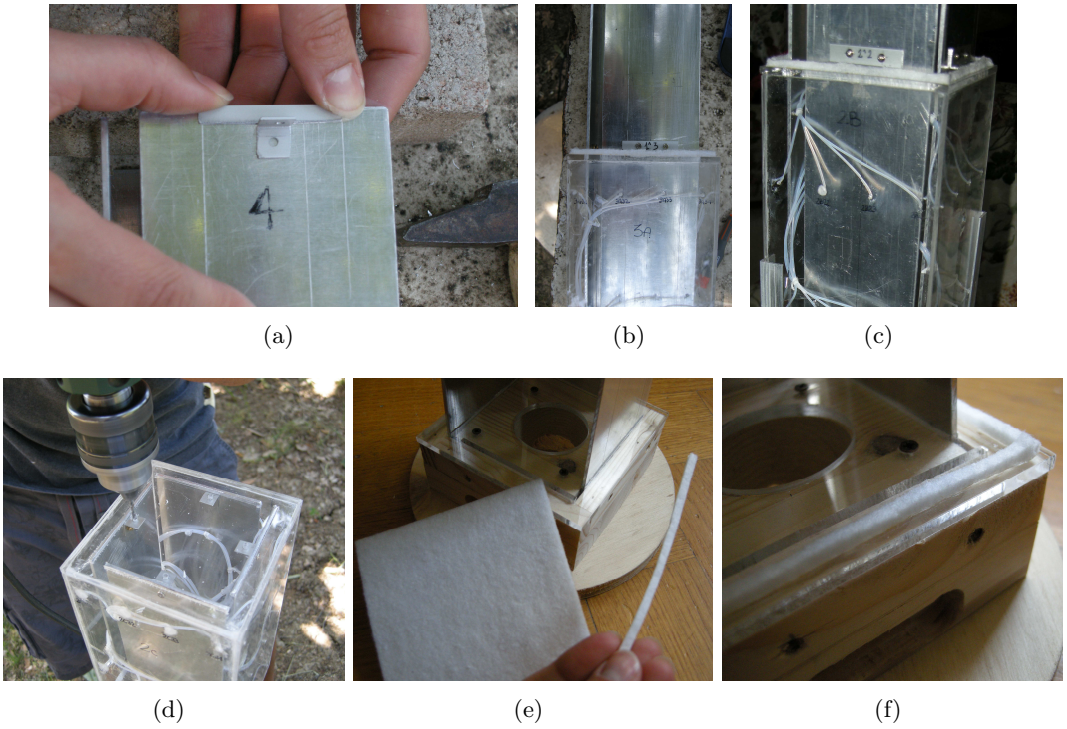

Fig. 6.15 Model construction details: a) L-shaped aluminum element for the connection between the aluminum plates and the top floor; b) connection between the plates and the first box from the bottom (box A); c) connection between the plates and the second box (box B); d) connection between the plates and the box at the top (box C); e) self adhesive felt sheet; f) self adhesive felt strips mounted on the support surface at the level of the tunnel floor.

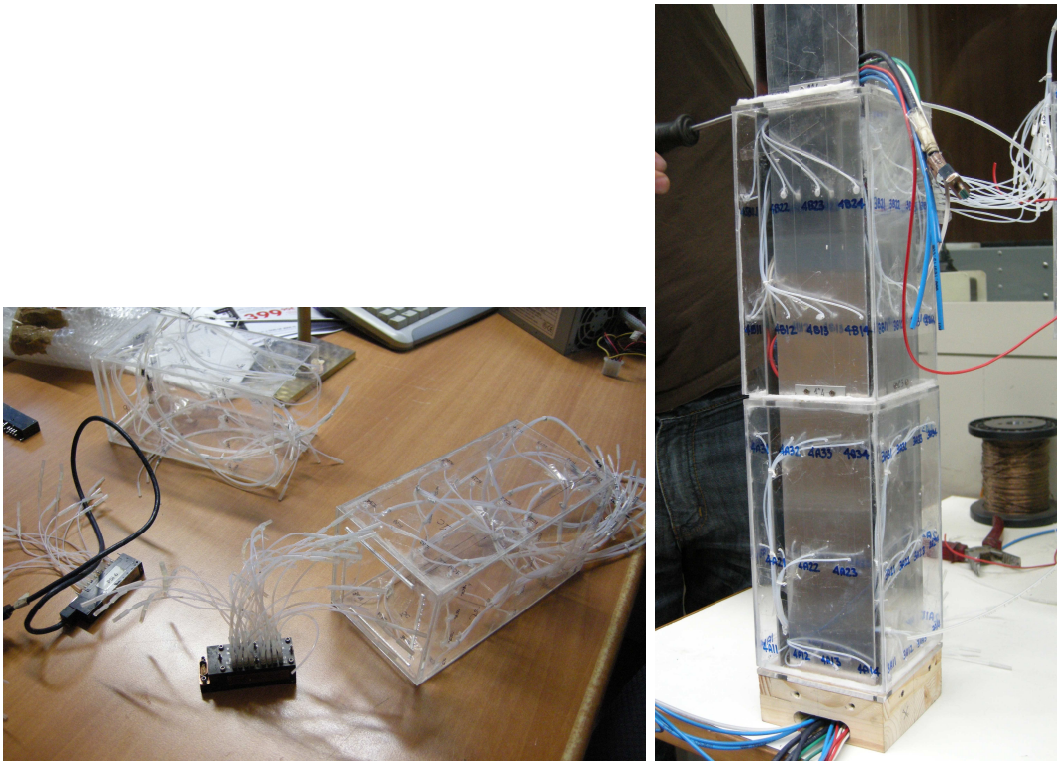

(a) (b)

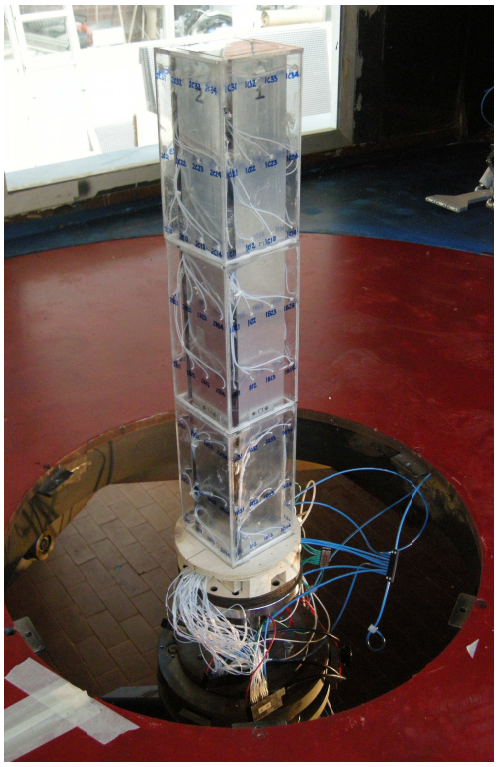

(c)

Fig. 6.16 Assembly of the model in the wind tunnel: a) pneumatic tubes connections from the boxes sides to the pressure transducers; b) box A and box B mounted; c) view of the model completely assembled and mounted in the test section of the wind tunnel.

6.4.3 Identification of dynamic properties

The natural frequencies and mode shapes of the model-support system are measured by means of four mono-axial accelerometers (their technical characteristics are illustrated in subsection 6.3.6). Two configurations are used in order to measure the free vibration response of the model along two orthogonal directions. Once they are mounted on face 4 (Fig. 6.17) and once on face 3 (Fig. 6.18). In both cases, three of them are placed along the mid axis of the model face, while one is eccentric. The model is then excited with both symmetric and eccentric impulsive excitations.

From the peaks of the power spectral density, S, of the measured acceleration

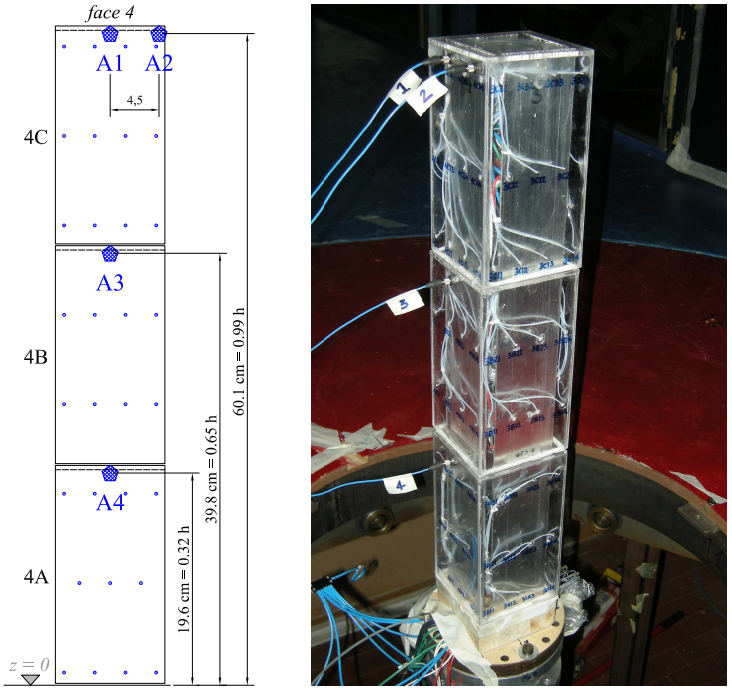

(a) (b)

Fig. 6.17 Distribution of the accelerometers on the face 4 of the model: a) dimensional drawing; b) view from the wind tunnel.

signals (Fig. 6.19 and Fig. 6.20), the first three natural frequencies of the model are derived, corresponding to the first bending mode along the weak axis (face 2 - face 4 direction), the first bending mode along the strong axis (face 1 - face 3 direction) and the torsional mode. The presence of a weak and a strong axis related to different natural frequencies of vibration in the two orthogonal bending modes, is thought to be due to the asymmetric geometry of the model support, described in subsection 6.4.2. Moreover the complexity of the accommodation of pneumatic tubes and PSI units inside the model can also contribute to not symmetric characteristics of the model.

The free decay acceleration signals (Fig. 6.21, Fig. 6.22, Fig. 6.23) are compared with those simulated by means of the eigenvalues and eigenvectors estimated through the MULS method (Bartoli *et al.*, 2009). The latter is based on the improvement of the Unifying Least-Square (ULS) algorithm (Gu *et al.*, 2000) and is, therefore, called Modified Unifying Least-Square (MULS). This identification method is used

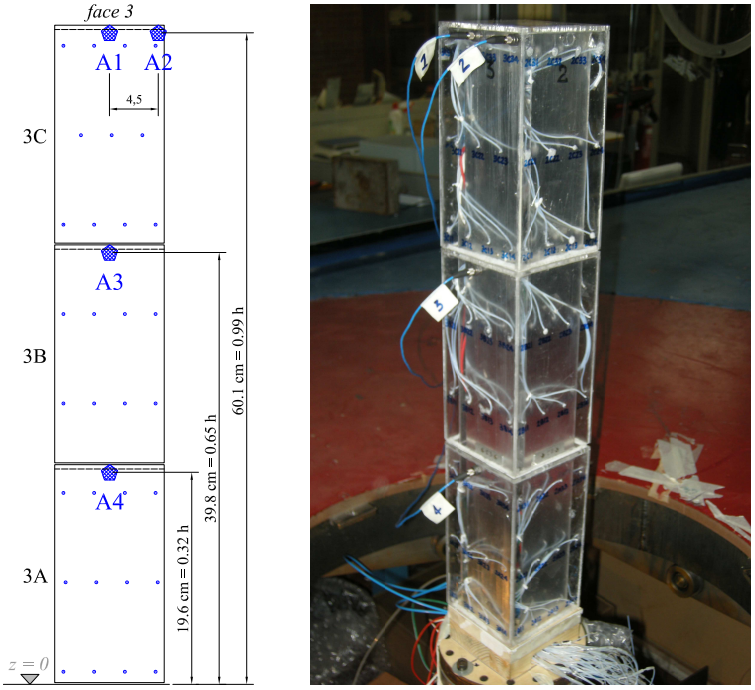

Fig. 6.18 Distribution of the accelerometers on the face 3 of the model: a) dimensional drawing; b) view from the wind tunnel.

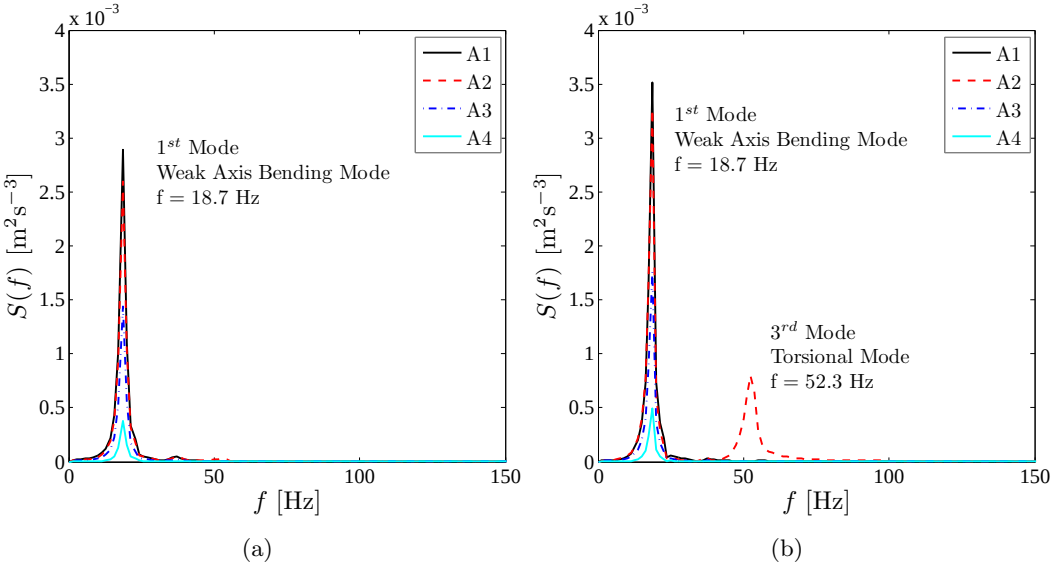

Fig. 6.19 Spectra of the measured accelerations. Free vibration response along the weak axis: a) symmetric excitation; b) eccentric excitation.

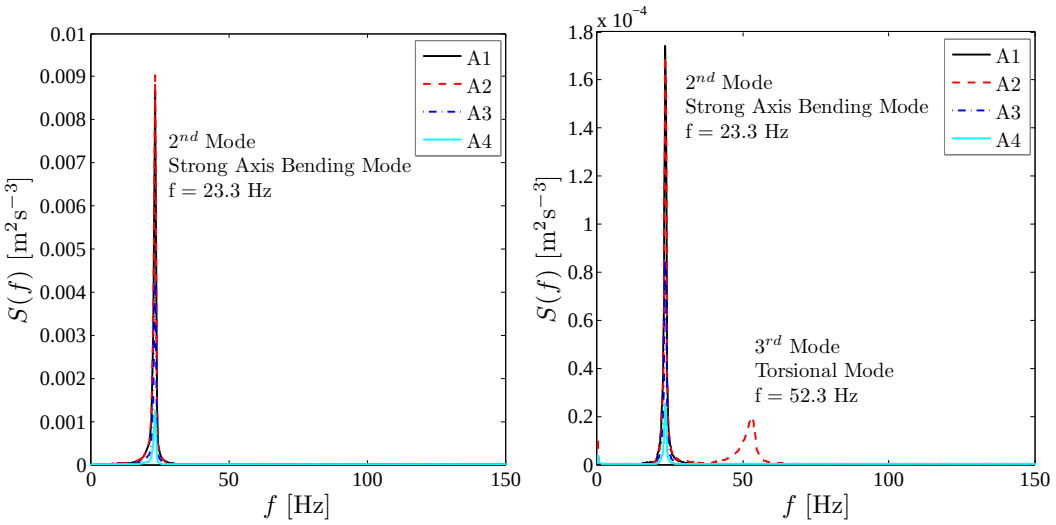

Fig. 6.20 Spectra of the measured accelerations. Free vibration response along the strong axis: a) symmetric excitation; b) eccentric excitation.

to confirm the natural frequencies of the model estimated by the spectral analysis, and to assess the mode shapes (Fig. 6.24) of the first two bending modes and the damping ratios. The results of the identification of the first three modal frequencies and damping ratios are illustrated in Table 6.4. The angular acceleration, a_α, (Fig. 6.23) that is the rate of change of angular velocity over time, measured in radians per second squared (rad/s^2), is obtained by the following relation:

$$a_\alpha = \frac{(a_{A2} - a_{A1})}{l} \tag{6.3}$$

where a_{A1} and a_{A2} are the linear accelerations (in m/s^2), measured by the accelerometer A2 at the corner and by the accelerometer A1 at the center, respectively, and l is the horizontal distance between them, equal to 0.045 m.

Fig. 6.24 shows that the measured components of the identified mode shapes

Table 6.4 First three modes frequencies and damping ratios.

Mode	Description	Frequency Hz	Damping ratio %
1	bending - weak axis	18.7	5.0
2	bending - strong axis	23.3	1.6
3	torsional	52.3	4.6

are approximately linear.

Before wind tunnel tests, from the free vibration response of the model it has also been checked whether structural damping is stable, i.e. invariable with vibration amplitude of the building model. Fig. 6.25 shows the identified damping ratios from different sections of the free decay response with different vibration amplitude.

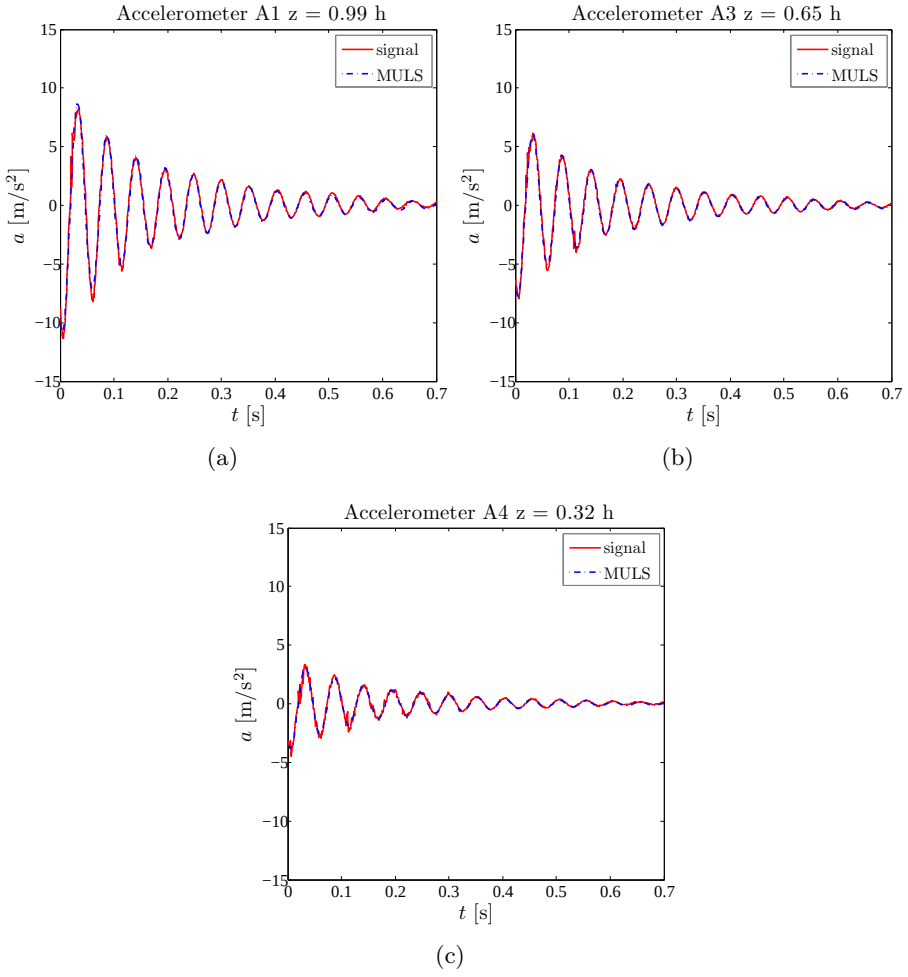

Fig. 6.21 Free vibration response. Decay acceleration signals along the weak axis direction: a) acceleration at $z = 0.99h$ (A1) ; b) acceleration at $z = 0.65h$ (A2); c) acceleration at $z = 0.32h$ (A3).

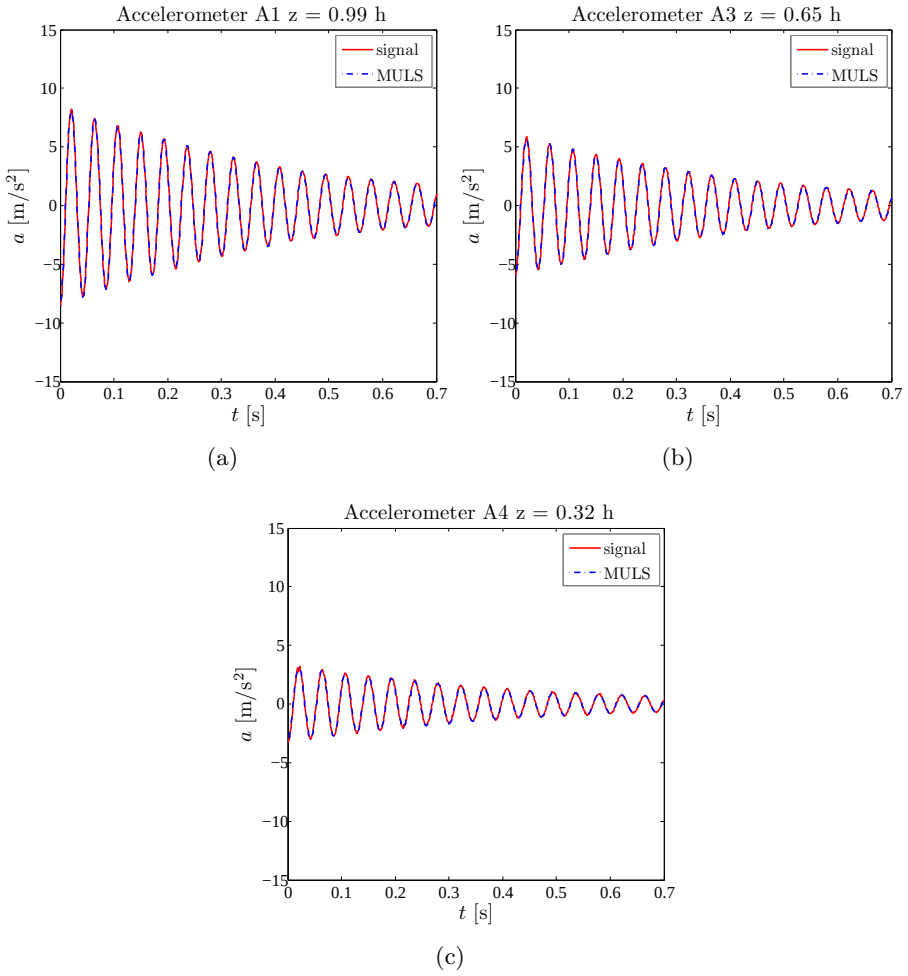

Fig. 6.22 Free vibration response. Decay acceleration signals along the strong axis direction: a) acceleration at $z = 0.99h$ (A1); b) acceleration at $z = 0.65h$ (A2); c) acceleration at $z = 0.32h$ (A3).

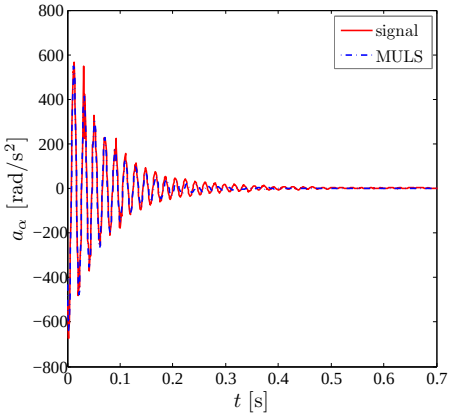

Fig. 6.23 Torsional response from free vibration test.

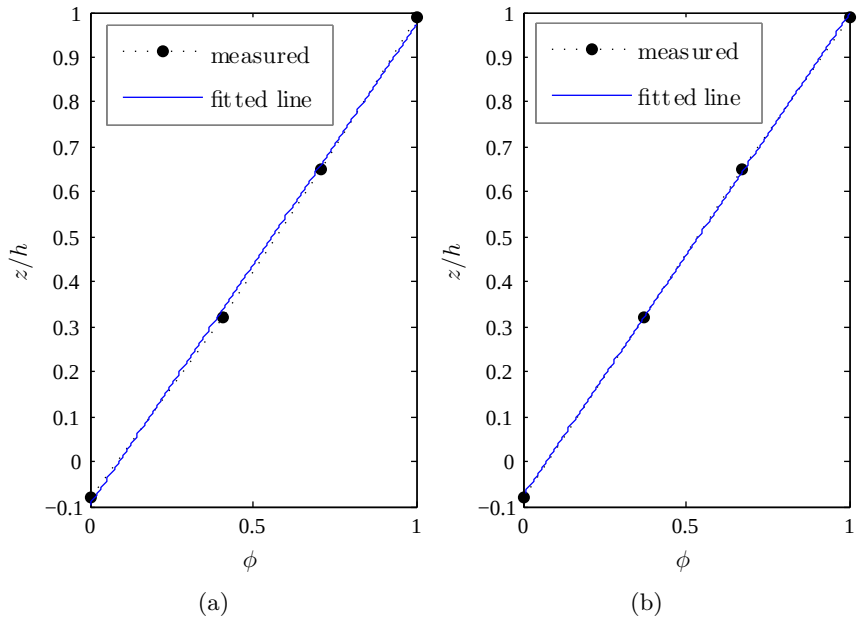

Fig. 6.24 Identified mode shapes: a) first mode (measured component along the weak axis); b) second mode (measured component along the strong axis).

For the first and the second bending modes the signal registered by accelerometer A1 is used [Fig. 6.21(a) and Fig. 6.22(a)], while for the torsional response the signal shown in Fig. 6.23 is used.

From Fig. 6.25(b) and Fig. 6.25(c), the identified structural damping ratios for the second and the third identified natural modes of vibration are almost the same for different vibration amplitudes, while for the first bending mode the damping ratio largely varies with the vibration amplitude. This behavior is thought to be related to the presence and direction of the pneumatic tubes. As a matter of fact, the first mode is translational along the weak axis of the model which also corresponds to the direction along which the pneumatic tubes are aligned towards the exit from the model.

Assuming that the total mass of the model, approximately equal to 2.2 kg, is uniformly distributed along the model height and using the modal damping ratios reported in Table 6.4, from Eq. (4.3) and Eq. (4.4) the Scruton number is easily derived and it is equal to 165.0 and 52.8 for the first and the second bending modes, respectively. The air density ρ is taken equal to 1.25 kg/m^3. When a torsional mode is considered, the mass per unit span length in Eq. (4.3) is replaced by the moment of inertia per unit span, Iz, and the Scruton number, Sc_α, is, therefore, defined as:

$$Sc_\alpha = \frac{2\delta_\alpha I_z}{\rho b^4} \tag{6.4}$$

where δ_α indicates the logarithmic decrement for the torsional mode. For a rectangular building of height h, breadth b and depth d, the moment of inertia per unit

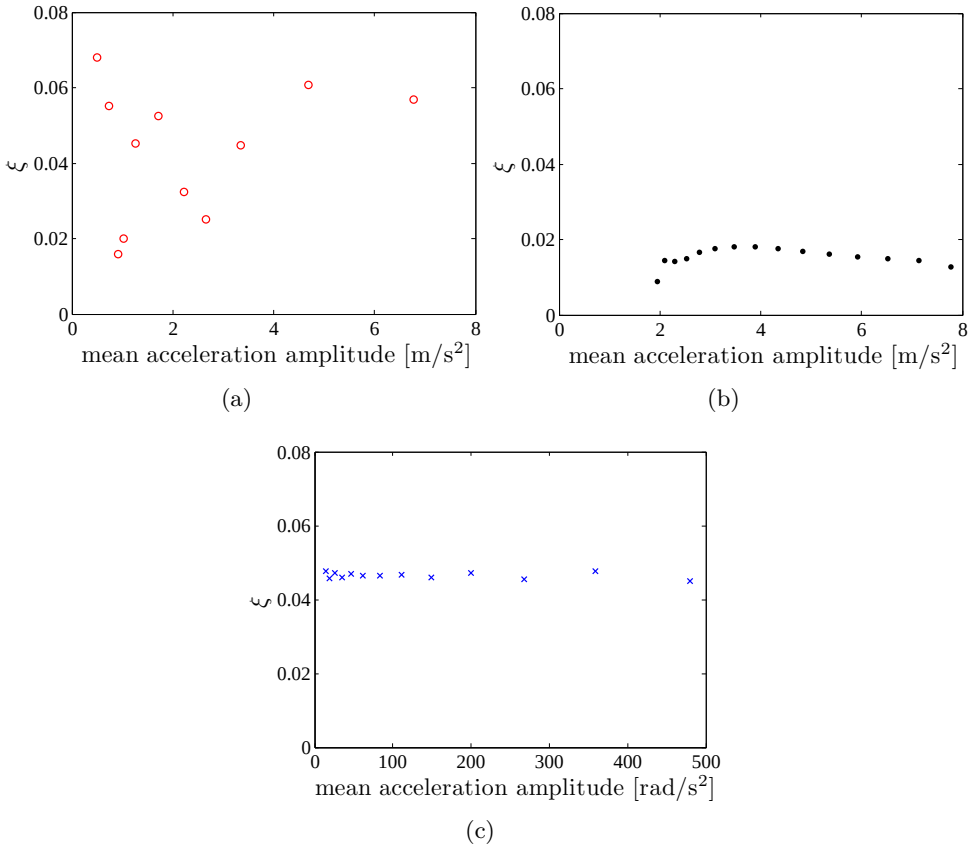

Fig. 6.25 Dependence of structural damping ratio on vibration amplitude: a) first bending mode; b) second bending mode; c) torsional mode.

length about the vertical axis, I_z, is defined as:

$$I_z = \frac{1}{12} m(b^2 + d^2) \tag{6.5}$$

where m indicates the mass per unit length. From Eqs. (6.4) and (6.5), the Scruton number for the torsional mode is equal to 12.6.

6.5 Simulated flow

The simulated flow conditions correspond to suburban terrain. The wind profile in the tunnel is developed through 4 spires and 3 Counihan at the inlet and the use of wood panels partially covering the tunnel floor, furnished with $5\times5\times5$ cm^3, equally spaced, cubic roughness elements (see Fig. 6.26).

Before installing the model in the wind tunnel, hot wire anemometer (see sub-

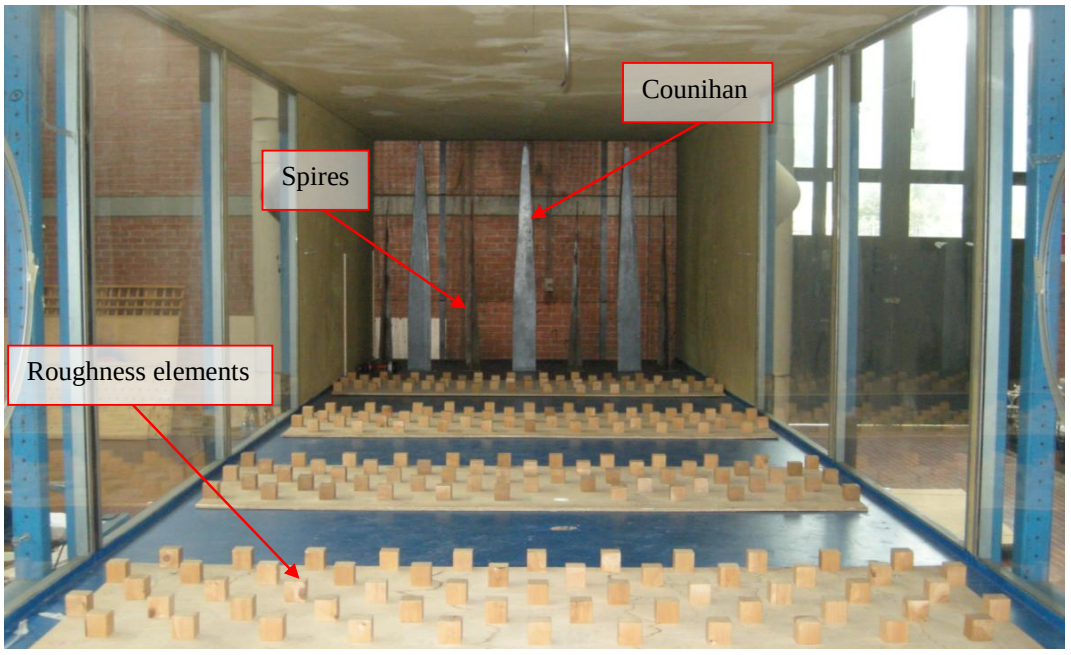

Fig. 6.26 CRIACIV-DICEA BLWT: roughness elements, Counihan and spires for the development of the boundary layer.

section 6.3.2) measurements are carried out in order to evaluate the characteristics of the incoming wind flow. A number of 18 measurement points are located along a vertical line at the center of the test section. The wind velocity, at each point, is recorded for approximately 65 seconds, with a sampling frequency of 2000 Hz, resulting in approximately 130000 data signals. In the following sections the characteristics of the wind flow are described.

The simulated wind flow in the boundary layer wind tunnel, as in the atmospheric boundary layer, is turbulent. Wind velocity is characterized by the mean velocity U and the turbulence components u, v and w (Dyrbye and Hansen, 1997), which can be described by means of their standard deviation and turbulence intensity (subsection 6.5.2), time scales and integral length scales (subsection 6.5.2).

6.5.1 Mean wind speed profile

Wind profile models

Various mathematical models exist for describing the variation with height above the ground, z, of the mean wind speed, U, within the atmospheric boundary layer. One of these models is the empirical *power law* profile, which is primarily used because of its simplicity, e.g. in the Canadian code NBC 1990. It is expressed as:

$$U(z) = U(z_{ref}) \left(\frac{z}{z_{ref}} \right)^{\alpha} \tag{6.6}$$

where z_{ref} is the reference height, usually 10 m. The exponent of the power law, α characterizes the terrain roughness, giving a lower value of $\alpha = 0.17$ for the smoother open country and a higher value of $\alpha = 0.24$ for the rougher urban terrain.

The power law profile, which has been universally employed for many years has, however, three major shortcomings (Cook, 1986):

1. it is independent of the length scale,
2. it has no theoretical justification,
3. it fits properly the measured data in the upper region of the Atmospheric Boundary Layer, but is poor near the surface.

A model which is capable for adequately describing the boundary layer in the lower regions, which are of greatest interest to the design of buildings, especially in strong wind conditions, is the *logarithmic law* (Cook, 1986, 1990). It was originally derived for the turbulent boundary layer on a flat plate by Prandtl, and it has been found to be valid in an unmodified form in strong wind conditions in the atmospheric boundary layer near the surface. The logarithmic law can be derived in a number of different ways. The simplest one, which is a form of dimensional analysis, and is illustrated in Holmes (2001), leads to the following expression for the logarithmic profile:

$$U(z) = u_* \frac{1}{\kappa} \ln \frac{z}{z_0} \tag{6.7}$$

where κ is the von Kármán's constant ($\kappa \sim 0.4$) and z_0 is the roughness length, which is a measure of the roughness of the ground surface and can be interpreted as the size of the characteristic vortex, which is formed as a result of the friction between the air and the ground surface (Dyrbye and Hansen, 1997).

Appropriate values for z_0 can be found in both the Eurocode 1 (UNI-EN 1991-1-4, 2005) and the ASCE 7-10 commentary (ASCE 7-10, 2010). A detailed classification for various roughness types is illustrated in Wieringa (1993).

The friction velocity u_* is defined by:

$$u_* = \sqrt{\frac{\tau_0}{\rho}} \tag{6.8}$$

where τ_0 is the shear stress at the ground surface and ρ is the air density. For extreme winds, in nature, typical friction velocities are of the order of 1-2 m/s. For urban areas and forests, where the terrain is very rough, the height z, in Eq. (6.7), is often replaced by an effective height, $z - z_h$, where z_h is a *zero-plane displacement*. Thus in this case,

$$U(z) = u_* \frac{1}{\kappa} \ln \frac{z - z_h}{z_0}. \tag{6.9}$$

The zero-plane displacement can be taken as about three-quarters of the general height of the obstacles.

The most useful way of applying Eq. (6.9) is to use it to relate the mean wind speeds at two different heights, z_1 and z_2, as follows:

$$\frac{U(z_1)}{U(z_2)} = \frac{\ln\left[(z_1 - z_h)/z_0\right]}{\ln\left[(z_2 - z_h)/z_0\right]} \tag{6.10}$$

Fitting with the experimental data

The experimental data of the mean wind speed along the height, $U(z)$, are fitted with both the power law profile and the logarithmic profile, using the *best fitting*, in the least square sense, procedure (Fig. 6.27).

From Eq. (6.6), after applying the logarithm to both sides, the following substitution is used:

$$\begin{cases} x = \ln(z) \\ y = \ln\left[U(z)\right] \end{cases} \tag{6.11}$$

The line $y = mx + q$ which best fits the data in the (x, y) plane is estimated. The exponent, α, of the power law profile, which is the slope of this regression line, is found to be equal to 0.2335.

The logarithmic law in Eq. (6.7) can be written as:

$$U(z) = u_* \frac{1}{\kappa} \ln z - u_* \frac{1}{\kappa} \ln z_0 \tag{6.12}$$

Applying the substitution:

$$\begin{cases} x = \ln z \\ y = U(z) \end{cases} \tag{6.13}$$

the line $y = mx + q$ which best fits the data in the (x, y) plane is estimated. From the slope and intercept of this line, the roughness length and the friction velocity are calculated as follows:

$$z_0 = e^{\frac{-q}{m}} = 0.2469 \text{ cm} \tag{6.14}$$

$$u_* = \kappa \cdot m = 1.3974 \text{ m/s} \tag{6.15}$$

where $\kappa = 0.4$.

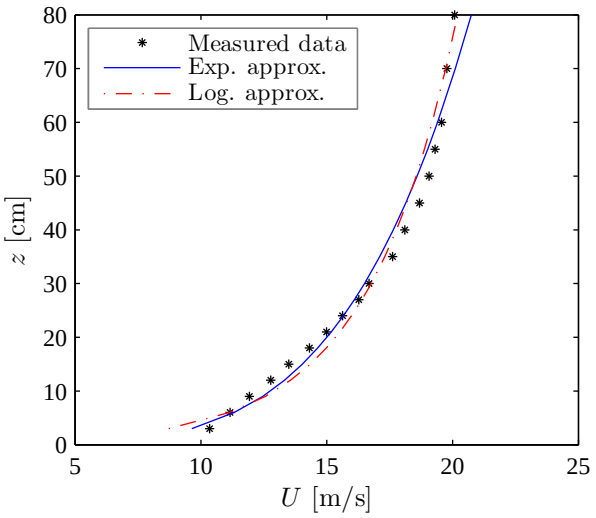

Fig. 6.27 Mean wind speed profile.

6.5.2 Turbulence intensity

The turbulence intensity, $I_u(z)$, for the along-wind turbulence component, u, at height z above ground is defined as (Dyrbye and Hansen, 1997):

$$I_u(z) = \frac{\sigma_u(z)}{U(z)} \tag{6.16}$$

where $\sigma_u(z)$ is the standard deviation of the turbulence component u and $U(z)$ is the longitudinal mean wind speed, both at height z.

The longitudinal turbulence intensities measured at the test section are shown in Fig. 6.28.

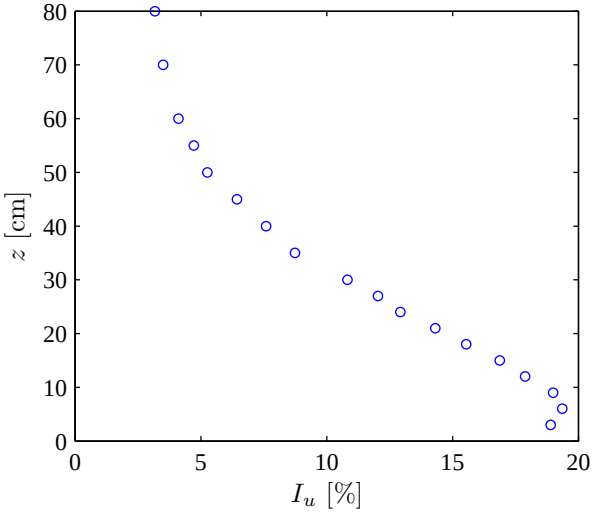

Fig. 6.28 Profile of the turbulence intensity of the longitudinal turbulence component.

6.5.3 Integral length scale of the longitudinal turbulence

Integral length scales are a measure of the sizes of vortices in the wind, or, in other words, the average size of a gust in a given direction.

The integral length scale L_u^x for the turbulence component u measured in the longitudinal direction x is defined as:

$$L_u^x = \int_0^\infty \rho_u(z, r_x), dr_x \tag{6.17}$$

in which $\rho_u(z, r_x)$ is the cross correlation function between the turbulence component u in two points separated longitudinally by a distance r_x and measured simultaneously. According to Taylor's hypothesis of convected *frozen turbulence* [see Dyrbye and Hansen (1997)], which is normally considered to be an accurate approximation in natural wind, $\rho_u(z, r_x) = \rho_u^T(z, \tau)$, that is the autocorrelation function, for $r_x = U(z)\tau$, indicating that the longitudinal integral length scale is equal to the time scale multiplied by the mean wind velocity, $L_u^x(z) = U(z)T(z)$.

In total, 9 integral length scales are defined similarly as shown in Eq. (6.17):

- for the longitudinal turbulence component u: $L_u^x \quad L_u^y \quad L_u^z$
- for the lateral turbulence component v: $L_v^x \quad L_v^y \quad L_v^z$
- for the vertical turbulence component w: $L_w^x \quad L_w^y \quad L_w^z$

It is possible to calculate the longitudinal integral length scale from the registered wind speed data, following two different ways. The first one consists in evaluating the integral scale of turbulence from the autocorrelation function of the fluctuating wind speed, on the basis of Eq. (6.17) and the Taylor's hypothesis.

Alternatively, the integral length scale can be calculated fitting the power spectral density function of the longitudinal wind speed with theoretical expressions. One of the most widely used is that proposed by von Kármán and is given by:

$$\frac{fS_{uu}(f)}{\sigma_u^2} = \frac{4f_r}{(1 + 70.8f_r^2)^{5/6}} \tag{6.18}$$

where the non dimensional frequency, f_r, is a function of the integral length scale:

$$f_r = \frac{fL_u^x(z)}{U(z)} \tag{6.19}$$

Fig. 6.29 shows the estimated spectrum of the u component of turbulence at height $z = 18$ cm (measuring point number 6 from the ground floor) and wind speed $U = 14.32$ m/s, compared with the fitted von Kármán spectrum. The estimated value of the integral length scale, resulting from the fitting procedure, L_u^x is equal to 0.2929 m. Fig. 6.30 illustrates the profile of the longitudinal length scale of turbulence estimated by analogous fitting for each height.

6.6 Model instrumentation and wind tunnel setup

The model mounted on the HFFB and equipped with the pressure taps is installed in the wind tunnel. Fig. 6.31 shows the wind tunnel setup. The model is

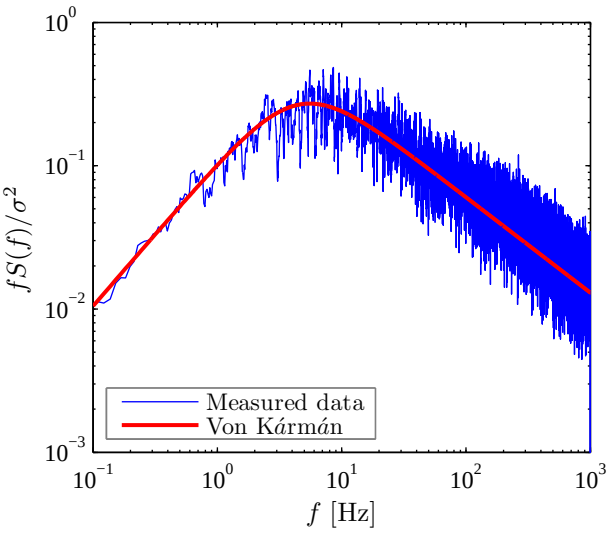

Fig. 6.29 Spectrum of the longitudinal turbulence component, u at height $z = 18$ cm and $U = 14.32$ m/s. Measured data and fitting with equation (6.18) with $L_u^x = 0.2929$ m.

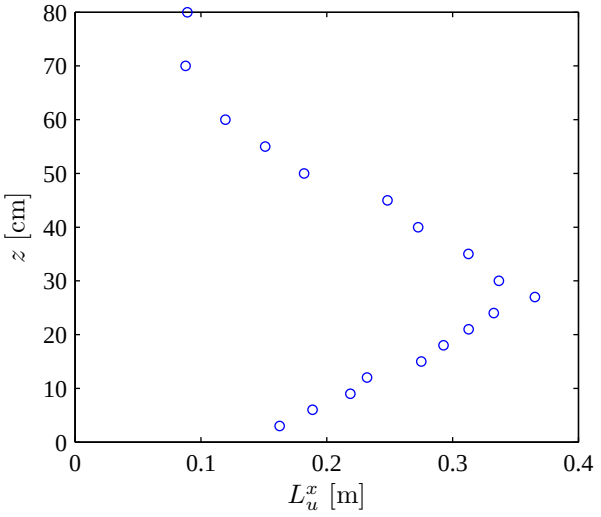

Fig. 6.30 Profile of the longitudinal length scale of turbulence.

oriented with the turning table so the the wind direction is normal to face 1 (upwind face).

The *blockage ratio*, defined as the ratio between the frontal area of the model and the cross-sectional area at the wind tunnel test section is equal to 1.6%, that means less than 5%. Its distorsion effect can be therefore neglected (ASCE, 1999).

Three laser displacement transducers are positioned in the tunnel [Fig. 6.32(a)] in order to measure the across-wind response (y-direction). Laser L1 is at the top of the model in the middle of face 4C, L2 is approximately 20 cm below it, at the top of box B and L3 is at the same level of L1, but near the corner. It is located at x = 4.5 cm.

The opposite sideward face, number 2, is equipped with two accelerometers at the top, A2 and A3, whose positions are symmetric with respect to those of L1 and L3. Accelerometer A1 is placed on face 3 downwind in order to measure the along-wind acceleration response [Fig. 6.32(b)].

Simultaneous measures of pressures, overall forces, displacements and accelerations are performed for a wide range of wind speeds, from approximately 7.1 to 27.6 m/s at the reference height, $z_{ref} = 60.8$ cm, corresponding to the model height h. A total of 25 tests, each referred to a certain value of the wind speed, maintained constant during the test, are performed. The corresponding Re number [Eq. (3.12)] ranges from approximately 5×10^4 to 2×10^5, assuming as reference dimension $b = 0.105$ m and the kinematic viscosity of air, $\nu = 15 \times 10^{-6}$ m^2/s (CNR-DT 207, 2008). The 25 mean wind speed values at reference height, referred to as U_h, are reported in Table 6.5.

6.7 Identification of the Strouhal number from pressure measurements

6.7.1 Dynamic pressure measurements

The pressure transducers available in the CRIACIV BLWT (subsection 6.3.3) allow for the simultaneous measuring of 128 pressures (SMPSS technique, subsection 5.2.2), recorded with a sampling frequency of 250 Hz. However only 126 channels are connected to the pneumatic tubes distributed on the model faces. In order to measure the pressure coefficients, Eq. (3.1), one channel is used to measure the static pressure, p_0, and another one to measure the dynamic pressure, p_{dyn}, of the undisturbed flow. These measures are provided during each test by the Pitot tube mounted near the tunnel ceiling [Fig. 6.33(a)].

Before mounting the model in the tunnel, a second Pitot tube is installed on a moving mechanical arm [Fig. 6.33(b)], in order to refer the static and dynamic pressures measured by the Pitot tube during the tests precisely to different levels of interest. A number of 12 levels is considered, corresponding to the 8 levels of the pressure taps, to the reference height and to 3 additional higher levels. These measures, repeated for different wind speeds, result in conversion coefficients that allow the estimation of p_0 and p_{dyn} at the considered levels, at which it is, therefore, possible to refer the pressure coefficients.

A further one of the 128 channels is let free and used to measure an artificial impulsive pressure signal which is simultaneously recorded by the system that acquires data from the balance, the laser transducers and the accelerometers. This procedure

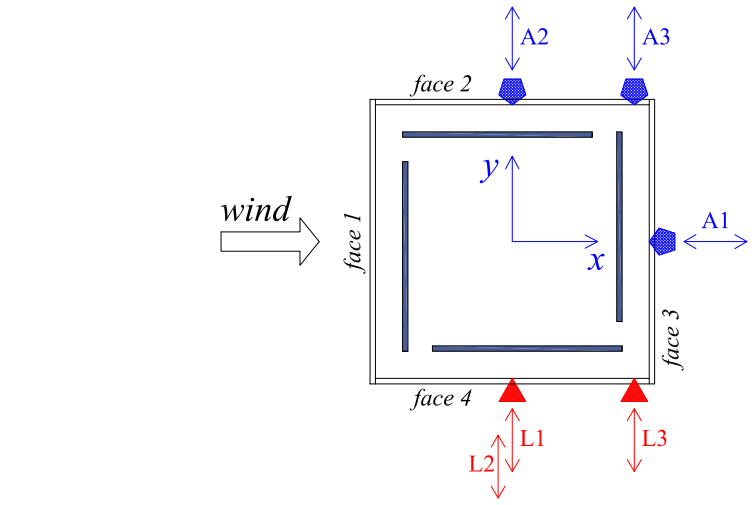

(a)

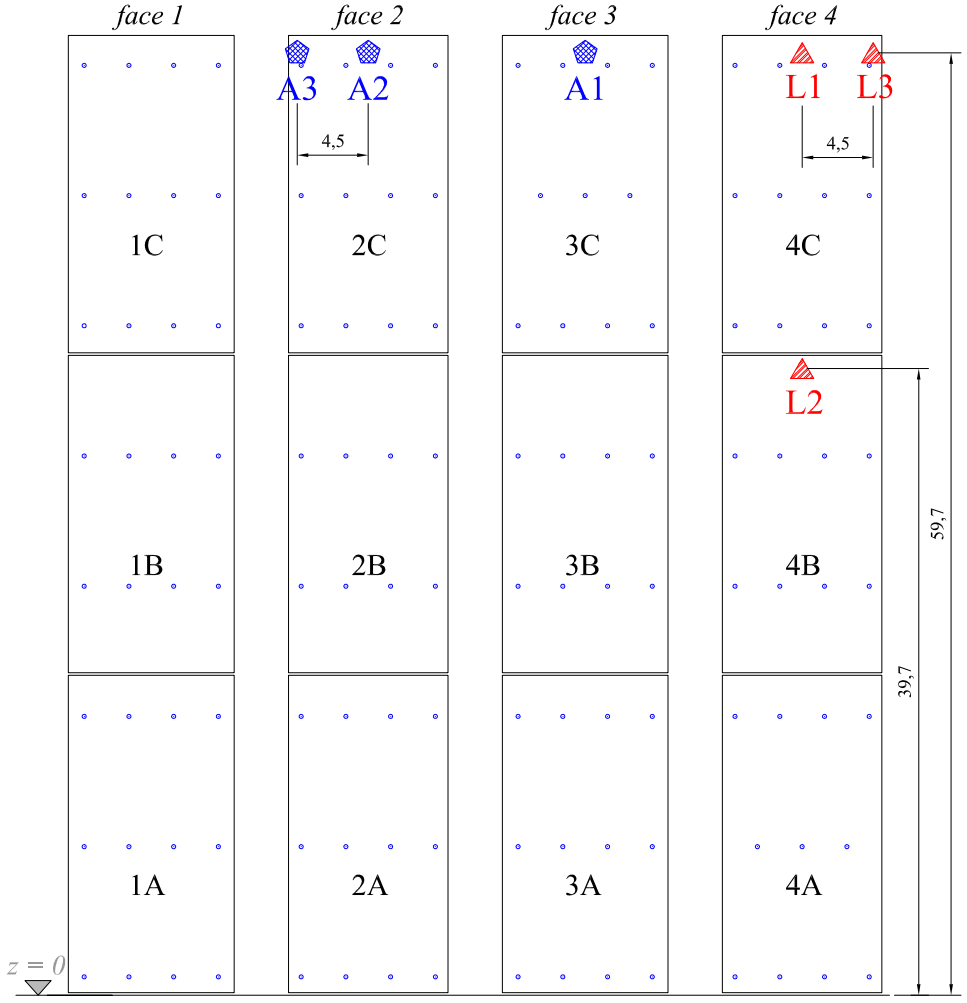

(b)

Fig. 6.31 Wind tunnel setup. Pressure taps distribution and positions of displacements transducers (L1, L2, L3) and accelerometers (A1, A2, A3): a) plan view; b) view from the model sides.

Table 6.5 Mean wind speed at reference height, U_h, for the 25 tests performed.

Test Number	U_h m/s
1	7.08
2	8.73
3	10.39
4	12.05
5	13.73
6	15.41
7	17.06
8	18.80
9	20.49
10	21.02
11	21.56
12	22.13
13	22.70
14	23.25
15	23.81
16	24.34
17	24.93
18	25.46
19	26.04
20	26.30
21	26.57
22	26.82
23	27.09
24	27.33
25	27.60

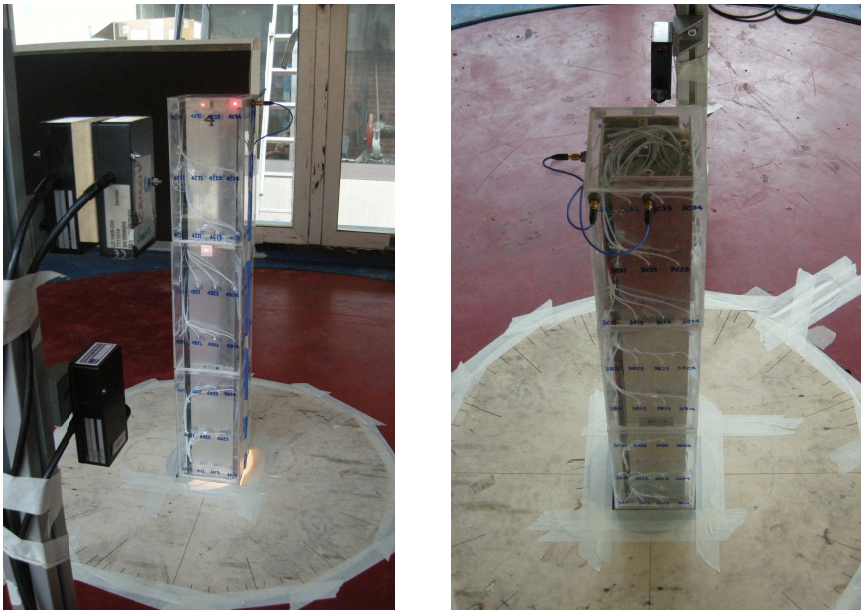

(a) (b)

Fig. 6.32 Wind tunnel setup: a) position of laser displacement transducers; b) position of accelerometers.

permits the time synchronization of all the registered signals.

From pressure measurements, at each pressure tap, sets of time varying non-

(a) (b)

Fig. 6.33 Wind tunnel setup: a) Pitot tube at the tunnel ceiling; b) Pitot tube mounted on the moving arm.

dimensional pressure coefficients are evaluated, according to Eq. (3.1), as follows:

$$C_p(t) = \frac{p(t) - p_0(z)}{p_{dyn}(z)} = \frac{p(t) - p_0(z)}{\frac{1}{2}\rho U(z)^2} \tag{6.20}$$

where z refers to the tap level above the tunnel floor. In the equation above, $\frac{1}{2}\rho U(z)^2$ indicates the dynamic pressure of the undisturbed flow at the tap level z, measured as previously explained.

Fig. 6.34 depicts the distribution of the pressure coefficients on the cylinder sur-

face measured at the 16 taps at level B2, $z = 34.2$ cm $= 0.56h$. At this height above the tunnel floor, the turbulence intensity is approximately equal to 9% (see Fig. 6.28). Results from different tests are shown, namely test 2, 7 and 25, corresponding to different Reynolds numbers, approximately equal to 45000, 97000 and 172000, respectively, evaluated with reference to the mean velocity at the taps level. Both mean [Fig. 6.34(a)] and standard deviation [Fig. 6.34(b)] pressure coefficients are compared to those obtained from Liang *et al.* (2011) in 15% homogeneous turbulent 2-D flow conditions around a fixed square section prism at the same incidence (see also Fig. 3.12) and at two Re levels. In order to facilitate comparisons between the results of the current study and data from Liang *et al.* (2011), the contour of the square section is described by means of an auxiliary coordinate, ξ, defined in Fig. 6.35. Results from the current study are found to be in good agreemeent with those of Liang *et al.* (2011).

6.7.2 Spectral analysis of the across-wind pressure coefficients

In Fig. 6.36, the normalized power spectra of the pressure coefficients referred to eight pressure taps located on sideward face 4, along a vertical axis, are shown. For each pressure tap, five curves corresponding to five different tests (number 3, 6, 9, 15, 23) and, therefore, to five values of the reference wind speed (equal to 10.39, 15.41, 20.49, 23.81 and 27.09 m/s respectively) are considered. All the curves, at each level, show a peak at a certain value of the reduced frequency fb/U, where $U = U(z)$, that is dependent on height. It seems, however, that the spectral peak is not significantly affected by the wind velocity.

Defining the Strouhal number as the peak reduced frequency $fb/U(z)$ in the power spectra, it is possible to assess the variation of the Strouhal number with height, illustrated in Fig. 6.37. The tap level on the tunnel floor is expressed as z/h, where h is the model height. The Strouhal number decreases with height. Once above $0.5h$, it varies less rapidly and then becomes almost constant and equal to approximately 0.095. Similar results are obtained by Kim and Kanda (2010).

The variation of the mean wind speed along the height, related to the wind profile, can be expressed, for each test, in terms of the non-dimensional parameter $U(z)/U_h$ illustrated in Fig. 6.38(a). It is therefore possible to establish the variation of the Strouhal number along the height, not influenced by the effect of the mean wind profile [Fig. 6.38(b)], calculating the Strouhal number as fb/U_h.

From the knowledge of the Strouhal number, the value of the reference wind speed U_h at which the shedding frequency is expected to reach the natural frequency of the model in the across-wind bending mode, from Eq. (6.2), is equal to:

$$U_{crit} = \frac{bf_n}{St} = \frac{0.10518.7}{0.095} = 20.7 \text{ m/s} \tag{6.21}$$

This value of the velocity falls in the tested wind speed range. It suggests that at a certain value of the wind speed the lock-in condition has been reached, although not clear effect of velocity on pressure peaks have been observed.

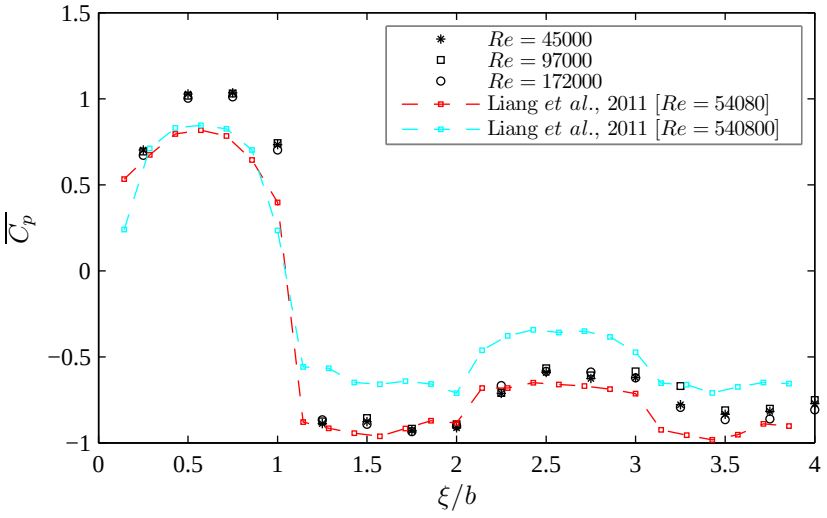

(a)

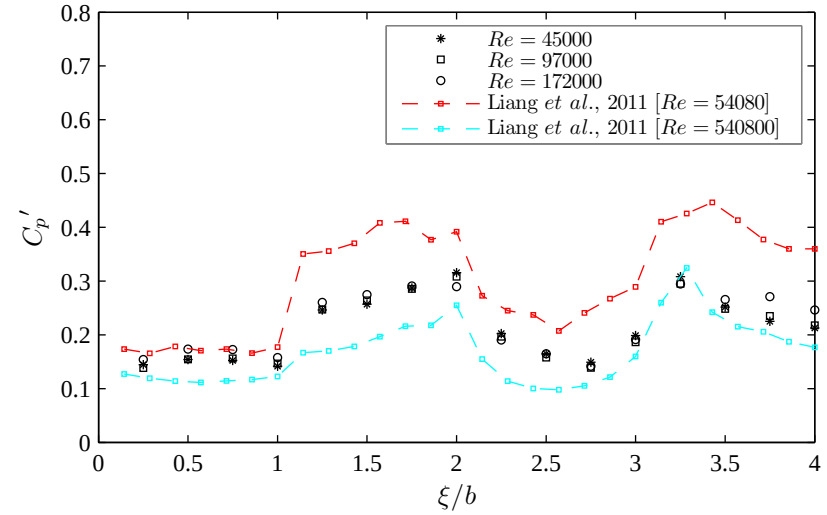

(b)

Fig. 6.34 Distribution of the mean (a) and standard deviation (b) pressure coefficient at level $z = 0.56h$. Comparison with results from Liang *et al.* (2011).

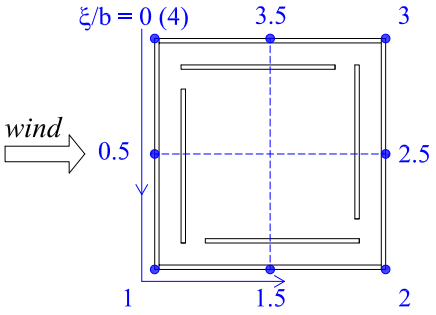

Fig. 6.35 Definition of the coordinate ξ describing the contour of the square section of the model.

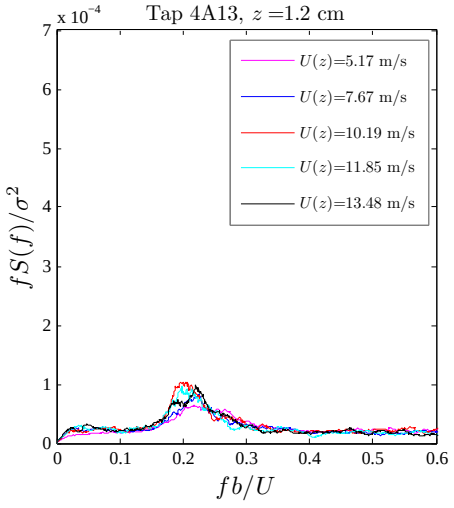
x 10^-4
Tap 4A13, z =1.2 cm
U(z)=5.17 m/s
U(z)=7.67 m/s
U(z)=10.19 m/s
U(z)=11.85 m/s
U(z)=13.48 m/s
fS(f)/σ^2
fb/U

(a)

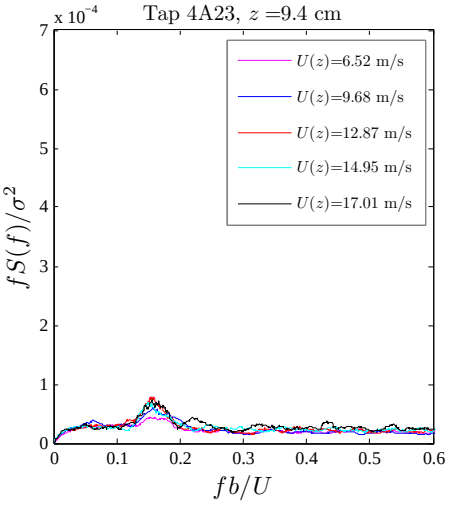
x 10^-4
Tap 4A23, z =9.4 cm
U(z)=6.52 m/s
U(z)=9.68 m/s
U(z)=12.87 m/s
U(z)=14.95 m/s
U(z)=17.01 m/s
fS(f)/σ^2
fb/U

(b)

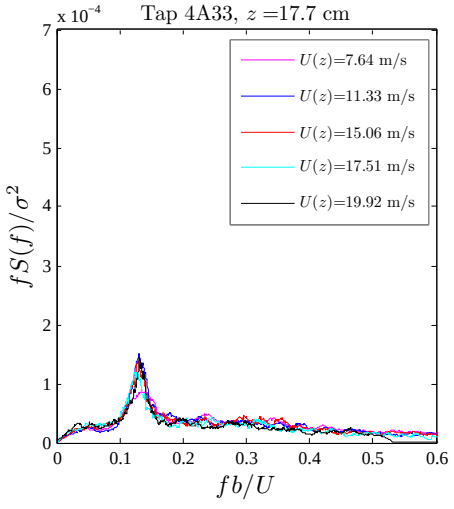
x 10^-4
Tap 4A33, z =17.7 cm
U(z)=7.64 m/s
U(z)=11.33 m/s
U(z)=15.06 m/s
U(z)=17.51 m/s
U(z)=19.92 m/s
fS(f)/σ^2
fb/U

(c)

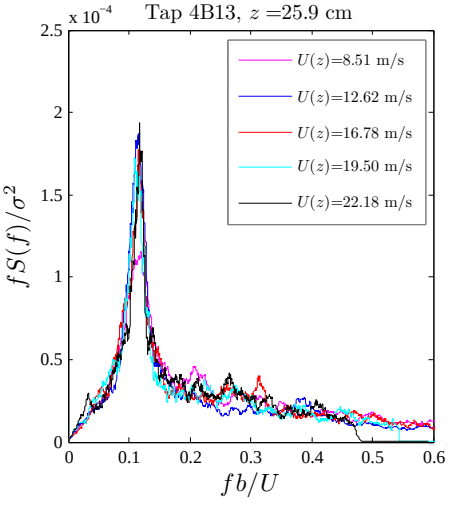
x 10^-4
Tap 4B13, z =25.9 cm
U(z)=8.51 m/s
U(z)=12.62 m/s
U(z)=16.78 m/s
U(z)=19.50 m/s
U(z)=22.18 m/s
fS(f)/σ^2
fb/U

(d)

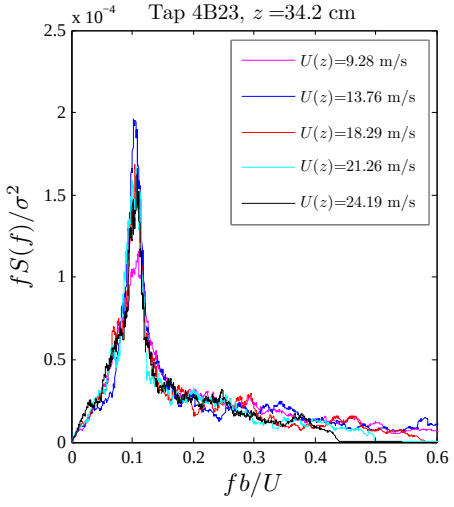
x 10^-4
Tap 4B23, z =34.2 cm
U(z)=9.28 m/s
U(z)=13.76 m/s
U(z)=18.29 m/s
U(z)=21.26 m/s
U(z)=24.19 m/s
fS(f)/σ^2
fb/U

(e)

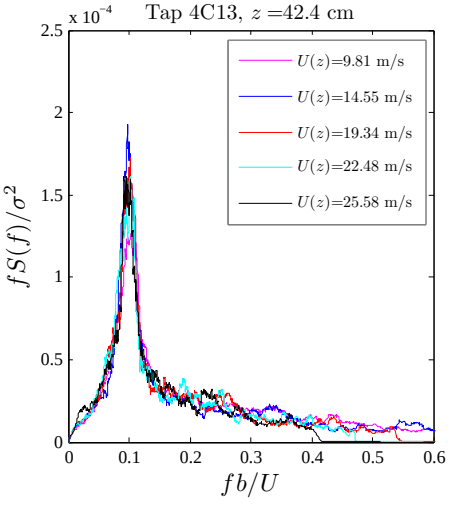
x 10^-4
Tap 4C13, z =42.4 cm
U(z)=9.81 m/s
U(z)=14.55 m/s
U(z)=19.34 m/s
U(z)=22.48 m/s
U(z)=25.58 m/s
fS(f)/σ^2
fb/U

(f)

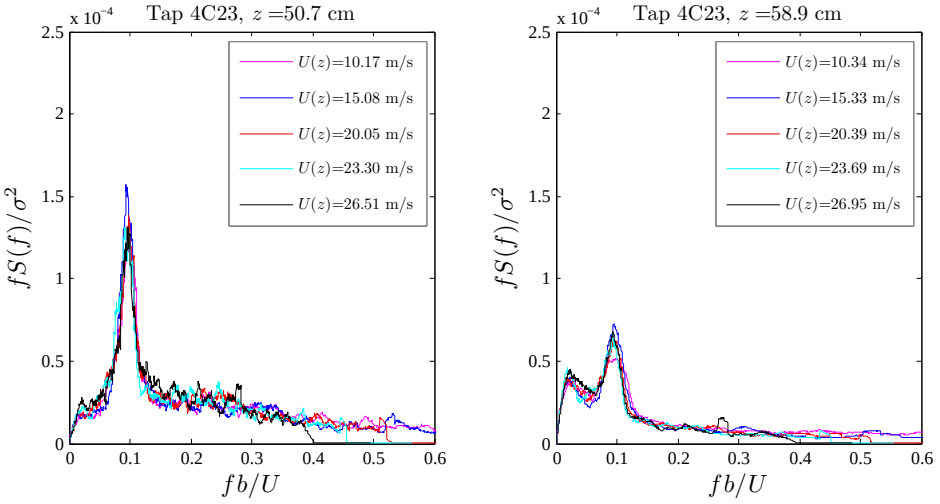

Fig. 6.36 Pressure coefficients power spectra at sideward surface.

6.8 Spectral analysis of the response

For each test and, therefore, each wind speed, the power spectra of the measured response are evaluated, including the overall forces and moments measured by the HFFB, the along-wind and across-wind acceleration response measured by the three accelerometers, A1, A2, A3, and the across-wind displacement response, measured by the three laser transducers, L1, L2, L3. (Fig. 6.39 - Fig. 6.63). At low values of the wind speeds (Fig. 6.39 - Fig. 6.42), from the across-wind response spectra, the two peaks corresponding to the shedding frequency f_s and to the natural frequency of the model in the lateral bending mode f_1 are distinguished. From the along-wind response spectra, sharp peaks are observed at the along-wind natural frequency f_2 [Fig. 6.39(b)]. The shedding frequency f_s increases with the wind speed. The presence of a peak at the across-wind natural frequency f_1 in the along-wind response (accelerometer A1 and signals F_x, M_y from the HFFB) spectra [e.g. Fig. 6.39(b)] and, on the other hand, of a peak at the along-wind frequency f_2 in the across-wind response spectra (F_y, M_x, A1, A2, L1, L2, L3), e.g. Fig. 6.39(c), reveals a certain coupling between the two bending modes of the model. In test 6, $U_h = 15.41$ m/s, f_s approaches f_1. The across-wind response spectra show only one sharp high peak at the frequency f_1. The along-wind response is also dominated by the f_1 component, as shown in Fig. 6.44(b), curve A2. This vortex resonance condition, corresponding to higher spectral peaks values, is clearly visible from test 6 to test 8 (Fig. 6.44 - Fig. 6.46). Then the shedding frequency, f_s, exceeds f_1 and gradually the shedding peak becomes noticeable from the across-wind response spectra, after that corresponding to f_1 (Fig. 6.49). At higher values of the reference wind speed U_h the shedding frequency f_s synchronizes with the along-wind natural frequency f_2 (Fig. 6.50 - Fig. 6.53). Then f_s continues increasing beyond the value of f_2 (Fig. 6.54 - Fig. 6.63).

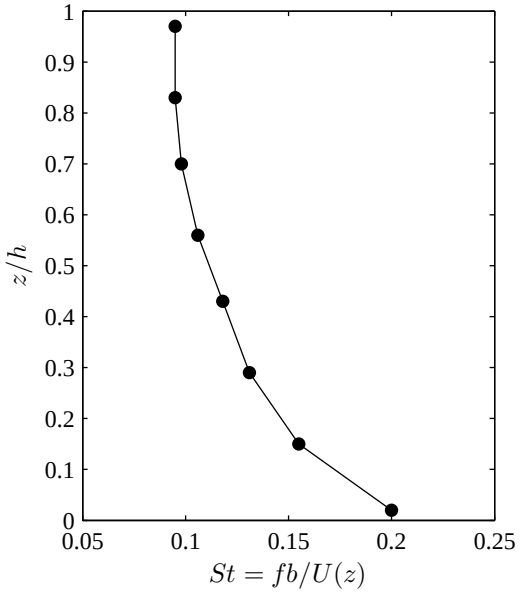

Fig. 6.37 Strouhal number variation with height over wind tunnel floor.

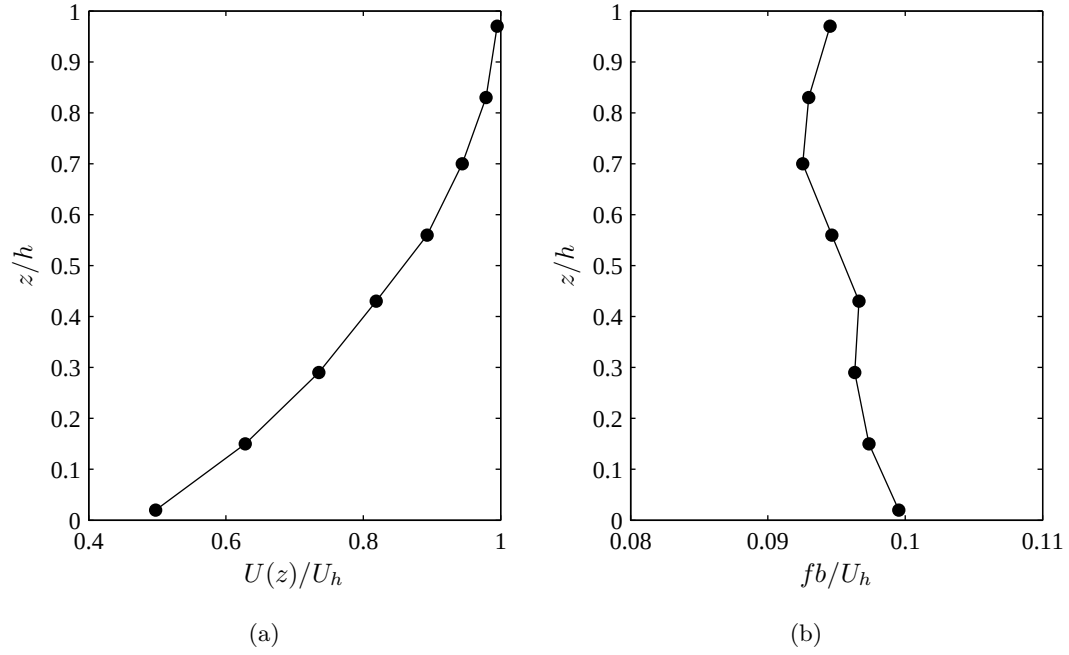

Fig. 6.38 a) Variation of the mean wind speed along the height; b) variation of the reduced frequency fb/U_h along the height.

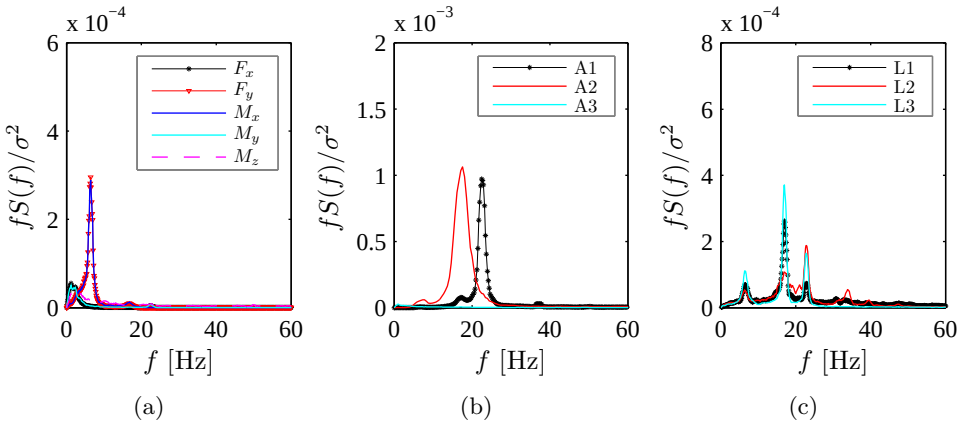

Fig. 6.39 Response spectra, test number 1.

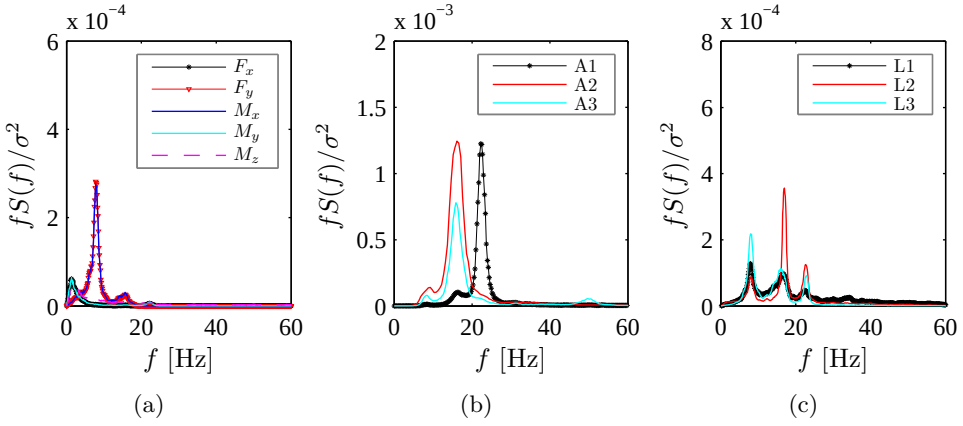

Fig. 6.40 Response spectra, test number 2.

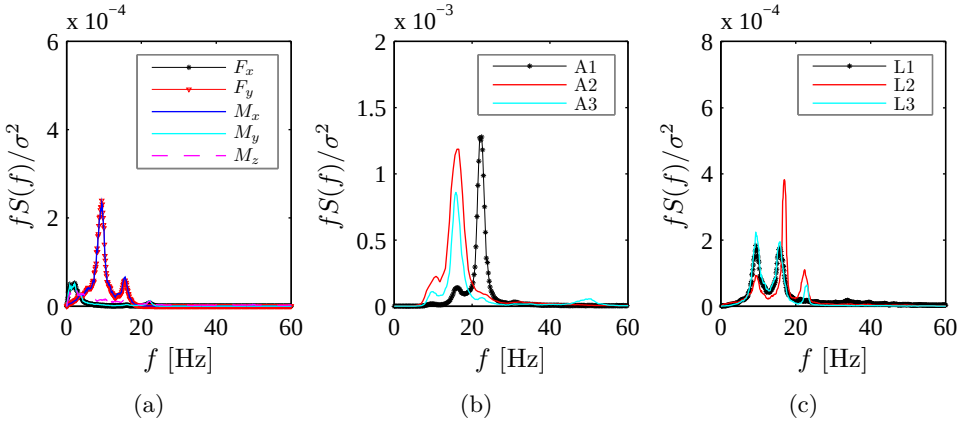

Fig. 6.41 Response spectra, test number 3.

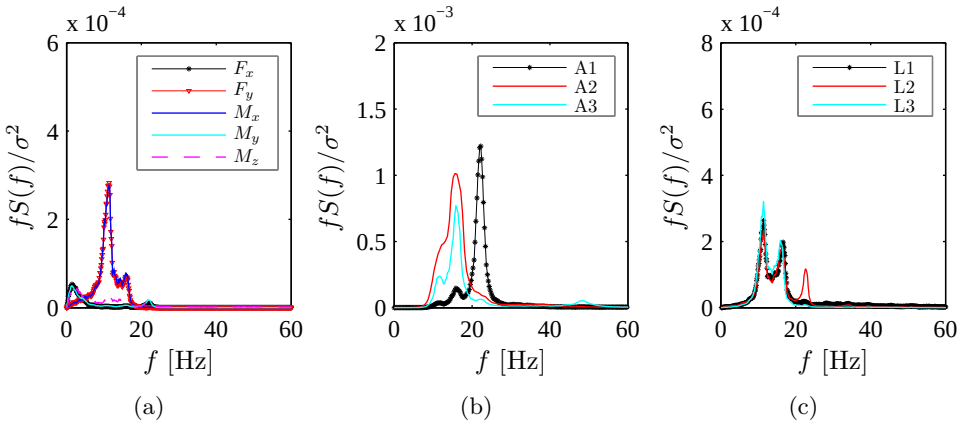

Fig. 6.42 Response spectra, test number 4.

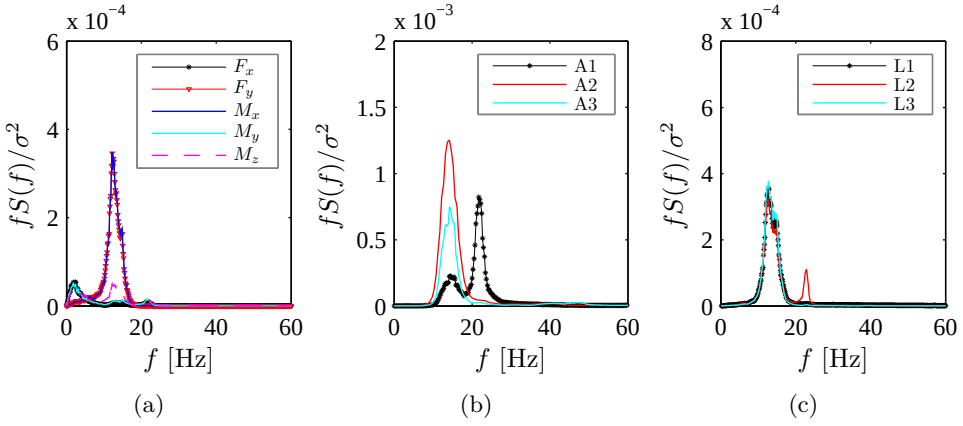

Fig. 6.43 Response spectra, test number 5.

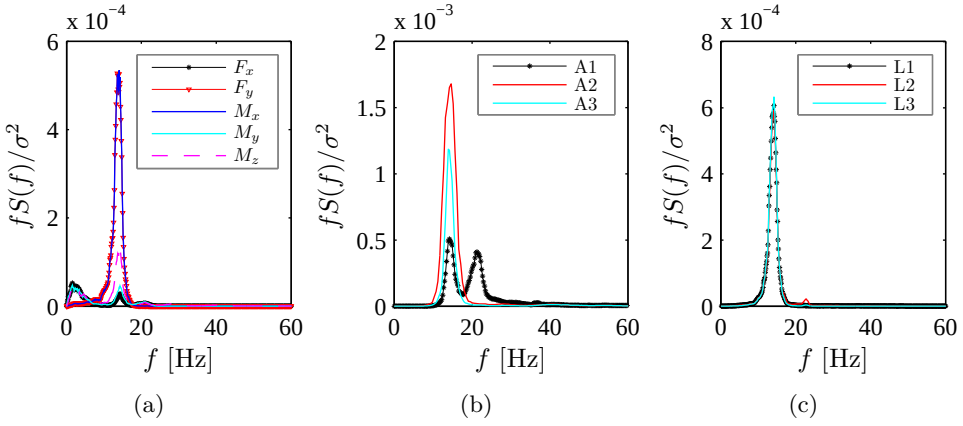

Fig. 6.44 Response spectra, test number 6.

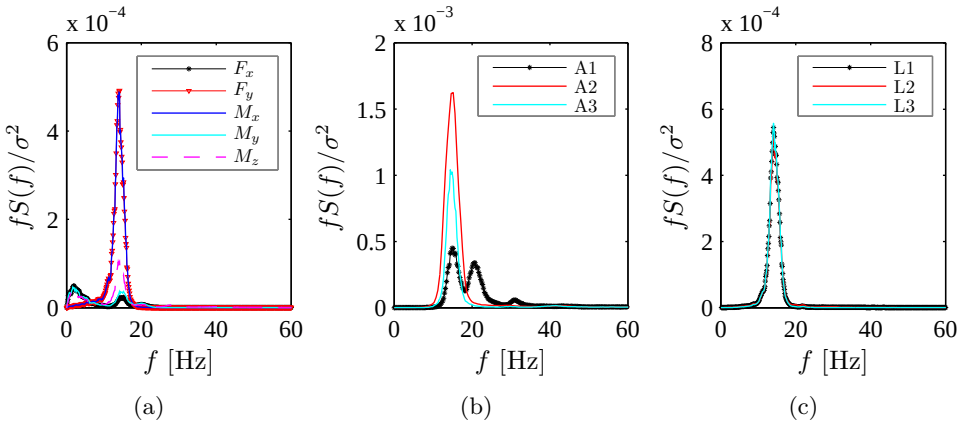

Fig. 6.45 Response spectra, test number 7.

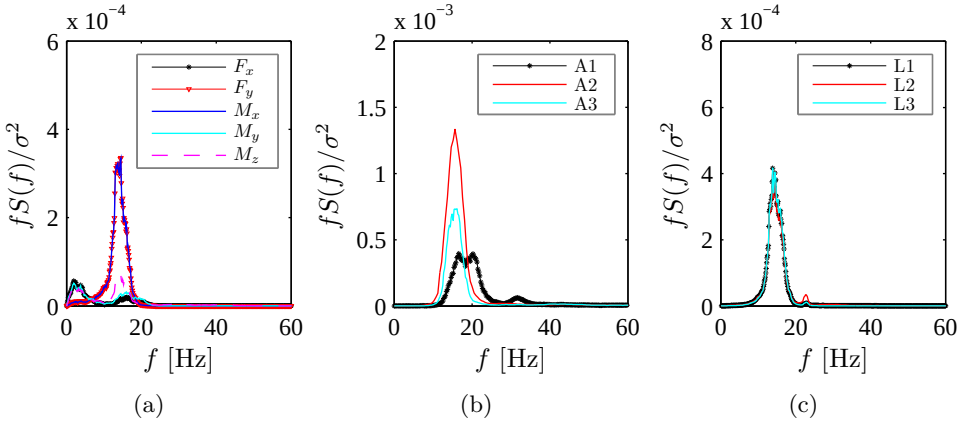

Fig. 6.46 Response spectra, test number 8.

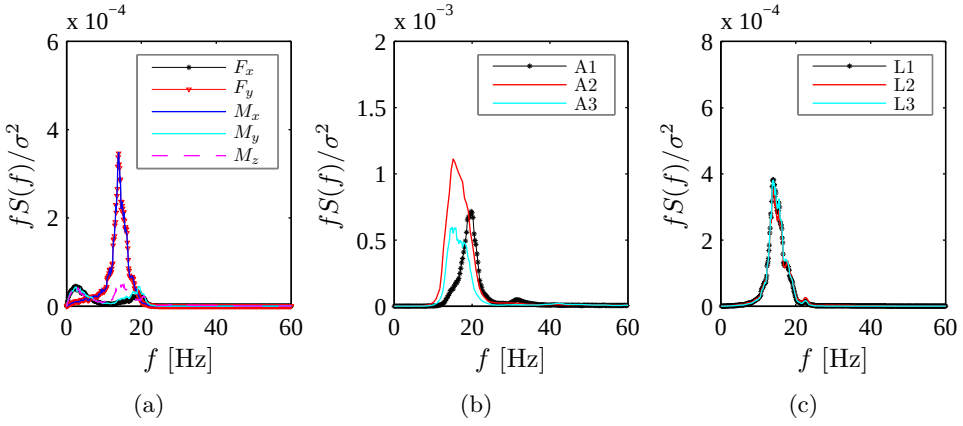

Fig. 6.47 Response spectra, test number 9.

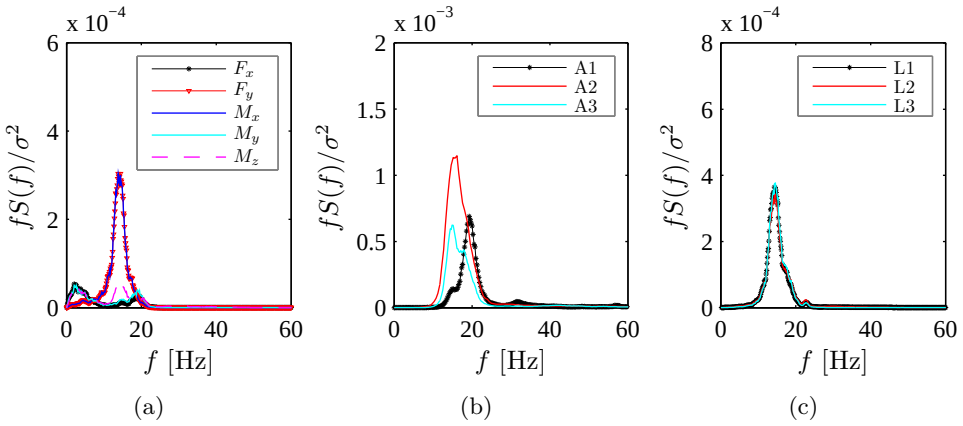

Fig. 6.48 Response spectra, test number 10.

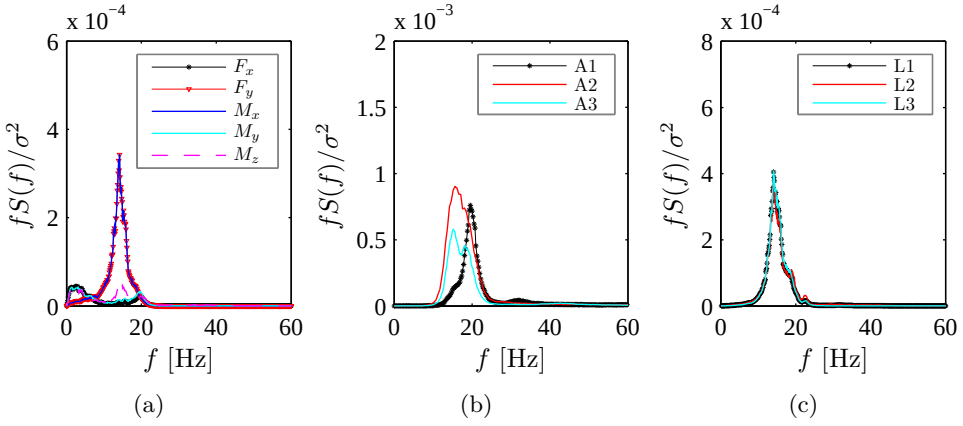

Fig. 6.49 Response spectra, test number 11.

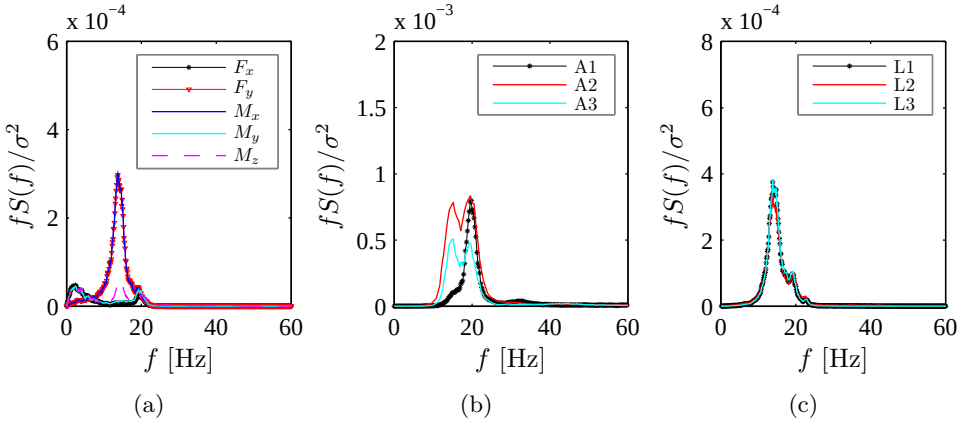

Fig. 6.50 Response spectra, test number 12.

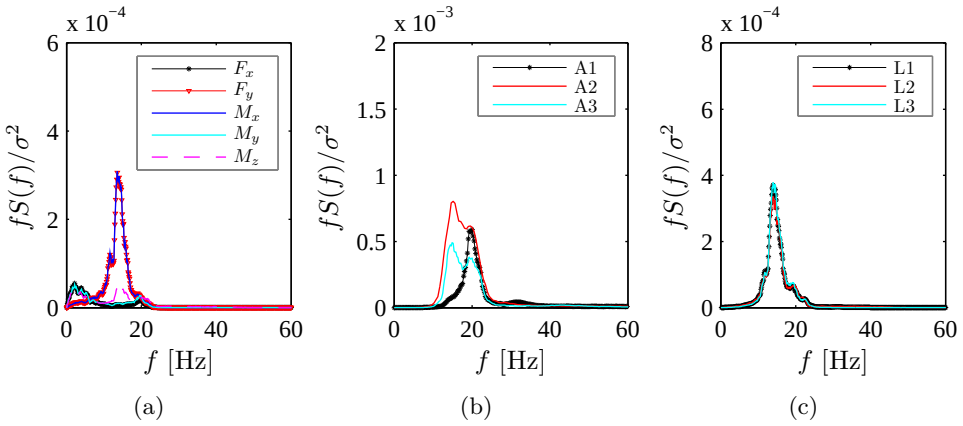

Fig. 6.51 Response spectra, test number 13.

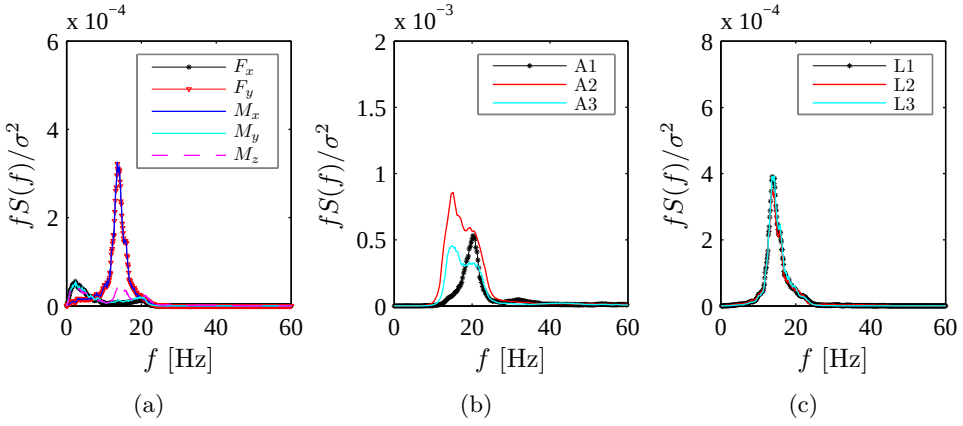

Fig. 6.52 Response spectra, test number 14.

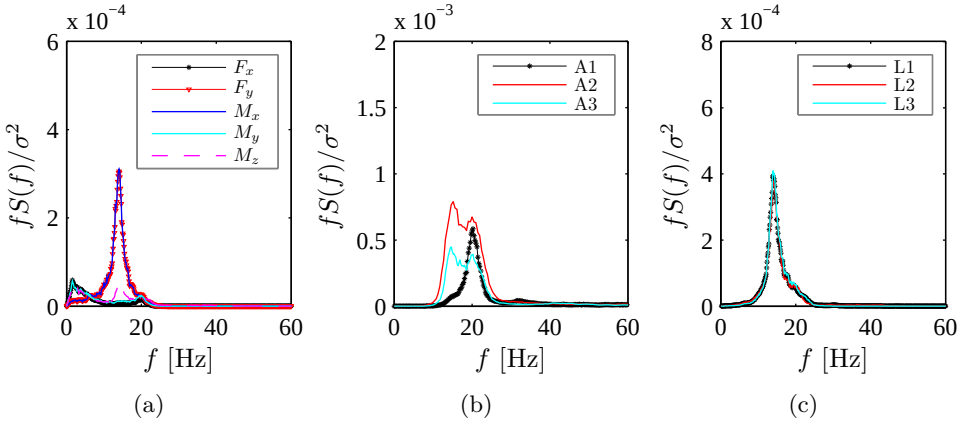

Fig. 6.53 Response spectra, test number 15.

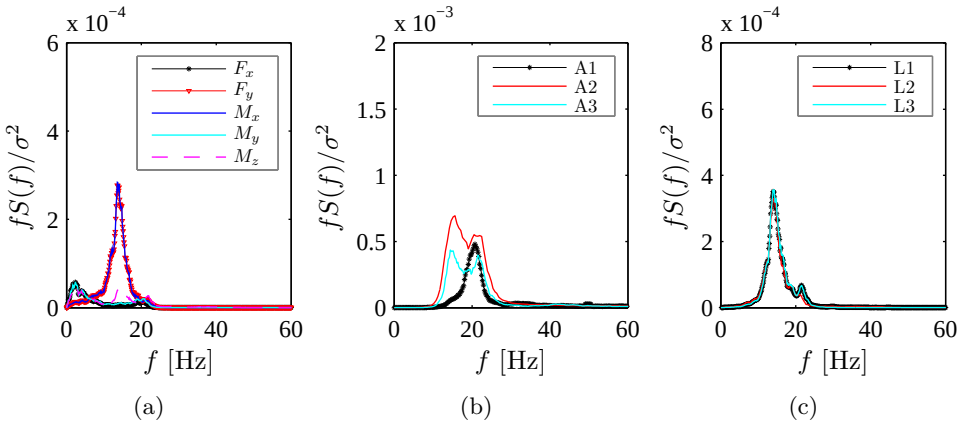

Fig. 6.54 Response spectra, test number 16.

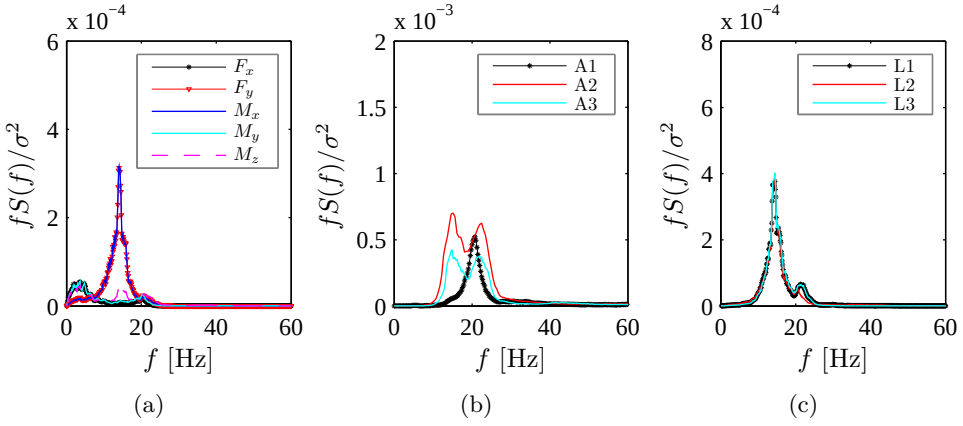

Fig. 6.55 Response spectra, test number 17.

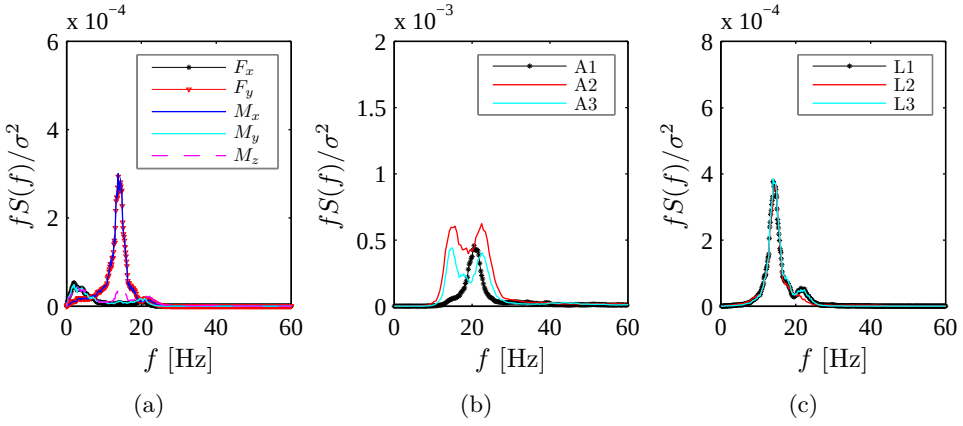

Fig. 6.56 Response spectra, test number 18.

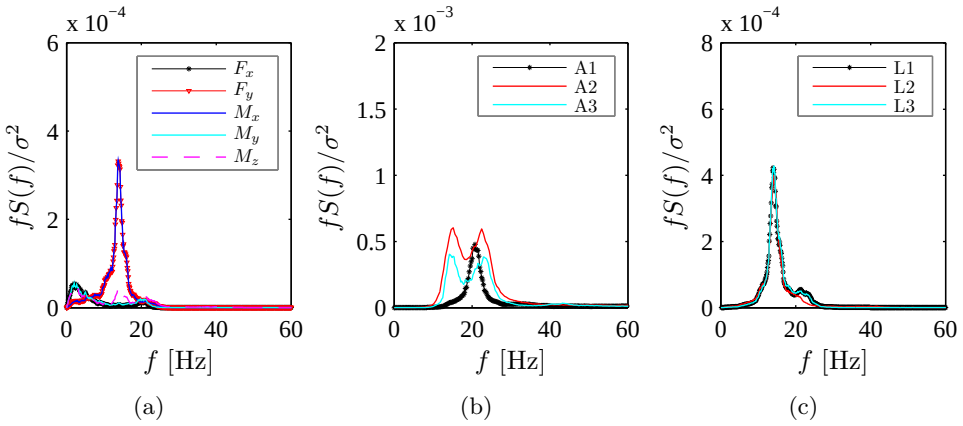

Fig. 6.57 Response spectra, test number 19.

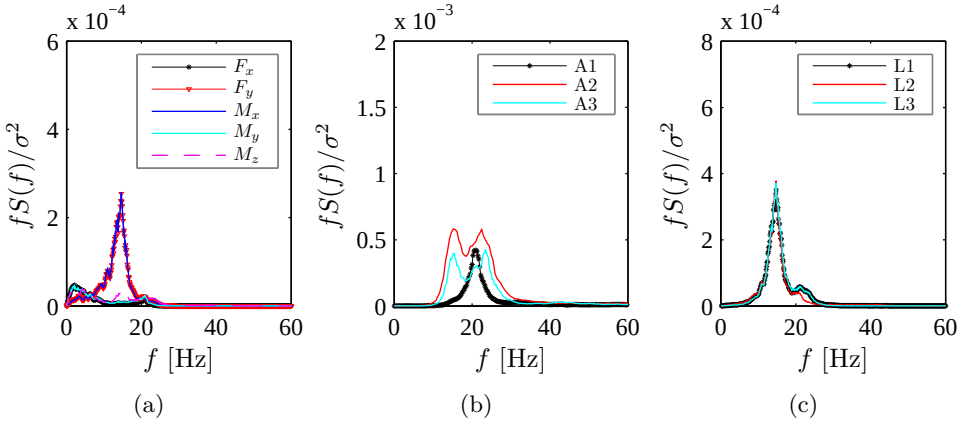

Fig. 6.58 Response spectra, test number 20.

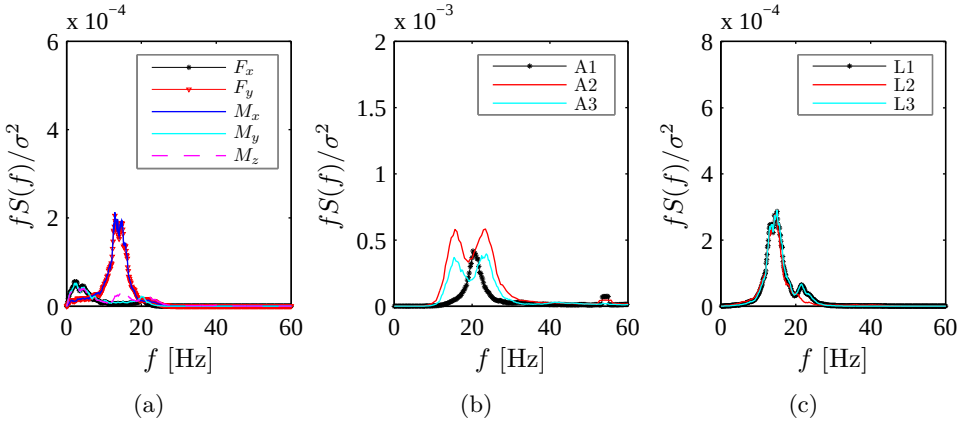

Fig. 6.59 Response spectra, test number 21.

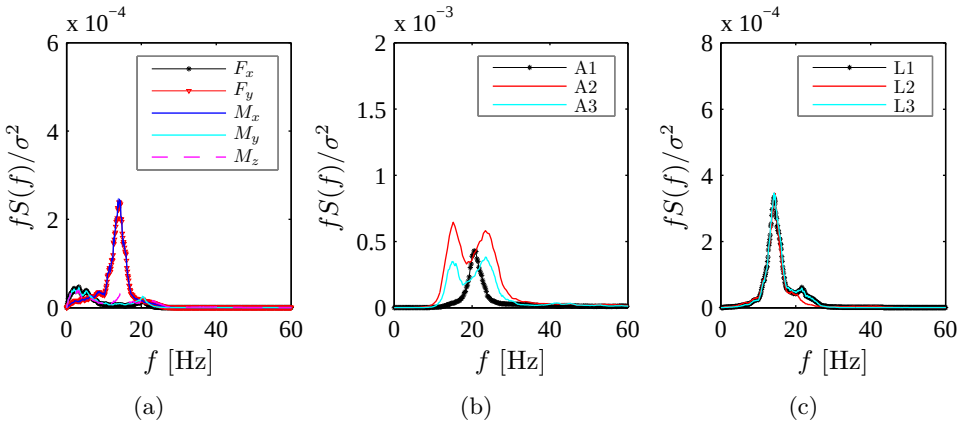

Fig. 6.60 Response spectra, test number 22.

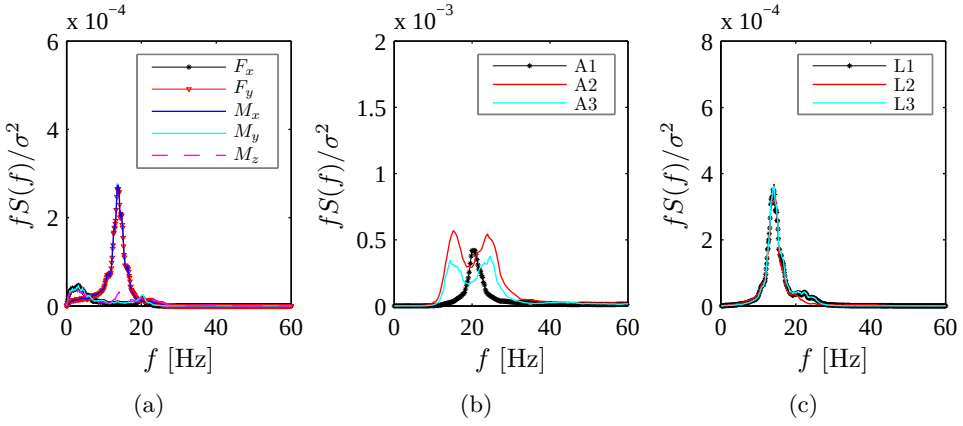

Fig. 6.61 Response spectra, test number 23.

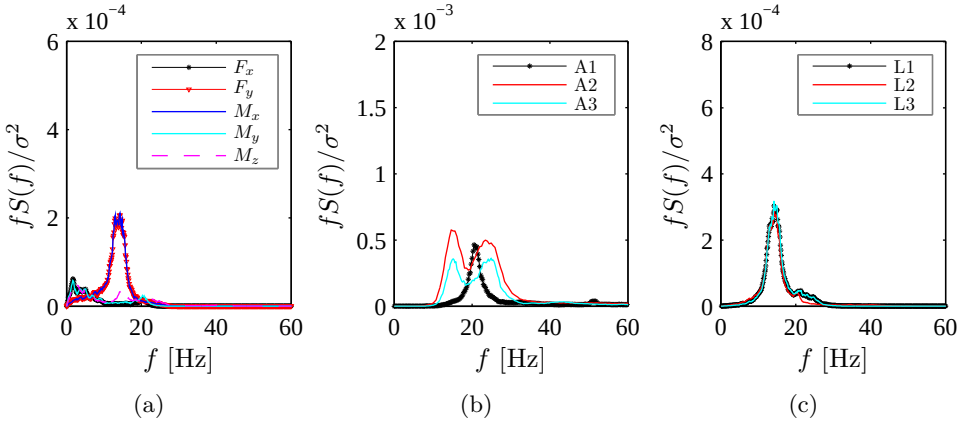

Fig. 6.62 Response spectra, test number 24.

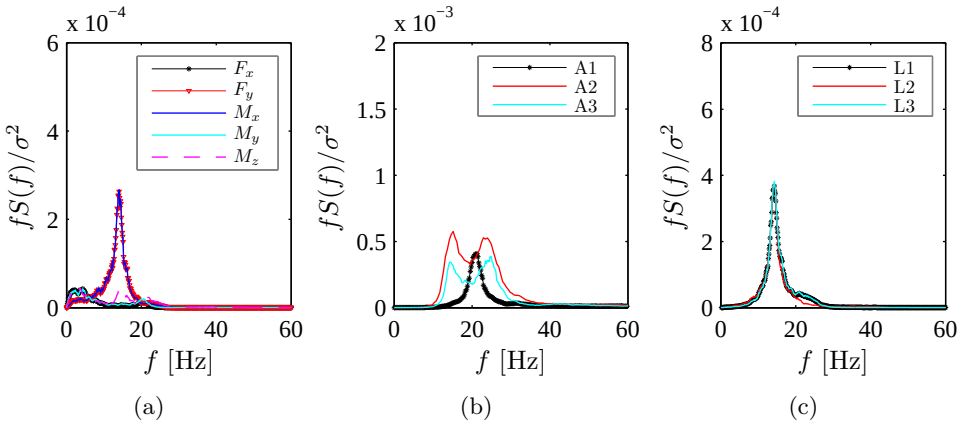

Fig. 6.63 Response spectra, test number 25.

6.9 Experimental identification of the lock-in phenomenon

From the spectral analysis of the across-wind loads and responses of the model for the different wind speeds considered, the variation of shedding frequency, f_s, with the reference mean wind speed U_h at the model height is derived [Fig. 6.64(a)]. Fig. 6.64(b) illustrates the same data expressed in terms of the following non-dimensional quantities:

- $U_h/(f_1 b)$, which is known as reduced velocity, U_r
- f_s/f_1.

The frequency f_1 in Fig. 6.64(b) is taken equal to 18.7 Hz, as measured from the free vibration response tests (subsection 6.4.3). The measured data fit the Strouhal law, that, in this plane, is expressed by the line:

$$\frac{f_s}{f_1} = St\frac{U_h}{f_1 b} \tag{6.22}$$

where St is taken equal to 0.095, at all the values of the reduced velocity, except within two wind speed ranges, identified with the vertical blue and red lines. In these ranges the shedding frequency violates the Strouhal law, since it is synchronized with the natural frequencies of the model.

In the first and prominent vortex resonance or lock-in range, f_s synchronizes with f_1, as seen from the coincidence of the spectral peaks in Fig. 6.44 - Fig. 6.47. The lower bound of the this wind speed range is taken equal to 14.6 m/s, that is the mean value between the reference wind speed at test 5, before synchronization, and that at test 6, when lock-in starts. The upper limit is assumed equal to 20.8 m/s, that is the mean wind speed at test 9, the last test in which the spectral peaks corresponding to f_s and f_1 can be considered overlapped, and that at test 10, after lock-in.

On the basis of analogous considerations, the second lock-in range, where f_s is synchronized with the natural frequency f_2 of the along-wind bending mode (Fig. 6.50 - Fig. 6.54), starts at $U_h = 21.9$ m/s and ends at $U_h = 24.1$ m/s.

The vertical blue and red lines in Fig. 6.64 are employed to limit the first and

second lock-in ranges, respectively, and will be displayed in the following figures in order to easily identify the synchronization ranges.

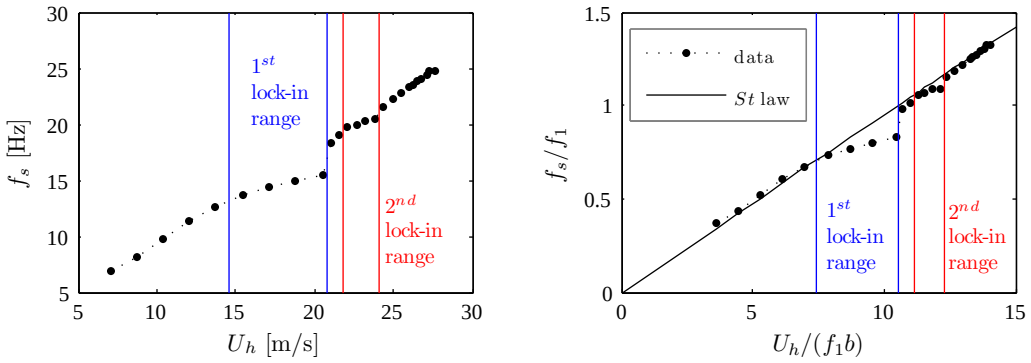

Fig. 6.64 Identification of the lock-in ranges: a) shedding frequency vs reference wind speed; b) non-dimensional representation and fitting to the Strouhal (St) law.

6.10 Dependence of modal frequencies on reference wind speed

From the spectral analysis of the response, a certain variation of the frequencies of vibration of the model, $f_n = f_1$ and $f_n = f_2$, corresponding to the across-wind and along-wind bending modes, respectively, is observed (Fig. 6.65). Fig. 6.65(a) illustrates the values of f_1 and f_2, taken from the spectral peaks of the response for the different tests performed (Fig. 6.39 - Fig. 6.63). In Fig. 6.65(b), the ratio between the actual value of the modal frequency, f_n, and its initial value measured from the free vibration tests (section 6.4.3), referred to as $f_{n,i}$ is shown. The variation of the modal frequencies observed is considered not related to aerodynamic stiffness, because of its significant value. It may rather be due to undesired modifications of the model stiffness encountered during the tests in which the model itself is subjected to increasing wind loads and vibrations. This consideration will be further explained and confirmed in section 7.3.

Taking into account the measured variation of the modal frequency, f_1, Fig. 6.64(b) is changed into Fig. 6.66 where the non-dimensional quantities $U_h/(f_1 b)$ and f_s/f_1 are calculated considering, at each step, the actual value of f_1. The lock-in ranges, where the Strouhal law is violated, are now more clearly identified from the figure. As shown in many literature works, e.g. Kwok and Melbourne (1981), the critical reduced velocity, at which the shedding frequency synchronizes with the lateral frequency in the case of a square-section aeroelastic model is close to 10 and it should correspond to $1/St$.

Since the straight line in Fig. 6.66 displays the Strouhal number law and, therefore, the variation of the shedding frequency of a stationary model with increasing wind speed, the reduced velocity at which f_s/f_1 is 1 is equal to the inverse of stationary body Strouhal number (Bearman and Obasaju, 1982).

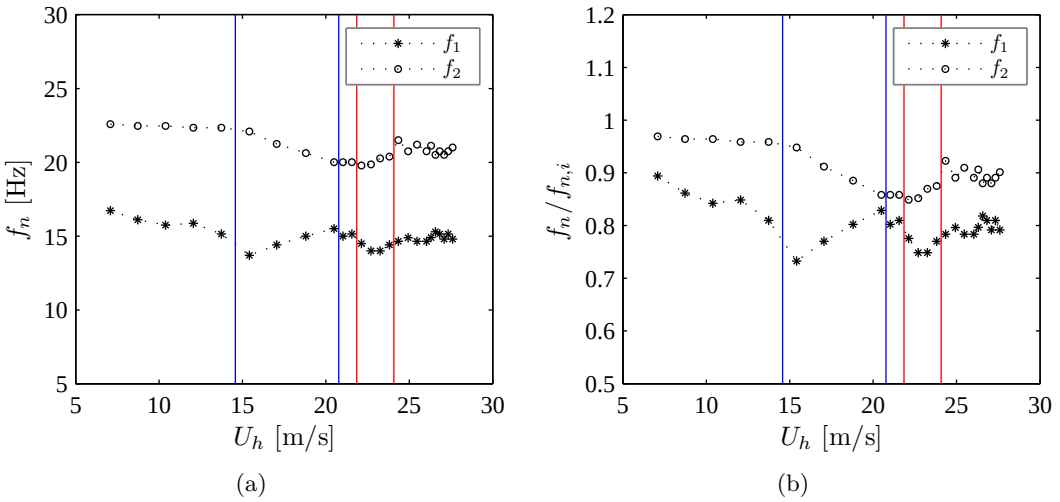

Fig. 6.65 Variation of the modal frequencies with reference wind speed: a) f_1 and f_2 versus U_h; b) variation with wind speed of the ratio between the current value of the modal frequency and its initial value from free vibration response tests.

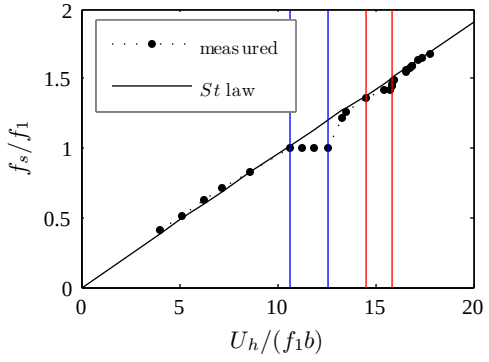

Fig. 6.66 Identification of the lock-in ranges and fitting to the Strouhal (St) law, considering the variation of the across-wind natural frequency.

6.11 Correlation analysis of across-wind pressure coefficients

Using the pressure measurements, an analysis of the correlation structure of the sideward pressure coefficients is carried out, considering first pressures registered at different taps on the same horizontal level (subsection 6.11.1) and then pressures at different levels above the tunnel floor, but measured along the same vertical axis (subsection 6.11.2). Fig. 6.67 shows the distribution of the pressure taps, with their identification codes, on sideward face 4, that will be referred to hereinafter.

The correlation coefficient between pressure coefficients, C_p^i and C_p^j, measured

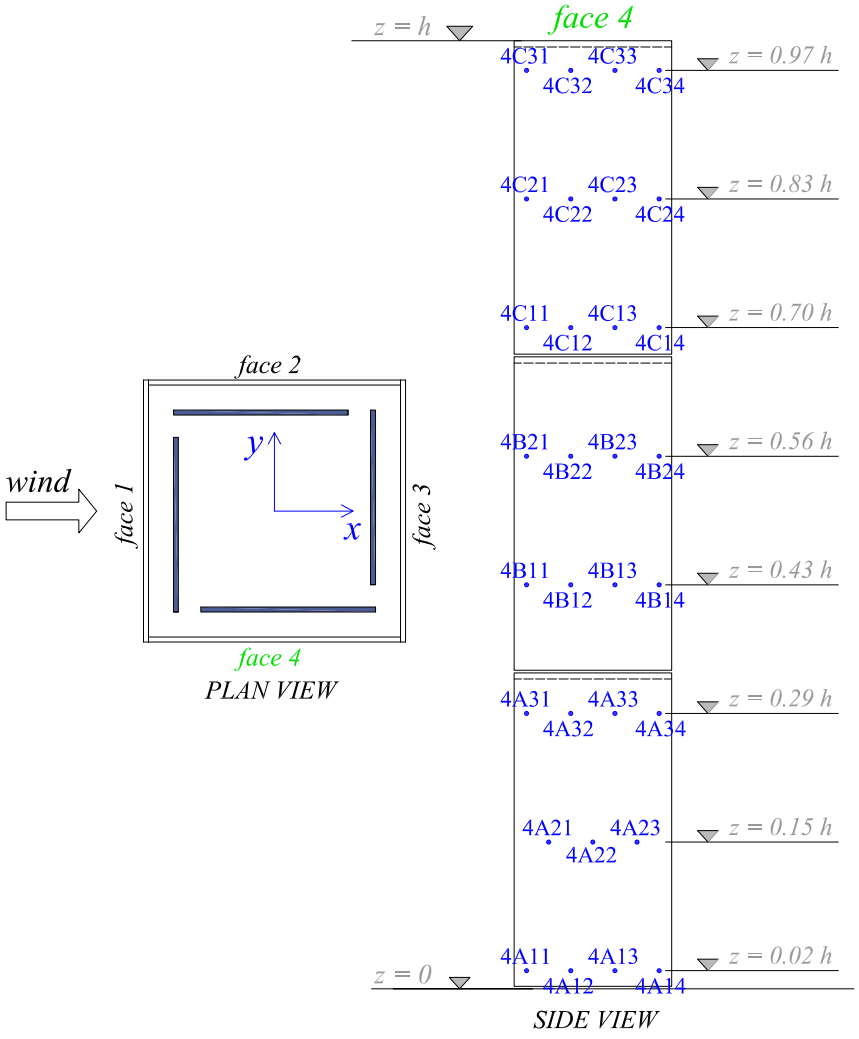

Fig. 6.67 Taps on sideward face 4 at different levels.

at two different taps, i and j, respectively can be estimated by:

$$r\left(C_p^i, C_p^j\right) = r_{i,j} = \frac{C_{ij}}{\sqrt{C_{ii}C_{jj}}} \tag{6.23}$$

where

$$C_{ij} = \frac{1}{N} \sum_{k=1}^{N} \left(C_{p_k}^{i} - \mu_{C_p^i} \right) \left(C_{p_k}^{j} - \mu_{C_p^j} \right) \tag{6.24}$$

In the following sections, for simplicity of notation, $C_{FBLN,i-FBLN,j}$ indicates the correlation coefficient between pressure coefficients at taps $FBLN, i$ and $FBLN, j$.

6.11.1 Correlation between sideward pressure coefficients at the same level

Figs. 6.68, 6.69, 6.70 and 6.71 illustrate the correlation coefficient between pressure coefficients at different taps located at the same level, for different values of the reference wind speed, U_h. Only taps on the sideward face 4 are considered (Fig. 6.67).

For example, Fig. 6.69 refers to the correlation between pressure coefficients at the four taps, namely 4B11, 4B12, 4B13 and 4B14, located on face 4, box B, level 1, at height z over the tunnel floor, equal to 0.43 h. An initial increase in correlation is observed for increasing wind speeds (from test 1 to test 6) especially at the highest taps levels (Figs. 6.70, 6.71), characterized by greater vibration amplitudes. However, it seems that the lock-in condition doesn't affect significantly the correlation between pressures measured on the sideward face at the same level. As a matter of fact, in the lock-in ranges, identified with the vertical blue and red lines, significantly higher values of the correlation coefficient are not observed, in general.

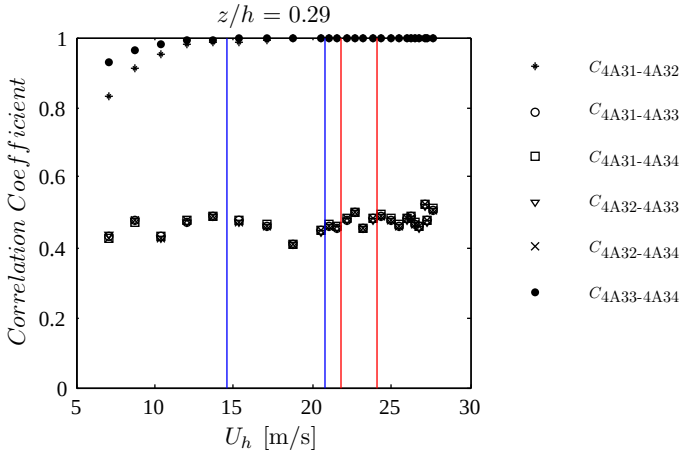

Fig. 6.68 Correlation between pressure coefficients at level $z/h = 0.29$ on sideward face number 4.

6.11.2 Correlation between sideward pressure coefficients at different levels

In this section an analysis of the correlation between pressure coefficients on the sideward face 4 at different levels above the tunnel floor is considered. Fig. 6.72 illustrates the correlation coefficient between pressures measured at eight taps, distributed on the sideward face 4 of the model at different heights. From some of the results (e.g curves $C_{4B12-4C12}$ and $C_{4B12-4C22}$) it seems that the correlation

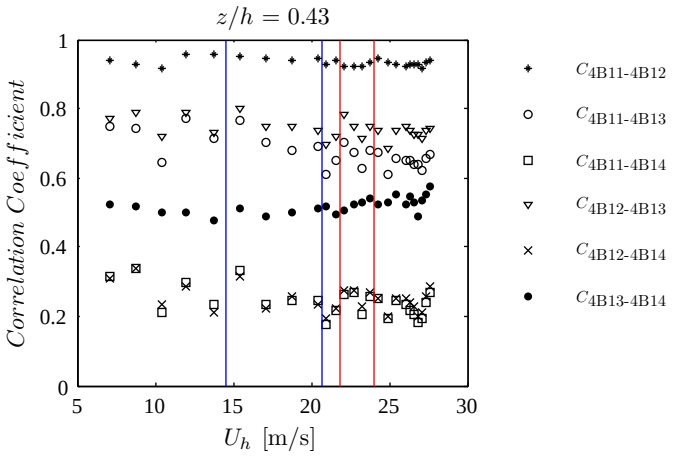

Fig. 6.69 Correlation between pressure coefficients at level $z/h = 0.43$ on sideward face number 4.

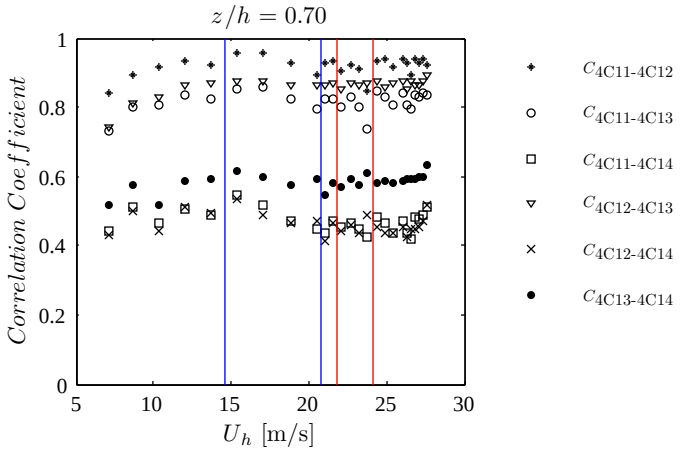

Fig. 6.70 Correlation between pressure coefficients at level $z/h = 0.70$ on sideward face number 4.

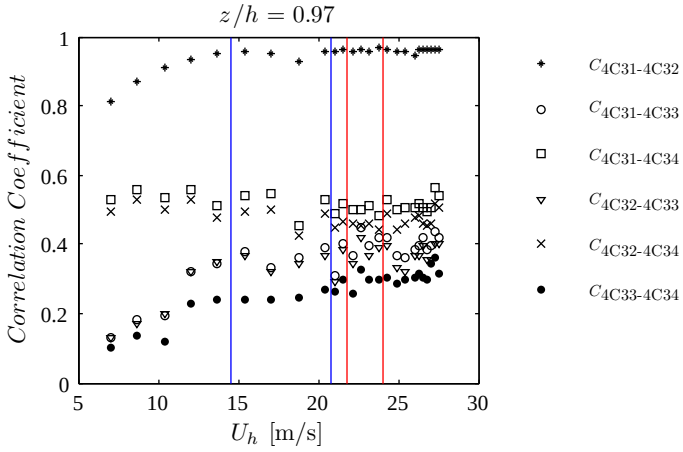

Fig. 6.71 Correlation between pressure coefficients at level $z/h = 0.97$ on sideward face number 4.

increases when lock-in condition is reached.

An alternative and further explaining representation is that of Fig. 6.73, which shows the correlation coefficient between pressures at the various levels, for different values of the reference wind speed, U_h, one before lock-in (7.08 m/s - test 3), one during lock-in (17.06 m/s - test 7) and one after lock-in (24.93 m/s - test 17). In each of the four pictures, one tap is fixed, e.g. that of level $z/h = 0.70$ in Fig. 6.73(b), and then the correlation is evaluated between pressure coefficients at this tap and at all the others under and above it along the same vertical axis. In Figs. 6.73(a), 6.73(b), 6.73(c) and 6.73(d) the correlation coefficients take their highest values during lock-in (red circles). The synchronization of the shedding frequency to the across-wind frequency of the model has, therefore, an effect in increasing the correlation between pressures on the sideward faces of the model.

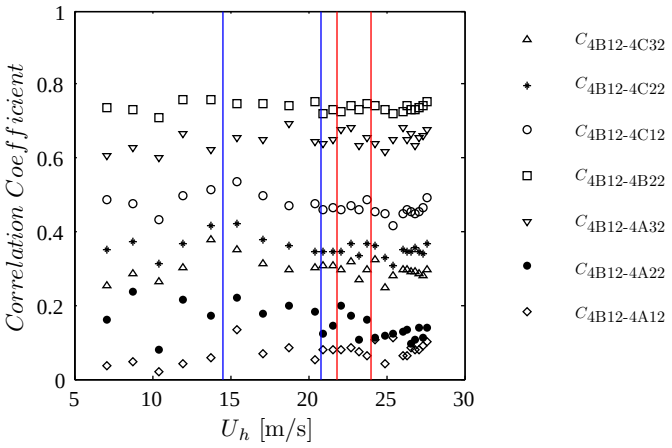

Fig. 6.72 Correlation between pressure coefficients measured at eight taps, distributed on the sideward face 4 of the model at different heights.

6.12 Across-wind displacement response

As previously mentioned, the across-wind response is measured by means of three displacement laser transducers, L1, L2, L3 (see Fig. 6.31). Figs. 6.74 - 6.76 illustrate the tip transverse displacement response measured by laser L1, before (Fig. 6.74), during (Fig. 6.75) and after (Fig. 6.76) lock-in, together with displacement spectra, where f_s, f_1 and f_2 indicate the shedding frequency and the first and the second natural frequencies, respectively. The across-wind displacement amplitude, y, is normalized with respect to the side dimension of the model $b = 10.5$ cm. It may be recognized that the lock-in condition produces resonant narrow-band [see Fig. 6.75(b)] vibrations. The resulting displacement signal can be regarded as quasi-sinusoidal with randomly varying amplitudes (beating oscillation).

The signals, measured by the three laser displacement transducers with a sampling frequency of 1000 Hz, are filtered using a low-pass filter with cutoff frequency of 100 Hz. Then, the mean square value of the across-wind displacement response σ_d^2 is calculated by integrating its PSD as follows [see also Eq. (4.12)]:

$$\sigma_d^2 = \int_0^\infty S_d(f)\, df \tag{6.25}$$

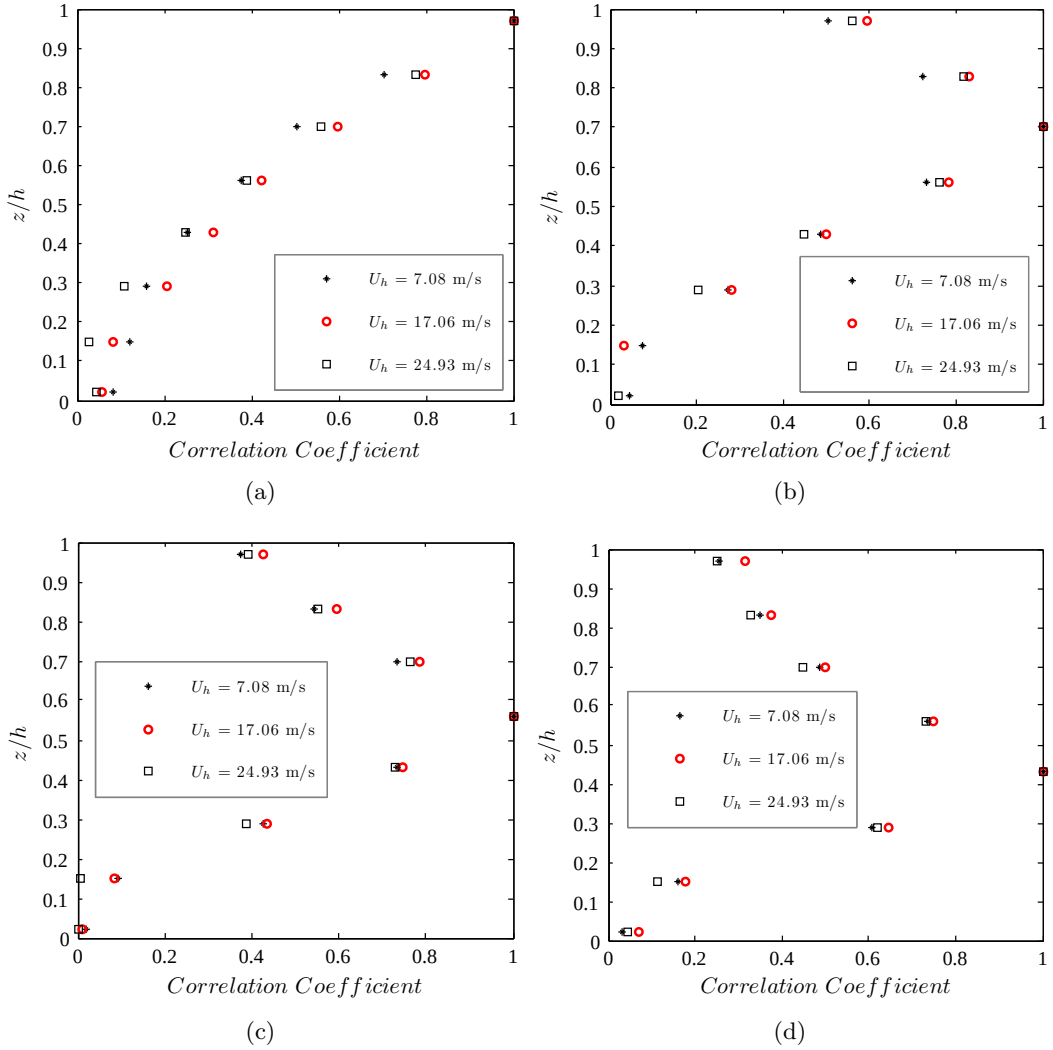

Fig. 6.73 Correlation between taps at different levels (sideward face 4, second tap at each level from the left side) before (U_h = 7.08 m/s), during (U_h = 17.06 m/s) and after (U_h = 24.93 m/s) lock-in: a) between tap 4C32 at level z/h = 0.97 and the others; b) between tap 4C12 at level z/h = 0.70 and the others; c) between tap 4B22 at level z/h = 0.56 and the others; d) between tap 4B12 at level z/h = 0.43 and the others.

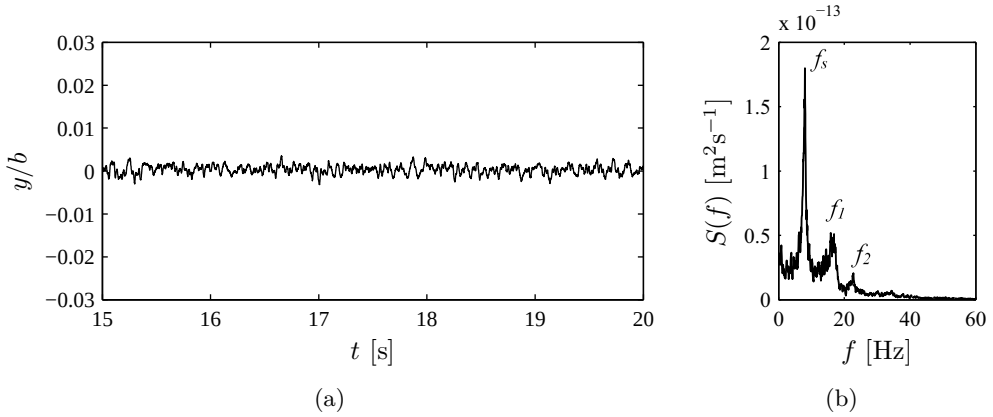

Fig. 6.74 Normalized across-flow tip displacement, measured by laser sensor L1, before lock-in (test 2): a) time-history; b) spectrum.

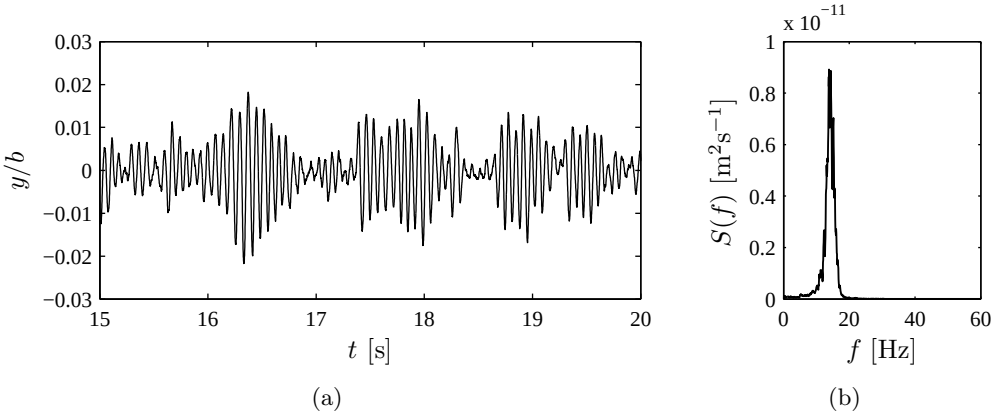

Fig. 6.75 Normalized across-flow tip displacement, measured by laser sensor L1, during lock-in (test 7): a) time-history; b) spectrum.

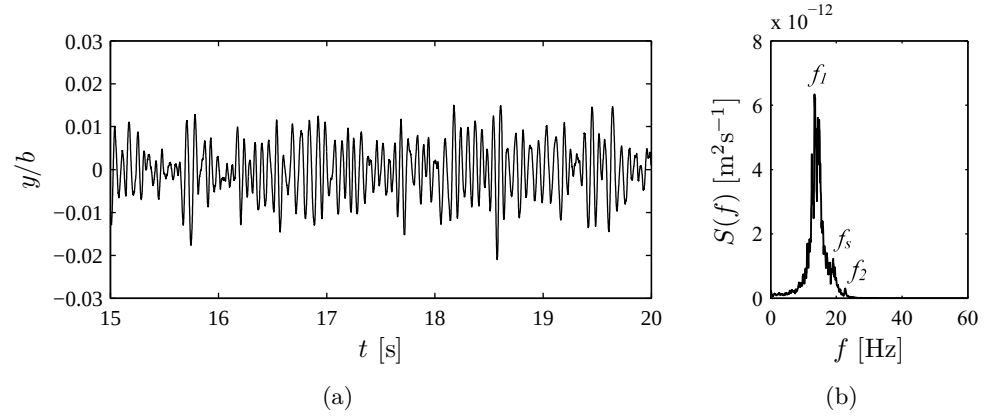

Fig. 6.76 Normalized across-flow tip displacement, measured by laser sensor L1, after lock-in (test 12): a) time-history; b) spectrum.

where d indicates in this case the lateral displacement y.

The standard deviation across-wind displacement response σ_d is then calculated from the square root of σ_d^2 and is shown in Fig. 6.77.

The standard deviation displacement response is then normalized as σ_d/b and presented as a function of the reduced velocity, calculated considering at each test the actual value of f_1 [Fig. 6.65(a)].

The RMS normalized tip deflection is the form most often observed in literature [Reinhold and Sparks (1979); Kwok and Melbourne (1981); Kareem (1982); Boggs (1992); Kawai (1992, 1995); Marukawa *et al.* (1996)]. Fig. 6.78 shows in logarithmic scales the normalized tip transverse deflection of the model, compared with other literature results achieved in similar experimental conditions. Results from Kwok and Melbourne (1981) refer to a 9:1:1 square tower with 6% structural damping ratio, tested in suburban wind conditions (power law exponent equal to 0.23, longitudinal turbulence intensity at the top equal to 0.07). Data from Boggs (1992), on the other hand, correspond to an 8:1:1 square tower model with 2.6 % structural damping ratio, tested again in suburban environment (power law exponent equal to 0.22 and turbulence intensity at model height approximately equal to 0.09).

Reminding that the tested aeroelastic model of the present study is a 6:1:1 aeroelastic square tower, with a mean structural damping associated to the first lateral mode equal to 5% and the simulated wind conditions are:

- exponent of the power law profile, $\alpha \approx 0.23$ (see paragraph 6.5.1),
- turbulence intensity at the model height, $I_u(h) \approx 0.04$ (paragraph 6.5.2),

it is possible to conclude that the measured transverse response is substantially in agreement with the literature results considered.

Increases of the measured across-wind tip displacement response are observed at reduced velocity close to 10, corresponding to its critical value, equal to the reciprocal of the identified Strouhal number. This response enhance is achieved in the lock-in range, where the model is operating near the peak of the wake energy spectrum illustrated in Figs. 6.44 - 6.47.

The evidence that the measured aeroelastic response is lower than that of the other literature works cited is attributed mainly to the higher structural damping and lower slenderness of the model under investigation.

6.13 Acceleration response

The tip acceleration response of the model is measured by means of accelerometer A1 in along-wind direction and accelerometer A2 in the across-wind direction. The model is also equipped with an eccentric accelerometer A3 [see Figs. 6.31 and 6.32(b)], used to calculate the angular acceleration a_α from Eq. 6.3.

Figs. 6.79 - 6.81 show the tip along-wind, $\ddot{x}$, and across-wind, $\ddot{y}$, acceleration responses measured by accelerometer A1 and A2, respectively, before (Fig. 6.79), during (Fig. 6.80) and after (Fig. 6.81) lock-in, together with acceleration spectra. Before synchronization the lateral acceleration amplitude already exceeds the longitudinal one [Fig. 6.79(a)]. The acceleration signals are dominated by the natural frequencies of vibration f_1 and f_2 and from the across-wind spectra the shedding

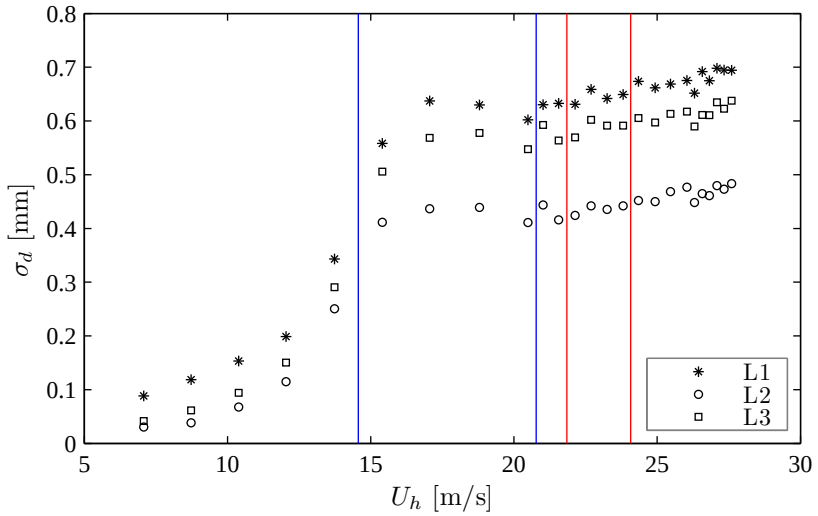

Fig. 6.77 Across-wind displacement response: a) tip displacement at the center (L1); b) tip displacement at the corner (L3); c) displacement at the center (L2) at level $z = \frac{2}{3}h$.

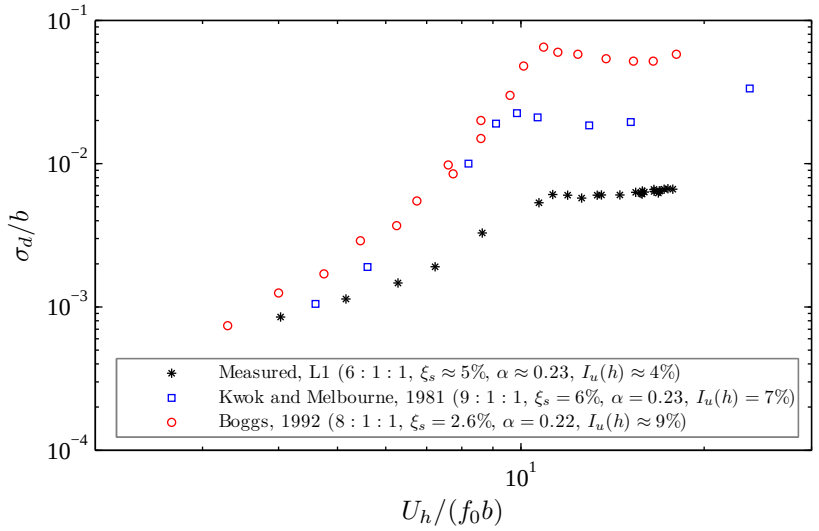

Fig. 6.78 Normalized tip lateral deflection versus reduced velocity (f_0 indicates the natural frequency in a lateral mode). Measured data compared with other literature results (Kwok and Melbourne, 1981; Boggs, 1992).

frequency f_s can be distinguished on the left side of f_1 peak [Fig. 6.79(b)]. During synchronization the lateral acceleration amplitude largely exceeds the longitudinal one [Fig. 6.80(a)] becoming up to one order of magnitude greater. As seen in the displacement response, the lock-in condition produces resonant narrow-band [see Fig. 6.80(b)] accelerations characterized by a single peak power spectrum. The resulting signal shows beating oscillations. After lock-in (test 12) the shedding frequency f_s is larger than the lateral frequency f_1 [see Fig. 6.81(b)]. The across-wind acceleration amplitude still largely exceeds the along-wind one [Fig. 6.81(a)].

As done for the displacements, the acceleration signals are filtered with a

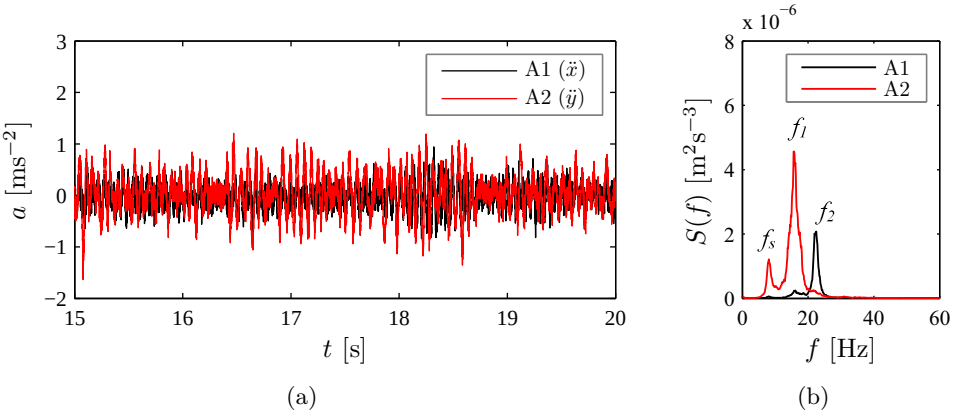

(a) (b)

Fig. 6.79 Along (A1) and across-flow (A2) tip accelerations, measured before lock-in (test 2): a) time-history; b) spectrum.

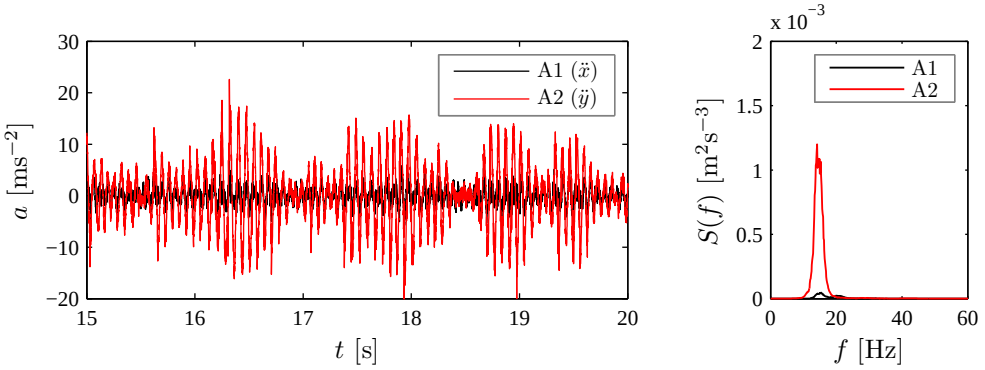

(a) (b)

Fig. 6.80 Along (A1) and across-flow (A2) tip accelerations, measured during lock-in (test 7): a) time-history; b) spectrum.

low-pass filter with 100 Hz cutoff frequency. The standard deviation acceleration response σ_a is then calculated as the square root of σ_a^2, defined as:

$$\sigma_a^2 = \int_0^\infty S_a(f)\, df \tag{6.26}$$

where a indicates acceleration.

The standard deviation along-wind and across-wind acceleration responses are

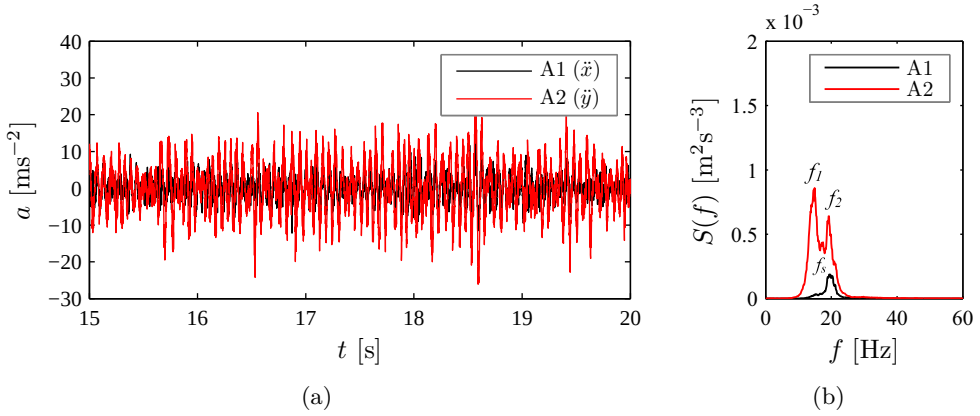

(a) (b)

Fig. 6.81 Along (A1) and across-flow (A2) tip accelerations, measured after lock-in (test 12): a) time-history; b) spectrum.

plotted as a function of the mean reference wind speed, U_h, in Fig. 6.82(a) and Fig. 6.82(b), respectively. The across-wind response exceeds the along-wind one, especially in the lock-in range where the former is more than twice the latter. The standard deviation angular acceleration σ_{a_α} versus U_h is illustrated in Fig. 6.83(a). The power spectral density of the angular acceleration response, calculated at test 2 [Fig. 6.83(b)], shows a dominating peak at the torsional mode frequency. Spectra for other tests show a prominent peak at approximately the same torsional frequency.

In Fig. 6.84(a) the standard deviation of the acceleration response at the side-

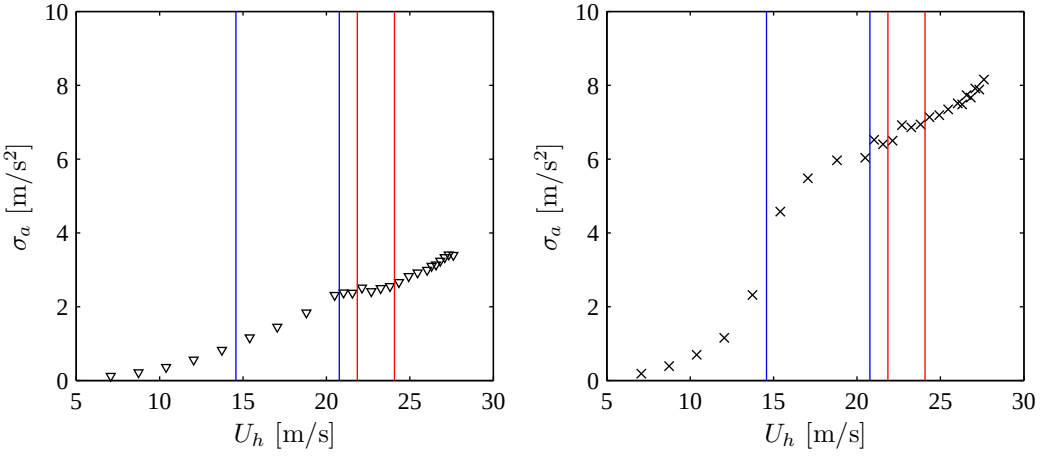

(a) (b)

Fig. 6.82 Acceleration response: a) along-wind direction (A1); b) across-wind direction (A2).

ward downwind corner (A3) is shown. It is very close to that measured by the accelerometer A2, placed at the center of the sideward face 2. Furthermore, the power spectral density of the across-wind acceleration response at the corner [Fig. 6.84(b)], evaluated before (test 4, $U_h = 12.05$ m/s), during (test 7, $U_h = 17.06$ m/s) and after (test 12, $U_h = 22.13$ m/s) lock-in does not show a significant contribution of the torsional mode. The response at the corner, where torsional effects could increase

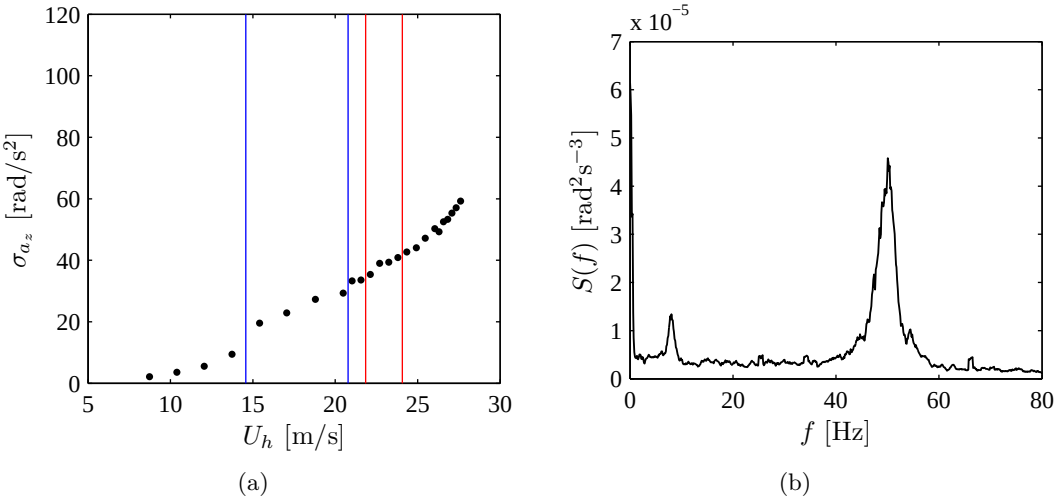

Fig. 6.83 Angular acceleration response: a) standard deviation vs reference wind speed; b) power spectral density ($U_h = 8.73$ m/s).

accelerations, is, in this case, that at the center of the face.

It can be concluded that, as expected, the lateral acceleration response exceeds

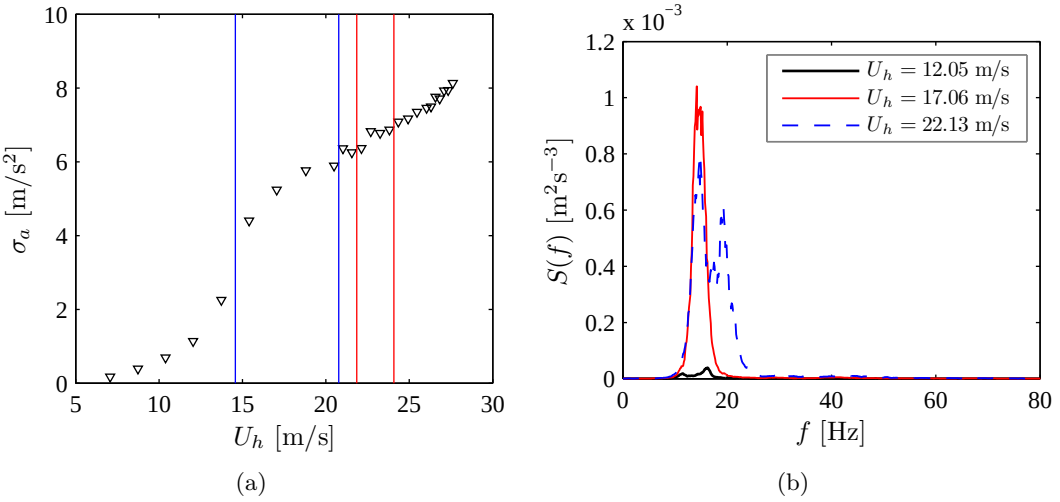

Fig. 6.84 Acceleration response at the corner (A3): a) standard deviation vs reference wind speed; b) power spectral density.

that in the along-wind direction, especially at high values of the wind speed and shows an increase in the lock-in range. For this reason the acceleration response which will be used for the serviceability checking procedure and risk assessment in chapter 8 is the tip across-wind acceleration.

6.14 Overall forces and moments from HFFB and SMPSS measurements

6.14.1 Forces and moments at the base of the model form HFFB tests

The global forces at the base of the aeroelastic model measured by the High Frequency Force Balance, HFFB, described in subsection 6.3.4, are two shear forces, F_x and F_y, two bending moments, M_x and M_y, and a torsional moment M_z. The global reference system with respect to the incoming wind direction is that illustrated in Fig. 6.31(a), where z is the vertical axis pointing "out of the page" towards the viewer.

For the description of the results, force and moment coefficients are defined, according to subsection 3.2.2, respectively, as:

$$C_{F_i}(t) = \frac{F_i(t)}{\frac{1}{2}\rho {U_h}^2 bh}, \text{ with } i = x, y \tag{6.27}$$

$$C_{M_i}(t) = \frac{M_i(t)}{\frac{1}{2}\rho {U_h}^2 bh^2}, \text{ with } i = x, y, z \tag{6.28}$$

where ρ is the air density, calculated on the basis of pressure and temperature conditions in the wind tunnel, b is the width of the model (10.5 cm), h is the height (60.8 cm) and U_h is the mean wind speed at the top of the model (see Table 6.5 for U_h values during the 25 tests performed).

6.14.2 Overall wind loads from pressure measurements

From pressure measurements (Synchronous Multi-Pressure Sensing System, SMPSS, in subsection 5.2.2), the global wind-induced forces acting on the model can be estimated by means of the following relationships:

$$F_x(t) = \sum_{i=1}^{N} p_i(t) A_i n_{ix} \tag{6.29}$$

$$F_y(t) = \sum_{i=1}^{N} p_i(t) A_i n_{iy} \tag{6.30}$$

where p_i indicates the pressure at tap i and is equal to the pressure coefficient multiplied by the dynamic pressure at the tap level [see Eq. (6.20)]. Pressures are positive when directed towards the interior of the model. A_i indicates the tributary area of tap i (Fig. 6.85), where pressure is assumed constant. N is the total number of pressure taps, while n_{ix} and n_{iy} are the direction cosines of the normal to the model surface at tap i.

Bending moments M_x and M_y at the base are defined, accordingly, as:

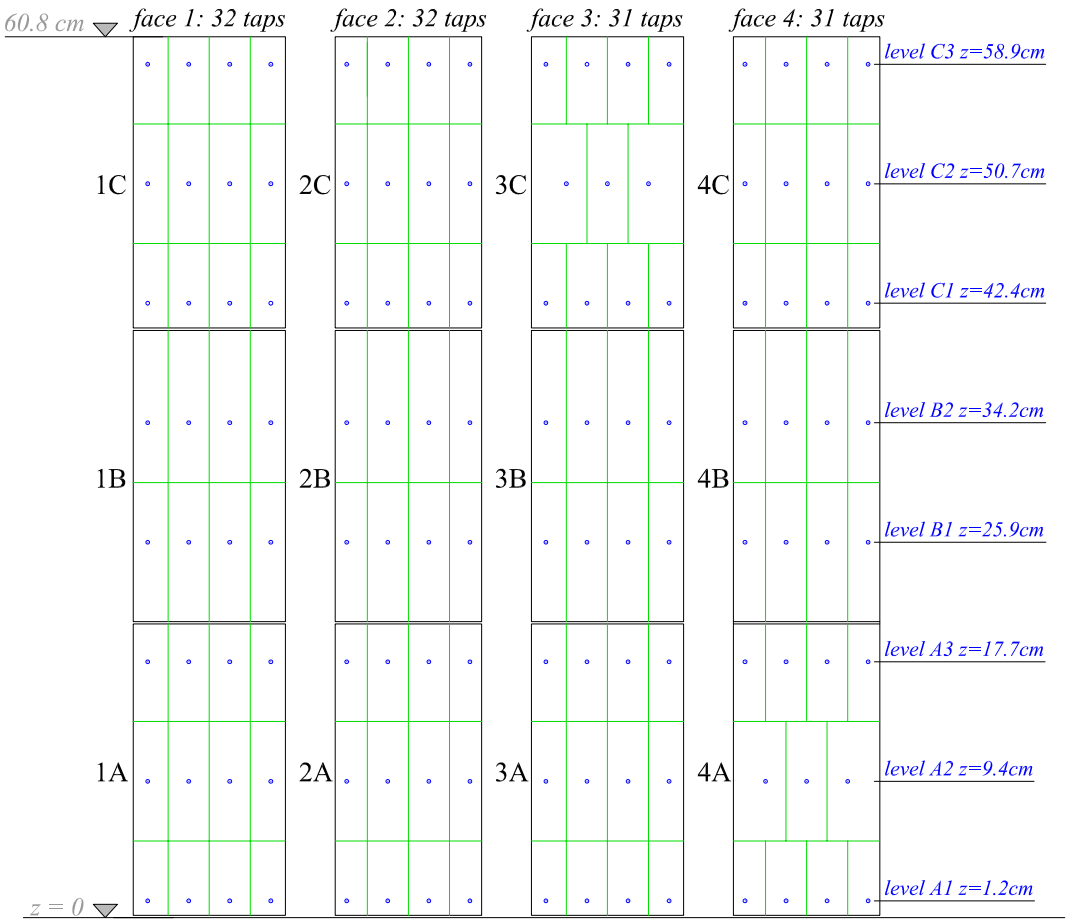

Fig. 6.85 Pressure taps distribution and tributary areas.

$$M_x(t) = -\sum_{i=1}^{N} p_i(t) A_i z_i n_{iy} \tag{6.31}$$

$$M_y(t) = \sum_{i=1}^{N} p_i(t) A_i z_i n_{ix} \tag{6.32}$$

where z_i is the level of the center of tributary area of tap i above the tunnel floor (base of the model). The minus sign in Eq. (6.31) is motivated by the fact that positive forces along y direction correspond to negative moments about x axis.

Finally, the torsional moment M_z can be calculated multiplying each force component by the horizontal arm with respect to the vertical axis, l_i, taken with the proper sign, as:

$$M_z(t) = \sum_{i=1}^{N} p_i(t) A_i l_i \tag{6.33}$$

Forces and moments from pressure measurements can be normalized using Eqs. 6.27 and 6.28, respectively.

6.14.3 Comparison between HFFB and SMPSS results

Results about overall forces, F_x and F_y, and moments, M_x, M_y and M_z, from HFFB and SMPSS are given in Figs. 6.86, 6.87 and 6.88 in terms of mean values of the corresponding coefficients, indicated with $\overline{C_{F_x}}$, $\overline{C_{F_y}}$, $\overline{C_{M_x}}$, $\overline{C_{M_y}}$, $\overline{C_{M_z}}$, respectively. Results from HFFB and SMPSS are compared only in terms of mean values because dynamic measurements with the balance have proved unreliable. Results form HFFB are displayed with the symbol '$*$' while those form SMPSS with 'o'.

According to the reference system adopted, since wind direction is parallel to x axis, C_{F_x} and C_{F_y} can be regarded as drag and lift coefficient, respectively.

Force and moment coefficients from HFFB and SMPSS are in a general good agreement in the entire wind speed range tested.

The mean drag coefficient [Fig. 6.86(a)] is approximately equal to 1.2 and slightly decreasing with wind speed. Comparing this value with the literature results illustrated in chapter 3, it is possible to conclude that a mean drag coefficient of 1.2, lower than that referred to 2-D flows (see Table 3.1), is in agreement with results from Scruton and Rogers (1972) in Fig. 3.21 for an aspect ratio $2h/b \approx 12$. Reading directly Fig. 3.21, referred to smooth flow conditions, the drag coefficient should be approximately 1.5. The fact that, in the current research, a lower value is obtained is thought due to the presence of turbulence. Furthermore, plotting the mean drag coefficient as a function of Reynolds number (Fig. 6.89), a certain decrease of $C_D = C_{F_x}$ with Re is shown. This result is considered in substantial agreement with Fig. 3.17 from Scruton (1981). This consideration suggests the idea that the flow around the model is influenced by possible Reynolds effects.

The mean lift coefficient [Fig. 6.86(b)] form pressure measurements is, as expected, equal to zero and in agreement with literature results. The values, greater than zero, obtained from the balance may be motivated, as later explained, by a small degree of orientation of the balance axes to the model ones. A similar con-

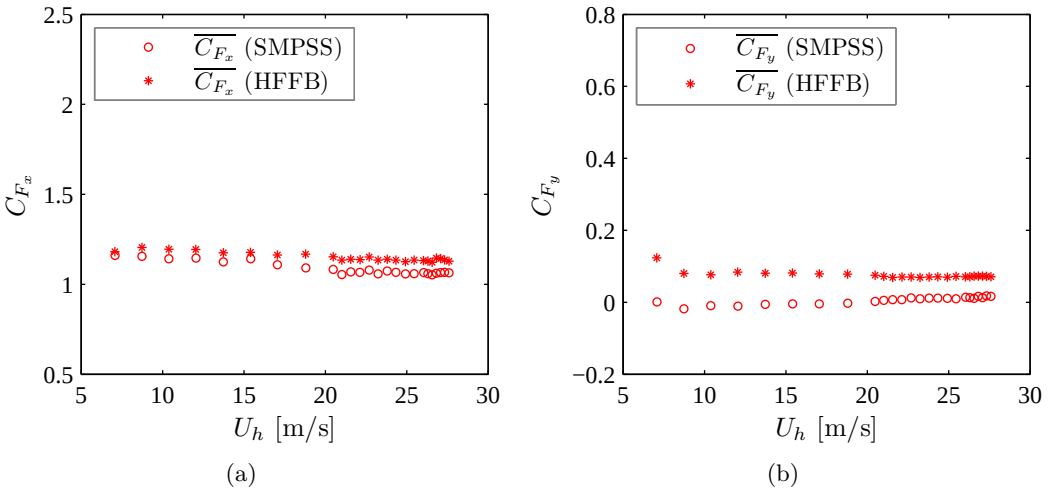

Fig. 6.86 Mean drag coefficient (a) and lift coefficient (b) from HFFB and SMPSS as functions of wind speed.

sideration can be derived from the across-wind bending moment coefficient C_{M_x} in Fig. 6.87(a).

The mean value of C_{F_x} is about 1.2 and a mean value of 0.75 can be estimated

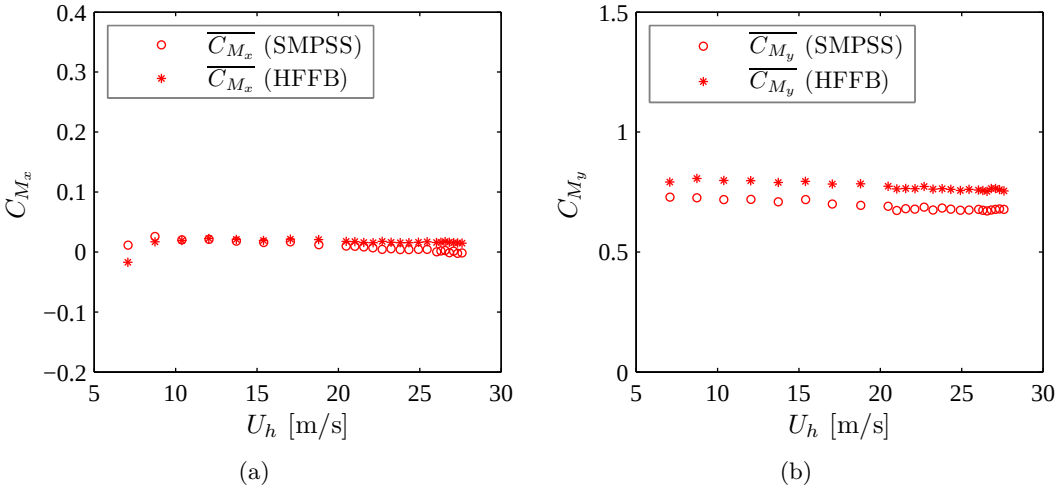

Fig. 6.87 Mean bending moment coefficient in across-wind (a) and along-wind directions (b) from HFFB and SMPSS as functions of wind speed.

for C_{M_y} [from SMPSS results in Fig. 6.87(b)]. The ratio $\frac{\overline{C_{M_y}}}{\overline{C_{F_x}}} = \frac{\overline{M_y}}{h\overline{F_x}}$ is approximately equal to 0.63, i.e. the overall wind force can be considered applied at approximately 2/3 of the model height.

Fig. 6.88 illustrates, for the sake of completeness, the results concerning the torsional moment coefficient, whose mean values are approximately equal to zero.

As previously mentioned, the observed distance between mean coefficients measured with the balance and calculated from pressure measurements is considered due to a certain orientation between the model axes and the balance axes. In other

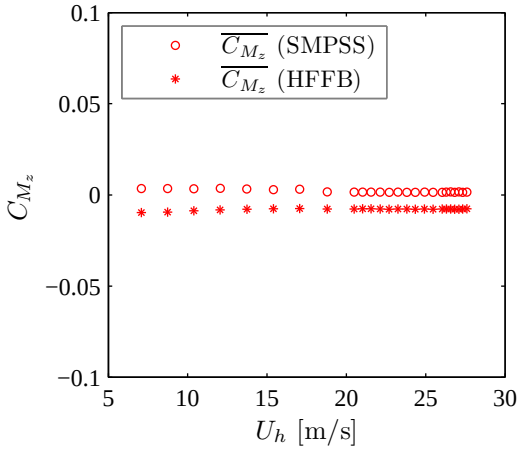

Fig. 6.88 Mean torsional moment coefficient from HFFB and SMPSS as functions of wind speed.

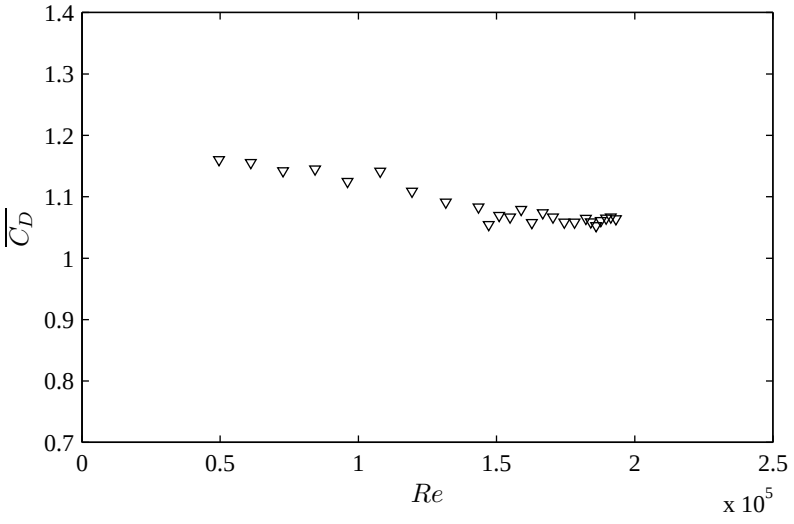

Fig. 6.89 Mean drag coefficient as a function of Reynolds number.

words, the forces measured by the balance are not exactly along the x and y axes of the model along which the overall resultants from surface pressures are evaluated. If a certain orientation angle between balance axes and body axes exists, the forces measured from the balance can be compared to those measured from the pressures only properly combining their components along the body axes. Fig. 6.90 illustrates the force coefficients from HFFB and SMPSS calculated with an angle of 3° between the balance and the body axes. Agreement between HFFB and SMPSS results is significantly improved.

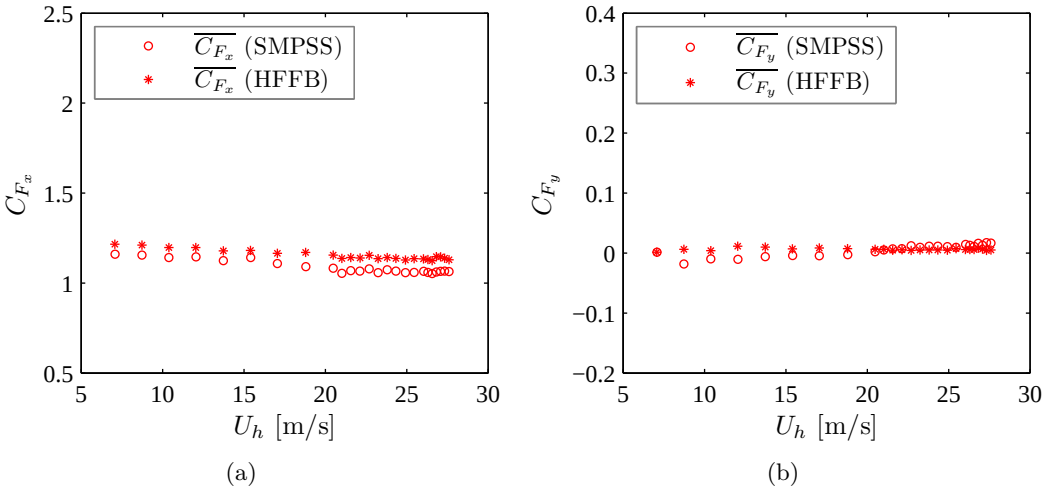

Fig. 6.90 Mean drag coefficient (a) and lift coefficient (b) from HFFB and SMPSS as functions of wind speed, having considered an angle of 3° between the model axes and the balance axes.

6.15 Summary and main remarks

In this chapter the experimental activity carried out in the boundary layer wind tunnel is illustrated. The model tested is a continuous equivalent aeroelastic model of a regular 6:1:1 tall building, made of an external non-structural "skin" to maintain the overall geometry and an internal "skeleton" providing the stiffness properties to the model. The natural frequencies and mode shapes of the model mounted on its supporting system are identified through free vibration tests.

The simulated flow conditions correspond to suburban terrain. The mean wind speed profile is characterized by a power law exponent approximately equal to 0.23. The roughness length is approximately equal to 0.25 cm. The wind flow direction is perpendicular to one face (zero angle of incidence).

The model is equipped with a quite complex instrumentation setup, which allows the simultaneous measurement of pressures, overall forces, across-wind displacements and along-wind and across-wind accelerations. Wind tunnel tests are carried out for a wide range of wind speeds, including the vortex resonance condition, at which the shedding frequency locks on the transverse natural frequency of the model.

From the spectral analysis of the pressure coefficients on the sideward faces the Strouhal number is evaluated and its possible variation along the model height is discussed. The spectral analysis of the different components of the response enables

the identification of the lock-in wind speed range. A certain variation of the modal frequencies is also observed. The vortex resonance condition is found to affect the correlation structure of pressures. A slight increase in the correlation coefficient between sideward pressures at different levels is recognized during lock-in.

At the critical velocity both displacement and acceleration responses in the across-wind direction display an increase in the RMS values. The normalized tip displacement response is compared with that from other literature studies. As expected, the tip across-wind acceleration response largely exceeds that in the along-wind direction. Torsional mode effects on the across-wind acceleration response at the top of the model can be considered negligible.

Mean values of the overall forces and moments measured with the base balance are in general agreement with the corresponding values calculated from integration of pressures on the model surface.

Chapter 7

Identification of aeroelastic effects in across-wind response

7.1 Introduction

For many tall buildings the acceleration response, that has to be limited under proper thresholds for the comfort of the occupants, is usually larger in the across-wind direction than in the along-wind direction and possible aeroelastic phenomena, such as lock-in, can affect this response. Principle questions which may arise are: "how does aeroelasticity affect the across-wind acceleration response?" and "is it conservative or not to neglect motion-induced effects?".

In this chapter the motion-induced or aeroelastic effects involving the across-wind response of the physical aeroelastic model tested in the wind tunnel (chapter 6) are identified. For this purpose a numerical model replicating the physical one is developed (section 7.2). In section 7.3 the numerical model is validated. In other words, it is adjusted until its numerical across-wind response meets the measured one. Then, in section 7.4 aeroelastic effects in terms of across-wind aerodynamic damping, are identified comparing, for different wind speed values, the measured response with the numerical one, calculated from pressures on a rigid model.

7.2 Numerical model

7.2.1 Description of the finite element model

The response of the aeroelastic model to wind loads measured from wind tunnel tests is numerically evaluated by means of a shell-type Finite Element Method (FEM) model (Figs. 7.1 and 7.2). Time-domain dynamic analysis is performed applying to the numerical model the time histories of wind loads as they were directly measured in the wind tunnel on the aeroelastic model tested.

In order to reproduce numerically the behavior of the aeroelastic model tested in the wind tunnel, the FEM model has to be developed according to the geometric and dynamic characteristics of the physical one (subsection 6.4.3), including natural frequencies, mode shapes and modal damping values.

The material and geometric features of the aluminum plates and the plexiglas boxes are defined in order to correspond, as close as possible, to reality. Additional masses due to pneumatic tubes and pressure transducers, accommodated inside the

model, are also assigned.

The internal structure is connected at the bottom to a rigid frame that models the wooden support which, approximately 5 cm under the tunnel floor, connects the physical model to the HFFB. The FEM model is restrained by means of a one-joint grounded link, whose stiffness properties can be properly assigned in order to meet the identified natural frequencies. The small coupling between the bending modes observed from the spectral analysis of the response (section 6.8), is neglected.

In order to numerically evaluate the response of the FEM model to the loads

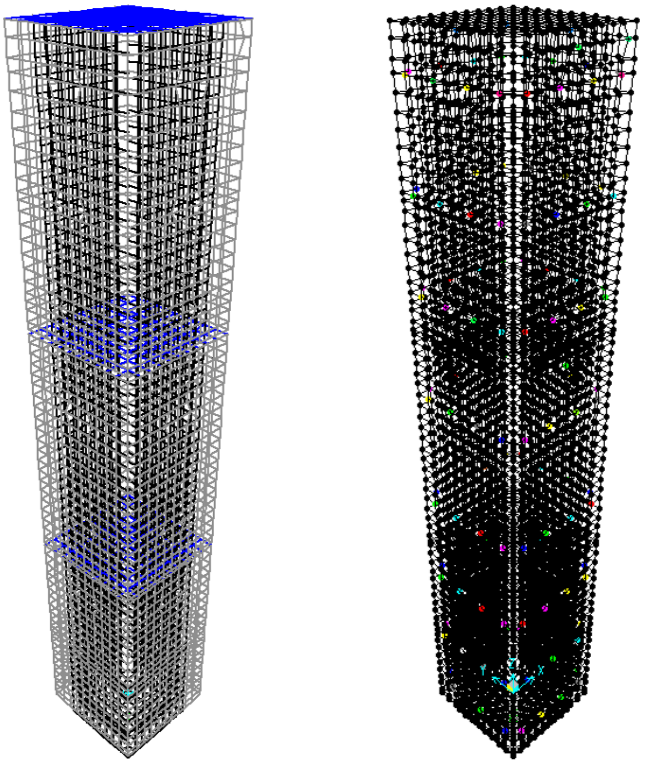

(a) (b)

Fig. 7.1 Finite element model: a) global three-dimensional view illustrating the outer shell (in gray), the rigid floors (in blue), the internal structure (in black); b) three-dimensional view showing the joints where wind loads are applied.

measured in the wind tunnel, a set of joints is defined to properly replicate the point of application of wind loads [Fig. 7.1(b)]. Wind forces are obtained from the pressure time histories, measured in the wind tunnel at each pressure tap, multiplying each pressure signal by the corresponding tributary area (Fig. 6.85). The point of application of each force coincides with the geometric center of the tributary area.

Disregarding the variation of the modal frequencies f_1 and f_2, measured during wind tunnel tests, with respect to their values identified from free vibration tests (Fig. 6.65), the stiffness properties of the grounded link are initially calibrated in order to obtain the natural frequencies of the physical model measured during test 1 (at the minimum value of the mean wind speed). Modal damping is assigned to the three modes included in the modal analysis, according to its identified mean values (Table 6.4), corresponding to damping ratios equal to 0.05, 0.016, 0.046, for the first bending mode, the second bending mode and the torsional mode, respectively.

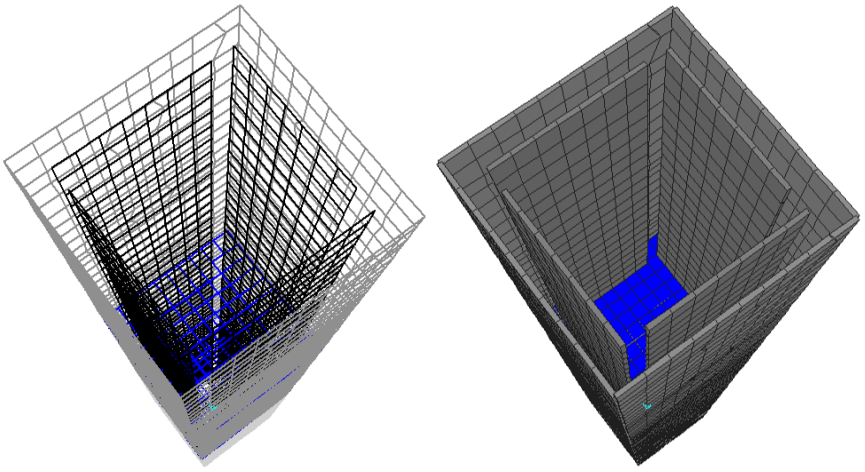

(a) (b)

Fig. 7.2 View from the top of the model (the rigid floor at the top is hidden for a better displaying of the internal structure): a) shell edges representation; b) extruded view.

Table 7.1 illustrates modal frequencies and damping values of the numerical model, at its first setting. Fig. 7.3 shows the first three mode shapes (linear bending modes) obtained from modal analysis.

With the aim of identifying aeroelastic effects involving the across-wind response of the physical model, with particular reference to the acceleration response governing the serviceability design of tall buildings addressed in this study, a special joint is defined in the FEM model, replicating the position of the accelerometer A2. At this joint the across-wind acceleration response of the FEM model is estimated through the definition of a proper output time history.

Table 7.1 First three modes frequencies and damping ratios of the FEM model at its first setting.

Mode	Description	Frequency Hz	Damping ratio %
1	bending - weak axis	16.7	5.0
2	bending - strong axis	22.6	1.6
3	torsional	52.3	4.6

7.3 Validation of the numerical model

During wind tunnel tests wind pressures and responses of the aeroelastic model were simultaneously measured for 25 different values of the mean wind speed (Table 6.5). In order to validate the FEM model, a comparison is carried out between the tip across-wind acceleration response, measured in the tunnel (later indicated

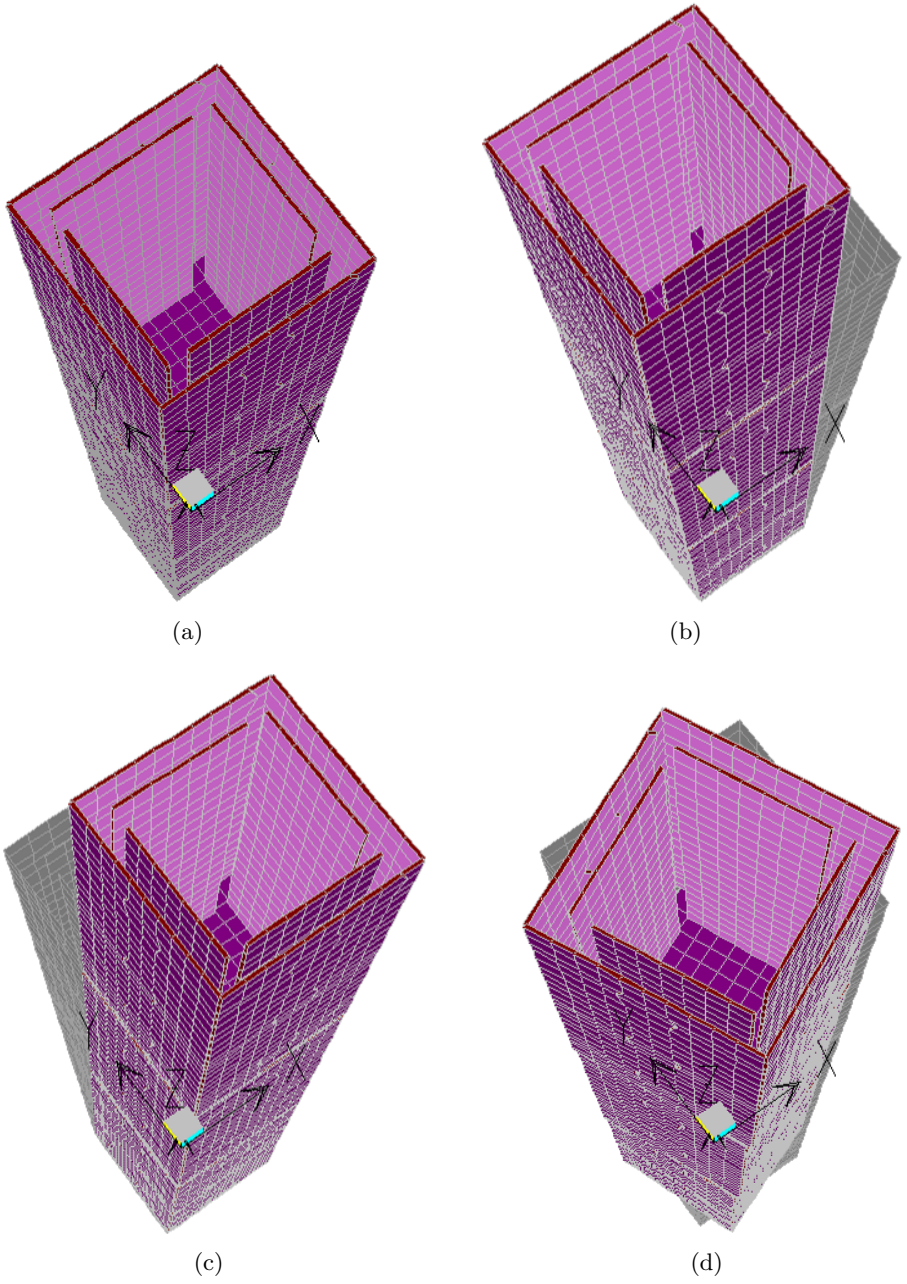

Fig. 7.3 Modal analysis results: a) undeformed shape; b) first bending mode; c) second bending mode; d) torsional mode.

with "Measured"), and that calculated from the FEM model, loaded with the pressure field measured on the aeroelastic model (indicated with "Num. Aer."). These two responses have to be coincident, if all measurements were properly carried out, since any motion-induced effects should be accounted for in the pressure signals themselves.

Wind loads are obtained from pressure measurements and applied to the model as time-histories forcing functions. A reduced selection of the 25 wind speeds tested is considered, namely tests 1-9, 12, 15, 18, 20, 25, judging less relevant the numerous tests after lock-in with close values of wind speed. The dynamic response is evaluated performing a linear modal time-history analysis (modal superposition).

The free vibration tests highlighted a significant dependence of the first mode damping on vibration amplitude [Fig. 6.25(a)]. Furthermore, the spectral analysis of the measured response has pointed out a relevant variation of the first mode frequency with wind speed (Fig. 6.65, section 6.10). For these reasons, the across-wind response, calculated for each wind speed from the numerical model, with the chosen values of the first mode frequency and damping, is reasonably different from the measured one.

Fig. 7.4 illustrates the response spectra at mean wind speed U_h equal to 8.63

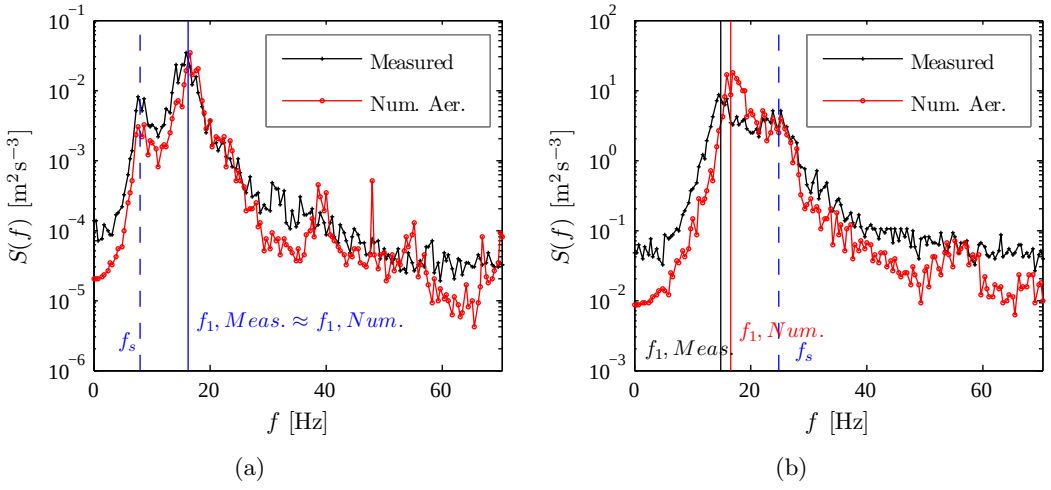

Fig. 7.4 a) Across-wind tip acceleration response spectra from measurements and numerical prediction. a) $U_h = 8.73$ m/s; b) $U_h = 27.60$ m/s.

m/s [Fig. 7.4(a)] and 17.60 m/s [Fig. 7.4(b)]. In Fig. 7.4(a) the distance between the across-wind peaks from the measured and the numerical response is negligible. It is not the case at a higher value of the wind speed, where the measured frequency f_1 is significantly lower than its initial value, as seen in section 6.10, Fig. 6.65.

This mismatch of the spectral peaks confirms that the measured frequency variation is not related to motion-induced effects. If that had been the case, indeed, the responses calculated from pressure measurements, at the several speeds tested, would have accounted for it. This would have resulted in the coincidence of the natural frequency peaks in both "Measured" and "Num. Aer." response spectra. Therefore, for a proper validation of the FEM model, at each test, the across-wind bending stiffness of the grounded link, is accurately calibrated in order to achieve the measured value of the lateral frequency of vibration.

Assuming 5% modal damping in the first mode, the numerical response from loads on the aeroelastic model is then evaluated and compared to the measured one (Fig. 7.5). The distance between the two responses is considered due to the fact that the structural damping ratio in the lateral bending mode is not constant and equal to 5%, in fact, as seen in Fig. 6.25. Imposing the coincidence between these responses, the actual value of the structural damping can be calculated at each wind speed.

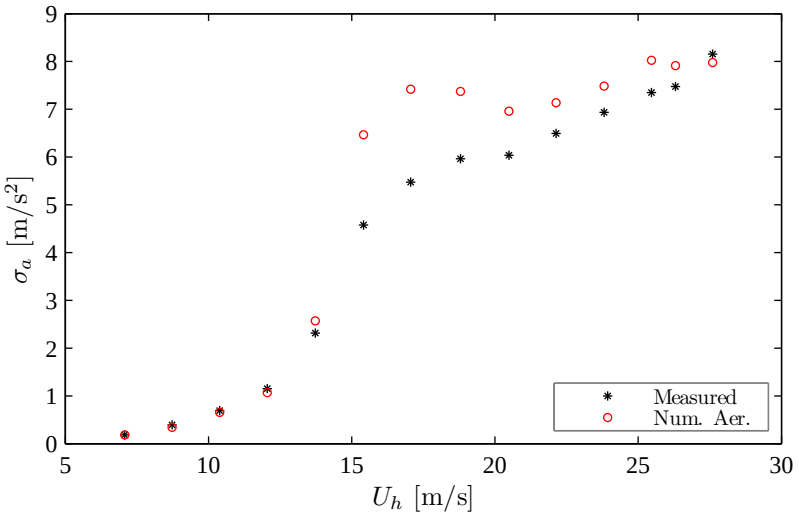

Fig. 7.5 Tip across-wind acceleration response: comparison between "Measured" response and numerical response obtained from FEM model with 5% modal damping, loaded with pressures from aeroelastic tests ("Num. Aer.").

7.3.1 Identification of the structural damping

The actual value of the structural damping ξ_s for the lateral mode of vibration, at each wind speed, is, therefore, obtained by adjusting it iteratively so that the "Num. Aer." response equals the measured one. In order to fix a criterion for equality of the two responses, the parameter $\delta_{\sigma_a,A}$ is defined as:

$$\delta_{\sigma_a,A} = \frac{\sigma_a, \text{Measured} - \sigma_a, \text{Num. Aer.}}{\sigma_a, \text{Measured}} \times 100 \tag{7.1}$$

The two responses are considered equal when $\delta_{\sigma_a,A}$, in absolute value, is lower than 2%.

In other words, the structural damping is numerically adjusted in the FEM model, until the distance between the measured and calculated across-wind acceleration responses, expressed by the parameter $\delta_{\sigma_a,A}$, is lower than 2%. Fig. 7.6 illustrates these two responses and the parameter $\delta_{\sigma_a,A}$ at the end of the procedure for identification of structural damping.

The structural damping values, identified in this way, are shown in Fig. 7.7 as a function of the reference wind speed U_h [Fig. 7.7(a)] and of the RMS acceleration [Fig. 7.7(b)].

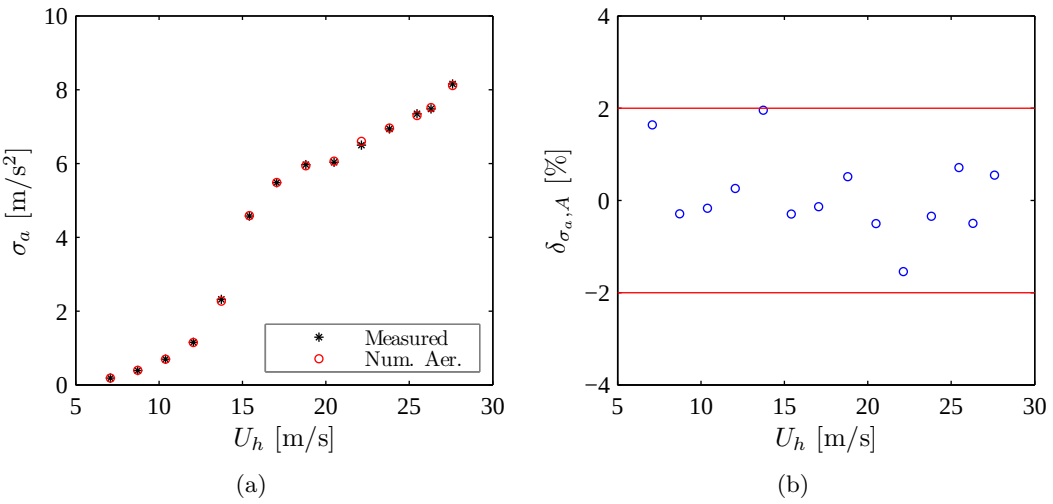

Fig. 7.6 Measured and numerical across-wind responses for the identified structural damping ratio: a) RMS tip lateral acceleration σ_a vs. reference wind speed U_h, b) $\delta_{\sigma_a,A}$ vs. U_h.

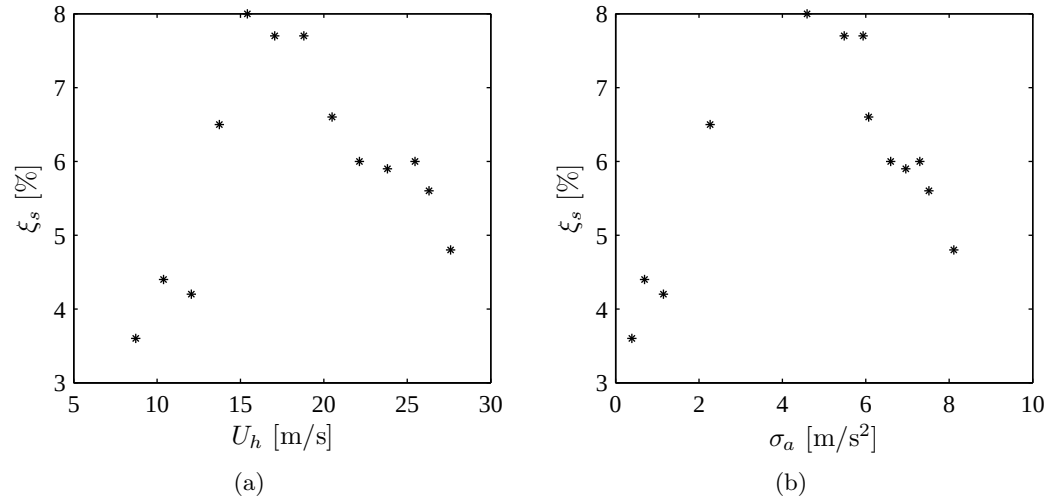

Fig. 7.7 Measured and numerical across-wind responses for the identified structural damping ratio: a) RMS tip lateral acceleration σ_a vs. reference wind speed U_h, b) $\delta_{\sigma_a,A}$ vs. U_h.

7.4 Identification of aeroelastic effects in terms of aerodynamic damping

The FEM model, as described in the previous section, is validated in order to guarantee that it can be considered the numerical analog of the real model tested in the wind tunnel for the estimation of its across-wind response. With the aim of identifying aeroelastic or motion-induced effects involving the across-wind response, the FEM model is loaded with pressures measured on a stationary or rigid model. Its numerical response is then compared with that measured on the aeroelastic model. The definition of wind forces for different wind speeds from rigid model tests is illustrated in subsection 7.4.1.

7.4.1 Pressure time-histories from rigid model tests

Non-dimensional pressures measured in test 1 are taken as the rigid model loads, considering negligible motion-induced effects during this test, because of the low value of the mean reference wind speed, corresponding to negligible vibrations. The pressure field measured from the aeroelastic model, during test 1, can be, indeed, considered equivalent to that measured on the stationary model used by Spence (2009). The advantage of using "stationary" pressures measured from the same aeroelastic model, instead of taking them from the rigid model studied by others, lies in two main aspects:

1. the same pressure taps distribution on the FEM model can be used for simulating both the response of the model to loads measured on the vibrating model and those measured on the stationary model;
2. discrepancies of wind fields around two different models, due, for example, to different sharpness of corners, are avoided.

From test 1, at each pressure tap, the time history of the non-dimensional pressure coefficient is evaluated using Eq. (3.1), and can be written as:

$$C_p(t) = \frac{p_1(t)}{\frac{1}{2}\rho U_{h,1}^2} \tag{7.2}$$

where $p_1(t)$ and $U_{h,1}$ are the pressure time history (for simplicity of notation, p indicates here the difference between the pressure measured at the tap and the static pressure) and the reference wind speed measured during test 1, respectively. Assuming that the pressure coefficient is independent on wind speed, it is possible to calculate the pressure time history, $p_2(t)$, at a given different reference wind speed, $U_{h,2}$, as:

$$p_2(t) = \frac{1}{2}\rho U_{h,2}^2 C_p(t) \tag{7.3}$$

Since pressure is time-dependent, a proper calculation of the pressure time history requires the definition of the time scaling. The latter can be derived assuming equality of the reduced velocities:

$$\left(\frac{U_h}{fb}\right)_1 = \left(\frac{U_h}{fb}\right)_2 \tag{7.4}$$

that can be written as:

$$\left(\frac{U_h t}{b}\right)_1 = \left(\frac{U_h t}{b}\right)_2 \tag{7.5}$$

since $f = 1/t$. Hence, in view of b constant,

$$t_2 = t_1 \frac{U_{h,1}}{U_{h,2}}, \tag{7.6}$$

which means that the time scale, λ_t, is equal to:

$$\lambda_t = \frac{t_2}{t_1} = \frac{1}{\lambda_{U_h}}, \tag{7.7}$$

where the velocity scale, λ_{U_h}, is equal to:

$$\lambda_t = \frac{U_{h,2}}{U_{h,1}}. \tag{7.8}$$

From Eq. (7.7), the frequency scale, λ_f, is:

$$\lambda_f = \frac{f_2}{f_1} = \frac{1}{\lambda_t} = \lambda_{U_h}. \tag{7.9}$$

From the pressure coefficients measured on the stationary model, time histories of pressures are calculated for all the wind speeds reported in Table 6.5, corresponding to the 25 aeroelastic tests performed. For each reference mean wind speed, U_h, the velocity scale, λ_{U_h}, and then the time vector, from Eq. (7.7), are calculated. The pressure coefficient vector is estimated by Eq. (7.3).

Pressures from the stationary model are measured with a sampling frequency, or sampling rate, indicated here with SR, equal to 250 Hz. It means that the signal is registered at time intervals $\delta t = 1/250 = 0.004$ sec $= 4$ milli-s. Because of the scaling considerations illustrated before, the pressure signals generated from those measured on the stationary model, for the different values of the wind speed, have different δt values [Fig. 7.8], that have to be taken into account in estimating the response numerically from the FE model.

7.4.2 Aeroelastic Factor

The aeroelastic effects involving the across-wind response of the model are identified comparing the "Measured" response (equivalent to the "Num. Aer." one with the identified structural damping values) with the numerical response to wind pressures form the stationary model test, indicated with "Num. Rig." [Fig. 7.9(a)].

A normalized representation of Fig. 7.9(a) is given in Fig. 7.9(b). The standard deviation across-wind acceleration responses are normalized as:

$$\text{Non-dimensional RMS acceleration} = \frac{\sigma_a b}{U_h^2} \tag{7.10}$$

where σ_a is the standard deviation of the acceleration, b is the model breadth, equal to 0.105 m, and U_h is the mean speed at the model height, h. The quantity defined

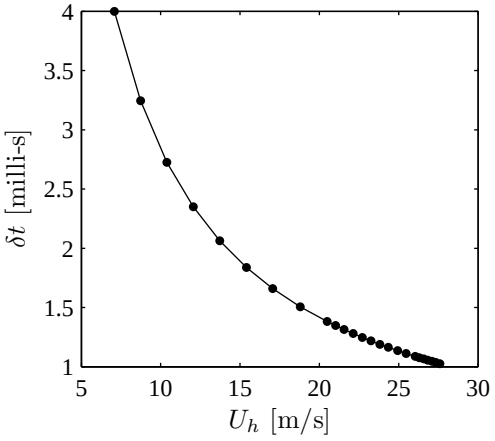

Fig. 7.8 Time interval for pressure time histories generated from rigid model tests at different wind speeds.

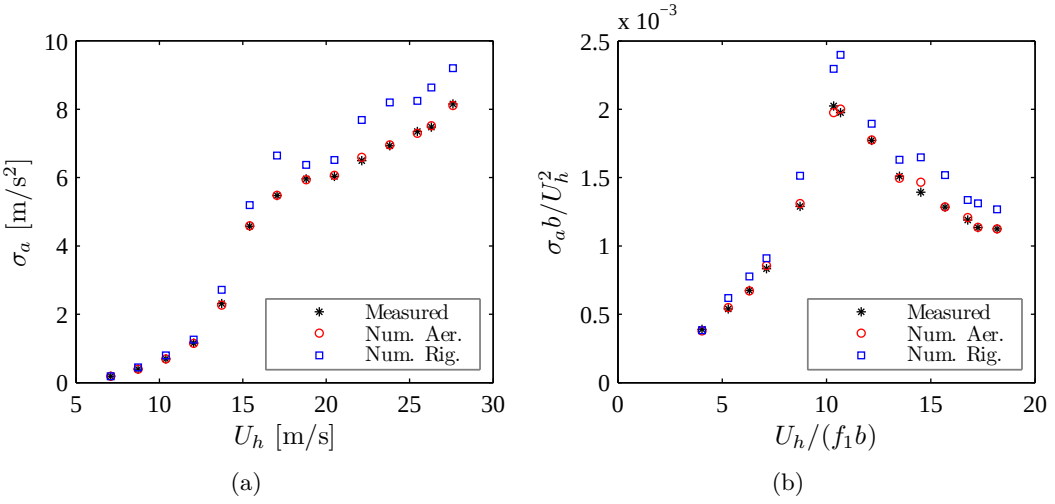

Fig. 7.9 Comparison between the measured aeroelastic response and the numerical one obtained from pressures on the rigid model: a) standard deviation vs. reference wind speed; b) non-dimensional representation of a).

in Eq. (7.10) is non-dimensional, as results from the following dimensional analysis:

$$\left[\frac{\sigma_a b}{U_h^2}\right] = \left[\frac{AL}{V^2}\right] = \left[\frac{LT^{-2}L}{(LT^{-1})^2}\right] = \left[\frac{LT^{-2}L}{L^2T^{-2}}\right] = [\,] \tag{7.11}$$

where A, V, L, T are used here to indicate acceleration, velocity, length and time, respectively.
The mean wind speed, U_h, is normalized as reduced velocity, U_r, which is already defined in section 6.9 as:

$$U_r = U_h/(f_1 b) \tag{7.12}$$

where f_1 is the actual value of the lateral natural frequency at each wind speed.

Similarly to what was done by Boggs (1992), aeroelastic effects are computed through an *aeroelastic factor* AF, defined as:

$$AF = \frac{\sigma_a b/U_h^2, \text{Measured}}{\sigma_a b/U_h^2, \text{Num. Rig.}}. \tag{7.13}$$

where $\sigma_a, \text{Num. Rig.}$ is evaluated from the FEM model considering at each wind speed the identified structural damping value ξ_s which leads to $\sigma_a, \text{Measured} = \sigma_a, \text{Num. Aer.}$. Fig. 7.10 shows that the aeroelastic factor is always lower than 1. It

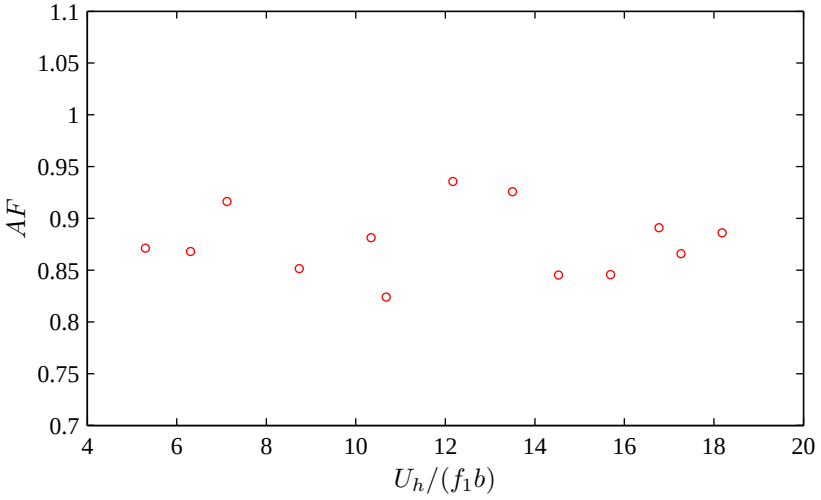

Fig. 7.10 Aeroelastic factor AF as a function of the reduced velocity $U_h/(f_1 b)$.

means that aeroelastic effects weaken the across-wind response. The least reducing effect occurs at the mid of the lock-in range.

7.4.3 Aerodynamic damping ratio

The distance between the "Measured" aeroelastic response and the "Num. Rig." one denotes that the aeroelastic system under investigation has not negligible motion-induced effects. These are valued here in terms of aerodynamic damping. The total damping of the aeroelastic model ξ_{tot} consists of structural damping ξ_s and aerody-

namic damping ξ_a:

$$\xi_{tot} = \xi_s + \xi_a \tag{7.14}$$

In a similar manner to what has been done in subsection 7.3.1, the system's total damping is obtained adjusting it numerically so that the calculated response from stationary model loads, "Num. Rig.", matches the "Measured" aeroelastic one. The two responses are considered equivalent when the absolute value of the parameter $\delta_{\sigma_a,R}$, defined as:

$$\delta_{\sigma_a,R} = \frac{\sigma_a, \text{Measured} - \sigma_a, \text{Num. Rig.}}{\sigma_a, \text{Measured}} \times 100 \tag{7.15}$$

is lower than 2%.
From the total damping ξ_{tot} values, identified in this way, it is therefore possible to calculate the aerodynamic damping ξ_a as:

$$\xi_a = \xi_{tot} - \xi_s \tag{7.16}$$

recurring to a kind of "inverse response approach", even used by Cheng *et al.* (2002).
Fig. 7.11(a) illustrates the "Measured" response and "Num. Aer." one, evaluated

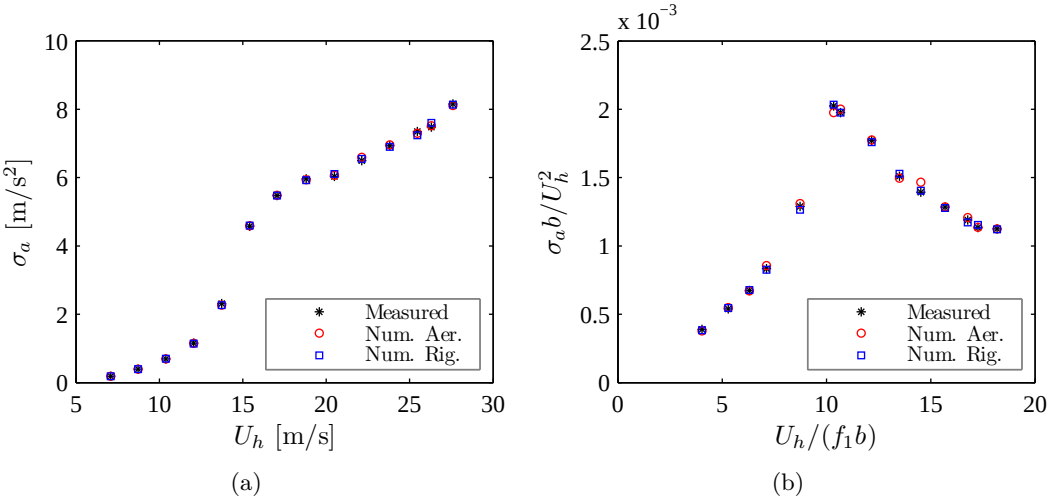

Fig. 7.11 Comparison between "Measured", "Num. Aer." and "Num. Rig." tip across-wind responses at the end of the identification procedure of structural and total damping values: a) σ_a vs. U_h, b) normalized representation of a).

on the basis of the identified structural damping values, together with the numerical response from stationary model pressures, "Num. Rig.", at the end of the procedure of identification of total damping values. The two responses are also compared using a normalized representation [Fig. 7.11(b)]. The parameter $\delta_{\sigma_a,R}$, for the identified ξ_{tot} values is in the range [-2;+2]% for all the wind speeds considered (Fig. 7.12). The identified structural, total and aerodynamic damping ratios are shown as a function of the reference wind speed in Fig. 7.13(a) and of the reduced velocity in Fig. 7.13(b).

Coincidence of "Num. Rig." and "Num. Aer." (or analogously "Measured")

is also given in terms of power spectral densities $S(f)$ for different wind speeds [Fig. 7.14]: two values lower than the critical wind speed at which the shedding frequency fs is lower than the natural frequency of lateral vibration f_1 [Figs. 7.14(a) and 7.14(b)], two values in the lock-in range where $f_s \approx f_1$ [Figs. 7.14(c) and 7.14(d)] and two higher values at which f_s exceeds f_1 [Figs. 7.14(e) and 7.14(f)]. The fact that the coincidence of "Num. Rig." and "Num. Aer." responses is obtained not only in terms of RMS values but also in terms of power spectral density validates the identified total and, therefore, aerodynamic damping values.

The results illustrated in this chapter show that, for the model under examina-

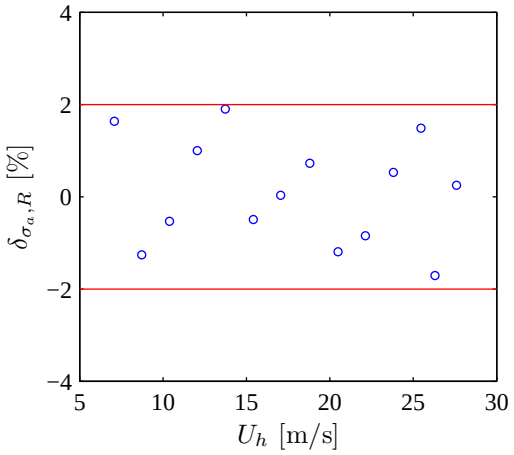

Fig. 7.12 $\delta_{\sigma_a,R}$ vs. U_h for the identified total damping ratio ξ_{tot} values.

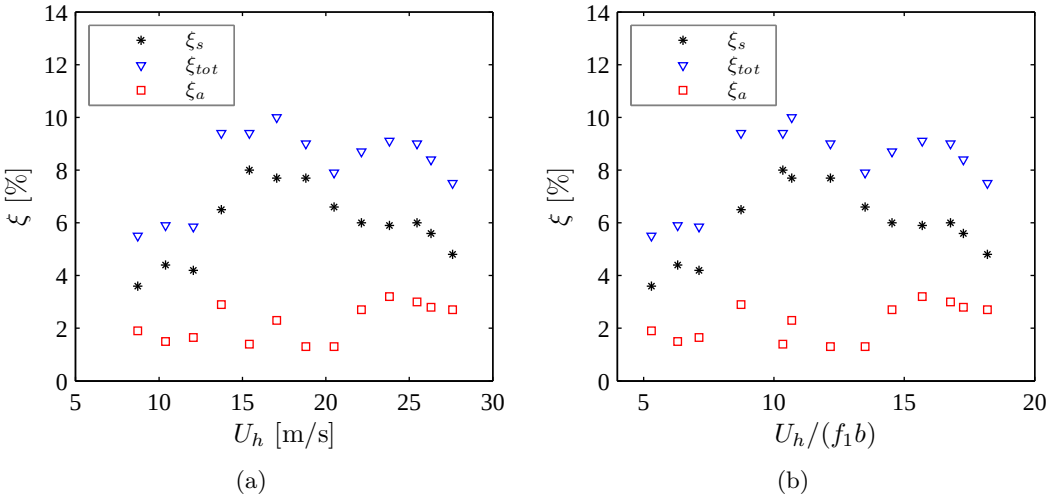

Fig. 7.13 Identified structural, total and aerodynamic damping ratios versus reference wind speed (a) and reduced velocity (b).

tion, aeroelastic effects involving its across-wind response, even in lock-in conditions, can be easily accounted for adding aerodynamic damping to the structural damping. In other words, it is possible to predict numerically the aeroelastic response, which includes motion-induced effects, from aerodynamic loads measured on a stationary model, adding aerodynamic damping to the structural damping.

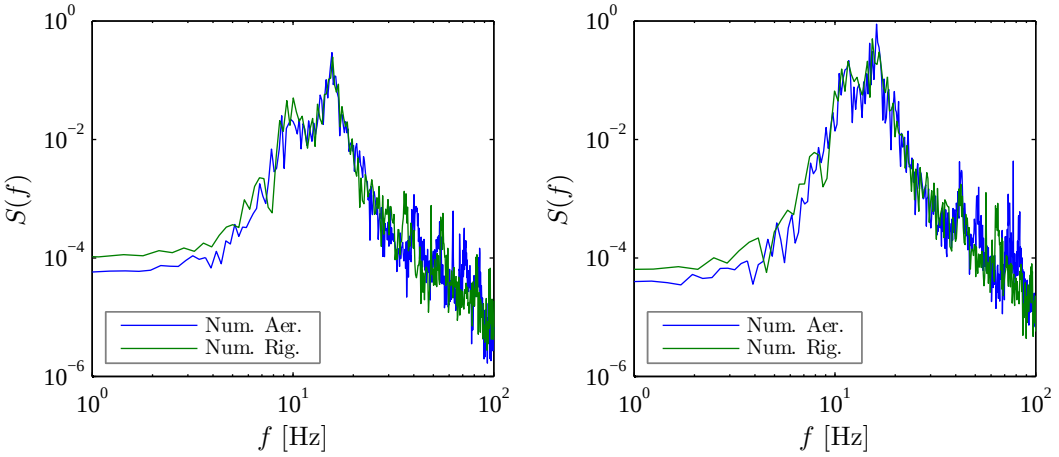

(a) $U_h = 10.39$ m/s (b) $U_h = 12.05$ m/s

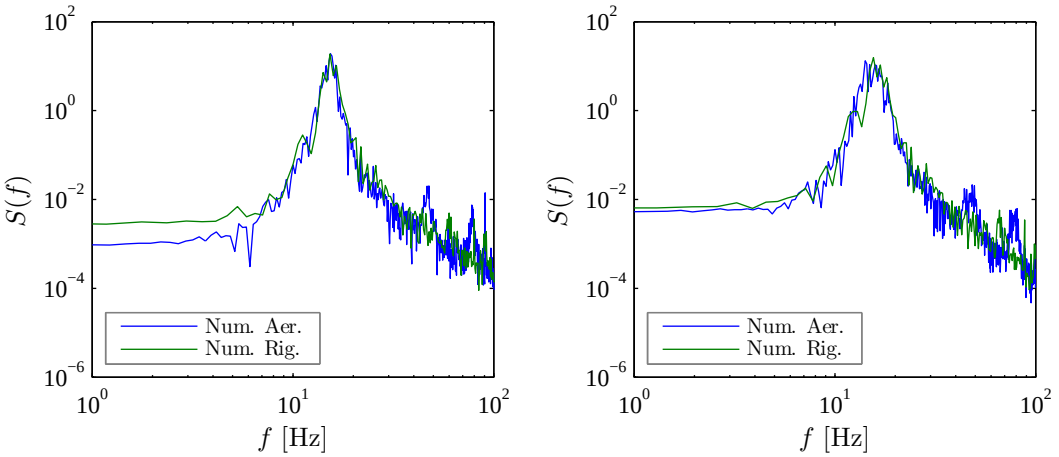

(c) $U_h = 17.06$ m/s (d) $U_h = 18.80$ m/s

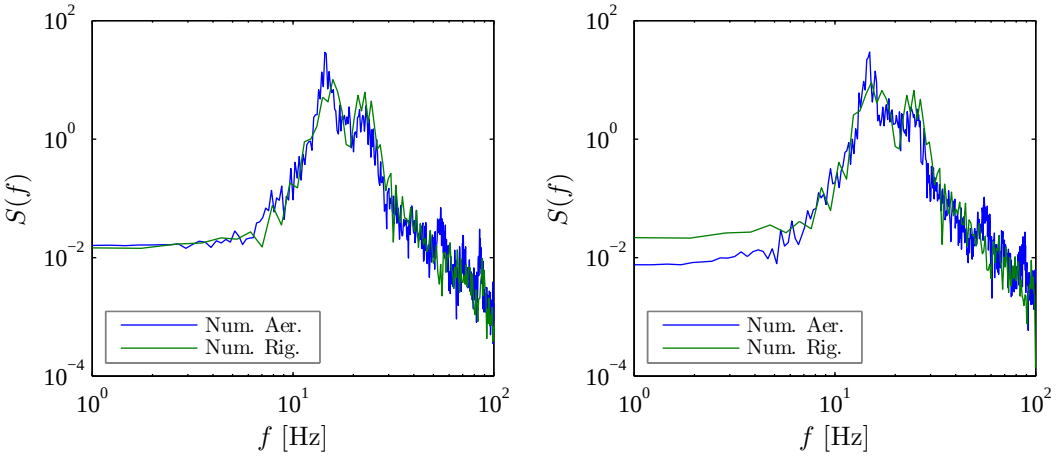

(e) $U_h = 25.46$ m/s (f) $U_h = 26.30$ m/s

Fig. 7.14 Power spectral densities of across-wind responses from pressures on aeroelastic model, "Num. Aer.", and from pressures on the stationary model, "Num. Rig.", accounting for the identified aerodynamic damping.

7.4.4 Identified aerodynamic damping compared with other literature studies results

In this section the identified aerodynamic damping ratio values are compared with those from other literature studies, characterized by similar testing conditions. Fig. 7.15 illustrates the identified damping ratio values versus reduced velocity, com-

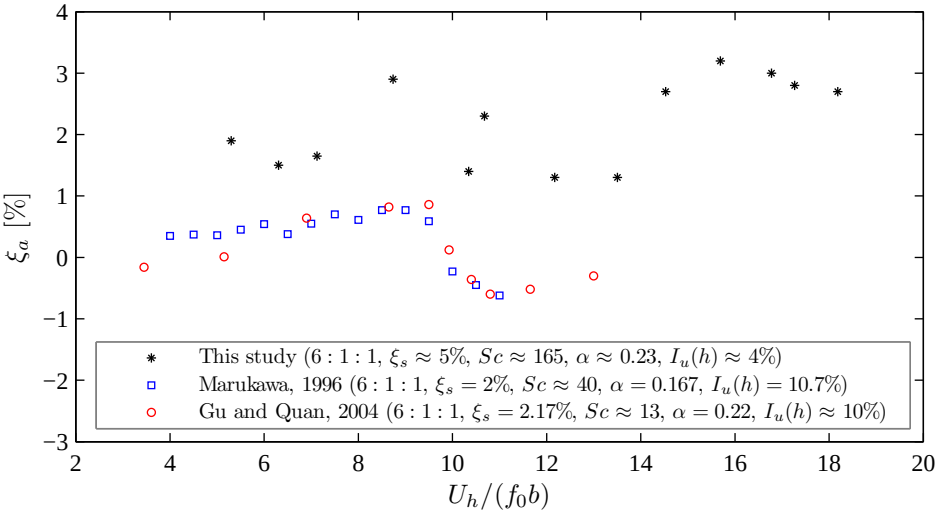

Fig. 7.15 Aerodynamic damping ratio values versus reduced velocity identified in the current study in comparison with results from Marukawa *et al.* (1996) and from Gu and Quan (2004).

pared with data from Marukawa *et al.* (1996) and from Gu and Quan (2004) (see subsection 4.4.5). Aerodynamic damping values obtained by Marukawa *et al.* (1996) refer to a 6:1:1 ($h : d : b = 0.48$ m : 0.08 m : 0.08 m) stick model with structural damping equal to 2%. The simulated mean wind speed profile is characterized by an exponent of the power law $\alpha = 1/6 = 0.167$. The tubulence intensity at the model top $I_u(h)$ is 10.7%. Assuming the model mass is uniformily distributed, from the model density equal to 20.4 kgs^{2}m^{-4}, it is possible to calculate the Scruton number Sc that results approximately equal to 40. Data from Gu and Quan (2004) are those relative to a 6:1:1 ($h : d : b = 0.60$ m : 0.10 m : 0.10 m) model in terrain C flow conditions ($\alpha = 0.22$ and $I_u(h) = 10\%$). The Scruton number in this case is $Sc \approx 13$, having assumed that the total mass (0.36 kg) is uniformely distributed. It can be noticed that there is a significant distance between data from the current study and data from these other two studies. It has to be specified that there are also differencies in the testing conditions, related both to the turbulence intensity and to structural damping, which together with the mass of the models leads to differences in the Scruton number.

In Fig. 7.16 the identified damping ratio as a function of reduced velocity is compared with results from Cheng *et al.* (2002), illustrated in sections 4.4.3 and 4.4.5. The Scruton number in the across-wind bending mode for the aeroelastic model tested in this study is 165. Considering that the mass-damping parameter M_D defined by Cheng *et al.* (2002) can be regarded as $Sc/(4\pi)$, it is possible assess

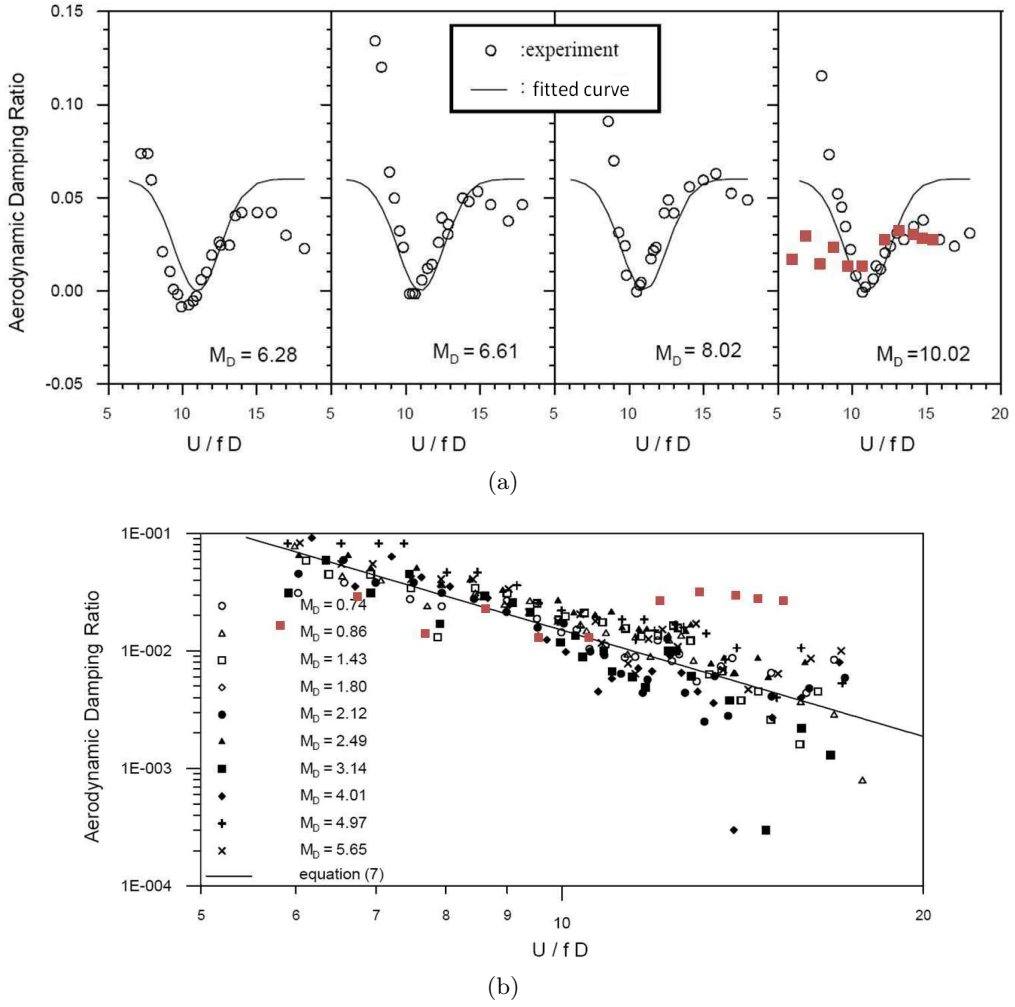

Fig. 7.16 Identified aerodynamic damping values (red squares) compared with results from Cheng *et al.* (2002) for BL1 in the aerodynamic stable region (a) and BL2 (b).

that M_D in this study would be equal to approximately 13. For this reason the identified damping ratio values are overlapped in Fig. 7.16(a) to those obtained by Cheng *et al.* (2002) for the closest value of M_D equal to 10.02. This figure refers to the BL1, corresponding to open terrain conditions and power law exponent $\alpha = 0.15$ that is quite different from the current study. However, results are in good agreement with Cheng *et al.* (2002). It can be noticed that a certain difference is obtained for very low values of reduced velocity. Even if in this range results are less reliable, because at low wind speed the instrumentation errors can be a significant percentage of the measured quantities, this result seems reasonable, since aerodynamic damping, which is a motion-induced effect, should reach zero for zero displacements and, therefore, zero velocity. Since in this research the simulated flow conditions are intermediate between BL1 and BL2 ($\alpha = 0.32$), results are compared also with those by Cheng *et al.* for BL2. In the scales of Fig. 7.16(b) current study results are in good agreement with those by Cheng *et al.* (2002).

7.5 Summary and main remarks

This chapter is aimed at identifying the motion-induced or aeroelastic effects involving the across-wind response of the physical aeroelastic model tested in the wind tunnel. For this purpose a numerical FEM model replicating the physical one is developed.

At first, the numerical model is loaded with pressures from aeroelastic tests. The corresponding responses match the measured ones having properly defined the geometric and dynamic features of the model.

The FEM model is then loaded with pressure from rigid model tests. The response evaluated from these loads at different wind speed values is compared with the measured aeroelastic one, at the same wind speeds. The distance between the measured and the predicted response from rigid model loads, is evaluated by means of an aeroelastic factor, defined as the ratio between the normalized RMS of the acceleration responses.

Through this comparison the identification of aeroelastic effects in terms of aerodynamic damping is carried out. The identification procedure is based on an inverse approach, that consists in adjusting the total damping numerically, until the predicted response matches the measured one. Aerodynamic damping ratio is then calculated from the difference between the total damping ratio and the structural damping ratio. Across-wind aerodynamic damping estimated in this way is positive for the entire wind speed range considered, indicating that for the highly damped system considered aeroelastic effects mitigate the across-wind responses, providing additional damping to the system.

The identified aerodynamic damping is compared with that identified in other literature works. Good agreement is found with results from Cheng *et al.* (2002) obtained in similar turbulence and Scruton number conditions.

Chapter 8

Serviceability wind risk assessment of tall buildings

8.1 Introduction

In this chapter a general procedure for the serviceability wind risk assessment of tall buildings is illustrated. This procedure is line with the risk management framework reviewed in section 2.2 and follows the Performance-Based Design approach presented in section 2.3. In this research, only the hazard analysis and structural analysis stages are dealt with.

In section 8.2 a case study tall building is illustrated. It will be used in order to provide an illustrative example of the risk assessment procedure proposed. The direct application to this structure of the comfort checking practice, recommended by the ISO-6897 (ISO 6897, 1984), will be also illustrated (section 8.5).

A brief section (8.3) is devoted to the statistical analysis of historical wind data and is aimed at the definition of the Weibull and the Gumbel distributions. Real wind data registered from a real anemometric station are fitted to these distributions and used in the following sections.

Section 8.4 is dedicated to the description of the procedure for the discomfort risk assessment of tall buildings proposed in this work. Its different stages, corresponding to hazard analysis and vulnerability analysis, are illustrated in detail. The procedure is then applied to the case study building, as previously mentioned.

8.2 Case study tall building

In order to provide an illustrative example of application of the discomfort risk assessment procedure proposed in this research a case study tall building is considered. It is a square-section regular tall building, made of steel. Its height h is 304 m. The side dimension $b = d$ is 52.5 m. Its geometric proportion is h:b:d = 6:1:1. The building is located in a city center characterized by roughness length $z_0 = 1.2$ m.

Suda *et al.* (1996) suggested the following equation, also used in Quan *et al.* (2005), to estimate the first frequency of general super-tall buildings after their in-

vestigations of a great number of tall buildings in Japan (Fig. 8.1):

$$f_1 = \begin{cases} 1/(0.015h): & \text{RC and SRC buildings (small amplitude)} \\ 1/(0.020h): & \text{steel buildings (small amplitude)} \end{cases} \tag{8.1}$$

where h is the building height. CNR-DT 207 (2008) suggests the following relations

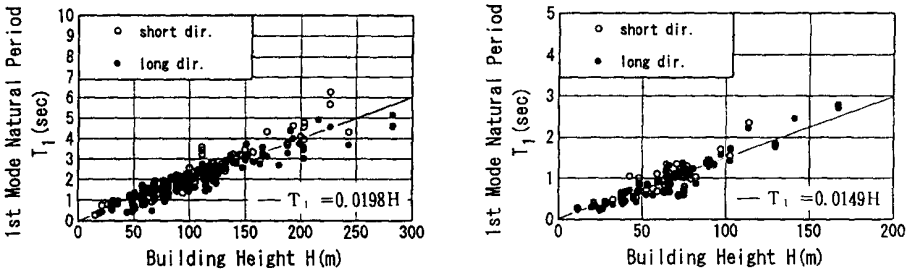

Fig. 8.1 First mode natural period versus building height (Suda *et al.*, 1996): a) steel structures; b) reinforced concrete structures.

for the first bending frequency f_1 in function of the building height, h:

$$f_1 = \begin{cases} \text{from } 1/(0.018h) \text{ to } 1/(0.015h): & \text{RC and SRC buildings} \\ \text{from } 1/(0.024h) \text{ to } 1/(0.020h): & \text{steel buildings} \end{cases} \tag{8.2}$$

In agreement with these formulas, the case study building is characterized by a fundamental bending frequency equal to $1/(0.024h) \approx 0.14$ Hz.

The discomfort risk assessment procedure proposed in this study is based on the lateral response which usually exceeds that in the direction of wind. In order to simulate the across-wind dynamic behavior of the case study building (prototype) with the aeroelastic 6:1:1 model tested in the wind tunnel and described in chapter 6, the following scales are considered.

The length scale of the model to the prototype, λ_L, is equal to:

$$\lambda_L = \frac{L_m}{L_p} = \frac{h_m}{h_p} = \frac{0.608}{304} = \frac{1}{500} \tag{8.3}$$

The length scale is also satisfied by the roughness length:

$$\frac{z_{0,m}}{z_{0,p}} = \frac{0.2469 \text{ cm}}{1.2 \text{ m}} \approx \frac{1}{500} \tag{8.4}$$

The frequency scale λ_f is equal to:

$$\lambda_f = \frac{f_{1m}}{f_{1p}} \approx 150 \tag{8.5}$$

taking the value of f_{1m}, measured in the first test, thus neglecting its observed variations.

The prototype structure has the same bending frequency along the x and y axes. Therefore, differently from the model, no distinction is made between a weaker and

a stronger direction, as it is reasonable for a square-section symmetric building. As explained later, in order to derive the across-wind response of the prototype from that of the model, it is assumed that the building has the same Scruton number of the model.

From the similarity requirement for elastic forces, replaced by the reduced frequency fb/U, the velocity scale value λ_U can be derived as follows:

$$\lambda_U = \lambda_L \lambda_f \approx 0.3 \tag{8.6}$$

Hence, the time scale λ_t and the acceleration scale λ_a can be calculated as:

$$\lambda_t = \frac{1}{\lambda_f} \approx 0.007 \tag{8.7}$$

and

$$\lambda_a = \lambda_L \lambda_f^2 \approx 45 \tag{8.8}$$

respectively.

8.2.1 Prototype acceleration response

Wind tunnel tests on the aeroelastic model investigated in this study led to the estimation of the across-wind RMS acceleration response at the model top as a function of reference wind speed in the case of zero-incidence incoming flow. The dimensionless representation of the response introduced in subsection 7.4.2 enables the direct transfer of model experimental results to full scale. In other words, the curve in Fig. 8.2(a) is the non-dimensional across-wind RMS acceleration tip response of the prototype, if the geometric proportion (h:b:d), flow conditions (e.g. z_0) and Scruton number are equal to those in model scale. Since the prototype is assumed to have the same fundamental frequency and Scruton number along the x and y axes, this curve represents the response for both 0° (or 180°) and 90° (or 270°) of angle of attack, that means for wind flow direction orthogonal to one face.

Knowing the side dimension of the prototype, $b = 52.5$ m, and its natural frequency, $f_1 = 0.14$ Hz, the across-wind RMS acceleration response σ_a can be derived as a function of the reference wind speed at the top height U_h [Fig. 8.2(b)].

8.3 Wind speed statistics

This section deals with the statistical analysis of historical data of recorded wind speeds. The main features of the hybrid Weibull distribution are described (subsection 8.3.1). The population of wind data from a real anemometric station will be fitted to this distribution in subsection 8.4.3. The Type I extreme value distribution is also presented here (subsection 8.3.2) and will be fitted to annual maxima of the wind speed registrations in subsection 8.5.1.

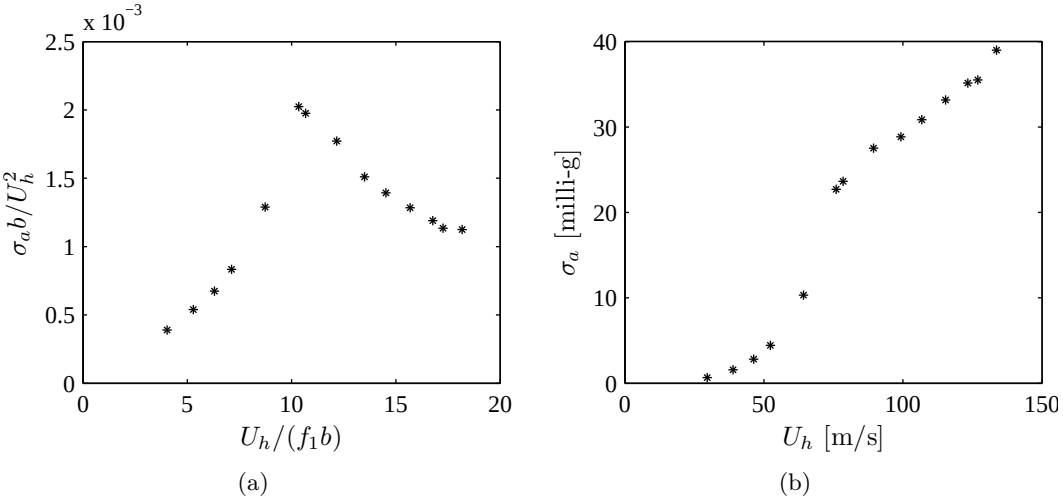

Fig. 8.2 Across-wind RMS acceleration tip response of the case study square-section tall building: a) non-dimensional representation valid for both model and full scale; b) standard deviation as a function of the mean wind speed at the building site.

8.3.1 Probability distribution of the population of wind speeds

The statistical analysis of the population of wind data is carried out using the so called Hybrid density function of the Weibull distribution (Weibull, 1951). The hybrid model, proposed by Takle and Brown (1978), is a slight variation of the Weibull density function aimed at the improvement of the applicability of the latter, through proper treatment of zero wind speed data (wind calms), as later illustrated.

The hybrid Weibull distribution

Weibull distribution is commonly accepted as the mean wind speed distribution at any wind velocity (Deaves and Lines, 1997). Considering the generic random variable X, the Weibull probability density function, $p_X^W(x)$, and the cumulative distribution function, $F_X^W(x)$, are defined as:

$$p_X^W(x) = \begin{cases} \frac{k}{c}\left(\frac{x}{c}\right)^{k-1} \exp\left[-\left(\frac{x}{c}\right)^k\right], & \text{if } x \geq 0 \\ 0, & \text{otherwise} \end{cases} \tag{8.9}$$

and

$$F_X^W(x) = \begin{cases} 1 - \exp\left[-\left(\frac{x}{c}\right)^k\right], & \text{if } x \geq 0 \\ 0, & \text{otherwise} \end{cases} \tag{8.10}$$

respectively, where c is the scale parameter, having the same dimensions as X, and k is the non-dimensional shape parameter. If the Weibull distribution is fitted to wind data, the probability of having zero wind speed values is, therefore, not properly estimated, since $F_X^W(0) = 0$. Takle and Brown (1978) have proposed to solve the problem of including wind calms by defining a hybrid probability density function:

$$p_X^H(x) = F_0\delta(x) + (1 - F_0)p_X^W(x), \ \forall x \in \mathbb{R} \tag{8.11}$$

where F_0 is the probability of observing zero wind value and $\delta(x)$ is the Dirac delta function. The corresponding cumulative distribution function is:

$$F_X^H(x) = \begin{cases} F_0 + (1 - F_0) F_X^W(x), & \text{if } x \geq 0 \\ 0, & \text{otherwise} \end{cases} \tag{8.12}$$

The Hybrid distribution method simply removes those measurements judged as wind calms, and fits the Weibull distribution to the other nonzero wind speed values. Wind calms are reintroduced to give the proper mean and variance and to renormalize the distribution. According to the Hybrid distribution for the measured wind speed, U, the complementary cumulative distribution, $1 - F_U^H(u)$, expressing the probability of having U greater then a certain value, u, $P^H(U > u)$, is equal to:

$$1 - F_U^H(u) = P^H(U > u) = (1 - F_0) P^W(U > u) \tag{8.13}$$

From Eq. (8.10), $P^W(U > u)$ is equal to:

$$P^W(U > u) = 1 - F_U^W(u) = \exp\left[-\left(\frac{u}{c}\right)^k\right] \tag{8.14}$$

Estimation of the Weibull parameters

From Eq. (8.10), considering the wind speed, U, as the random varible, X:

$$F_U^W(u) = 1 - \exp\left[-\left(\frac{u}{c}\right)^k\right] \tag{8.15}$$

Taking logarithms twice, Eq. (8.15) becomes:

$$\ln\left\{-\ln\left[1 - F_U^W(u)\right]\right\} = k \ln u - k \ln c \tag{8.16}$$

In Eq. (8.16), $\ln\left\{-\ln\left[1 - F_U^W(u)\right]\right\}$ *vs* $\ln u$ gives a linear relationship. In order to estimate the parameters of the distribution, it is therefore possible to define the following auxiliary variables:

$$\begin{cases} x = \ln u \\ y = \ln\left\{-\ln\left[1 - F_U^W(u)\right]\right\} \end{cases} \tag{8.17}$$

Eq. (8.16) becomes the straight line:

$$y = mx + q \tag{8.18}$$

where $m = k$ and $q = k \ln c$. From the slope m and the zero intercept, q, of the straight line [Eq. (8.18)], the parameters of the distribution can be, therefore, estimated as:

$$\begin{cases} k = m \\ c = exp\left(-\frac{q}{k}\right) \end{cases} \tag{8.19}$$

8.3.2 Extreme value analysis of wind speeds

The Gumbel approach to extreme wind estimation

Gumbel (1954, 1958) gave an usable methodology for fitting recorded maxima to the Type I Extreme Value Distribution. The latter can be regarded as a special case of the Generalized Extreme Value Distribution (Holmes, 2001; Beirlant *et al.*, 2004). Denoting the maximum wind speed in one year as a the random variable, U, the Type I Gumbel Extreme Value distribution is expressed as:

$$F_U(u) = \exp\left\{-\exp\left[-\frac{u-\mu}{\beta}\right]\right\} \tag{8.20}$$

where $F_U(u)$ is the cumulative distribution function, CDF, expressing the probability, P, that the random variable, U, does not exceed the value u:

$$F_U(u) = P(U \leq u) \tag{8.21}$$

μ and β are the location parameter, or mode of the distribution (Holmes, 2001), and the scale parameter, respectively (Beirlant *et al.*, 2004). Taking logarithms twice, Eq. (8.20) becomes:

$$u = \mu + \beta\{-\ln[-\ln F_U(u)]\} \tag{8.22}$$

Eq. (8.22) corresponds to a straight line in the plane $\{-\ln[-\ln F_U(u)]\}$, u. The slope and the zero intercept of this line correspond to the scale and the location parameter, respectively.

The Return Period, R, is defined as the inverse of the complementary cumulative distribution of the extremes:

$$R = \frac{1}{1 - F_U(u)} \tag{8.23}$$

If the annual maximum is being considered, then R is measured in years. Thus a 50-year return period wind speed has, for example, a probability of exceedance of $1/50 = 0.02$ in any one year. It should not be interpreted as recurring regularly every 50 years.

From Eq. (8.23), $F_U(u)$ can be written as:

$$F_U(u) = 1 - \frac{1}{R} \tag{8.24}$$

Substituting Eq. (8.24) in Eq. (8.22), the wind speed, $\bar{U}_R$, corresponding to a return period, R, is equal to:

$$\bar{U}_R = \mu + \beta\left\{-\ln\left[-\ln\left(1 - \frac{1}{R}\right)\right]\right\} \tag{8.25}$$

8.4 PBWE approach for discomfort risk assessment

In this section a procedure for assessment of wind-induced discomfort risk of tall buildings is presented. Following the PEER's equation approach, already adopted in the field of wind engineering (Performance-Based Wind Engineering, PBWE, in

section 2.3), regardless of the target performance, structural risk induced by the wind action can be measured in terms of the probability of exceeding a relevant value of the corresponding decision variable, DV, expressed by Eq. (2.1). The performance considered in this case is the comfort of the users related to the perception of vibrations under moderate winds. This is an example of a high performance level as serviceability limit state. Since models of costs associated to the loss of occupant comfort are still missing, the DV can be simply evaluated in terms of engineering demand parameter EDP and Eq. (2.1) simply becomes:

$$g\left[EDP\right] = \int p\left[EDP|IM\right] g\left[IM\right] \, dIM \tag{8.26}$$

The risk can be, therefore, measured by the probability of exceedance of a certain EDP that describes the structural response.

With reference to the PEER's analysis methodology, sketched in Fig. 2.4, the procedure presented here is only related to the first two boxes, corresponding to the *hazard analysis* and the *structural analysis*.

The definition of risk given by Eq. (8.26) can be also related to the risk management framework proposed by Pliefke *et al.* (2006, 2007), described in section 2.2. In this case only the *risk identification* phase and the *risk assessment* one are accounted for. Risk identification consists in the definition of the system as well as of the hazard. The former is represented by a tall building and the latter corresponds to the wind action exciting the building. The risk assessment phase consists only in risk analysis which quantifies risk in terms of a probability of exceeding a defined threshold, while the risk evaluation part is not included, since only one source of risk is considered.

Since the performance considered is the comfort of tall buildings occupants and motion perception is closely related to the acceleration response of buildings, in terms, for example, of RMS value (see chapter 2), the structural performance may be expressed through the RMS acceleration response. Moreover, since strongest accelerations are expected, in general, at the top of the building in the across-wind direction, the decision variable representing the structural performance can be the RMS value of the across-wind acceleration at the top of the building. Hence, the EDP in Eq. (8.26) can be expressed in terms of standard deviation across-wind acceleration at the top, σ_a.

Basic components characterizing the intensity measure IM are considered the mean wind velocity at a reference height, equivalent here to the building height, U_h, and the direction of the mean velocity of the incoming wind, θ.

The probability of failure P_f can be, therefore, expressed by the probability of exceeding a threshold value of the standard deviation across-wind acceleration $\overline{\sigma_a}$ and can be calculated as:

$$P_f = P(\sigma_a \geq \overline{\sigma_a}) = 1 - P(0 \leq \sigma_a \leq \overline{\sigma_a}) \tag{8.27}$$

From Eq. (8.26), covering all the possible values of U_h and θ in their domains of definition, the probability $P(0 \leq \sigma_a \leq \overline{\sigma_a})$ can be written as:

$$P(0 \leq \sigma_a \leq \overline{\sigma_a}) = \int_0^{\overline{\sigma_a}} \int_0^{\infty} \int_0^{2\pi} p(\sigma_a|U_h, \theta) q(U_h, \theta) \, dU_h \, d\theta \, d\sigma_a \tag{8.28}$$

8.4.1 Hazard analysis

The function $q(U_h, \theta)$ corresponds to the *hazard* term $g\,[IM]$, and indicates the joint probability density function of both the mean reference wind speed U_h and the angle of attack θ. Hence[1]:

$$q(U_h, \theta) = P\left[(u_h \leq U_h \leq u_h + du_h) \cap (\vartheta \leq \theta \leq \vartheta + d\vartheta)\right] \tag{8.29}$$

Considering the conditional probability definition[2],

$$\begin{aligned} &q(U_h, \theta) = P\left[(u_h \leq U_h \leq u_h + du_h) \cap (\vartheta \leq \theta \leq \vartheta + d\vartheta)\right] = \\ &P(u_h \leq U_h \leq u_h + du_h | \vartheta \leq \theta \leq \vartheta + d\vartheta) P(\vartheta \leq \theta \leq \vartheta + d\vartheta) \end{aligned} \tag{8.30}$$

The knowledge of hazard term $q(U_h, \theta)$ is achieved through a directional probability analysis of registered wind speed data. Under the simplifying assumption, considered later in this study in order to provide a simple illustrative example (subsection 8.4.3), that the investigated structure is located at the site of the anemometric station, registered wind data don't have to undergo any corrections such as, for example, those related to ground roughness. The anemometric station is at a height h_a usually equal to 10 m over the ground. It means that the wind speed at the building height U_h has to be related to the wind speed at the anemometer height U_{h_a}. Assuming the logarithmic profile [Eq. (6.7)], the wind speeds U_1 and U_2 at heights z_1 and z_2, respectively, are related by:

$$\frac{U_2}{U_1} = \frac{\ln(z_2/z_0)}{\ln(z_1/z_0)} \tag{8.31}$$

where z_0 is the roughness length. Then, considering the prototype structure located at the anemometric station position, the wind speed at the building top U_h can be related to that at the anemometer level U_{h_a} by the following relation:

$$\frac{U_h}{U_{h_a}} = \frac{\ln(h/z_0)}{\ln(h_a/z_0)} \tag{8.32}$$

From the registered wind speeds U_{h_a} it is possible to derive the population of wind speeds at the building height U_h as:

$$U_h = U_{h_a} \frac{\ln(h/z_0)}{\ln(h_a/z_0)} \tag{8.33}$$

Dividing the possible incoming wind directions, corresponding to angles of attack from 0° to 360°, in N sectors $[\theta_{inf,i}; \theta_{sup,i}]$, where $i = 1, 2, 3...N$, a directional probability analysis can be performed considering separately the wind data which fall

[1] Capitol letters are used here to indicate the variable, while small letters refer to values taken from the variable.

[2] Given two arbitrary events A and B, associated with a random experiment, the conditional probability $P(A|B)$ is equal to $\frac{P(A \cap B)}{P(B)}$.

within each sector. For each sector, the joint probability $q(U_h, \theta)$ can be written as:

$$q(U_h, \theta) = P\left[(u_h \leq U_h \leq u_h + du_h) \cap (\theta_{inf,i} \leq \theta \leq \theta_{sup,i})\right] = \\ P(u_h \leq U_h \leq u_h + du_h | \theta_{inf,i} \leq \theta \leq \theta_{sup,i}) P(\theta_{inf,i} \leq \theta \leq \theta_{sup,i}) \tag{8.34}$$

The probability that the direction θ falls between the lower and the upper bounds of the considered sector, $P(\theta_{inf,i} \leq \theta \leq \theta_{sup,i})$, without further analysis, can be estimated, to a first approximation, as:

$$P(\theta_{inf,i} \leq \theta \leq \theta_{sup,i}) = \frac{\text{number of wind data in the i-th sector}}{\text{total number of wind data}} \tag{8.35}$$

Adopting, for example, the Weibull distribution, illustrated in subsection 8.3.1, the conditional probability in Eq. (8.34) can be written as:

$$P(u_h \leq U_h \leq u_h + du_h | \theta_{inf,i} \leq \theta \leq \theta_{sup,i}) = \\ = \frac{k_i}{c_i} \left(\frac{u_h}{c_i}\right)^{k_i - 1} \exp\left[-\left(\frac{u_h}{c_i}\right)^{k_i}\right] \tag{8.36}$$

where c_i and k_i are the parameters of the distribution for the i-th sector and u_h is non-negative.

8.4.2 Vulnerability analysis

The function $p(\sigma_a | U_h, \theta)$ in Eq. (8.28) is the *vulnerability* term $p\left[EDP|IM\right]$ and represents the probability density function of the across-wind standard deviation acceleration conditioned on reference velocity U_h and direction θ. The knowledge of this term requires the probabilistic assessment of the dependence of the acceleration response on velocity U_h and direction θ. More precisely, σ_a indicates the global RMS acceleration response at the top of the building in the direction perpendicular to the sideward faces and can be defined as a kind of *lateral* response. It coincides with the across-wind response only in the case of wind blowing perpendicularly to the windward face. For non zero angles of incidence, the maximum response can be slightly greater than this lateral response, but, for the sake of simplicity, the latter is used to express the performance of the building in serviceability conditions.

For a regular, square-section tall building with the same bending frequency along x and y axes, the lateral response in y direction, σ_{ay}, which occurs when the wind blows at θ incidence with respect to x axis is equal to the response along x, σ_{ax}, when the wind blows with the same velocity (and turbulence) at θ incidence with respect to y (Fig. 8.3, left side). Moreover, equal responses will occur for wind directions symmetric with respect to the diagonals of the square section.

According to Reinhold and Sparks (1979) the greatest response of a slender square-section tall building occurs in the across-wind direction when the wind is blowing directly onto a face. Kawai (1995) measured the response in y direction of a 10:1:1 building model in both smooth an turbulent flow, for angles of attack of 0°, 15°, 30° and 45° (see Fig. 4.9). The y direction means across-wind direction where

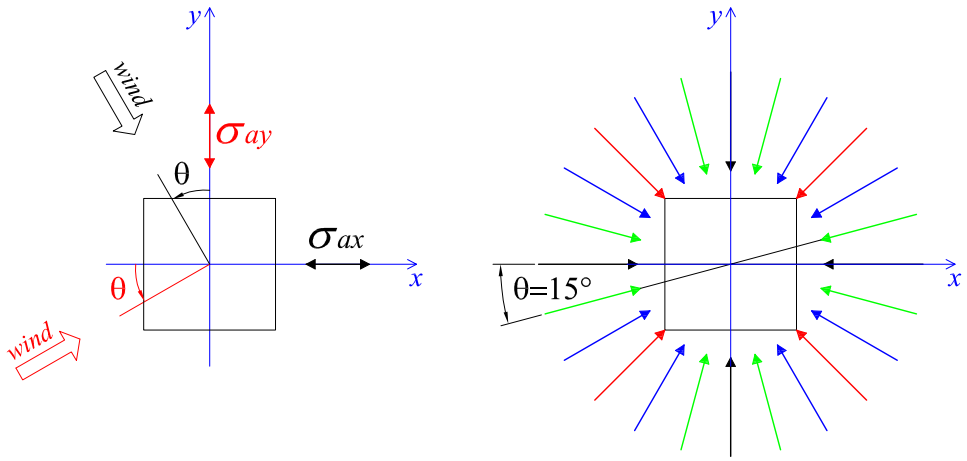

Fig. 8.3 Sketches of the symmetries of the across-wind acceleration response for a square-section building.

the wind is normal to the windward face (parallel to the x axis) as shown in the left side of Fig. 8.3. The normalized RMS displacement response was found to vary significantly with the angle of attack for the different values of the damping ratio considered. This variation is also a function of the wind speed.

In order to describe the variation of the lateral response of a square-section tall building with wind speed and angle of incidence, results from Kawai (1995) relative to urban turbulent layer flow conditions and high critical damping ratio ($\approx 4\%$), illustrated in Fig. 4.9, are used. On the basis of the considerations previously stated about symmetries of the response, from the normalized RMS displacement for the 4 angles of incidence considered by Kawai, it is possible to assess the variability of the response at each value of the incoming wind speed for all the possible wind directions from 0° to 360°, equally spaced by an amplitude of 15°. The sketch in the right side of Fig. 8.3 shows with the same color the incoming wind directions which produce the same lateral response. Hence, a *response surface* is derived, as shown in Fig. 8.4, relating the normalized lateral RMS displacement response σ_d/h with the angle of incidence θ and the reference velocity U_h, expressed here in terms of the non-dimensional reduced velocity $U_h/(f_1 b)$. This normalized representation allows direct transfer from model to full scale as long as model and prototype satisfy the similarity requirements on flow conditions and Scruton number and have the same geometric proportions. Simply knowing the side dimension b, the height h and fundamental bending frequency f_1 of the real building, the lateral RMS displacement response σ_d in full scale can be expressed as a function of the angle of incidence and the mean wind speed at the building top.

The RMS of the lateral displacement response σ_d can be written as:

$$\sigma_d(U_h, \theta) = \sigma_{d,0}(U_h) f(U_h, \theta) \tag{8.37}$$

where $\sigma_{d,0}(U_h)$ is the across-wind response at zero incidence, when wind blows perpendicularly to one face (angle of attack equal to $k\pi/2$, $k = 0, 1, 2, 3, 4$). The function $f(U_h, \theta)$, calculated at each wind speed as the ratio between the response at incidence θ and the response at zero incidence, describes the surface illustrated in Fig. 8.5 where $f(\theta, U_h) = 1$, $\forall U_h$ and $\theta = k\pi/2$, with $k = 0, 1, 2, 3, 4$.

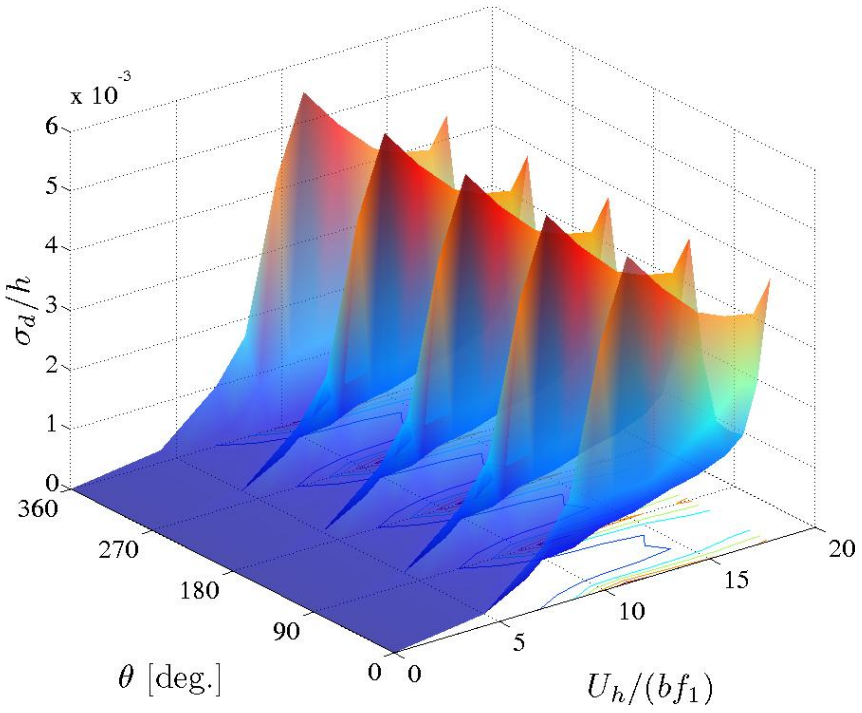

Fig. 8.4 Normalized RMS displacement response for a 10:1:1 tall building in urban flow conditions as a function of reduced velocity and angle of attack (Kawai, 1995).

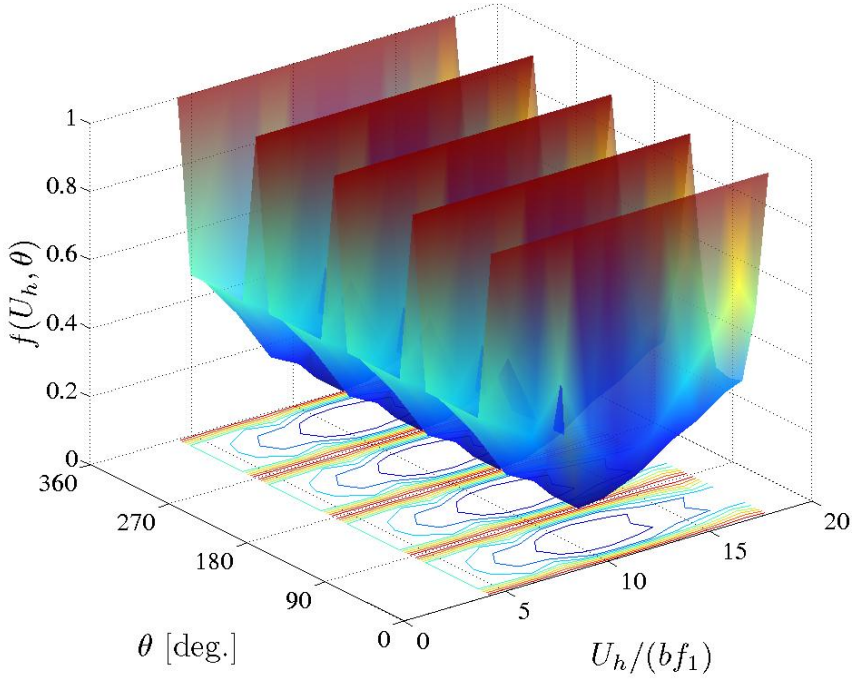

Fig. 8.5 Surface describing the function $f(U_h, \theta)$ in Eq. (8.37) calculated from results by Kawai (1995).

Fig. 8.6 illustrates the dependence of the response measured by Kawai (1995) on the angle of incidence for different values of the reduced mean wind speed at the top of the building. A reduced velocity approximately equal to 10 indicates vortex resonance. These curves show that the response has a significant dependence on the angle of incoming wind speed, while the reduced velocity plays a minor role. A possible simplification of the function $f(U_h, \theta)$ could be therefore achieved neglecting the dependence on U_h and transforming it in a function $f^*(\theta)$.

The estimation of the probability of wind-induced discomfort risk, defined in

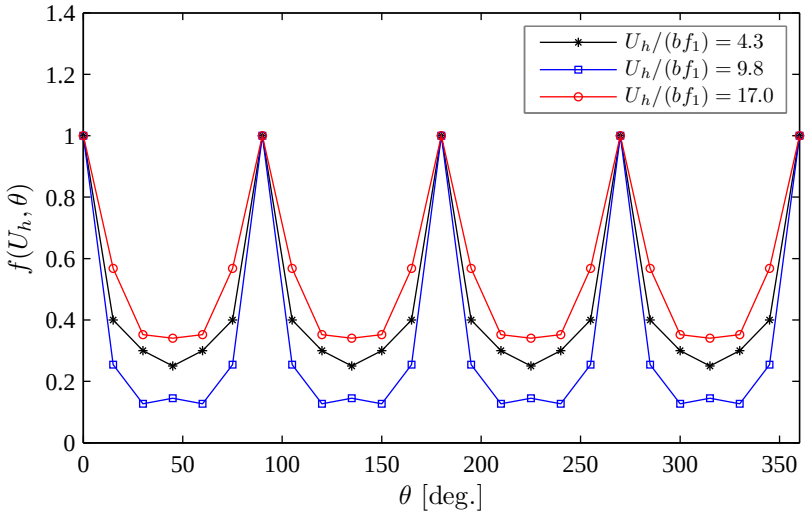

Fig. 8.6 Curves describing the dependence of response on the angle of incidence for different values of the reduced velocity at the building height, from results by Kawai (1995).

Eqs. (8.27) and (8.28), requires the knowledge of the vulnerability term $p(\sigma_a|U_h, \theta)$. As seen for the lateral RMS displacement response, the RMS acceleration response at the top of the building $\sigma_a(U_h, \theta)$ can be written as:

$$\sigma_a(U_h, \theta) = \sigma_{a,0}(U_h) g(\theta, U_h) \tag{8.38}$$

where $\sigma_{a,0}(U_h)$ is the across-wind acceleration response at zero incidence and $g(U_h, \theta) = 1$, $\forall U_h$ and $\theta = k\pi/2$, with $k = 0, 1, 2, 3, 4$. In order to give a qualitative description of the possible variability of the acceleration response with wind speed and angle of attack, considering a substantially harmonic motion, the function $g(U_h, \theta)$ can be assumed equal to $f(U_h, \theta)$, obtained from results by Kawai (1995) and the shape of the curve $\sigma_{a,0}(U_h)$ can be assumed equal to $\sigma_{d,0}(U_h)$ from the same literature work. The lateral RMS acceleration response at the top of a real building will be, therefore, that illustrated in Fig. 8.7. The horizontal light green plane in Fig. 8.7 represents a possible RMS acceleration threshold $\overline{\sigma_a}$. Discomfort risk is the probability of exceeding this acceleration threshold.

Eq. (8.28) can be written as:

$$P(0 \leq \sigma_a \leq \overline{\sigma_a}) = \int_0^{\infty} \int_0^{2\pi} \left[\int_0^{\overline{\sigma_a}} p(\sigma_a|U_h, \theta)\, d\sigma_a \right] q(U_h, \theta)\, dU_h\, d\theta \tag{8.39}$$

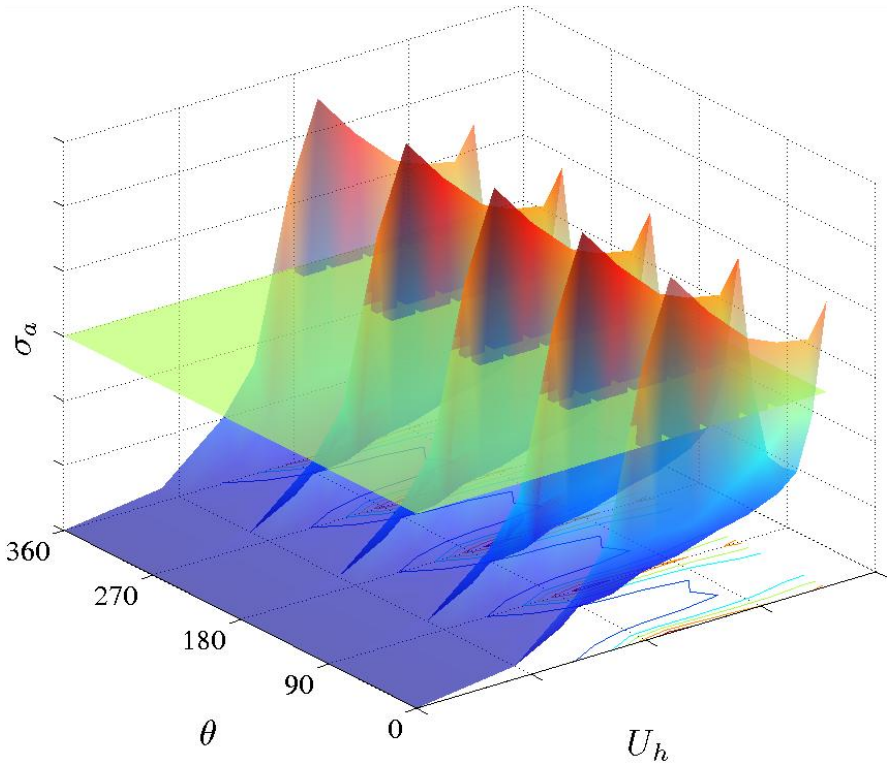

Fig. 8.7 Qualitative description of the lateral RMS acceleration response at the top of a tall building as a function of angle of attack and wind speed at the building height.

The term in square brackets in Eq. (8.39) represents the probability of having σ_a values, conditioned on the value of U_h and θ, lower than the threshold $\overline{\sigma_a}$. From the deterministic knowledge of the response surface $\sigma_a(U_h, \theta)$ in Fig. 8.7, this probability is equal to 1 for all the couples (U_h, θ) where $\sigma_a \leq \overline{\sigma_a}$ (*Safety Domain* D_S), that means response surface under the threshold plane, and is equal to zero for all the couples (U_h, θ) where $\sigma_a > \overline{\sigma_a}$ (*Risk Domain* D_R), that means response surface above the threshold plane.
A scalar field $F(U_h, \theta)$, can be therefore defined as:

$$F(U_h,\theta) = \int_0^{\overline{\sigma_a}} p(\sigma_a|U_h,\theta)\, d\sigma_a = \begin{cases} 1, & \text{if } (U_h,\theta) \in D_S \\ 0, & \text{if } (U_h,\theta) \in D_R \end{cases} \tag{8.40}$$

Eq. (8.39) can be written as:

$$P(0 \leq \sigma_a \leq \overline{\sigma_a}) = \int_0^{\infty} \int_0^{2\pi} F(U_h,\theta) q(U_h,\theta)\, dU_h\, d\theta \tag{8.41}$$

and the integrals can be split into two complementary parts:

$$\begin{aligned} P(0 \leq \sigma_a \leq \overline{\sigma_a}) = & \int\int_{D_S} F(U_h,\theta) q(U_h,\theta)\, dU_h\, d\theta + \\ & + \int\int_{D_R} F(U_h,\theta) q(U_h,\theta)\, dU_h\, d\theta \end{aligned} \tag{8.42}$$

Considering the definition of the scalar field $F(U_h, \theta)$ in Eq. (8.40), Eq. (8.42) becomes:

$$P(0 \leq \sigma_a \leq \overline{\sigma_a}) = \int \int_{D_S} q(U_h, \theta)\, dU_h\, d\theta \tag{8.43}$$

The probability of failure is, therefore, equal to:

$$P_f = 1 - P(0 \leq \sigma_a \leq \overline{\sigma_a}) = 1 - \int \int_{D_S} q(U_h, \theta)\, dU_h\, d\theta \tag{8.44}$$

The procedure for evaluating the probability of failure illustrated so far, could be further simplified. As long as, for example, for each value of θ, $\sigma_a(U_h, \theta)$ is an injective function, monotonically increasing with U_h, the horizontal threshold plane intersects the response surface along a horizontal curve whose projection on the (U_h, θ) plane defines a frontier curve $\bar{U_h}(\theta)$ between the Safety Domain and the Risk Domain. Even if the response does not possibly maintain this injective feature, especially in the lock-in range, as seen with the results from Kawai (1995), the assumption that the threshold plane crosses the response surface along a frontier curve only is believed acceptable until the threshold meets the response surface at low values of wind speeds, before lock-in conditions.

Assuming that the response is a monotonically increasing function of U_h at each θ, the scalar field $F(U_h, \theta)$ is defined as:

$$F(U_h, \theta) = \begin{cases} 1, & \text{if } U_h \leq \overline{U_h}(\theta) \\ 0, & \text{if } U_h > \overline{U_h}(\theta) \end{cases} \tag{8.45}$$

And Eqs. (8.41) and (8.42) become:

$$\begin{aligned} P(0 \leq \sigma_a \leq \overline{\sigma_a}) = &\int_0^{\overline{U_h}(\theta)} \int_0^{2\pi} F(U_h, \theta) q(U_h, \theta)\, dU_h\, d\theta + \\ &+ \int_{\overline{U_h}(\theta)}^{\infty} \int_0^{2\pi} F(U_h, \theta) q(U_h, \theta)\, dU_h\, d\theta \end{aligned} \tag{8.46}$$

In Eq. (8.46) $F(U_h, \theta)$ is equal to 1 in the first integral, and equal to 0 in the second one. The probability of failure can be, therefore, written as:

$$P_f = 1 - \int_0^{\overline{U_h}(\theta)} \int_0^{2\pi} q(U_h, \theta)\, dU_h\, d\theta \tag{8.47}$$

8.4.3 Application of the procedure

The procedure aimed at the assessment of wind-induced discomfort risk, illustrated in the previous section, is applied to the case study tall building illustrated in section 8.2. The risk is quantified in terms of the probability of exceeding a threshold value of the RMS lateral acceleration at the building height and is calculated using Eqs. (8.27) and (8.28).

In order to simply provide an example of application of the procedure, the motion perception threshold of the ISO-6897 [(ISO 6897, 1984)] is used. It gives the limit value of standard deviation acceleration for a 10-min duration in 5-year-recurrence

wind speed, as a function of the vibration frequency [Eq. (2.2)]:

$$\overline{\sigma_a} = exp(-3.65 - 0.41 \ln f_1) \approx 0.0582 \text{ m/s}^2 \approx 5.9 \text{ milli-g} \tag{8.48}$$

where $f_1 = 0.14$ Hz is the fundamental frequency of the building.

From wind tunnel tests on its aeroelastic model, the lateral acceleration response at the top of the building is known only for wind blowing perpendicularly to one face, when lateral response coincides with across-wind response. This response, illustrated in (Fig. 8.2) as a function of the mean wind speed at the building height, considering the building symmetries assumed, occurs for angle of incidence $\theta = k\pi/2$, with $k = 0, 1, 2, 3, 4$. No information is available on the dependence of the lateral response on the angle of incidence from wind tunnel data. As seen in subsection 8.4.2, the RMS acceleration response at the top of the building $\sigma_a(U_h, \theta)$ is a function of both wind speed and angle of incidence and should be written as:

$$\sigma_a(U_h, \theta) = \sigma_{a,0}(U_h) g(U_h, \theta) \tag{8.49}$$

where $\sigma_{a,0}(U_h)$ is the known across-wind response at zero incidence and $g(U_h, \theta) = 1$, $\forall U_h$ and $\theta = k\pi/2$, with $k = 0, 1, 2, 3, 4$. Assuming that the function $g(U_h, \theta)$ is that obtained from measurements by Kawai (1995), for example, the response surface is that depicted in Fig. 8.8. Since the response is monotonically increasing for each θ

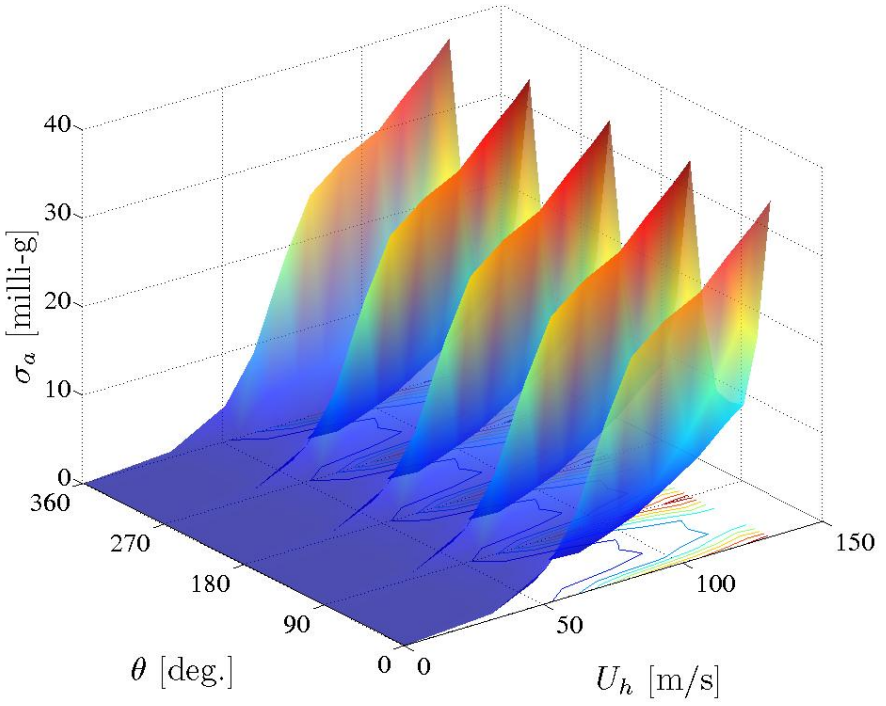

Fig. 8.8 Surface representing the lateral RMS acceleration response at the top of the prototype, assuming that its variation with angle of incidence and wind speed is represented by the function $f(U_h, \theta)$ derived from measurements by Kawai (1995).

with wind speed U_h, the horizontal plane, representing the acceleration threshold $\overline{\sigma_a}$ would intersect the surface along a frontier curve. Risk could be calculated according to Eqs. (8.47), (8.46) and (8.45). Moreover the function $g(U_h, \theta)$ could be simplified in a function $g^*(\theta)$, neglecting the dependence on wind speed.

In this case, however, a strongly simplifying and conservative assumption is

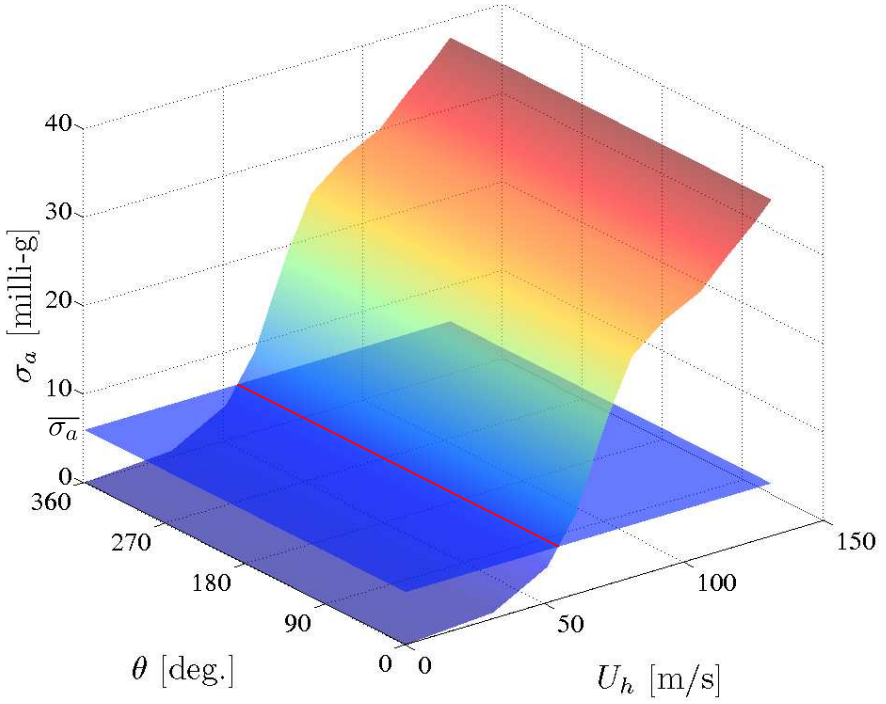

Fig. 8.9 Surface of acceleration response under the conservative assumption of non-dependence of the response on incoming flow direction.

made. Since the real response variation with angle of incidence and mean wind speed could have been assessed by proper directional wind tunnel measurements, and it is supposed to be affected by several factors as turbulence conditions, Scruton number, aspect ratio, taking the results from other studies could not lead to accurate estimates of risk. Therefore, for the sole purpose of applying the procedure, the lateral tip acceleration known only at zero incidence is conservatively assumed to represent the real response for all the possible incoming wind directions. This assumption consists in taking $g(U_h, \theta) = 1 \; \forall U_h$ and $\forall \theta$. The surface response becomes that shown in Fig. 8.9. The horizontal threshold plane intersects the surface along a straight line, that means that the dependence of the frontier value $\overline{U_h}$ on the angle θ in Eq. (8.47) is lost. The probability of risk, that means the probability of exceeding the acceleration threshold, can be simply written as:

$$P_f = 1 - \int_0^{\overline{U_h}} p(U_h)\, dU_h \tag{8.50}$$

where the hazard term is $p(U_h)$, that is the non-directional probability density function of the reference wind speed.

It is clear that the simplifying assumption made leads to a strong overestimation of the response and, therefore, of the discomfort risk. What is estimated from Eq. (8.50) represents an upper bound of the real risk of experiencing unacceptable accelerations.

The integral in Eq. (8.50) is the cumulative distribution function of the reference velocity, regardless of incoming flow direction, and expresses the probability of having wind velocities at the top of the building lower than the value $\overline{U_h}$, which is

the wind velocity at which the acceleration threshold intersects the response surface. The probability of failure becomes equal to the complementary cumulative distribution function (CCDF) of the reference mean wind speed:

$$P_f = 1 - F(\overline{U_h}) = P(U_h > \overline{U_h}) \tag{8.51}$$

The calculation of the probability of discomfort risk is reduced to the definition of the threshold value $\overline{U_h}$ known from the response surface and the acceleration limit considered and to the probabilistic analysis of wind speed data at the building site.

With the assumption of non-dependency of the response on incoming wind direction, the projection of the response surface on each vertical (U_h, θ) plane is the curve reported in Fig. 8.2. The acceleration threshold crosses this curve at a value of the reference wind speed $\overline{U_h}$ of approximately 55 m/s (Fig. 8.10). The probability of risk is therefore the probability of exceeding a mean wind speed, regardless of direction, of 55 m/s at the building top.

Wind data used in this application have been obtained from the Monte Argen-

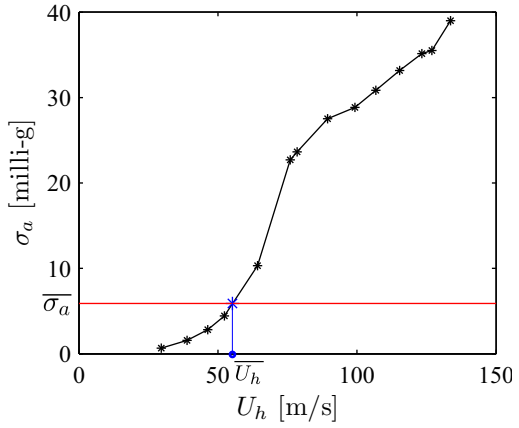

Fig. 8.10 Estimation of the limit value of the reference wind speed for the evaluation of risk.

tario station, located in Tuscany, Italy[3]. They consist in 50 years (from 1^{st} January 1961 to 31^{st} December 2010) registrations of 8 daily measures, one of each 3 hours, of the mean wind speed over 10 minutes for 36 directional sectors. A total amount of 143672 data is available. However, because of undesired errors occurred in some registrations, only 143097 of them are serviceable. These are comprehensive of *wind calms*. The height of the anemometer head has the standard meteorological value of 10 m.

The analysis of the non-directional probability of the population of wind data is performed, using the hybrid Weibull distribution presented in section 8.3.1. The population of wind data consists of 129002 non-zero wind speed measurements. From the registered data the auxiliary variables [Eq. (8.17)] are calculated and fitted, by means of the least-square method, to a straight line (Fig. 8.11). The parameters of the distribution, estimated from the slope and the zero-intercept of the line

[3]Wind data are kindly provided by Col. G. P. Cesolari, from "Centro Nazionale di Meteorologia e Climatologia Aeronautica - Servizio Climatologia e Documentazione", Pomezia (RM), Italy.

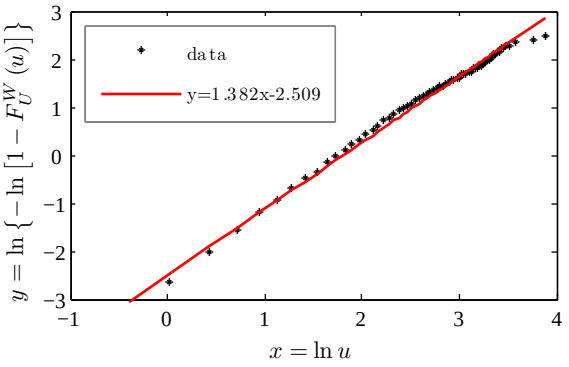

Fig. 8.11 Estimation of the distribution parameter.

[Eq. (8.19)], are:

$$\begin{cases} k = 1.3820 \\ c = 6.1441 \end{cases} \tag{8.52}$$

Fig. 8.12 shows the Weibull probability of exceedance, $P^W(U > u)$, calculated from equation Eq. (8.14), using the estimated parameters [Eq. (8.52)].

The probability of having wind calms is equal to:

$$F_0 = \frac{\text{number of wind calms data}}{\text{total number of wind data}} = 0.0985 \tag{8.53}$$

From Eq. (8.13) the probability of exceedance of the Hybrid distribution $P^H(U > u)$ is equal to $(1 - F_0)\, P^W(U > u)$ and is also reported in Fig. 8.12. Under the assump-

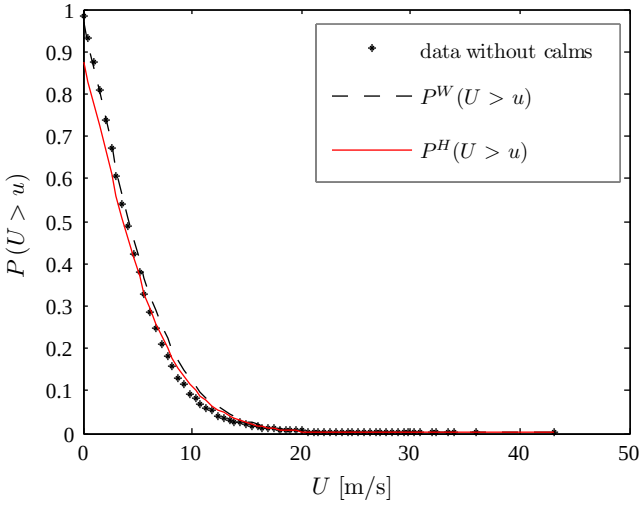

Fig. 8.12 Probability of exceedance $P(U > u)$: Weibull distribution $[P^W(U > u)]$ fitted to non-zero wind speed data and Hybrid model, $P^H(U > u)$.

tion that the case study building is located at the anemometric station position, it is possible to relate the mean wind speed at the building height U_h to the mean wind speed at the anemometer head, indicated here for the sake of simplicity with

U, according to Eq. (8.33), as follows:

$$U = U_h \frac{\ln(10/z_0)}{\ln(h/z_0)} \tag{8.54}$$

where 10 is the height of the anemometer in meters and h is the building height equal to 304 m and $z_0 = 1.2$ m. The probability of failure in Eq. (8.51) can be written as:

$$P_f = 1 - F(\overline{U}) = P(U > \overline{U}) \tag{8.55}$$

where the threshold value at the anemometer head $\overline{U}$ is derived from Eq. (8.54) and is equal to:

$$\overline{U} = \overline{U_h} \frac{\ln(10/z_0)}{\ln(304/z_0)} \approx 21 \text{ m/s} \tag{8.56}$$

Wind-induced discomfort risk is finally estimated from the Hybrid model probability of exceedance shown in Fig. 8.12 as:

$$P_f = P(U > 21 \text{ m/s}) = 0.0047 \tag{8.57}$$

Risk can be expressed in terms of the average number of days per year in which the building experiences unacceptable acceleration values as:

$$\text{Risk} = P_f \times d_y \approx 1.7 \text{ days/year} \tag{8.58}$$

where d_y is the number of days per year (365).

It has to be pointed out that the ISO-6897's comfort criterion is used here only to provide an illustrative example of application of the discomfort risk assessment procedure. However, the estimation of risk performed is not related to the comfort checking procedure recommended by the ISO-6897 Standards. The next section is, therefore, aimed at illustrating how this ISO-6897 procedure could be directly applied to the considered structure.

8.5 Checking of the building comfort based on ISO-6897's criterion

In this section the checking procedure for perception of wind-induced vibrations proposed by the ISO-6897 recommendations is applied to the case study tall building introduced in section 8.2. This motion perception threshold is expressed in terms of standard deviation acceleration for a 10-min duration in 5-year-recurrence wind speed and is that calculated in Eq. (8.48). As previously done, the lateral RMS acceleration response at the top of the prototype structure is conservatively assumed equal to the across-wind response for wind normal to one face, for all the possible incoming flow directions [Fig. 8.2(b)]. The checking of the comfort requirement consists in calculating the 10-min duration wind speed with 5-year return period and in verifying that the corresponding RMS tip acceleration does not exceed the calculated frequency-dependent threshold. The design wind speed at the top of the building with a return period of 5 years is estimated by means of the probabilistic

analysis of the annual maxima from registered wind data.

8.5.1 Design wind speed at the top of the building

From the available wind data, that are those mentioned in subsection 8.4.3, the largest wind speed in each calendar from 1961 to 2010 is extracted, regardless of direction (Fig. 8.13). The series of the annual maxima is then ranked in order of

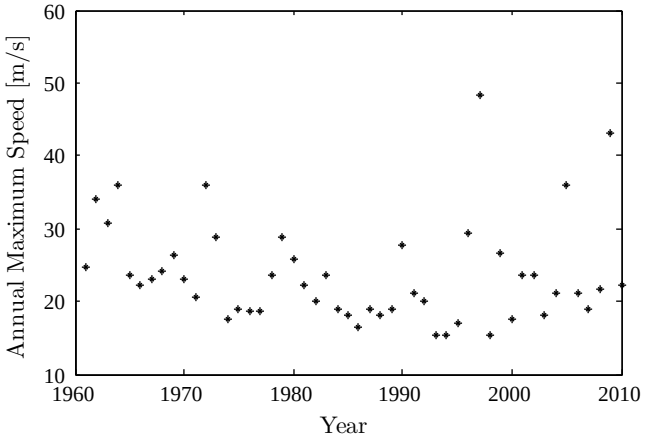

Fig. 8.13 Annual wind speed maxima.

smallest to largest. Each value of the wind speed is assigned to a probability of non-exceedance according to:

$$p \approx \frac{m}{N+1} \tag{8.59}$$

where m is equal to the number of maxima taking this value and N is the number of maxima equal to 50. Then the series of $x = -\ln(-\ln p)$ values is calculated. The wind speed is plotted against x and a straight line of "best fit" is drawn by means of the linear least square method (Fig. 8.14). The estimated parameters of the Gumbel

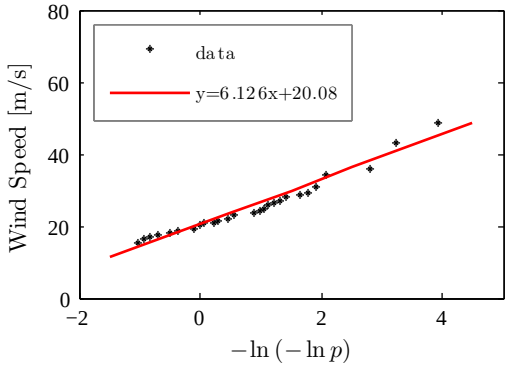

Fig. 8.14 Analysis of annual maximum wind speeds using the Gumbel method.

distribution are:

$$\begin{cases} \mu = 20.08 \\ \beta = 6.126 \end{cases} \tag{8.60}$$

Fig. 8.15 illustrates the probability of exceedance $1 - F_U(u)$. From Eq. (8.25) it is

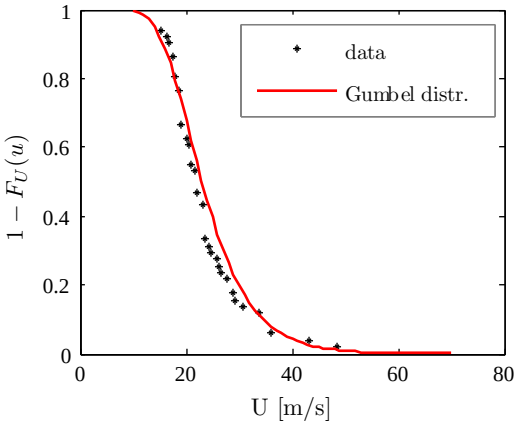

Fig. 8.15 Probability of exceedance.

now possible to calculate the wind speed with a certain return period. For example, the wind speed with 5-year return period, $\bar{U}_{R=5}$ is equal to:

$$\bar{U}_{R=5} = 20.08 + 6.126 \left\{ -\ln\left[-\ln\left(1 - \frac{1}{5}\right)\right]\right\} \approx 29.3 \text{ m/s} \tag{8.61}$$

8.5.2 Checking of the ISO-6897 comfort requirement

As previously specified, the prototype structure is assumed located at the anemometric station position. From Eq. (8.33), the 5-year-recurrence wind speed at the top of the building, $\bar{U}_{h,R=5}$, is related to that at the anemometer height (10 m), $\bar{U}_{10,R=5}$, by:

$$\frac{\bar{U}_{h,R=5}}{\bar{U}_{10,R=5}} = \frac{\ln(h/z_0)}{\ln(10/z_0)} \tag{8.62}$$

Therefore, the design wind speed to be considered for ISO-6897 comfort criterion is:

$$\bar{U}_{h,R=5} = \bar{U}_{10,R=5} \times \frac{\ln(h/z_0)}{\ln(10/z_0)} = 77 \text{ m/s} \tag{8.63}$$

where $z_0 = 1.2$ m, $h = 304$ m and $\bar{U}_{10,R=5}$ is equal to 29.3 m/s, as calculated in Eq. (8.61).

The across-wind acceleration response corresponding to the 5-year recurrence wind speed is approximately equal to 24 milli-g. This value violates the ISO-6897 criterion, being more than four times greater than the comfort threshold $\overline{\sigma_a}$ [Eq. (8.48)]. The ISO-6897 threshold crosses the acceleration response curve at a reference wind speed of approximately 55 m/s. The latter corresponds to a wind speed at the anemometric station approximately equal to 21 m/s. From Eq. (8.20),

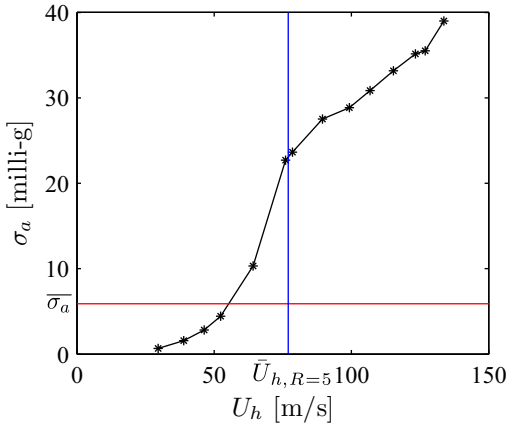

Fig. 8.16 Comparison between the tip across-wind acceleration response from aeroelastic tests and the ISO-6897 comfort threshold.

considering the estimated parameters of the distribution [Eq. (8.60)], the probability $P(U_h < 55) = F_{U_h}(55)$ equal to $P(U_{10} < 21) = F_{U_{10}}(21)$ m/s is:

$$F_{U_h}(55) = F_{U_{10}}(21) = \exp\left\{-\exp\left[-\frac{21 - 20.08}{6.126}\right]\right\} = 0.423 \tag{8.64}$$

The Return Period [Eq. (8.23)] is :

$$R = \frac{1}{1 - F_{U_h}(55)} = 1.73 \tag{8.65}$$

It means that the wind speed at the top of the building, corresponding to the ISO-6897 Standard, has a return period of 1.73 years, that is lower than the recommended 5 years. It has, therefore, a probability of exceedance of 0.58 (1/1.73) in any one year, greater than 0.2 (1/5).

8.6 Summary and main remarks

The main goal of this chapter is the definition of a general procedure for discomfort risk assessment of tall buildings. The procedure is based on the risk management framework reviewed in section 2.2 and is mathematically framed according to the Performance-Based Design approach illustrated in section 2.3. Once defined the parameter of the response to be checked for ensuring comfort of the occupants, e.g. the RMS acceleration at the top, wind risk can be estimated through the *hazard analysis*, which defines the joint probability density function of wind speed and direction, characterizing the wind hazard, and the *vulnerability analysis*, which evaluates the probability density function of response of the building conditioned on the hazard.

Once defined a proper comfort threshold, wind risk can be estimated in terms of average number of days per year in which the building response exceeds the threshold.

The building performances in serviceability conditions are expressed here in terms of lateral (that means across-wind for wind blowing perpendicularly to one face) RMS accelerations at the top. However, the procedure could be easily varied if a comfort criterion based on peak values of the acceleration is preferred. This would

imply only that the vulnerability analysis is carried out in terms of peak acceleration response as a function of wind speed and direction.

Possible simplifications of the procedure are illustrated for an easier risk calculation.

In order to provide an illustrative example, the procedure is applied to a regular square-section tall building. Registered wind data from a real anemometric station are used. Since the response of this building is known from wind tunnel data for different wind speeds only for wind blowing perpendicularly to one face and not for all the other possible angles of incidence, for the sole purpose of application, the response as a function of wind speed is assumed to be independent on direction. This assumption obviously leads to an overestimation of risk. The calculation of discomfort risk is reduced to the estimation of the probability of exceeding a frontier value of the mean wind speed, regardless of direction. This probability is estimated through the probabilistic analysis of wind data fitted to the Hybrid model.

The same building is also used to provide an example of application of the comfort checking procedure which follows the motion perception design criteria of ISO Standard 6897. The 5-year-recurrence wind speed, required by this Standard, is estimated from the probabilistic analysis of the annual maxima from registered wind data, using the Gumbel distribution.

Chapter 9

Conclusions and recommendations

9.1 Conclusions

This thesis deals with the serviceability design of tall buildings under the wind action. The major goals achieved in this study can be summarized as follows.

1. Wind tunnel tests on a 6:1:1 equivalent aeroelastic model were carried out in a boundary layer wind tunnel for a wide range of wind speeds. This experimental activity represents one of the first attempts in an international context aimed at the simultaneous measurement of pressures, overall forces, displacements and accelerations on an aeroelastic model of a tall building, even in lock-in conditions.

2. The vortex resonance condition is identified from wind tunnel tests and its effects on both wind loads and responses are investigated.

3. A non-dimensional representation of the across-wind acceleration response measured in the wind tunnel is introduced in order to be directly translated from model scale to full scale to be used for the comfort evaluation of a case study building.

4. Aeroelastic effects in the across-wind response are identified in terms of aerodynamic damping through an inverse approach based on the comparison between the aeroelastic measured response and the response predicted from a numerical model loaded with pressures from rigid model tests. Aerodynamic damping for the considered structure with high structural damping and Scruton number is positive. Aeroelasticity, therefore, damps its response.

5. A general procedure for assessment of wind-induced discomfort risk of tall buildings is proposed and mathematically framed according to the Performance-Based Design approach. This procedure deals with the hazard analysis and structural vulnerability analysis stages and allows the estimation of risk in terms of probability of exceeding a comfort threshold, for any comfort criteria adopted. This probability can be easily translated in average number per year in which the building experiences unacceptable accelerations.

9.2 Recommendations for future work

The experimental activity in the boundary layer wind tunnel was a laborious stage of the work. The equivalent aeroelastic model technique is extremely powerful, but resulted quite inconvenient in practical use. The elaborated structure of the model complicated a lot the assembly phase which resulted in a time consuming stage of the work. The mode shapes of the model are approximately linear, maybe also because of the connections with the base-balance and the supporting system which influenced the model. Thus, the possibility of studying 3-D mode shapes inherent in equivalent models, different from "stick" type models, was lost.

Another critical feature of the aeroelastic model tested is that the structural damping ratio in the across-wind direction was not constant, but varied during the various tests in which different vibration amplitudes were reached. This evidence complicated the numerical-experimental procedure for the identification of aerodynamic damping, since a preliminary stage of validation of the system structural damping, at each wind speed tested, had proved necessary.

On the basis of these considerations, it can be suggested to prefer the simple rigid base-pivoted "stick" type model when the studying of non linear and/or coupled mode shapes is not necessarily addressed or to pay greater attention to the effects on mode shapes that may result from the connection of the model to the base balance and/or the supporting system, when continuous models with non linear mode shapes are investigated.

Greater attention should be payed to the structural damping of the model, since it is recommendable to avoid structural damping dependence on vibration amplitude. In this research the structural damping was not easily adjustable. A system for controlling damping could have allowed a richer analysis of the results in function of damping or Scruton number. The evaluation of across-wind aerodynamic damping in function of the Scruton number would be even possible and significant.

Concerning the proposed procedure for discomfort risk assessment, it has to be pointed out that it is limited to the hazard analysis and the structural analysis stages only. Further improvements of the procedure could be achieved introducing damage and/or loss analysis stages. The achievement of unacceptable thresholds, could be, for example, related to business interruption times.

The risk assessment procedure proposed is applied to a case study building under the conservative assumption that the lateral response of the building is equal to the across-wind response at zero incidence, regardless of incoming wind direction. This is, obviously, a strongly conservative assumption. A more accurate estimation of risk could be performed measuring the response for the same wind speed range but for different angles of attack.

Finally, the risk assessment procedure proposed is fully probabilistic. However, the vulnerability analysis is performed deterministically. Therefore, uncertainties could be considered and the response could be described probabilistically in function of the hazard.

Bibliography

AIJ (1991). Architectural Institute of Japan Recommendations. Guidelines for the Evaluation of Habitability to Building Vibration, AIJ-GEH-2004, Tokyo, Japan.

AIJ (2004). Architectural Institute of Japan Recommendations. Guidelines for the Evaluation of Habitability to Building Vibration, Tokyo, Japan.

Alan G. Davenport Wind Engineering Group (2007). Wind tunnel testing: a general outline. Technical report, The Boundary Layer Wind Tunnel Laboratory, University of Wester Ontario, Faculty of Engineering Science.

Ali, M. M. and Moon, K. S. (2007). Structural developments in tall buildings: current trends and future prospects. *Architectural Science Review*, **50**(3), 205–223.

ASCE (1931). Designing wind bracing for skyscrapers. *ASCE Civil Engineering*, **1**(8), 700.

ASCE (1999). Wind Tunnel Studies of Buildings and Structures. American Society of Structural Engineers Manuals and Reports on Engineering Practice No. 67. Technical report, Task Committee on Wind Tunnel Testing of Buildings and Structures - Aerodynamics Commettee - Aerospace Division.

ASCE 7-10 (2010). Minimum Design Loads for Buildings and Other Structures. American Society of Civil Engineers, Reston, VA.

AS/NZS-Standard (1999). Risk management.

Augusti, G. and Ciampoli, M. (2006). First steps towars performance-based wind engineering. In G. Bartoli, F. Ricciardelli, A. Saetta, and V. Sepe, editors, *Performance of wind exposed structures: results of the PERBACCO project*, pages 13–20. Firenze University Press.

Augusti, G. and Ciampoli, M. (2008). Performance-based design in risk assessment and reduction. *Probabilistic Engineering Mechanics*, **23**, 496–508. Dedicated to Professor Ove Ditlevsen.

Augusti, G., Borri, C., and Niemann, H. J. (2001). Is aeolian risk as significant as other environmental risks? *Reliability Engineering & System Safety*, **74**(3), 227–237.

Bartoli, G., Contri, S., Mannini, C., and Righi, M. (2009). Toward an improvement in the identification of bridge deck flutter derivatives. *Journal of Engineering Mechanics*, **135**(8), 771–785.

Bashor, R. and Kareem, A. (2007). Probabilistic performance evaluation of buildings: an occupant comfort perspective. In *Proceedings of 12th International Conference on Wind Engineering*, volume 2, pages 1335–1342, Cairns, Australia.

Bearman, P. W. and Obasaju, E. D. (1982). An experimental study of pressure fluctuations on fixed and oscillating square section cylinders. *Journal of Fluid Mechanics*, **119**, 297–321.

Beirlant, J., Goegebeur, Y., Teugels, J., and Segers, J. (2004). *Statistics of Extremes*. John Wiley & Sons, Ltd.

Bergstrom, D. J. and Wang, J. (1997). Discrete vortex model of flow over a square cylinder. *Journal of Wind Engineering and Industrial Aerodynamics*, **67-68**, 37–49.

Bérnard, H. (1908). Formation de centres de giration à l'arrière d'un obstacle en mouvement. *Comptes rendus de l'Académie des Sciences*, **147**, 839–842.

Boggs, D. (1995). *Acceleration indexes for human comfort in tall buildings - peak or RMS?* CTBUH Monograph Chapter 13, Council on Tall Buildings and Urban Habitat.

Boggs, D. W. (1992). Validation of the aerodynamic model method. *Journal of Wind Engineering and Industrial Aerodynamics*, **42**, 1011–1022.

Boggs, D. W. and Peterka, J. A. (1989). Aerodynamic model tests of tall buildings. *Journal of Engineering Mechanics*, **115**(3), 618–635.

Burton, M. D., Kwok, K. C. S., Hitchcock, P. A., and Denoon, R. O. (2006). Frequency dependence of human response to wind-induced building motion. *Journal of Structural Engineering*, pages 296–303.

Burton, M. D., Kwok, K. C. S., and Hitchcock, P. A. (2007). Occupant comfort criteria for wind-excited buildings; based on motion duration. In *Proceedings of 12th International Conference on Wind Engineering*, pages 1207–1214, Cairns, Australia.

Cermak, J. E. (1977). Wind-tunnel testing of structures. *Journal of the Engineering Mechanics Division, ASCE*, **103**(6), 1125–1140.

Chang, F. K. (1967). Wind and movement in tall buildings. *ASCE Civil Engineering*, **37**(8), 70–72.

Chang, F. K. (1973). Human response to motions in tall buildings. *Journal of the Structural Division. Proceedings of the ASCE*, **98**(ST6), 1259–1272.

Chen, J. M. and Liu, C. H. (1999). Vortex shedding and surface pressures on a square cylinder at incidence to a uniform air stream. *Journal of Heat and Fluid Flow*, **20**, 592–597.

Chen, P. W. and Robertson, L. E. (1972). Human perception thresholds of horizontal motion. *Journal of the Structural Division. Proceedings of the ASCE*, **98**(ST8), 1681–1696.

Cheng, C. M., Lu, P. C., and Tsai, M. S. (2002). Acrosswind aerodynamic damping of isolated square-shaped buildings. *Journal of Wind Engineering and Industrial Aerodynamics*, **90**, 1743–1756.

Cheong, H. F., Balendra, T., Chew, Y. T., Lee, T. S., and Lee, S. L. (1992). An experimental technique for distribution of dynamic wind loads on tall buildings. *Journal of Wind Engineering and Industrial Aerodynamics*, **40**, 249–261.

Ciampoli, M. and Petrini, F. (2012). Performance-based aeolian risk assessment and reduction for tall buildings. *Probabilistic Engineering Mechanics*, **28**, 75–84.

Ciampoli, M., Petrini, F., and Augusti, G. (2011). Performance-based wind engineering: towards a general procedure. *Structural Safety*, **33**, 367–378.

Clark, R., Strganac, T. W., Curtiss, H. C., Cox, D., Edwards, J. W., Hall, K. C., Peters, D. A., Scanlan, R. H., Simiu, E., and Sisto, F. (2004). *A Modern Course in Aeroelasticity*. Springer-Verlag New York Inc.

CNR-DT 207 (2008). Instruction for the evaluation of wind induced forces and effects on contructions. Italian National Research Council.

Cook, N. (1986). *The designers guide to wind loading of building structures. Part 1: Background, Damage Survey, Wind Data and Structural Classification*. Butterworths, London.

Cook, N. J. (1990). *The designers guide to wind loading of building structures. Part 2: Static Structures*. Butterworths, London.

Davenport, A. G. (1963). The buffeting of structures by gusts. In *Proceedings, International Conference on Wind Effects on Buildings and Structures*, pages 358–391, Teddington U.K.

Davenport, A. G. (2002). Past, present and future of wind engineering. *Journal of Wind Engineering and Industrial Aerodynamics*, **90**(12-15), 1371–1380.

Davenport, A. G. and Novak, M. (1976). Vibration of structures induced by wind. In *Shock and Vibration Handbook*. McGraw Hill Book Inc., New York.

Deaves, D. M. and Lines, I. G. (1997). On the fitting of low mean windspeed data to the Weibull distribution. *Journal of Wind Engineering and Industrial Aerodynamics*, **66**, 169–178.

Denoon, R. O. (2000). *Designing for serviceability accelerations in buildings*. Ph.D. thesis, The University of Queensland.

Dutta, S., Muralidhar, K., and Panigrahi, P. K. (2003). Influence of the orientation of a square cylinder on the wake properties. *Experiments in Fluids*, **34**, 16–23.

Dutta, S., Panigrahi, P. K., and Muralidhar, K. (2008). Experimental investigation of flow past a square cylinder at an angle of incidence. *Journal of Engineering Mechanics*, **134**(9), 788–803.

Dyrbye, C. and Hansen, S. (1997). *Wind Loads on Structures*. John Wiley & Sons, i edition.

Feng, C. (1968). *The Measurement of Vortex Induced Effects in Flow Past Stationary and Oscillating Circular and D-Section Cylinders*. Ph.D. thesis, University of British Columbia, Canada.

GB50009-2001 (2001). Chinese Code for Loading on Buildings and other Structures. (in Chinese).

Goldman, D. E. and von Gierke, H. E. (1976). Effect of shock and vibration on man. In *Shock and Vibration Handbook*. McGraw Hill Book Inc., ii edition.

González, M. A., Ezquerro, J. M., Lapuerta, V., Laverón, A., and Rodrígez, J. (2011). Components of a Wind Tunnel Balance: Design and Calibration. In Dr. Jorge Colman Lerner and Dr. Ulfilas Boldes, ISBN 978-953-307-623-2, editor, *Wind Tunnels and Experimental Fluid Dynamics*. InTech.

Goto, T. (1983). Studies on wind-induced motion of tall buildings based on occupants' reactions. *Journal of Wind Engineering and Industrial Aerodynamics*, **13**(1-3), 241–252.

Gu, M. and Quan, Y. (2004). Across-wind loads of typical tall buildings. *Journal of Wind Engineering and Industrial Aerodynamics*, **92**(13), 1147–1165.

Gu, M., Zhang, R., and Xiang, H. (2000). Identification of flutter derivatives of bridge decks. *Journal of Wind Engineering and Industrial Aerodynamics*, **84**(2), 151–162.

Gumbel, E. J. (1954). Statistical theory of extreme values and some practical applications. In *Applied Math Series 33*. National Bureau of Standards, Washington, D.C.

Gumbel, E. J. (1958). *Statistics of Extremes*. Columbia University Press, New York.

Gurley, K., Kijewski, T., and Kareem, A. (2001). Higher order correlation detection in nonlinear aerodynamic systems using wavelet transforms. In *Proc. Int. Conf. on Structural Safety and Reliability*, Newport Baech, Calif.

Hansen, R. J., Reed, J. W., and Vanmarcke, E. H. (1973). Human response to wind-induced motion of buildings. *Journal of the Structural Division. Proceedings of the ASCE*, **99**(ST7), 1589–1605.

HKCOP 2004 (2004). Hong Kong Code of Practice. Code of Practice for Structural Use of Concrete. Buildings Department, Hong Kong.

HKCOP 2005 (2005). Hong Kong Code of Practice. Code of Practice for Structural Use of Steel. Buildings Department, Hong Kong.

Holmes, J., Rofail, A., and Aurelius, L. (2003). High frequency base balance methodologies for tall buildings with torsional and coupled resonant modes. In T. T. Univ., editor, *Proc. 11th International Conference on Wind Engineering*, pages 2381–2388, Lubbock, Texas.

Holmes, J. D. (1998). Response of cylindrical structures to vortex shedding in the natural wind. In *Proc. 13th Australasian Fluid Mechanics Conference*, Monash University, Melbourne, Australia.

Holmes, J. D. (2001). *Wind Loading of Structures*. Spoon Press.

Holmes, J. D., Melbourne, W. H., and Walker, G. R. (1990). A commentary on the australian standard for wind load - AS1170.2-1989. Technical report, Australian Wind Engineering Society.

Huang, M. (2008). *Performance-based Serviceability Design Optimization of Wind Sensitive Tall Buildings*. Ph.D. thesis, Hong Kong University of Science and Technology.

Irwin, A. (1986). Motion in tall buildings. In *Proceedings of Conference on tall buildings, Second Century of the Skyscraper*, Chicago.

Irwin, A. W. (1978). Human response to dynamic motion of structures. *The Structural Engineer*, **56**(9), 237–243.

ISO 6897 (1984). Guidelines for the Evaluation of the Response of Occupants of Fixed Structures, Especially Buildings and Offshore Structures, to Low- Frequency Horizontal Motion (0.063 to 1.0 Hz). International Organization for Standardization, Geneva, Switzerland.

Isyumov, N. (1982). The aeroelastic modeling of tall buildings. In T. A. Reynhold, editor, *Wind tunnel modeling for civil engineering applications*, pages 373–407.

Isyumov, N. (1993). Criteria for acceptable wind-induced motions of tall buildings. In *International Conference of Tall Buildings*, Rio de Janerio. Council of Tall Buildings and Urban Habitat, CTBUH.

Isyumov, N., Davenport, A. G., and Monbaliu, J. (1984). CN Tower, Toronto - Model and full scale response to wind. In *Proc. 12^{th} Congress IABSE*, Vancouver, Canada.

Jeary, A. P., Morris, R. G., and Tomlinson, R. W. (1988). Perception criteria of vibration - tests in a tall building. *Journal of Wind Engineering and Industrial Aerodynamics*, **28**, 361–370.

JGJ 3-2002 (2002). National Standard of the People's Republic of China. Thecnical Specification for Concrete Structures of Tall Buildings. New World Press, Beijing, China.

Kanda, J., Tamura, Y., and Fujii, K. (1988). Probabilistic criteria for human perception of low-frequency horizontal motions. In *Symposium/Workshop on Serviceability of Buildings (Movements, Deformations, Vibrations)*, volume 1, pages 260–269.

Kanda, J., Tamura, Y., and Fujii, K. (1990). Probabilistic perception limits of low-frequency horizontal motions. In *Proceedings of the Conference with International Participation on Serviceability of Steel and Composite Structures*, pages 61–72.

Kareem, A. (1982). Acrosswind response of buildings. *Journal of the Structural Division. ASCE*, **108**(ST4), 869–887.

Kareem, A. (1985). Lateral-torsional motion of tall buildings. *Journal of Structural Engineering*, **111**(11), 2479–2496.

Kareem, A. (1988). Wind-induced response of buildings: A serviceability viewpoint. In *Proceedings of National Engineering Conference*, American Institute of Steel Construction, Miami Beach, FL.

Kareem, A. (1992). Serviceability issues and motion control of tall buildings. In *Proc. of Structures Congress*, San Antonio.

Kareem, A., Kijewski, T., and Tamura, Y. (1999). Mitigation of motions of tall buildings with specific examples of recent applications. *Wind and Structures*, **2**(3), 201–251.

Kawai, H. (1983). Pressure fluctuations on square prisms - applicability of strip and quasi-steady theories. *Journal of Wind Engineering and Industrial A*, **13**, 197–208.

Kawai, H. (1992). Vortex induced vibrations of tall buildings. *Journal of Wind Engineering and Industrial Aerodynamics*, **41-44**, 117–128.

Kawai, H. (1995). Effects of angle of attack on vortex induced vibration and galloping of tall buildings in smooth and turbulent boundary layer flows. *Journal of Wind Engineering and Industrial Aerodynamics*, **54-55**, 125–132.

Kawai, H., Okuda, Y., and Ohashi, M. (2009). Three dimensional structures of flow behind a square prism. In *Proceedings of the 7^{th} Asia-Pacific Conference on Wind Engineering*, Taipei, Taiwan.

Kawai, H., Okuda, Y., and Ohashi, M. (2011). Near wake structure behind a 3D square prism with an aspect ratio of 2.7 in a shallow boundary layer flow. In *Proceedings of the 13^{th} International Conference on Wind Engineering (ICWE13)*, Amsterdam, The Netherlands.

Kijewski, T. and Kareem, A. (1998). Dynamic wind effects: A comparative study of provisions in codes and standars with wind tunnel data. *Wind and Structures*, **1**(1), 77–109.

Kijewski, T., Haan, F., and Kareem, A. (2000). *Wind-Induced Vibrations*. Academic Press.

Kilpatrick, J. (1996). *The Influence of Wind-Induced Motions on the Performance of Tall Buildings*. Master's thesis, Faculty of Graduate Studies. The University of Western Ontario, London Ontario.

Kim, Y. and Kanda, J. (2010). Characteristics of aerodynamic forces and pressures on square plan buildings with height variations. *Journal of Wind Engineering and Industrial*, **98**, 449–465.

Kwok, K. C. S. (1982). Cross-wind response of tall buildings. *Engineering Structures*, **4**, 256–262.

Kwok, K. C. S. and Melbourne, W. H. (1981). Wind-induced lock-in excitation of tall structures. *Journal of the Structural Division. ASCE*, **107**(ST1), 57–72.

Kwok, K. C. S., Hitchcock, P. A., and Burton, M. D. (2009). Perception of vibration and occupant comfort in wind-excited tall buildings. *Journal of Wind Engineering and Industrial Aerodynamics*, **97**, 368–380.

Laneville, A., Gartshore, I. S., and Parkinson, G. V. (1977). An explanation of some effects of turbulence on bluff bodies. In *Proceedings 4th International Conference, Wind Effects on Buildings and Structures*. Cambridge University Press, Cambridge, U.K.

Lee, B. E. (1975). The effect of turbulence on the surface pressure field of a square prism. *Journal of Fluid Mechanics*, **69**, 263–282.

Liang, S., Liu, S., Li, Q. S., Zhang, L., and Gu, M. (2002). Mathematical model of acrosswind dynamic loads on rectangular tall buildings. *Journal of Wind Engineering and Industrial Aerodynamics*, **90**, 1757–1770.

Liang, S., Chen, Y., Tang, H., and Xu, F. (2011). Investigation of Reynolds number effect of wind pressure on square cylinder by wind tunnel test. In *Proceedings of the 13th International Conference on Wind Engineering (ICWE13)*, Amsterdam, The Netherlands.

Marra, A. M. (2011). *Vortex-Shedding Risk Assessment of Bridge Decks*. Ph.D. thesis, University of Florence and TU Braunschweig.

Marukawa, H., Kato, N., Fujii, K., and Tamura, T. (1996). Experimental evaluation of aerodynamic damping of tall buildings. *Journal of Wind Engineering and Industrial Aerodynamics*, **59**, 177–190.

McNabb, J. W. and Muvdi, B. B. (1975). Drift reduction factors for belt high-rise structures. *Engineering Journal*, **3nd Quarter**, 88–91.

McNamara, R., Kareem, A., and Kijewski, T. (2002). Ask the experts... perception of motion criteria for tall buildings subjected to wind: a panel discussion. In *Proc. Structures Congress*.

Melbourne, N. H. and Cheung, J. C. K. (1988). Designing for serviceable accelerations in tall buildings. In *4th International Conference on Tall Buildings*, pages 148–155.

Melbourne, W. H. and Palmer, T. R. (1992). Accelerations and comfort criteria for buildings undergoing complex motions. *Journal of Wind Engineering and Industrial Aerodynamics*, **41-44**, 105–116.

Nakata, S., Tamura, Y., and Otsuki, T. (1993). Study on the habitability to horizontal vibration of low-rise buildings. In *International Colloquium on Structural Serviceability of Buildings*.

NBCC (1977). National Building Code of Canada. Structural Commentaries (Part 4). National Research Council of Canada, Ottawa, Ontario.

NBCC (1990). National Building Code of Canada. Structural Commentaries (Part 4). National Research Council of Canada, Ottawa, Ontario.

Oka, S. and Ishihara, T. (2009). Numerical study of aerodynamic characteristics of a square prism in a uniform flow. *Journal of Wind Engineering and Industrial Aerodynamics*, **97**, 548–559.

Ozgoren, M. (2006). Flow structure in the downstream of square and circular cylinders. *Flow Measurement and Instrumentation*, **17**, 225–235.

Pastò, S. (2008). Vortex-induced vibrations of a circular cylinder in laminar and turbulent flows. *Journal of Fluids and Structures*, **24**(7), 977–993.

Paulotto, C., Ciampoli, M., and Augusti, G. (2004). Some proposals for a first step towards a performance-based wind engineering. In *Proceedings of the IFED - International Forum in Engineering Decision making. First Forum.*, Stoos, Switzerland, December, 5-9. `http://www.ifed.ethz.ch`.

Pliefke, T., Sperpeck, S., and Urban, M. (2006). The probabilistic risk management chain - general concepts and definitions. Technical report, Internal discussion paper, International Graduate College 802.

Pliefke, T., Sperbeck, S., Urban, M., Peil, U., and Budelmann, H. (2007). A standardized methodology for managing disaster risk - an attempt to remove ambiguity. In *V International Pobabilistic Workshop*.

Porter, K. A. (2003). An overview of PEER's performance-based earthquake engineering methodology. In *Proc. Ninth International Conference on Applications of Statistics and Probability in Civil Engineering (ICASP9)*, volume 2, pages 973–980, Civil Engineering Risk and Reliability Association (CERRA), San Francisco, CA, USA.

Quan, Y., Gu, M., and Tamura, Y. (2005). Experimental evaluation of aerodynamic damping of square super high-rise buildings. *Wind and Structures*, **8**(6), 309–324.

Rathburn, J. C. (1940). Wind forces on a tall building. *Transactions, American Society of Civil Engineers*, **105**, 1–41.

Reed, J. W. (1971). Wind induced motion and human comfort. Research Report 71-42, MIT - Massachusetts Institute of Technology.

Reiher, H. and Meister, F. J. (1931). The effect of vibration on people. *Forschung auf dem Gebeite des Ingenieurwesens*, **2**(II). (transl. by Headquarters Air Material Command, Wright Field, Ohio, Report F-TSL-616-RE, 1946).

Reinhold, T. A. and Sparks, P. R. (1979). The influence of wind direction on the response of a square-section tall building. In J. Cermak, editor, *Wind Engineering (Proceedings of the Fifth International Conference)*, pages 685–698. Pergamon Press.

Ruscheweyh, H. (2010). Experience with vortex-induced vibrations. *CICIND Report*, **26**(2), 49–57.

Saha, A. K., Muralidhar, K., and Biswas, G. (2000). Experimental study of flow past a square cylinder at high Reynolds numbers. *Experiments in Fluids*, **29**, 553–563.

Saunders, J. W. and Melbourne, W. H. (1975). Tall rectangular building response to cross-wind excitation. In *Proc. 4th Int'l Conf. on Wind Effects on Buildings and Structures*, pages 369–379. Cambridge University Press, London.

Scruton, C. (1981). *An Introduction to Wind Effects on Structures. Engineering Design Guides, 40.* Published for the Design Council, the British Standards Institution and the Council of Engineering Institutions by Oxford University Press.

Scruton, C. and Rogers, E. W. E. (1972). Steady and unsteady wind loading of buildings and structures. *Philosophical Transactions Royal Society, A*, **269**, 353–383.

Shioya, K. and Kanda, J. (1993). Human perception thresholds of horizontal motion. In *International Colloquium on Structural Serviceability of Buildings - IABSE Reports*, volume 65, pages 45–52.

Shioya, K., Kanda, J., Tamura, Y., and Fujii, K. (1992). Human perception thresholds of two dimensional horizontal motion. In *Structures Congress '92*, pages 480–483. American Society of Civil Engineers - ASCE.

Simiu, E. and Scanlan, R. (1996). *Wind Effects on Structures.* John Wiley & Sons, Inc.

Spence, S. M. J. (2009). *Time Domain Non-Gaussian Optimization of Wind Excited Tall Buildings Under Vulnerability Constraints.* Ph.D. thesis, University of Florence and TU Braunschweig.

Spurr, H. V. (1930). *Wind Bracing: the Importance of Rigidity in High Towers.* McGraw-Hill, first edition.

Stafford Smith, B. and Coull, A. (1991). *Tall Building Structures: Analysis and Design.* Wiley, New York.

Steckley, A. C., Lythe, G., Isyumov, N., and Davenport, A. G. (1985). Aeroelastic wind tunnel model study of the new Bank of China Building, Hong Kong. Technical report, BLWT-SS-85, The University of Western Ontario, Canada.

Strouhal, V. (1878). Über eine besondere Art der Tonerregung. *Annalen der Physik und Chemie*, pages 216–251.

Suda, K., Sataka, N., Ono, J., and Sasaki, A. (1996). Damping properties of buildings in Japan. *Journal of Wind Engineering and Industrial Aerodynamics*, **59**, 383–392.

Takle, E. S. and Brown, J. M. (1978). Note on the use of Weibull statistics to characterize wind-speed data. *Journal of Applied Meteorology*, **17**.

Tamura, Y. (2003). Design issues for tall buildings from accelerations to damping - tribute to Hatsuo Ishizaki and Vinod Modi. In *Proceedings of the 11th International Conference of Wind Engineering - ICWE11.* International Association for Wind Engineering - IAWE.

Taylor, I. and Vezza, M. (1999). Prediction of unsteady flow around square and rectangular section cylinders using a discrete vortex method. *Journal of Wind Engineering and Industrial Aerodynamics*, **82**, 247–269.

Tschanz, T. (1982a). *The Base Balance Measurement Technique and Applications to Dynamic Wind Loading of Structures*. Ph.D. thesis, University of Western Ontario, Faculty of Engineering Science.

Tschanz, T. (1982b). Measurement of total dynamic loads using elastic models with high natural frequencies. In T. A. Reynhold, editor, *Wind tunnel modeling for civil engineering applications*, pages 296–312.

Tschanz, T. and Davenport, A. G. (1983). The base balance technique for the determination of dynamic wind loads. *Journal of Wind Engineering and Industrial Aerodynamics*, **13**, 429–439.

Tse, K. T., Hitchcock, P. A., and Kwok, K. C. S. (2009). Mode shape linearization for HFBB analysis of wind-excited complex tall buildings. *Engineering Structures*, **31**, 675–685.

UNI-EN 1991-1-4 (2005). Eurocode 1. Actions on Structures. Part 1-4: General actions - Wind actions.

Van Oudheusden, B. W., Scarano, F., van Hinsberg, N. P., and Roosenboom, E. W. M. (2008). Quantitative visualization of the flow around a square-section cylinder at incidence. *Journal of Wind Engineering and Industrial Aerodynamics*, **96**, 913–922.

Vickery, B. J. (1966). Fluctuating lift and drag on a long cylinder of square cross-section in a smooth and in a turbulent stream. *Journal of Fluid Mechanics*, **25**(3), 481–494.

Vickery, B. J. (1990). Experimental techniques for the determination of the dynamic responses of structures to wind. *Meccanica*, **25**, 147–158.

Vickery, B. J. and Basu, R. I. (1983). Across-wind vibrations of structures of circular cross-section. Part 1. Development of a mathematical model for two-dimensional conditions. *Journal of Wind Engineering and Industrial Aerodynamics*, **12**, 49–73.

Vickery, B. J. and Clark, A. W. (1972). Lift or across-wind response of tapered stacks. *Journal of Stuctural Division, ASCE*, **98**, 1–20.

Von Gierke, H. E. and Brammer, A. J. (1996). Effect of shock and vibration on humans. In C. Harris, editor, *Shock and Vibration Handbook*, pages 44.1–44.67. McGraw Hill, New York, USA, ii edition.

Von Kármán, T. (1911). Über den Mechanismus des Widerstandes den ein bewegter körper in einer Flüssigkeit erfärt. In *Nachrichten der Königlichen Gesellschaft der Wissenschaften*, pages 509–517, Göttingen.

Šoda, A., Mannini, C., and Sjirić, M. (2011). Investigation of unsteady air flow around two-dimensional rectangular cylinders. *Transactions of FAMENA*, **35**, 11–34.

Wang, H. F. and Zhou, Y. (2009). The finite-length square cylinder near wake. *Journal of Fluid Mechanics*, **638**, 453–490.

Wang, H. F., Zhou, Y., Chan, C. K., Wong, W. O., and Lam, K. S. (2004). Flow structure around a finite-length square prism. In *Proc. 15th Australasian Fluid Mechanics Conference*, The University of Sidney, Sydney, Australia.

Weibull, W. (1951). A statistical distribution function of wide applicability. *Journal of Applied Mechanics*, **18**.

Whitbread, R. E. (1975). The measurement of non-steady wind forces on small-scale building models. In *Proc. 4th Int'l Conf. on Wind Effects on Buildings and Structures*, pages 567–574, Heathrow, England. Cambridge University Press, London.

Wieringa, J. (1993). Representative roughness parameters for homogeneous terrain. *Buondary-Layer Meteorology*, **63(4)**, 323–363.

Willamson, C. H. K. (1996). Vortex dynamics in the cylinder wake. *Annual Review of Fluid Mechanics*, **28**, 477–539.

Willamson, C. H. K. and Govardhan, R. (2004). Vortex-induced vibrations. *Annual Review of Fluid Mechanics*, **36**, 413–455.

Willamson, C. H. K. and Govardhan, R. (2008). A brief review of recent results in vortex-induced vibrations. *Journal of Wind Engineering and Industrial Aerodynamics*, **96**, 713–735.

Zhou, Y. and Kareem, A. (2003). Aeroelastic balance. *Journal of Engineering Mechanics*, **129**(9), 283–292.

Zhou, Y., Gu, M., and Xiang, H. F. (1999). Along-wind static equivalent loads and responses of tall buildings. Part II: Effects of mode shapes. *Journal of Wind Engineering and Industrial Aerodynamics*, **79**(1-2), 151–158.

Zhou, Y., Kareem, A., and Gu, M. (2002). Mode shape corrections for wind load effects. *Journal of Engineering Mechanics*, **128**(1), 15–23.

Zhou, Y., Kijewski, T., and Kareem, A. (2003). Aerodynamic loads on tall buildings: interactive database. *Journal of Structural Engineering, ASCE*, **129**(3), 394–404.